

This electronic thesis or dissertation has been downloaded from the King's Research Portal at <https://kclpure.kcl.ac.uk/portal/>



**MRI with zero echo time  
quick, quiet, quantitative**

Ljungberg, Emil

*Awarding institution:*  
King's College London

The copyright of this thesis rests with the author and no quotation from it or information derived from it may be published without proper acknowledgement.

**END USER LICENCE AGREEMENT**



**Unless another licence is stated on the immediately following page** this work is licensed

under a Creative Commons Attribution-NonCommercial-NoDerivatives 4.0 International

licence. <https://creativecommons.org/licenses/by-nc-nd/4.0/>

You are free to copy, distribute and transmit the work

Under the following conditions:

- Attribution: You must attribute the work in the manner specified by the author (but not in any way that suggests that they endorse you or your use of the work).
- Non Commercial: You may not use this work for commercial purposes.
- No Derivative Works - You may not alter, transform, or build upon this work.

Any of these conditions can be waived if you receive permission from the author. Your fair dealings and other rights are in no way affected by the above.

**Take down policy**

If you believe that this document breaches copyright please contact [librarypure@kcl.ac.uk](mailto:librarypure@kcl.ac.uk) providing details, and we will remove access to the work immediately and investigate your claim.

# MRI with Zero Echo Time: Quick, Quiet, Quantitative



**Emil Ljungberg**  
Department of Neuroimaging  
King's College London

A thesis submitted for the degree of  
*Doctor of Philosophy*  
*in Neuroimaging Physics*

June, 2020

**Supervisors:**  
Prof. Gareth Barker  
Dr. Shannon Kolind  
Dr. Florian Wiesinger



© 2020

The copyright of this thesis rests with the author and no quotation from it or information derived from it may be published without proper acknowledgement.

# MRI with Zero Echo Time: Quick, Quiet, Quantitative

Emil Ljungberg

## Abstract

Magnetic Resonance Imaging (MRI) is a powerful imaging method for studying the human body. One issue with MRI is the loud acoustic noise produced by the scanner, requiring the subject to wear hearing protection, which typically solves the problem, but in some cases, even the attenuated noise can cause discomfort. In other situations, hearing protection might not even be possible, such as in utero MRI. The reduction of acoustic noise during scanning can improve patient comfort and is believed to increase patient compliance.

The Rotating Ultra-Fast Imaging Sequence (RUFIS) is an inherently silent MRI acquisition technique using a zero echo time (ZTE), 3D radial acquisition. The sequence is designed to have minimal gradient switching which results in a near-silent acquisition. RUFIS has not yet been adopted in research studies nor in clinical settings, likely due to the lack of options for different image contrasts, such as  $T_1$  and  $T_2$ . This thesis aims to improve our understanding of how to produce useful contrasts using RUFIS through the development of quantitative  $T_1$  and  $T_2$  mapping methods.

Through theoretical analysis of the pulse sequence, it is shown that RUFIS can be treated as a spoiled gradient echo (SPGR) sequence. In a feasibility study, RUFIS is compared to Cartesian SPGR for variable flip angle  $T_1$  mapping at 3T, a study which is also extended to 1.5T and 7T scanners.  $T_2$  contrast is introduced in RUFIS using an adiabatic  $T_2$  preparation module. A multi-contrast acquisition is then developed, combining  $T_1$  and  $T_2$  magnetisation preparation for simultaneous  $T_1$  and  $T_2$  mapping. To further extend the usability of RUFIS, a novel retrospective motion correction technique is developed using a new k-space trajectory for self-navigation. The technique is validated through simulation and in a phantom.

This thesis proves that RUFIS can be used for silent  $T_1$  and  $T_2$  mapping. Combined with retrospective motion correction, RUFIS provides a competitive pulse sequence option in situations where silent imaging is warranted.

# Acknowledgements

This thesis would never have come together had it not been for the tremendous amount of help and support I have received from so many people over the last three years. First and foremost, I would like to extend the biggest thank you to my main supervisor Gareth Barker, who has been a fantastic supervisor with seemingly infinite amounts of patience, energy, and ideas. I feel very fortunate to have been working so closely with Gareth in my PhD. He constantly goes above and beyond what is expected in his role as supervisor. A big thank you also goes out to Shannon Kolind who has guided me in the field of MRI since my first day setting foot at UBC in Vancouver for my master's degree. Throughout both of my degrees, she has given me the opportunity to work independently while always giving support when needed. She also arranges the best trips for ISMRM! I want to acknowledge all the support I have received from my collaborators at GE Healthcare. Firstly, Florian Wiesinger who has an eye for detail, and analytic mind like no one else. Through visits to Munich, but mostly over Skype, he has provided invaluable advice on MR physics. He is also an amazing source of inspiration, constantly coming up with new ideas for projects. Thanks also to Ana-Beatriz Solana for support with pulse programming since day one, Brian Burns for helping out with experiments on the 7T scanner at UCSF, and Mark Symms for everything GE related basically. I also want to acknowledge and thank Peder Larson at UCSF for arranging the collaboration to work with the 7T scanner at UCSF.

There is a large group of people in the department of Neuroimaging at King's College London who have been instrumental in my PhD. Big thanks to Steven Williams for providing support and feedback on the project from day one. I'm also very happy that I got to work in the same department and so closely with Tobias Wood through my PhD. Toby is a great friend and colleague, and without his support and feedback about everything related to  $T_1$  mapping, MT, EPIC, Python, and C, I would not have finished this project (in this time frame). Big thanks to Nikou Damestani for being a great office buddy and confidant

as the other PhD student in *Team Silent* in the department, my work has improved a lot from our many discussions throughout the project.

My time in London and at King's would not have been the same without all the fantastic people I have met here. Thanks to: Nuria Mackes who gave me a place to stay for the first month in London and who has been a great office buddy; Anthony Gabbay for introducing me to D&D and being the one and only Dungeon Master; and Natalie Gottlieb, Richard Parker, and Niall Bourke for taking on the adventures of D&D and London together with me. Thanks to Katrina McMullen for always being up for heading to the pub when there is rugby on. I'm also very happy that got to know and work with Anna Combes during my time at UBC and that she had moved back to the department at King's when I started my PhD. Thanks to Kieran Gandhi for being an awesome housemate, and for making some amazing drinks and dinners over the years. I also want to dedicate a special thank you to Julia Schubert for being a great support through my PhD.

Finally, I want to thank my family for their support and encouragement in pursuing this PhD. Your support has been invaluable, and I could not have done this without your support. Tack!

## Funding

During my PhD I was funded jointly through a PhD studentship from the National Institute for Health Research (NIHR) Biomedical Research Centre at South London and Maudsley NHS Foundation Trust and King's College London and General Electric (GE) Healthcare. This thesis also represents independent research part funded by the NIHR-Wellcome Trust King's Clinical Research Facility and the National Institute for Health Research (NIHR) Biomedical Research Centre at South London and Maudsley NHS Foundation Trust and King's College London. The views expressed are those of the author and not necessarily those of the NHS, the NIHR or the Department of Health and Social Care.

I also received funding through: the King's College London Global Research Grant to visit collaborators at UCSF, Guarantors of Brain Travel Grant to attend ISMRM, student stipend from the ISMRM and a student stipend from ESMRMB.

# Contents

<b>List of Figures</b>	<b>6</b>
<b>List of Tables</b>	<b>17</b>
<b>Acronyms and Glossary</b>	<b>20</b>
<b>Publications</b>	<b>23</b>
<b>1 Introduction</b>	<b>27</b>
1.1 Thesis Overview . . . . .	28
1.2 Student Contribution . . . . .	29
1.3 Ethical Approval . . . . .	29
<b>2 Magnetic Resonance Imaging</b>	<b>31</b>
2.1 Introduction to Magnetic Resonance Imaging . . . . .	32
2.2 MRI of the Brain . . . . .	44
2.3 Contrast Weighted Imaging and Acquisition Parameters . . . . .	47
2.4 Quantitative Parameter Mapping . . . . .	48
2.5 Acoustic Noise in MRI . . . . .	54
<b>3 The Rotating Ultra-Fast Imaging Sequence - RUFIS</b>	<b>60</b>
3.1 MRI with Zero Echo Time . . . . .	61
3.2 The RUFIS Pulse Sequence . . . . .	63
3.3 Image Reconstruction . . . . .	69
3.4 Study A: Comparison of Gridding Methods . . . . .	73
3.5 Study B: A Quantitative Signal Equation for RUFIS . . . . .	77
3.6 Study C: A Rotating 3D Excitation Profile . . . . .	82
3.7 Study D: Acoustic Noise . . . . .	86
3.8 Chapter Discussion and Conclusions . . . . .	90
3.9 Publications and Contribution . . . . .	91
<b>4 <math>T_1</math> Mapping Using the Variable Flip Angle Method</b>	<b>92</b>
4.1 Introduction . . . . .	93
4.2 Considerations for VFA $T_1$ Mapping with RUFIS . . . . .	94
4.3 Silent $B_1^+$ Mapping . . . . .	96
4.4 Reproducibility and SPGR Comparison Study . . . . .	102
4.5 Chapter Discussion and Conclusion . . . . .	115
4.6 Publications and Contribution . . . . .	116

<b>5</b>	<b>T<sub>1</sub> Mapping Across Field Strengths</b>	<b>118</b>
5.1	Introduction . . . . .	119
5.2	A Theoretical Perspective on RUFIS Across Field Strengths . . . . .	120
5.3	RUFIS T <sub>1</sub> Mapping at 1.5, 3, and 7T . . . . .	130
5.4	Chapter Discussion and Conclusion . . . . .	148
5.5	Publications and Contribution . . . . .	149
<b>6</b>	<b>Multi-Contrast Magnetisation Prepared RUFIS</b>	<b>151</b>
6.1	Introduction . . . . .	152
6.2	T <sub>2</sub> Contrast Using Magnetisation Preparation . . . . .	152
6.3	A T <sub>2</sub> Prepared RUFIS Sequence . . . . .	158
6.4	Combined T <sub>1</sub> and T <sub>2</sub> Mapping with RUFIS . . . . .	166
6.5	Simulating MT Effects in Multi-Contrast RUFIS . . . . .	185
6.6	Chapter Discussion and Conclusion . . . . .	191
6.7	Publications and Contribution . . . . .	193
<b>7</b>	<b>Motion Correction with Self-Navigated RUFIS</b>	<b>195</b>
7.1	Introduction . . . . .	196
7.2	The Spiral Phyllotaxis Trajectory . . . . .	199
7.3	Translation and Rotation Correction in k-space . . . . .	213
7.4	A Numerical Brain Phantom . . . . .	215
7.5	Using 3D Phyllotaxis for Rotation Correction . . . . .	216
7.6	Using 3D Phyllotaxis for Translation Correction . . . . .	229
7.7	Rigid Body Motion Correction . . . . .	232
7.8	Chapter Discussion and Conclusion . . . . .	241
7.9	Publications and Contribution . . . . .	245
<b>8</b>	<b>Conclusions and Further Work</b>	<b>246</b>
8.1	Quick . . . . .	247
8.2	Quiet . . . . .	248
8.3	Quantitative . . . . .	250
8.4	Summary of Main Contributions . . . . .	251
<b>A</b>	<b>Delaunay Interpolation on Spherical Shells</b>	<b>253</b>
<b>B</b>	<b>Phantoms</b>	<b>255</b>
B.1	The Quantitative EUROSPIN Phantom . . . . .	255
B.2	Motion Correction Phantom . . . . .	257
<b>C</b>	<b>Restricted Linear Flip Angle Sampling Scheme</b>	<b>258</b>
<b>D</b>	<b>Bloch-Simulations</b>	<b>260</b>
<b>E</b>	<b>The Golden Angle and the 3D Spiral Phyllotaxis Trajectory</b>	<b>261</b>
E.1	Introduction . . . . .	261
E.2	The Golden Ratio and the Fibonacci Sequence . . . . .	261
E.3	The Golden Angle - From Botany to Brain Imaging . . . . .	263
	<b>References</b>	<b>268</b>

# List of Figures

2.1	Example of <b>(a)</b> $T_1$ recovery of $M_z$ and <b>(b)</b> $T_2$ relaxation of $M_\perp$ following a $\pi/2$ RF pulse. . . . .	37
2.2	Illustration of a simple spin echo experiment showing the pulse sequence diagram in <b>(a)</b> and the evolution of five isochromats in <b>(b)</b> . Excitation is performed at $t = t_0$ , a $180^\circ$ refocusing pulse is applied at $t = t_1 = TE/2$ producing a refocused spin echo at $t = t_2 = TE$ . . . . .	38
2.3	Illustration of a simple gradient echo experiment showing the pulse sequence diagram in <b>(a)</b> and the evolution of five isochromats in <b>(b)</b> . Excitation is performed at $t = t_0$ after which a gradient is applied to cause deliberate dephasing of the spins. At $t = t_1 = TE/2$ , the gradient amplitude is inverted and a gradient echo is produced at $t = t_2 = TE$ . The isochromats are not perfectly refocused, thus resulting in $T_2^*$ decay. . . . .	39
2.4	Schematic of a 2D spin echo pulse sequence. <b>(1)</b> Slice encoding along the $z$ axis is followed by <b>(2)</b> phase encoding along $y$ , the coloured lines indicate the gradient amplitude at subsequent repetitions with different amplitudes to traverse k-space along different frequency encoding lines. <b>(3)</b> At a time $TE/2$ , a $180^\circ$ refocusing pulse is played out to produce a spin echo at time $TE$ <b>(4)</b> where data is acquired with a frequency encoding gradient along $x$ . . . . .	41
2.5	<b>(a)</b> K-space sampling diagram for the spin echo sequence shown in figure 2.4 with <b>(b)</b> examples of where different spatial frequencies are located in k-space. . . . .	42
2.6	Example of contrast weighted images simulated by the BrainWeb platform [45]. <b>(a)</b> PD weighted spin echo (SE), $TE/TR$ : 10/5000ms. <b>(b)</b> $T_2$ weighted SE, $TE/TR$ : 100/5000ms. <b>(c)</b> Stronger $T_2$ weighted SE, $TE/TR$ : 200/5000ms. <b>(d)</b> $T_1$ weighted inversion recovery SE, $TE/TI/TR$ : 3/1100/2530ms. . . . .	48
2.7	Example of short repetition time (TR) spoiled gradient echo images for different flip angles simulated using the BrainWeb platform [45]. (Simulation parameters: $TE/TR=2/5$ ms) . . . . .	48
2.8	Maximum exposure time at different sound pressure levels. . . . .	56
3.1	Comparison between spin echo <b>(a)</b> , gradient echo <b>(b)</b> , and zero TE (ZTE) <b>(c)</b> pulse sequences. These pulse sequence diagrams are simplified for illustration of the different concepts, practical implementations will differ to these sketches. . . . .	61

3.2	Overview of the RUFIS sequence. <b>(a)</b> The sequence is divided into segments, where each segment <b>(b)</b> consists of a number of spokes, i.e. collection of data along centre-out radial projections in k-space. <b>(c)</b> Each spoke comprises a single hard radio frequency (RF) pulse and an free induction decay (FID) readout. The time from the centre of the RF pulse (when the trajectory through k-space beings) to the beginning of data collection leads to a dead-time gap $\Delta_1$ , resulting in missed k-space samples (gray dots in <b>(c)</b> ). The number of samples missed depends on the dwell time $\tau$ . . . . .	64
3.3	Example of a RUFIS k-space trajectory. <b>(a)</b> Gradient waveforms ( $G_x, G_y, G_z$ ) showing the spiral trajectory in $x$ and $y$ while the $z$ gradient is linear. <b>(b)</b> 3D view of the k-space trajectory showing the end-points of the spokes connected by a line, demonstrating the smooth changes between subsequent spokes, and thus near-silent readout. . . . .	65
3.4	<b>(a)</b> Schematic 2D view of a radial trajectory showing the spokes originating from the centre of k-space. <b>(b)</b> To satisfy Nyquist, the samples are spaced $\Delta k$ apart in the radial direction, and $\Delta k$ in the angular direction at the end of the spokes. <b>(c)</b> The endpoints of the spokes fall onto the same spherical shell in k-space, where each spoke occupies an area $A_{samp} = \Delta k^2$ <b>(d)</b> . . . .	67
3.5	Example of images acquired with four different readout bandwidths (7.8, 15.6, 31.2, 62.5 kHz) with and without centre k-space filling using WASPI. The effect of missing samples in the centre of k-space is seen in the top row. . . . .	68
3.6	Example of how a low resolution reconstruction of RUFIS data can be used to produce sensitivity maps. Radial data is Fermi filtered and gridded to produce a low resolution image. Image from each coil is divided by the root-sum-of-squares (RSS) image to produce complex valued coil sensitivity maps. . . . .	72
3.7	Example of RUFIS multi-coil reconstruction pipeline. In the top row, DC compensation is not applied resulting in significant blurring of the image. . . . .	73
3.8	Comparison of point spread functions obtained using <b>(a)</b> Kaiser-Bessel and <b>(b)</b> Nearest-Neighbour gridding. Top row shows the point function in image space, and bottom row the line profile through isocentre along each of the three axes. The data is visualised on a logarithmic scale. The dashed white rectangle in the top row outlines the nominal field of view. . . . .	75
3.9	Shep-Logan phantom after gridding using KB <b>(a)</b> and NN <b>(b)</b> visualised on linear scale and logarithmic scale, together with line profile <b>(c)</b> along the white dashed line. Top row shows data with $N_1$ number of spokes, and bottom row $3 \cdot N_1$ number of spokes. Solid rectangle indicates the nominal field of view. . . . .	76
3.10	Comparison of KB and NN gridding in vivo. Brain slices in <b>(a)</b> shows less gridding artefacts with NN compared to KB. Line profiles in <b>(b)</b> shows difference in image intensity in the middle of the brain, similar to the phantom examples. Solid rectangles in <b>(a)</b> and dashed black lines in <b>(b)</b> indicate the nominal field of view. . . . .	77
3.11	Example of RUFIS sequence with multiple magnetisation preparation modules. . . . .	79
3.12	<b>(a)</b> : Example of steady state signal simulations of the RUFIS sequence for different number of spokes per segment. With 512 spokes per segment (maximum), the error between the SPGR equation and analytical RUFIS equation is negligible. <b>(b)</b> : Error in quantitative $T_1$ fitting using the SPGR equation with simulated RUFIS data . . . . .	81



3.13	Simulation of contrast prepared RUFIS acquisition simulated using the iterative method. <b>(a)</b> 256 spokes per segment, $T_2=80\text{ms}$ , $TE=80\text{ms}$ . <b>(b)</b> $T_1=1\text{s}$ . $T_2=80\text{ms}$ , $TE=80\text{ms}$ . . . . .	81
3.14	<b>(a)</b> Effect of the rotating excitation profile at two different positions, on the same radius from iso-centre, over 1000 spokes for $\tau_{rf} = 64\mu\text{s}$ at $\pm 7.8\text{kHz}$ readout bandwidth. <b>(b)</b> Effective excitation profile for different pulse widths at $\pm 7.8\text{kHz}$ readout bandwidth, after averaging the excitation profile for all spokes. . . . .	84
3.15	Example of phantom data showing the effect of changing the width of the excitation pulse. Data obtained from spherical phantom with different pulse widths (top) and the corresponding line profiles through the phantom (bottom). . . . .	85
3.16	Average sound pressure levels, <b>(a)</b> LAeq and <b>(b)</b> LCpeak, from the 20s measurement period, comparing RUFIS at different bandwidths and resolutions, to SPGR and background noise levels. . . . .	87
3.17	Acoustic noise levels (LAeq [dB(A)]) across 11 octave bands from 16Hz to 16kHz. <b>(a)</b> Comparison between RUFIS ( $1.5 \times 1.5 \times 1.5 \text{ mm}^3$ and $BW=7.8\text{kHz}$ ), SPGR, and background noise levels. <b>(b)</b> Comparison of RUFIS acquisitions different readout bandwidths at resolution of $1.5 \times 1.5 \times 1.5 \text{ mm}^3$ . . . . .	88
3.18	Acoustic noise levels (LAeq [dB(A)]) across 11 octave bands from 16Hz to 16kHz comparison RUFIS acquisitions with different resolutions at bandwidths of <b>(a)</b> 7.8kHz, <b>(b)</b> 15.6kHz, <b>(c)</b> 31.2kHz. . . . .	88
4.1	Examples of SPGR curves showing the transverse magnetisation with the optimal pair of flip angles, indicated with dots, and the Ernst angle, crosses, for different $T_1$ <b>(a)</b> and TR <b>(b)</b> . . . . .	95
4.2	Pulse sequence diagram of the SIMBA sequence showing the composite magnetisation preparation module before the RUFIS readout. (Reproduced from my publication [166] with permission from Wiley and Sons.) . . . . .	99
4.3	Simulations showing the effects of <b>(A)</b> different $B_1^+$ efficiency ( $\lambda$ ) and <b>(B)</b> number of spokes in the RUFIS readout (Simulations parameters $\lambda = 1$ , $T_1 = 1\text{s}$ , RUFIS $\alpha=2^\circ$ and $TR=1 \text{ ms}$ . (Reproduced from my publication [166] with permission from Wiley and Sons.) . . . . .	100
4.4	Example of SIMBA acquisition showing axial slices from four volumes, the calculated $B_1^+$ map as well as signal curves from three regions of interest (ROI). (Reproduced from my ISMRM abstract [167]) . . . . .	101
4.5	Comparison of $B_1^+$ maps from SIMBA and the standard $B_1^+$ map on the GE platform, 2D Bloch-Siegert. The same patterns of the $B_1^+$ field are observed with both sequences. SIMBA was acquired with lower resolution and is therefore appearing less noisy. (Reproduced from my ISMRM abstract [167])	102
4.6	Comparison of $B_1^+$ maps between <b>(A)</b> SIMBA and <b>(B)</b> Bloch-Siegert. <b>(C)</b> $R_1$ maps ( $1/T_1$ ) calculated from RUFIS data without $B_1^+$ correction and with correction using the two different methods. <b>(D)</b> Relative $T_1$ error in RUFIS variable flip angle (VFA) when processed using the two different $B_1^+$ maps. (Reproduced from my publication (Ref [166]) with permission from Wiley and Sons.) . . . . .	107

4.7	Representative $T_1$ and proton density (PD) maps from one subject, acquired with RUFIS and SPGR. With RUFIS a $T_1$ and PD estimate can be obtained in the cortical bone (white arrow) due to effective $TE=0$ . (Reproduced from my publication (Ref [166]) with permission from Wiley and Sons.) . . . . .	108
4.8	$T_1$ histograms from WM and GM from each subject, obtained with RUFIS (black) and SGPR (gray). With RUFIS, $T_1$ is slightly higher in WM but lower in GM. Histograms calculated from the average of the two scans in the first visit. (Reproduced from my publication (Ref [166]) with permission from Wiley and Sons.) . . . . .	109
4.9	Comparison of $T_1$ estimates between RUFIS and SPGR within <b>(A)</b> in vivo ROIs and <b>(B)</b> the quantitative phantom. Both experiments shows similar results with lower estimates for longer $T_1$ with RUFIS. Data is from first scan in first visit. (Reproduced from my publication (Ref [166]) with permission from Wiley and Sons.) . . . . .	109
4.10	Simulation demonstrating the refocusing behaviour of the RUFIS trajectory with 1024 spokes, showing the integral of the X, Y, and Z gradient <b>(A-C)</b> , as well as the magnitude of the gradient along all three axes <b>(D)</b> (i.e. square root sum of squares), calculated using equation 4.9. . . . .	115
5.1	Demonstration of the in- and out-of-phase behaviour at 1.5, 3, and 7T. Lines shows k-space readout timings for different readout bandwidths. Greyscale background shows the in- and out-of-phase behaviour of water and fat, with white being in-phase and black out of phase. . . . .	121
5.2	Simulation of <b>(a)</b> $T_1$ and <b>(b)</b> $T_2^*$ as a function of field strength in white and gray matter. . . . .	125
5.3	Relative contrast to noise ratio (CNR) ( $CNR/B_0$ ) at four different field strength as a function of TR and flip angle. The relative CNR is shown to highlight the effects of the change in $T_1$ over field strengths. Solid line indicates maximum $T_1$ contrast, dashed vertical line indicates the in-phase TR ( $TR_{ip}$ ) . . . . .	128
5.4	<b>(a)</b> Achievable flip angle for different RF amplifier specifications together with the flip angle for optimal CNR. <b>(b)</b> Maximum CNR as a function of field strength for the same RF amplifier specifications. Dashed vertical lines indicate field strength for the maximum CNR. . . . .	129
5.5	Comparison of steady state RUFIS data collected at 7T with $\pm 7.8$ and $\pm 15.6$ kHz readout bandwidth. Severe off-resonance artefacts are seen around the sinuses (red arrow) and chemical shift artefacts around the skull (yellow arrow). . . . .	131
5.6	Comparison of the standard and linearised version of the SPGR equation, as proposed by Helms et al. [148], with an example 5 point sampling scheme. (Curves simulated with $TR=2$ ms and $T_1=1$ s) . . . . .	134
5.7	Quantitative maps from the 1.5T experiment, comparing the results from RUFIS and SPGR. Arrows indicate regions with short $T_2$ species where a good fit was obtained with RUFIS but not SPGR (pink: cortical bone, yellow: the clivus) . . . . .	138
5.8	Quantitative maps from the 3T experiment, comparing the results from RUFIS and SPGR. . . . .	139

5.9	Quantitative maps in axial slices from the 7T experiment, comparing the results from RUFIS and SPGR at both $\pm 15.6$ and $\pm 31.2$ kHz readout bandwidths. . . . .	139
5.10	Quantitative maps in sagittal slices from the 7T experiment, comparing the results from RUFIS and SPGR at both $\pm 15.6$ and $\pm 31.2$ kHz readout bandwidths. . . . .	140
5.11	Comparison of $T_1$ histograms between RUFIS and SPGR across field strengths.	140
5.12	Comparison of $T_1$ histograms across field strengths for RUFIS and SPGR in white matter (top) and gray matter (bottom). . . . .	141
5.13	Change in $T_1$ with field strength for within isolated ROIs for <b>(a)</b> RUFIS and <b>(b)</b> SPGR. 7T data point is the 15.6 kHz data. . . . .	141
5.14	Comparison of residual histograms across field strengths for <b>(a)</b> RUFIS and <b>(b)</b> SPGR calculated within the cerebral white matter (WM) mask. . . . .	143
5.15	Off resonance effects with increasing bandwidth seen around the sinuses (white arrow) on the raw low flip angle images at each field strength. By doubling the bandwidth at 7T to 31.2 kHz, the artefact is reduced. . . . .	144
5.16	$B_1$ inhomogeneity increase at higher field strength, both on the transmit and receive side. <b>(a)</b> $B_1^+$ maps acquired at 3T and 7T, showing substantially higher $B_1^+$ variation at 7T. <b>(b)</b> Low flip angle RUFIS images at all three field strengths showing the compound effect of $B_1^+$ and $B_1^-$ . The effect of $B_1^-$ is most clearly seen around the skull where there are localised areas of higher signal, which are strong at 7T but almost non-existent at 1.5T. . . . .	144
6.1	Examples of $T_2$ preparation using <b>(a)</b> a spin echo and <b>(b)</b> the adiabatic modified $B_1$ -insensitive rotation (mBIR)4 pulse. The inter pulse spacing $\Delta T$ which can be adjusted to change the TE is indicated with red arrows, along with the resulting effective TE. . . . .	153
6.2	<b>(a)</b> Plot of prepared magnetisation (circles) for 6 different mBIR4 pulses with different inter pulse spacing (in legend), and the best exponential fit to equation 6.4 (solid line). <b>(b)</b> Effective TE as a function of $2\Delta T$ in ms. . . . .	156
6.3	Off-resonance and $B_1^+$ profiles of <b>(a)</b> the spin echo preparation and <b>(b)</b> mBIR4 pulse at $T_2=80$ ms and $TE_{eff} = 80$ ms. The colour shows the relative error of the prepared magnetisation at a given off-resonance frequency and $B_1^+$ -error relative to the magnetisation on-resonance at nominal $B_1^+$ . . . . .	156
6.4	Curves showing the prepared magnetisation (dots) as a function of $T_2$ for 11 different TEs, for combinations of three different off-resonance frequencies and three values of $B_1^+$ error. Solid lines indicate the expected magnetisation under nominal conditions. The results for the combination that is on-resonance and with nominal $B_1^+$ are indicated with a red frame. . . . .	157
6.5	The mBIR4 pulse creates a complex magnetisation evolution, which can be partly understood by studying it under different conditions. Here the evolution is shown <b>(a)</b> on resonance and at nominal $B_1$ , <b>(b)</b> at 250Hz off resonance (at nominal $B_1$ ), and <b>(c)</b> on resonance but with 0.75 nominal $B_1$ . . . . .	158
6.6	Simulation of the mBIR4 pulse over a range of different $T_1$ and $T_2$ , demonstrating that the preparation produces weighting proportional to $T_2$ and is not influenced by $T_1$ . . . . .	158

6.7	Schematic of the multi TE $T_2$ prepared RUFIS pulse sequence. Each RUFIS segment, except the first, is coupled with a $T_2$ preparation module. After the repeated $T_2$ preparation and RUFIS readout, there is a wait period for $T_1$ recovery. . . . .	159
6.8	Effect of the RUFIS readout on $T_2$ prepared Rotating Ultra-Fast Imaging Sequence (RUFIS) for different number of spokes in the readout, compared to pure single exponential $T_2$ decay (dashed line), as would be observed in a spin echo sequence. In <b>(a)</b> , the curves are shown on a linear scale, and in <b>(b)</b> on a logarithmic scale. With increasing number of spokes, the RUFIS curves deviates more from the reference. (Simulation parameters: $TR=2ms$ , $\alpha=2^\circ$ , $T_1=1000ms$ , $T_2=80ms$ ) . . . . .	160
6.9	Example of the effects of interleaved $T_2$ preparation and RUFIS readouts. The repeated excitation in the RUFIS readout produces both $T_1$ and $T_2$ contrast. <b>(a)</b> : Higher number of spokes increases the deviation from the reference spin echo curve. <b>(b)</b> : Shorter $T_1$ results in more $T_1$ recovery during the RUFIS readout and larger deviation from the reference. <b>(c)</b> Signal curves obtained with different $T_2$ . (Simulation parameters: $TR=2ms$ , $\alpha=2^\circ$ , 128 spokes per segment. $T_2=80ms$ when $T_1$ is changed. $T_1=1s$ when $T_2$ is changed.) . . . . .	162
6.10	Signal curves from two vials in the EUROSPIN phantom with similar $T_2$ but different $T_1$ plotted on <b>(a)</b> linear and <b>(b)</b> logarithmic scale. Solid lines is data acquired with $T_2$ prepared RUFIS and dashed lines is FSE. The vial with shorter $T_1$ shows greater $T_1$ recovery and thus less apparent $T_2$ decay. . . . .	163
6.11	In vivo brain images, comparing $T_2$ prepared RUFIS at different effective TEs to fast spin echo (FSE) at the same TEs. Only axial slices shown with FSE as data were collected in 2D slices. Image intensity was normalised to 1 for the WM ROI in the $TE=10ms$ image, the window levels are the same for all slices. . . . .	164
6.12	Signal curves from isolated WM and GM ROIs acquired with $T_2$ prepared RUFIS and FSE shown on <b>(a)</b> linear and <b>(b)</b> logarithmic scale. $T_1$ contamination from the RUFIS readout results in less apparent $T_2$ decay in $T_2$ prepared RUFIS. ROIs used are shown in <b>(c)</b> . . . . .	165
6.13	Schematic of the proposed multi-contrast RUFIS acquisition (MUPA). An inversion pulse (IR) is played out followed by a series of RUFIS segments (RUFIS 1-4), similar to the Look-Locker method. $T_2$ preparation modules followed by RUFIS readouts are used to produce $T_2$ contrast (RUFIS 5-6). . . . .	167
6.14	<b>(a)</b> : Plot of the adiabatic inversion pulse with $\alpha = 180^\circ$ . The $B_0$ and $B_1$ profiles shown in <b>(b)</b> and <b>(c)</b> showed decreased sensitivity to off-resonance and $B_1$ variation with higher flip angle, at the cost of slightly reduced inversion efficiency. . . . .	168
6.15	Inversion efficiency as a function of $T_1$ and $T_2$ at nominal $B_1$ and on resonance for effective flip angle of <b>(a)</b> $180^\circ$ and <b>(b)</b> $250^\circ$ . . . . .	169
6.16	Simulation of the transient approach to steady state. <b>(a)</b> Comparison of different values of $\epsilon$ ( $T_1=1s$ , $TR=2ms$ ) <b>(b)</b> Time required to reach steady state with different TRs ( $T_1=1s$ , $\epsilon=0.05$ ). A shorter TR will, even though it produces less $T_1$ recovery, lead to a quicker approach to the steady state. . . . .	172
6.17	Maximum value of $g^2$ for different range of $T_2$ . The minimum of each curve, indicated with vertical dashed line, is the optimum TE for the given range of $T_2$ . . . . .	174

6.18	Outline of the MUPA schemes used for the phantom experiment. . . . .	175
6.19	Results from MUPA phantom experiment showing the estimated $T_1$ and $T_2$ values in each vial for the four different acquisition schemes. The true $T_1$ and $T_2$ values were provided by the phantom manufacturer. Dashed line is the identity line, i.e. a perfect 1 to 1 correspondence. . . . .	177
6.20	Results from MUPA phantom experiment visualised as Bland-Altman plots, showing the $T_1$ and $T_2$ estimation error in each vial for the four different acquisition schemes. Solid line indicate the average difference and dashed lines the 95% confidence interval (i.e. $\text{mean} \pm 1.96\sigma$ ). . . . .	178
6.21	Reconstructed images from the slow MUPA protocol showing the 4 $T_1$ weighted images following the inversion pulse (TI 1-4) and the $T_2$ weighted volume. . . . .	180
6.22	Reconstructed images from the fast MUPA protocol showing the 3 $T_1$ weighted images following the inversion pulse (TI 1-3) and the $T_2$ weighted volume. . . . .	180
6.23	Results from phantom experiment. Each vial is colour coded for comparison between $T_1$ and $T_2$ results. Top row showing $T_1$ and bottom row $T_2$ . <b>(a)</b> Comparison between the two protocols showing close to perfect agreement. <b>(b)</b> Fast protocol compared to calibrated phantom values. <b>(c)</b> Fast protocol with reduced $B_1$ showing better correlation to the calibrated values. Black dashed line indicate line of unity in all plots. . . . .	181
6.24	Quantitative $T_1$ , $T_2$ and PD maps from the two MUPA experiments and $T_2$ map from the spin echo acquisition. There is a clear underestimation in $T_2$ with MUPA, and the proton density is also badly estimated with apparent lower PD in CSF than WM and GM. . . . .	182
6.25	Results from MT simulation of the MUPA acquisition using the BM theory. <b>(a)</b> Time evolution of the longitudinal magnetisation of the free and bound pool with 16 $\mu$ s RF pulse width. <b>(b)</b> Evolution of the free pool with different pulse widths, and without MT, showing signal reduction as the pulse width is decreased. <b>(c)</b> Percentage signal change of the free pool ( $M_{zf}$ , top) and bound pool ( $M_{zb}$ , bottom) over 3 TRs, at $t = 2s$ , as indicated by the dashed line in <b>(b)</b> , normalised to the first data point. With shorter pulse widths, the bound pool saturation is greater, which in turn causes a reduction in the signal of the free pool, as indicated by the lower signal amplitude of the purple line. . . . .	190
6.26	Effects of MT on the MUPA parameter estimates showing the estimated $T_1$ <b>(a)</b> , $T_2$ , <b>(b)</b> and PD <b>(c)</b> . All quantitative parameters are consistently underestimated. (Nom pw.: nominal pulse width) . . . . .	190
7.1	Comparison of motion artefacts using RUFIS, <b>(a)</b> and <b>(b)</b> , and Cartesian spoiled gradient echo, <b>(c)</b> and <b>(d)</b> . With RUFIS, streaking and blurring artefacts are observed, while with SPGR, motion appear as ghosting artefacts in the phase encode direction (left-right here). Participant was instructed to move freely throughout the acquisition. . . . .	197
7.2	Spiral phyllotaxis arrangement of leaves. From <i>Mitchison G.J. Phyllotaxis and the Fibonacci Series. Science, 1977;196(4287):270-5. [269].</i> Reprinted with permission from AAAS. . . . .	200

7.3	Comparison of the standard trajectory <b>(a,b)</b> and phyllotaxis <b>(c,d)</b> for a trajectory with 1000 spokes. In <b>(a)</b> and <b>(c)</b> the spoke distribution is visualised as points. In <b>(b)</b> and <b>(d)</b> , subsequent spokes are connected by lines, showing a non-smooth path with the phyllotaxis trajectory. (The transparency of the lines were reduced in <b>(d)</b> to better visualise the overlapping lines) . . .	202
7.4	Phyllotaxis trajectory with 2000 spokes. <b>(a)</b> Spoke distribution as points. Trajectory sub-sampled by factor <b>(b)</b> $k = 8$ , <b>(c)</b> $k = 13$ , and <b>(d)</b> $k = 14$ . . .	203
7.5	Description of interleaves and segments in the phyllotaxis trajectory. <b>(a)</b> Each interleave consists of a few segments, here example shown with three segments, which are acquired in order. <b>(b)</b> As new interleaves are acquired, they fill up current gaps in k-space. <b>(c)</b> After all interleaves have been acquired, uniform sampling density has been achieved. . . . .	204
7.6	Comparison of acoustic noise levels with phyllotaxis trajectories with different number of interleaves ( $n_{int}$ ) at different readout bandwidths, compared to the standard trajectory and ambient background noise levels. Numbers in bars show the LAeq sound pressure level in dB(A). . . . .	206
7.7	Comparison of frequency profile of produced by the phyllotaxis trajectory with different number of interleaves ( $n_{int}$ ) at readout bandwidths of <b>(a)</b> $\pm 7.8\text{kHz}$ , <b>(b)</b> $\pm 15.6\text{kHz}$ , and <b>(c)</b> $\pm 31.2\text{kHz}$ , compared to the standard trajectory and background noise levels. . . . .	206
7.8	<b>(a)</b> Difference between LAFmax and LAFmin during the measurement period for the three phyllotaxis trajectories with different number of interleaves ( $N_{int}$ ) compared to the standard trajectory. <b>(b)</b> Magnitude of gradient of the MR gradient waveform for one interleave from the three phyllotaxis trajectories. . . . .	207
7.9	Point spread function in 1D and 2D using the phyllotaxis and standard trajectories. The dashed white lines shows the nominal field of view, as the RUFIS acquisition typically is twice oversampled. . . . .	209
7.10	Comparison of the sampling density in k-space with the phyllotaxis and standard trajectory. <b>(a)</b> Fully sampled trajectory with 2500 spokes, phyllotaxis trajectory with 5 interleaves. <b>(b)</b> Undersampled trajectories with 500 spokes. Phyllotaxis is undersampled by taking one interleave, standard trajectory by taking every 5 <sup>th</sup> spoke. <b>(c)</b> Comparison of how much the Nyquist criterion is violated with the two trajectories for the two closest spoke to every spoke. . . . .	210
7.11	Example of time resolved ZTE acquisition where each interleave is reconstructed individually <b>(a)</b> and then combined into a single high resolution image <b>(b)</b> . . . . .	212
7.12	Example of dynamic increase of image quality as additional data from a phyllotaxis sampling scheme are included. The numbers in each image indicate the number of interleaves used to reconstruct the image. . . . .	212
7.13	The Brainweb T <sub>1</sub> -weighted phantom used for the simulated MERLOT motion correction (MOCO) experiments. . . . .	216
7.14	Example of a Delaunay triangulation for a single shell of a RUFIS trajectory. <b>(a)</b> By default, the triangulation will not cover the full domain, as indicated by the convex hull shown in red. <b>(b)</b> Adding in the missing points, black markers, which are assigned the same value as the point acquired at the pole, the triangulation covers the full spherical domain. . . . .	217

7.15	Rotation of an image results in an equivalent rotation in k-space, here demonstrated by projecting the radial k-space data onto a sphere. The radius used for the spherical projection is indicated with a white line in the radial k-space data, an arbitrary choice but it shows the effect clearly. . . .	218
7.16	Results from the simulation showing the cost function evaluated as a function of rotation angle around the z-axis without filter in <b>(a)</b> and with density compensation filter in <b>(b)</b> . . . . .	222
7.17	Evolution of the minimisation algorithm in the registration algorithm for rotation around the $x$ <b>(a)</b> , $y$ <b>(b)</b> and $z$ <b>(z)</b> axes. . . . .	224
7.18	Example of the rotation correction algorithm applied to the BrainWeb $T_1$ phantom showing the first seven interleaves in the experiment. <b>(a)</b> Rotated phantom images. <b>(b)</b> Phantom sampled using the undersampled phyllotaxis trajectory. <b>(c)</b> Interleaves after rotation correction with the nominal number of spokes. . . . .	225
7.19	Accuracy of the rotation correction. <b>(a)</b> The true rotation angle $\theta$ , <b>(b)</b> the error in the estimated effective rotation angle with nominal and double number of spokes $\Delta\theta = \theta - \hat{\theta}$ . <b>(c)</b> The angle between estimated and true axis of rotation $\Theta$ . Interleave 5, 14, and 21 shows large errors in the estimated rotation axis; for these interleaves the true rotation angle is close to zero, as indicated with gray vertical lines in <b>(a)</b> . . . . .	226
7.20	Result from MOCO experiment showing the reference image without motion <b>(a)</b> , the motion corrupted image <b>(b)</b> , and the motion corrected image with the nominal <b>(c)</b> and twice <b>(D)</b> the number of spokes. . . . .	227
7.21	Comparison of reference volume sampled and reconstructed with the trajectory obtained from rotation correction <b>(a)</b> compared to the nominal trajectory <b>(b)</b> , showing streaking artefacts with the corrected trajectory . . . . .	228
7.22	Overview of the steps in the translation correction. <b>(a)</b> Radial k-space is generated from the BrainWeb phantom, and <b>(b)</b> gridded to Cartesian k-space. <b>(c)</b> Element wise multiplication of the two sets of k-space reveals wrapped phase ramp produced by the relative translation. <b>(d)</b> After an inverse Fourier transform the "phase roll" is transformed into a translation in the inverse domain. <b>(e)</b> The estimated translation of the data in this domain is then used to calculate a radial phase correction matrix $\mathcal{H}$ (using equation (7.24)) which is applied to the original k-space data $X_1^T$ <b>(f)</b> . Comparison of the corrected image to the reference now shows no shift. . . . .	230
7.23	<b>(a)</b> Axial slices of the BrainWeb $T_1$ phantom with translation motion. Top row shows the phantom with motion, middle row sampled phantom with motion, and bottom row motion corrected sampled data. <b>(b)</b> Actual and estimated translation of each interleave along $x$ , $y$ and $z$ . Perfect overlap is observed for all interleaves along all axes. . . . .	232
7.24	Results from the translation correction. <b>(a)</b> Reference image without motion. <b>(b)</b> Motion corrupted image, showing severe motion artefacts. After MOCO <b>(c)</b> , the image quality is restored, appearing identical to the reference. . . . .	233
7.25	Overview of the first seven interleaves in the simulated MERLOT experiment. Reference image for MOCO is indicated with red border. <b>(a)</b> Fully sampled BrainWeb phantom with motion. <b>(b)</b> Phantom sampled with phyllotaxis trajectory. <b>(c)</b> Rotation corrected. <b>(d)</b> Translation and rotation corrected. . . . .	234

7.26	Results from simulated rigid body MOCO experiment showing the combined reconstruction of all interleaves. <b>(a)</b> Fully sampled reference image. <b>(b)</b> Motion corrupted image. <b>(c)</b> Rotation corrected. <b>(d)</b> Full MOCO with both rotation and translation corrected. . . . .	235
7.27	Schematic showing how interleaves from the six different volumes, each in a different position, are combined into a single motion corrupted k-space data set. . . . .	237
7.28	<b>(a)</b> Overview the six acquired volumes reconstructed with two interleaves each, and <b>(b)</b> the combined reconstruction. Slices from two orthogonal planes at the same position are shown for each volume, chosen as they highlight structure of the phantom. The rotation and translational motion applied between the volumes can be clearly seen. . . . .	238
7.29	<b>(a)</b> Motion corrupted volume, <b>(b)</b> Volume after successful MOCO, <b>(c)</b> Fully sampled reference volume. <b>(d)</b> Line profiles through the phantom, as indicated with white lines in <b>(c)</b> comparing the image intensity in each voxel. .	239
7.30	<b>(a)</b> Estimated rotation on each axis. <b>(b)</b> Value of cost function for the rotation correction. <b>(c)</b> Estimated translation along each axis. Interleave permutations where the rotation registration algorithm failed are indicated with filled circles. . . . .	240
7.31	Schematic of the modular structure of MERLOT and how it can be integrated into the image acquisition pipeline before the standard image reconstruction step. Pathway <b>A</b> shows the standard reconstruction, resulting in a motion-corrupted image, while pathway <b>B</b> incorporates the motion correction step before the standard image reconstruction step. . . . .	244
A.1	<b>(a)</b> : Triangle circumcircles in a valid Delaunay triangulation. The circles are not allowed to contain any other points. <b>(b)</b> : Given a point within the triangle, it is possible to find barycentric coordinates $(\lambda_1, \lambda_2, \lambda_3)$ representing the distance to each corner point . . . . .	254
B.1	Photographs of the quantitative phantom consisting of vials from the EUROSPIN phantom in a Styrofoam mount. . . . .	256
B.2	Distribution of $T_1$ and $T_2$ values for the vials used from the EUROSPIN phantom at $T=20^\circ\text{C}$ . . . . .	256
B.3	Photographs of the home-made phantom used for the motion correction experiments in chapter 6, constructed of a cantaloupe and two British <i>Conference</i> pears kept together with Teflon tape. . . . .	257
E.1	<b>(a)</b> Graphical representation of the connection between the Fibonacci sequence and the golden ratio. Rectangles are built by squares with side length given by Fibonacci numbers. The ratio of the side lengths of the resulting rectangles approach the golden ratio. <b>(b)</b> Numerical example showing the convergence of the ratio of subsequent Fibonacci numbers towards the golden ratio. . . . .	262
E.2	Diagram of the golden angle in a circle . . . . .	263
E.3	The two first iterations in Vogel's approach to find the golden angle. . . .	265
E.4	Example of full diameter radial sampling with 13 spokes using different angular increments. Using $\alpha_g = 137.5^\circ$ , spokes appear in groups due to the diameter overlap. With the golden angle reduced to half the circle $\alpha_g = 111.2^\circ$ or $\alpha_g = 68.5^\circ$ , uniform sampling is achieved. . . . .	266



- E.5 Example of radial centre-out (half) sampling with 34 spokes using different angular increments. Using  $\alpha_g = 137.5^\circ$ , even sampling over the whole domain is achieved. With the golden angle reduced to half the circle  $\alpha_g = 111.2^\circ$ , the spokes appear in groups. Using  $\alpha_g = 360 - 137.5 = 222.5^\circ$  produces uniform sampling as well. . . . . 266
- E.6 Figure showing spacing between spokes using the golden angle distribution. **(a)** With 13 spokes (i.e. Fibonacci number 7) there are only two different gaps between spokes:  $|\Delta\phi_1| = 20.06^\circ$ ,  $|\Delta\phi_2| = 32.46^\circ$ . **(b)** Adding in a 14<sup>th</sup> spoke cuts the larger gap by the golden ratio creating two new smallest gaps of  $|\Delta\phi_3| = 20.06^\circ$ ,  $|\Delta\phi_4| = 12.40^\circ$ . . . . . 267

# List of Tables

2.1	T <sub>1</sub> relaxation values in the literature. ( <sup>a</sup> Magnetisation Prepared Rapid Gradient Echo, <sup>b</sup> Variable Flip Angle, <sup>c</sup> Inversion Recovery) . . . . .	45
2.2	T <sub>2</sub> relaxation values in the literature. ( <sup>a</sup> Carr-Purcell-Meiboom-Gill spin echo sequence) . . . . .	45
4.1	Summary of commonly used B <sub>1</sub> <sup>+</sup> mapping techniques. († Number of citations obtained from Google Scholar on January 28 <sup>th</sup> 2020) . . . . .	97
4.2	T <sub>1</sub> values in isolated ROIs averaged between the two scans in the first visit together with within session repeatability estimates ( <i>COR<sub>w</sub></i> ) from the first visit and between sessions reproducibility measurements ( <i>COR<sub>b</sub></i> ). Lower values of <i>COR</i> are better . . . . .	110
4.3	Summary of acoustic noise measurements from each sequence. Values are reported as mean±σ noise levels over a 40 s period. The large standard deviation in the noise levels for SIMBA is due to the periodic spoiling gradients. (LAEQ - A-weighted equivalent continuous sound level, LCPEAK - C-weighted peak sound level) . . . . .	110
5.1	Tissue specific design parameters for analytical models of T <sub>1</sub> and T <sub>2</sub> * relaxation in white and gray matter. . . . .	125
5.2	T <sub>1</sub> values in white matter (WM) and (gray matter (GM)) obtained from the current study and compared to previous studies. (Abbreviations, LL: Look-Locker, IR: Inversion Recovery) . . . . .	142
6.1	Example of what the file input to multi-contrast RUFIS sequence looks like. Duration of preparation pulses are controled by the <b>Time</b> parameter, and the flip angle by the <b>Scale</b> parameter. . . . .	168
6.2	Optimised TEs ( <i>TE<sub>opt</sub></i> ) for single TE measurement of T <sub>2</sub> in WM, GM and both WM and GM, together with the T <sub>2</sub> range used for the optimisation ( <i>T<sub>2,A</sub></i> to <i>T<sub>2,B</sub></i> ). Reference T <sub>2</sub> at 3T values taken from Stanisiz et al. [34] . . .	173
6.3	ROI T <sub>1</sub> and T <sub>2</sub> values given as average values within ROI ±σ. (WM - Frontal WM, GM - Caudate Nucleus, CSF - Lateral Ventricle) . . . . .	182
7.1	Trajectories used for the acoustic noise measurement comparing the standard trajectory <i>T<sub>s</sub></i> and the three phyllotaxis trajectories <i>T<sub>p,x</sub></i> , where <i>x</i> indicate the number of interleaves. The total number of spokes were matched as closely as possible. . . . .	205
7.2	Full Width Half Max (FWHM) of the point spread function obtained with the phyllotaxis and standard trajectory along each axis. . . . .	208
7.3	Mathematical notations used in this chapter. . . . .	214

7.4	Quantitative results from the cost function experiment with DC filter, as shown in figure 7.16b. The dynamic range is defined as the max-min value of the cost function. (FWHM: Full width half max, i.e. how narrow the valley of the cost function is) . . . . .	222
7.5	Results from rotation estimation using permutations of different interleave pairs. Values are reported as $\text{mean} \pm \sigma$ . Permutations where the rotation estimated failed were ignored. . . . .	239
B.1	$T_1$ and $T_2$ values in the vials used from the EUROSPIN phantom at $T=20^\circ\text{C}$ .	256

# Glossary

**$B_1^-$**  Receive RF field.

**$B_1^+$**  Transmit RF field.

**$T_1$**  Spin-lattice relaxation time constant.

**$T_2$**  Spin-spin relaxation time constant.

**$T_2^*$**  Effective  $T_2$  under magnetic inhomogeneities.

**Deadtime** Delay occurring during switching from transmit to receive mode when no data can be collected..

**Isochromat** Spins experiencing the same effective magnetic field and thus maintaining the same phase..

**K-space** Time domain in which MRI data is collected..

**Phyllotaxis** Term for arrangement of leafs in plants which has inspired a spiral k-space trajectory..

**Voxel** Smallest volume element in a 3D image volume..

# Acronyms

**AHP** adiabatic half-passage.

**BART** Berkeley Advanced Reconstruction Toolbox.

**bSSFP** balanced Steady-State Free Precession.

**BW** bandwidth.

**CNR** contrast to noise ratio.

**CSF** cerebrospinal fluid.

**DESPOT1** Driven Equilibrium Single Pulse Observation of T1.

**DESPOT2** Driven Equilibrium Single Pulse Observation of T2.

**EPI** echo-planar imaging.

**FFT** fast Fourier transform.

**FID** free induction decay.

**FLASH** fast low angle shot.

**fMRI** functional Magnetic Resonance Imaging.

**FOV** field of view.

**FWHM** full width half max.

**GM** gray matter.

**ihMT** inhomogeneous magnetisation transfer.

**LAeq** A-weighted equivalent continuous sound level.

**mBIR** modified B<sub>1</sub>-insensitive rotation.

**MERLOT** Motion Elimination in Radial acquisition Leveraging Overlapping Trajectories.

**MOCO** motion correction.

**MPRAGE** magnetisation prepared rapid gradient echo.

**MRF** MR fingerprinting.

**MRI** Magnetic Resonance Imaging.

**MT** magnetisation transfer.

**MTR** magnetisation transfer ratio.

**NEX** number of excitations.

**NIOSH** National Institute for Occupational Safety and Health.

**NIST** National Institute of Standards and Technology.

**NMR** nuclear magnetic resonance.

**NUFFT** non-uniform fast Fourier transform.

**PCM** phase correlation method.

**PD** proton density.

**PET** positron emission tomography.

**PETRA** Pointwise Encoding Time Reduction with Radial Acquisition.

**PSF** point spread function.

**QALAS** QuAntification using an interleaved Look-Locker Acquisition Sequence with T2 preparation pulse.

**qMRI** Quantitative Magnetic Resonance Imaging.

**QRAPMASTER** Quantification of Relaxation Times and Proton Density by Multiecho acquisition of a saturation-recovery using Turbospin-Echo Readout.

**RAGE** rapid gradient echo.

**RF** radio frequency.

**RMSE** root mean square error.

**RUFIS** Rotating Ultra-Fast Imaging Sequence.

**SAR** specific absorption rate.

**SIMBA** Silent Magnetisation prepared B<sub>1</sub>-map Acquisition.

**SNR** signal to noise ratio.

**SPGR** spoiled gradient echo.

**TE** echo time.

**TGV** total generalised variation.

**TI** inversion time.

**TR** repetition time.

**TV** total variation.

**TWIRL** twisting radial lines.

**VFA** variable flip angle.

**WASPI** Water- and Fat-Suppressed Solid-State Proton Projection Imaging.

**WM** white matter.

**ZTE** zero echo time.

# Publications

This work presented in this thesis has in part been published in the following journal and conference abstracts. A list specific to each chapter can be found at the end of each chapter.

## Journal Publications

1. **Ljungberg E**, Wood T, Solana AB, Kolind S, Williams SCR, Wiesinger F, et al. *Silent T1 mapping using the variable flip angle method with B1 correction*. Magn Reson Med. 2020;(December 2019):1–12. DOI:10.1002/mrm.28178

## Conference Proceedings

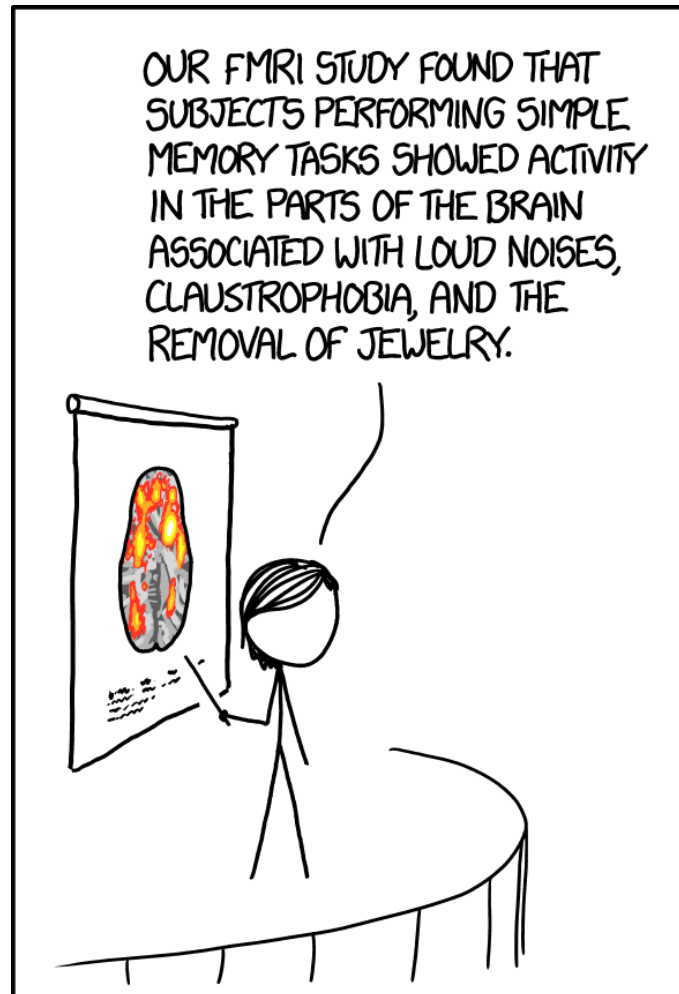
1. **Ljungberg E**, Burns B, Wood T, Solana AB, Larson PEZ, Barker GJ, et al. *ZTE Imaging Across Field Strengths; Opportunities for Low-Field Imaging*. In: Proc Intl Soc Mag Reson Med 28. 2020.
2. Wiesinger F, **Ljungberg E**, Engström M, Kaushik S, Wood T, Williams S, et al. *PSST ... Parameter mapping Swift and Silent*. In: Proc Intl Soc Mag Reson Med 28. 2020.
3. **Ljungberg E**, Wood T, Solana AB, Burns B, Williams SCR, Wiesinger F, et al. *Silent Multi-Contrast Neuroimaging*. In: ESMRMB 2019, 36th Annual Scientific Meeting, Rotterdam, NL. Rotterdam; 2019. p. S07.03.
4. **Ljungberg E**, Burns B, Larson PEZ, Kolind S, Symms M, Wiesinger F, et al. *Silent T<sub>1</sub>-Mapping at 7T Using the Variable Flip Angle Method*. In: Proc Intl Soc Mag Reson Med 27 [Internet]. Montreal; 2019. p. 4976.
5. **Ljungberg E**, Burns B, Wood T, Kolind S, Wiesinger F, Barker GJ. *Rapid, multi-TE, T<sub>2</sub>-prepared RUFIS for Silent T<sub>2</sub>-weighted imaging*. In: Proc Intl Soc Mag Reson Med 27. Montreal; 2019. p. 4571.



6. **Ljungberg E**, Wiesinger F, Solana AB, Barker GJ. *Silent Magnetization Prepared  $B_1$ -map Acquisition - SIMBA*. In: Proc Intl Soc Mag Reson Med 27. Montreal; 2019. p. 0448.
7. **Ljungberg E**, Beatriz A, Sanchez S, Wood TC, Kolind S, Wiesinger F, et al. *Silent  $T_1$ -Mapping Using the Variable Flip Angle Method with Zero Echo Time*. In: Proc Intl Soc Mag Reson Med 26. Paris; 2018. p. 0270.
8. Wiesinger F, Janich MA, **Ljungberg E**, Barker GJ, Solana AB. *Silent, 3D MR Parameter Mapping using Magnetization Prepared Zero TE*. In: Proc Intl Soc Mag Reson Med 26. Paris; 2018. p. 0061.

### Other Publications

1. Wiesinger F, **Ljungberg E**, (2018), *Zero TE MR neuro imaging: quick, quiet, quantitative*. In: GE Signa Pulse of MR, Volume 24 Autumn 2018, SIGNA Masters Neuro Summit Academic Supplement



*Reproduced with permission from xkcd. <https://xkcd.com/1453/>*

# Chapter 1

## Introduction

Magnetic Resonance Imaging (MRI) is a non-invasive medical imaging technique. It can be used for whole body, tomographic, imaging and in contrast to, for instance, computed tomography (CT) or positron emission tomography (PET) it does not have any associated ionising radiation dose. One area in which MRI is used frequently, both clinically and for research, is in the study of the central nervous system, especially the brain. MRI offers unparalleled soft tissue contrast compared to CT, enabling detailed study of both anatomy and pathology.

One of the reasons that MRI has found such widespread use, especially in research, is that there are no known health effects from repeated exposure to the magnetic and radio frequency fields inside the scanner. However, due to the strong magnetic field, the subject cannot wear any magnetic materials or have any implants that have not been classified as MR safe. Additionally, the acoustic noise produced by the scanner during data acquisition, which can reach up to 130dBA [1], requires the subject to wear ear protection during the whole scan [2]. There have been reports of temporary hearing loss after MRI scans [3, 4], however there is no evidence for permanent hearing loss. The acoustic noise during scanning is commonly reported as one of the main unpleasant features of the scan experience by patients [5, 6], and it is therefore assumed that reduced acoustic scanner noise would improve patient comfort and compliance.

Several methods have been developed, and are used clinically, for reducing acoustic noise during the MRI examination. The most important is the use of earplugs or headphones to passively reduce the acoustic noise. It is highly recommended for anyone inside the scan room to wear one, or both, of these devices [2]. Acoustic noise reduction is also

an important element in the design of the magnetic field gradient systems that form an essential part of the scanner. Torque balanced and mechanically dampened coils are commonly used to reduce the acoustic noise [5]. Additional noise reduction can be achieved by reducing the slew rate of the gradients, commonly referred to as *quiet* MRI [5]. Such quiet MRI techniques, *pulse sequences*, typically suffers from increased acquisition time and reduced performance due to the increased gradient rise time [5]. The technique used in this thesis builds on the **Rotating Ultra-Fast Imaging Sequence** (RUFIS)[7] in which acoustic noise is reduced by ensuring minimal changes in gradient amplitude, similar to quiet MRI techniques. However, unlike quiet MRI techniques, RUFIS has minimal changes in gradient amplitude by design, due to the design of the data acquisition, rather than through restriction of the gradient performance. The image contrast obtained with RUFIS is proton density weighted, and thus of limited use in research and clinical settings where additional contrasts such as  $T_1$  and  $T_2$  are crucial. The purpose of this thesis is therefore to investigate methods for introducing  $T_1$  and  $T_2$  contrast into RUFIS, and to extend these methods to allow RUFIS-based quantitative measurements of  $T_1$  and  $T_2$ .

## 1.1 Thesis Overview

Chapter 2 will introduce the relevant MRI concepts that will be referred to throughout this thesis. The explanation starts by introducing nuclear magnetic resonance (NMR), focusing on  $T_1$  and  $T_2$  relaxation. The transition to imaging will then be described, with an explanation of the theory behind spin-warp imaging together with a short note on image reconstruction. The distinction between *qualitative* and *quantitative* MRI will be made and a brief review of methods for quantitative  $T_1$  and  $T_2$  mapping will be given. The characteristics of brain tissue in terms of MR parameters ( $T_1$  and  $T_2$ ) will be described. The chapter concludes with a review of acoustic noise in MRI, together with strategies for noise reduction.

Chapter 3 provides a thorough description and characterisation of the Rotating Ultra-Fast Imaging Sequence (RUFIS) pulse sequence [7]. Acquisition parameters used in RUFIS, and how these interact, are described. A mathematical framework for studying the quantitative signal in RUFIS is developed and unique features of the RUFIS image acquisition, including the excitation profile and the deadtime gap are investigated. The acoustic noise produced by RUFIS is measured and characterised.

Chapter 4 describes  $T_1$  mapping using the variable flip angle (VFA) method [8] with RUFIS together with a novel  $B_1$  mapping technique called SIlent Magnetisation prepared  $B_1$ -map Acquisition (SIMBA). The proposed  $B_1$  mapping technique is similar to the double angle method, but utilises a preparation module and RUFIS readout for silent  $B_1$  mapping [9]. A feasibility study is presented, studying the repeatability and reproducibility of RUFIS for VFA  $T_1$  mapping, compared to standard Cartesian spoiled gradient echo imaging. This work is extended in chapter 5, which presents a study on VFA  $T_1$  mapping across field strengths of 1.5, 3, and 7T. Difficulties and opportunities at each field strength are investigated.

Chapter 6 combines the quantitative signal equations from chapter 3 and presents the development of a rapid  $T_2$  mapping sequence using  $T_2$  prepared RUFIS. It will be shown that the RUFIS readout inherently introduces  $T_1$  contrast, and that quantitative  $T_2$  estimates cannot be obtained without  $T_1$  correction. To solve this, a combined  $T_1$  and  $T_2$  method is presented.

Chapter 7 presents a novel technique for retrospective, self-navigated, motion correction using RUFIS. A 3D phyllotaxis k-space trajectory is introduced into RUFIS, which enables time resolved acquisition for self-navigation. A motion-correction framework, here called MERLOT (Motion Eliminating Radial acquisition Leveraging Overlapping Trajectories), is developed through simulations and validated using real data acquired on a phantom.

The thesis concludes with chapter 8, which summarises the main findings from this PhD thesis and discusses the contributions made to the field.

## 1.2 Student Contribution

Unless stated otherwise, the work presented in this thesis was carried out by me. However, the work presented herein would not have been possible without the help from my supervisors as well as numerous collaborators. Therefore, each chapter contains a separate section clarifying my contribution and the extent to which collaborators helped me with the work.

## 1.3 Ethical Approval

The data acquisition performed at King's College London to develop and test the techniques presented in this thesis is covered under an ethical approval entitled "*Development of Magnetic Resonance Imaging and Spectroscopy Methods*" (Research Ethics Commit-

tees (REF) reference: 04/Q0706/72, South London and Maudsley NHS Foundation Trust (SLaM) R&D Ref: CSA/09/008, King's College Hospital (KCH) R&D Ref: 05NB32), held by Professor Gareth Barker, King's College London. Data collected on the 7T scanner at University of California San Francisco, for the work presented in chapter 5, was collected under "*Determination of MR Acquisition Parameters for Human Studies at 7 Tesla*" (Institutional Review Board (IRB): 10-01710). Data for chapter 5 collected on the 1.5T scanner at Menlo Park was covered under "*Development of MR Systems, Components, and Accessories – Menlo Park*" (114.05-2015-GES-0003 WIRB<sup>©</sup> (Western Institutional Review Board) Protocol #20160876).

## Chapter 2

# Magnetic Resonance Imaging

### Contents

<b>2.1</b>	<b>Introduction to Magnetic Resonance Imaging</b>	<b>32</b>
<b>2.2</b>	<b>MRI of the Brain</b>	<b>44</b>
<b>2.3</b>	<b>Contrast Weighted Imaging and Acquisition Parameters</b>	<b>47</b>
<b>2.4</b>	<b>Quantitative Parameter Mapping</b>	<b>48</b>
<b>2.5</b>	<b>Acoustic Noise in MRI</b>	<b>54</b>

### Summary

IN this chapter, the basics of Magnetic Resonance Imaging (MRI) and the fundamental contrast mechanisms (proton density,  $T_1$ , and  $T_2$ ) will be introduced. Spatial localisation using spin warp imaging is described, and the basics of Fourier image reconstruction is provided. Features of brain tissue, in terms of MRI parameters, are described in the context of relaxometry. Commonly used methods for quantitative MRI are described. A review of acoustic noise in MRI, reasons and methods for reducing it is provided. Basic metrological concepts for quantitative MRI are discussed.

## 2.1 Introduction to Magnetic Resonance Imaging

Nuclear magnetic resonance (NMR) imaging, commonly referred to as MRI, is one of the most powerful and versatile medical imaging techniques. This section will outline the basic physical phenomenon behind NMR, using a classical approach, i.e. not quantum mechanical [10], followed by a brief description of how the spin warp technique enables spatial localisation, the foundation of MRI. Basic NMR/MRI contrast mechanisms are described both from a physical point of view and with respect to their biological interpretation.

### 2.1.1 Nuclear Magnetic Resonance Physics

MRI is an imaging extension of NMR, in which the properties of a range of nuclei can be studied using magnetic fields. In the human body, the nucleus of particular interest is  $^1\text{H}$  Hydrogen, which is in high abundance due to the high water content of the human body. Other nuclei that can be studied using MRI commonly referred to as *X-nuclei* include:  $^{23}\text{Na}$ ,  $^{39}\text{K}$ ,  $^{35}\text{Cl}$ , and  $^{17}\text{O}$  [11], however in this thesis only  $^1\text{H}$  is studied. When a piece of biological tissue is placed inside a strong magnetic field, all nuclei with non-zero spin, and thus a non-zero magnetic moment, will begin to precess at a frequency, referred to as the Larmour frequency, given by

$$\omega_0 = \gamma B_0 \quad (2.1)$$

where  $B_0$  is the strength of the static magnetic field and  $\gamma$  is the gyromagnetic ratio, which differs between nuclei (for  $^1\text{H}$   $\gamma/2\pi = 42.58 \text{ MHz/T}$ ). Consider a small volume  $V$  inside the sample, such that the magnetic field can be considered constant across it, containing a large number  $N$  of hydrogen nuclei, hereafter referred to as *spins*. Without any external field, the orientation of the spins will be random and evenly distributed in all directions. Inside a magnetic field, the distribution of spins will be skewed, making spins more likely to align with the direction of the magnetic field. In a review paper by Hanson, the classical analogy of compasses inside a tumble drier was used to describe this phenomenon; because of the tumbling (analogous to thermal energy) the direction of the compass pin will change randomly, but with a large number of compasses, there will be a tendency to measure the pin pointing north because of the earth's magnetic field [10]. In an MRI experiment, the fraction of spins,  $S_f$ , aligned with the magnetic field can be calculated as

$$S_f \approx \frac{\hbar \gamma B_0}{2kT} \quad (2.2)$$



where  $\hbar$  is the reduced Planck's constant ( $\frac{h}{2\pi}$ ),  $k$  is Boltzmann's constant, and  $T$  the absolute temperature of the sample [12]. At a typical field strength of 3T,  $S_f \approx 1 \cdot 10^{-5}$  at room temperature. The acquired signal in an NMR experiment is proportional to the excess magnetisation  $S_f$ , usually referred to as net magnetisation, hereafter labelled as  $M_0$ . Since  $S_f$  scales with  $B_0$ , higher field strength will increase the signal to noise ratio (SNR), which is the driving factor in development of MRI scanners with ultra-high magnetic field strengths. The change in SNR with field strength will be further studied and discussed in chapter 5.

The magnetisation is typically described as a vector  $\vec{M} = (M_x, M_y, M_z)$ , precessing around the  $z$ -axis by  $\omega_0$ , in a coordinate space where the  $z$ -axis is parallel to the main magnetic field. The magnitude of  $\vec{M}$  is given by  $M_0$ , which is directly proportional to the proton density (PD) inside the imaging volume, i.e. the number of  $^1\text{H}$  spins. To study the dynamics of  $\vec{M}$ , a frame of reference rotating around the  $z$ -axis with an angular frequency  $\omega_0$  is typically used [12]. In this rotating frame of reference,  $\vec{M}$  is static in the absence of additional magnetic fields or relaxation (described later), in contrast to the stationary frame of reference where  $\vec{M}$  is rotating with  $\omega_0$  around the  $z$ -axis. In the stationary frame of reference, the magnetisation vector can be tipped from the longitudinal axis toward the transverse plane, by applying a radio frequency (RF) field, oscillating with  $\omega_0$ , perpendicular to the main magnetic field. The angle through which the magnetisation will be tipped, the flip angle  $\alpha$ , is calculated as

$$\alpha = \int_0^\tau \gamma B_1(t) dt \quad (2.3)$$

where  $B_1$  and  $\tau$  are the amplitude and duration of the RF pulse. For a *hard pulse* (i.e. a  $B_1$  applied at a constant amplitude) this reduces to

$$\alpha = \gamma B_1 \tau. \quad (2.4)$$

In the rotating frame of reference, this will be observed as a rotation, while in the stationary frame of reference,  $\vec{M}$  will follow a complex path around the  $z$ -axis while being nutated by  $\alpha$  towards the transverse plane.

Application of an RF pulse with flip angle  $\alpha$  will produce a transverse component  $M_\perp = M_0 \sin \alpha$ , and a longitudinal component  $M_z = M_0 \cos \alpha$ . In the stationary frame of reference,  $\vec{M}$  is now rotating in the transverse plane with  $\omega_0$ , producing a magnetic

flux which can be observed as an induced voltage in a receive RF coil placed close to the sample, which is the signal measured by the MRI scanner. In the rotating frame of reference however, the transverse component will be stationary. After the magnetisation has been tipped into the transverse plane, it will try to align with the main magnetic field again, a process known as relaxation. The return to the equilibrium state takes place through two processes: recovery of  $M_z$  occurs with a time constant  $T_1$ , and decay of  $M_\perp$  with a time constant  $T_2$ .

If an additional magnetic field with strength  $\hat{B}$  is applied, the magnetisation vector will begin to precess in the rotating frame of reference with an angular frequency  $\hat{\omega}$

$$\hat{\omega} = \gamma \hat{B}. \quad (2.5)$$

The angle of  $\bar{M}$  in the transverse plane relative to the  $x$  or  $y$  axis (typically  $x$ , although the choice is arbitrary) is referred to as the *phase* of the magnetisation,  $\phi$ . A set of spins experiencing the same magnetic field will maintain the same relative phase, and are referred to as an *isochromat*. The concept of phase will return in the discussion of  $T_2$  relaxation and spin-warp imaging.

Magnetisation in the transverse plane produce a flux which can be detected by nearby receive coil tuned to  $\omega_0$ . The measured signal from a small volume element  $V$  can be written as [12]

$$s(t) = \Lambda \int_V d^3r \rho(\bar{r}) e^{i(\omega_0 t + \phi(\bar{r}, t))} \quad (2.6)$$

where  $\rho(\bar{r})$  is the proton density (PD) at position  $\bar{r}$ , and  $\Lambda$  includes scaling factors for the flip angle and parameters in the receive circuit such as gain.

### **$T_1$ Recovery Through Spin-Lattice Interactions**

The regrowth of the longitudinal magnetisation from the transverse plane is characterised by the time constant  $T_1$ . To use an analogy from thermodynamics, tipping the magnetisation into the transverse plane corresponds to increasing the spin temperature. To return to the equilibrium state, the *hot* spin system will exchange energy with the *cold* lattice, i.e. neighbouring atoms, which were not excited by the RF pulse. The rate of exchange of energy with the lattice is proportional to the longitudinal magnetisation, i.e. the spin temperature, similar to heat exchange. In NMR this is expressed in the Bloch equations [13], which give a phenomenological description of the NMR signal evolution. The longitudinal

component of the Bloch equation is expressed as an ordinary differential equation

$$\frac{dM_z(t)}{dt} = \frac{1}{T_1}(M_0 - M_z(t)) \quad (2.7)$$

with the solution

$$M_z(t) = M_z(0)e^{-t/T_1} + M_0(1 - e^{-t/T_1}). \quad (2.8)$$

In brain tissue,  $T_1$  is on the order of 1s, however it is field strength dependent and increases with increasing field strength [14]. Tissues with high water content will have a longer  $T_1$  [15], e.g. gray matter (PD  $\approx$  80%) has a longer  $T_1$  than white matter (PD  $\approx$  70%) [16]. Figure 2.1a shows examples of  $T_1$  recovery curves following an RF pulse with a flip angle of  $\frac{\pi}{2}$  (i.e. a pulse that fully tips  $M_0$  into the transverse plane) for a range of  $T_1$  values typical of biological tissues (note that the signal curves are normalised to 1.0, i.e. all tissues are assumed to have the same proton density).

## **$T_2$ Decay Through Spin-Spin Interactions**

The decay of the transverse magnetisation is characterised by the time constant  $T_2$ . It is driven by individual spins randomly reorienting at a rate characterised by the correlation time  $\tau_c$ , resulting in random fluctuations in the local magnetic field experienced by nearby spins. Variations in the magnetic field will result in slightly different precession frequencies for the spins, causing dephasing, i.e. loss of phase coherence. The signal detected by the MRI scanner is the sum of all spins inside each volume element  $V$ , and thus signals from spins with opposite phase will cancel and reduce the detected signal. The dephasing of the magnetisation is caused by random fluctuations and thus irreversible.

The decay of the transverse magnetisation is expressed by the Bloch equation [13] as

$$\frac{dM_{\perp}}{dt} = -\frac{1}{T_2} M_{\perp} \quad (2.9)$$

which has the solution

$$M_{\perp} = M_{\perp}(0)e^{-t/T_2}. \quad (2.10)$$

Figure 2.1b shows  $T_2$  relaxation curves for typical  $T_2$  times found in the brain (and again assuming the same proton density values for each tissue). Similar to  $T_1$ , gray matter has a longer  $T_2$  than white matter. However, since the interactions causing  $T_2$  relaxation occur between spins, the environment around the spins themselves will affect  $T_2$ . In brain tissue,

the clearest example is the difference in  $T_2$  between white and gray matter. White matter is characterised by its large number of myelinated axons as well as glial cells, with most of the water located around or within the axons, i.e. intra-extra cellular water. Myelin is a lipid-protein membrane structure which is wrapped in layers around the axons, creating compartments of water between the myelin layers [17, 18]. Water molecules between and within axons is free to move and will reorient at relatively fast rate, resulting in a long  $T_2$ . Due to the geometry, water molecules between the myelin bilayers will randomly reorient at a slower rate, which leads to a shorter  $T_2$  [19]. The combined effect is a shorter mean  $T_2$  in white matter compared to gray matter.

In a practical MRI system, the magnetic field is never perfectly uniform over the whole imaging volume. Local difference in magnetic susceptibility (for example between brain tissue and air in sinuses in the head, or between bone and other tissues) cause inhomogeneities in the magnetic field. These inhomogeneities, along with those due to magnet imperfections, contribute to dephasing and their effects are characterised by an additional relaxation time  $T_2'$ . The overall transverse decay in the presence of magnetic field inhomogeneities is denoted by  $T_2^*$ , which is given by

$$\frac{1}{T_2^*} = \frac{1}{T_2} + \frac{1}{T_2'}. \quad (2.11)$$

An important distinction between  $T_2$  and  $T_2'$  is that while  $T_2$  decay is irreversible, as it is caused by random fluctuations, decay by  $T_2'$  is potentially reversible as it is caused by static variations in the magnetic field. Whether the signal that is measured decays away as  $T_2^*$  or  $T_2$  depends on the details of the technique, "pulse sequence", used to perform the measurement, as described in the next section.

### Free Induction Decay, Gradient Echo and Spin Echo

Magnetisation precessing in the transverse plane can be detected using a coil tuned to the resonant frequency  $\omega_0$ . The signal decay observed following an RF pulse is called the free induction decay (FID), and will decay with  $T_2^*$ . Acquiring the FID results in very low contrast between tissues, as there is no time to produce tissue contrast from  $T_1$ ,  $T_2$ , or  $T_2^*$  relaxation. To enhance the contrast, the acquisition can be delayed from the time of excitation, which for the FID signal would result in  $T_2^*$  contrast. For pure  $T_2$  contrast, the effects of  $T_2'$  have to be removed which can be achieved using a spin echo [20], illustrated

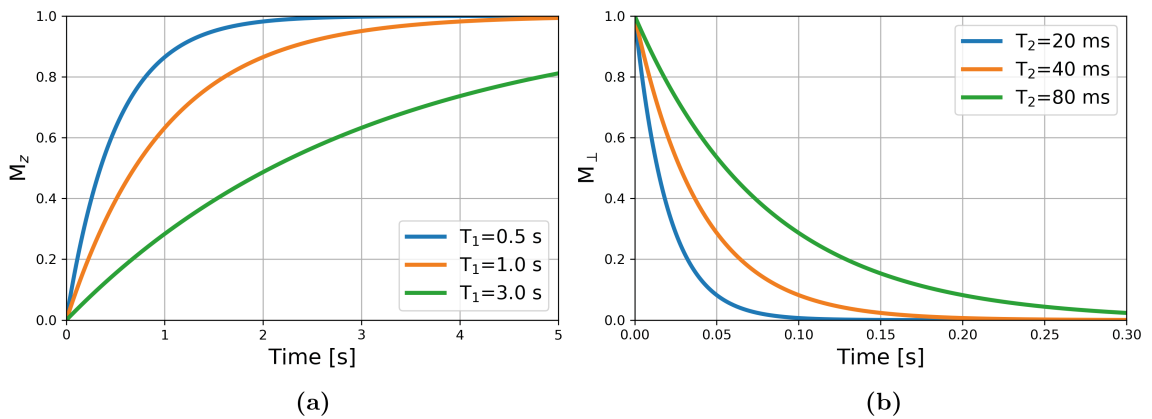


**Figure 2.1:** Example of (a)  $T_1$  recovery of  $M_z$  and (b)  $T_2$  relaxation of  $M_{\perp}$  following a  $\pi/2$  RF pulse.

in figure 2.2. An excitation RF pulse is applied at time  $t_0$  after which the signal decays with  $T_2^*$ , i.e. the spins dephase. At a time  $t_1$ , equal to half the echo time (TE), a  $180^\circ$  RF pulse is applied along an axis in the transverse plane perpendicular to the axis used for the excitation pulse (e.g.  $y$  and  $x$  respectively). This RF pulse flips the dephased magnetisation like a pancake in the transverse plane, causing the magnetisation which previously dephased with  $T_2^*$  to rephase at a time  $t_2 = TE$ , resulting in a signal which only has decayed by  $T_2$ .

To acquire a signal with a given amount of  $T_2^*$  weighting, i.e. allowing  $T_2^*$  decay to occur to differentiate between tissues with different  $T_2^*$ , a gradient echo is used instead, illustrated in figure 2.3. After RF excitation, an external magnetic field gradient is applied at time  $t = t_0$ , causing deliberate dephasing of the spins. The magnitude of the external field is then inverted at  $t = t_1 = TE/2$ , thus reversing the deliberate dephasing of the spins to produce a partly refocused magnetisation at  $t = t_2 = TE$ . At this point, the transverse magnetisation has decayed by  $T_2^*$ .

### 2.1.2 Spatial Localisation in MRI

To produce an image from an NMR experiment, a method for spatial localisation is required. The following sections will describe two related methods, projection reconstruction, and spin warp imaging. The discussion will begin with 1D examples, introduction of the Fourier transform, and finally extend to 2D and 3D methods.

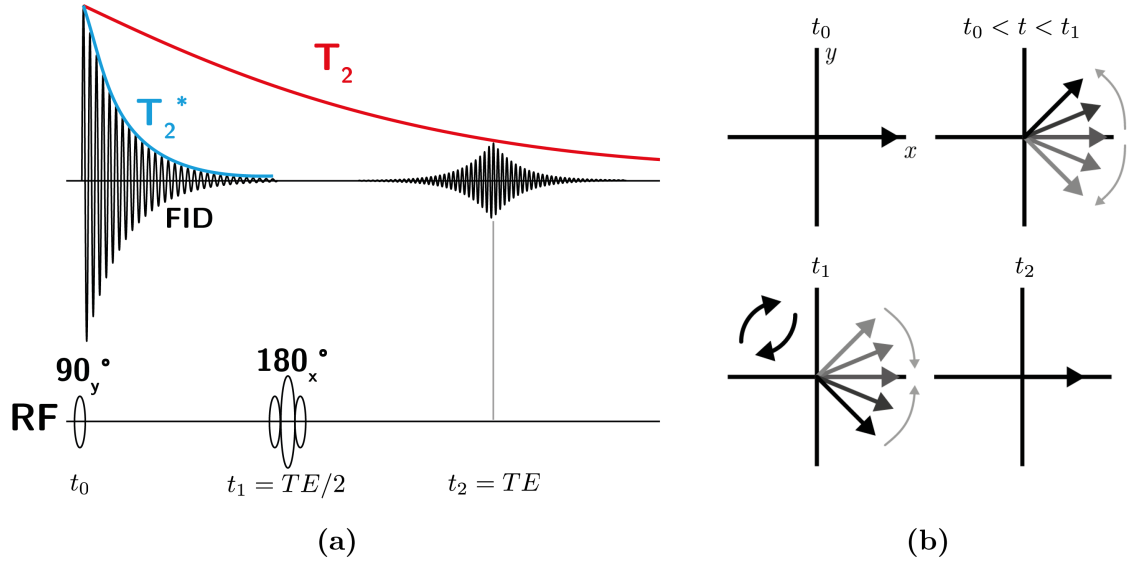


**Figure 2.2:** Illustration of a simple spin echo experiment showing the pulse sequence diagram in (a) and the evolution of five isochromats in (b). Excitation is performed at  $t = t_0$ , a  $180^\circ$  refocusing pulse is applied at  $t = t_1 = TE/2$  producing a refocused spin echo at  $t = t_2 = TE$ .

### Projection Reconstruction and the Fourier Transform

Spatial localisation in MRI relies on magnetic field gradients  $G$  in the three spatial dimensions,  $x$ ,  $y$ , and  $z$ . To begin, consider a 1D example. With a linear field gradient, which is typically used, the strength at position  $x_0$  is given by  $G(x_0) = x_0 \cdot G$ . Addition of a time varying field gradient results in a relative change of the resonant frequency relative to the Larmour frequency as

$$\omega_G(x, t) = \gamma x G(t). \quad (2.12)$$

At time  $t$ , spins at different locations will accumulate additional phase given by

$$\phi_G(x, t) = - \int_0^t \omega_G(x, \tau) d\tau. \quad (2.13)$$

In the data acquisition, the detected signal, as expressed in (2.6), is demodulated by  $\omega_0$  resulting in a signal in the time domain given by

$$s(t) = \int \rho(x) e^{-i\phi_G(x, t)} dx \quad (2.14)$$

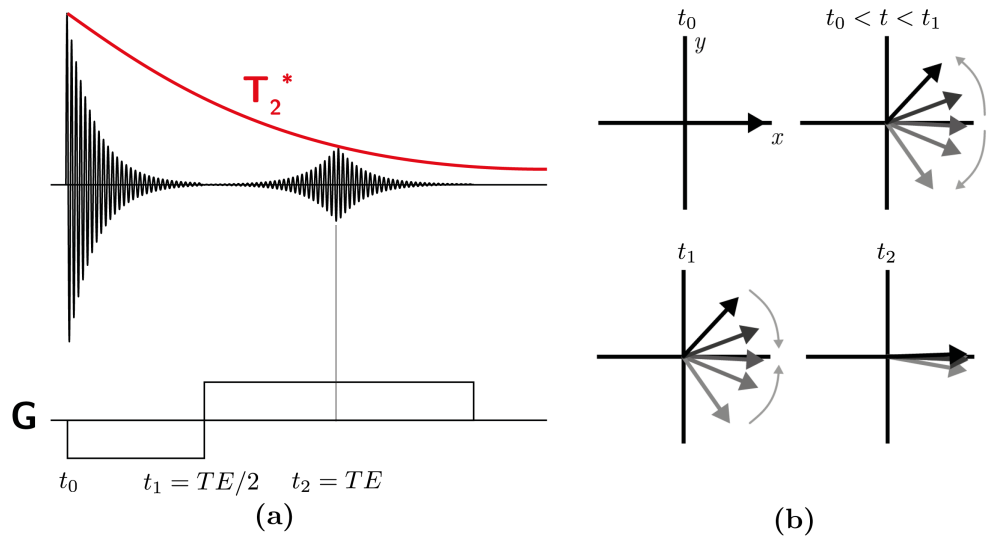


**Figure 2.3:** Illustration of a simple gradient echo experiment showing the pulse sequence diagram in **(a)** and the evolution of five isochromats in **(b)**. Excitation is performed at  $t = t_0$  after which a gradient is applied to cause deliberate dephasing of the spins. At  $t = t_1 = TE/2$ , the gradient amplitude is inverted and a gradient echo is produced at  $t = t_2 = TE$ . The isochromats are not perfectly refocused, thus resulting in  $T_2^*$  decay.

where  $\rho(x)$  is the unknown spin density. The time dependence of (2.14) is encoded in the phase by the field gradient. Equation (2.14) can elegantly be rewritten as

$$s(k) = \int \rho(x) e^{-i2\pi kx} dx \quad \text{where } k(t) = \frac{\gamma}{2\pi} \int_0^t G(\tau) d\tau \quad (2.15)$$

which is the Fourier transform of  $\rho(x)$  in  $k$ , and thus the spin density can elegantly be recovered through the inverse Fourier transform as

$$\rho(x) = \int s(k) e^{i2\pi kx} dk. \quad (2.16)$$

The Fourier relationship between  $\rho(x)$  and  $s(k)$  is the cornerstone of spatial localisation in MRI.

The method above only allows for acquisition of a 1D profile of the spin density, however the method is easily extended to 3D projection imaging by applying constant field gradients along  $y$  and  $z$  as well. The precession frequency relative to the Larmour frequency is then a function of all three spatial dimensions

$$\omega_G(x, y, z) = \gamma(xG_x + yG_y + zG_z) \quad (2.17)$$

and thus also the phase accumulation

$$\phi_G(x, y, z, t) = - \int_0^t \omega_G(x, y, z, \tau) d\tau. \quad (2.18)$$

The spin density along a given direction defined by the relative strength of the three field gradients is given by the 3D Fourier transform as

$$\rho(x, y, z) = \int \int \int s(k_x, k_y, k_z) e^{i2\pi(xk_x + yk_y + zk_z)} \quad (2.19)$$

To reconstruct an image of the whole object, numerous projections in different directions have to be acquired, after which an image can be recovered using projection reconstruction for instance [21]. The exact number of projections required to fully *sample* the image space will be described in chapter 3.

### Cartesian Spin-Warp Imaging

Projection reconstruction, as described in the previous section, was one of the first methods applied for spatial localisation in MRI, similar to the technique presented in the seminal 1973 *Nature* paper by Lauterbur [22]. One of the limitations of projection imaging, is that the data are acquired along radial projections. In the 1D example, the spin density could be recovered using the inverse Fourier transform, but in higher dimensions, this does not apply since the samples are not evenly distributed along  $k_x$ ,  $k_y$ , and  $k_z$ . If data could be sampled on a multi-dimensional Cartesian, i.e. rectangular evenly spaced grid, then the image could be reconstructed directly using the inverse Fourier transform.

In 1980, Edelstein et al. presented a method for spatial localisation in MRI known as *spin-warp* imaging [23] which allows 2D and 3D data to be efficiently acquired on a Cartesian grid and reconstructed using the inverse Fourier transform. The main difference to the acquisition of projections is the successive application of gradients along the different spatial dimensions. To illustrate the concept behind spin-warp imaging, a simple spin echo pulse sequence, shown in figure 2.4, is used. In section (1) of the pulse sequence, an excitation RF pulse is applied together with a gradient along the z-axis, a *slice select* gradient. Using an RF pulse with narrow bandwidth, only the part of the sample on resonance with the RF pulse is excited, i.e. a slice. In section (2), gradients are applied along  $y$  and  $x$  resulting in spatially dependent phase accumulation according to (2.18). The coloured lines in the  $y$ -gradient indicate that different amplitudes are applied at subsequent



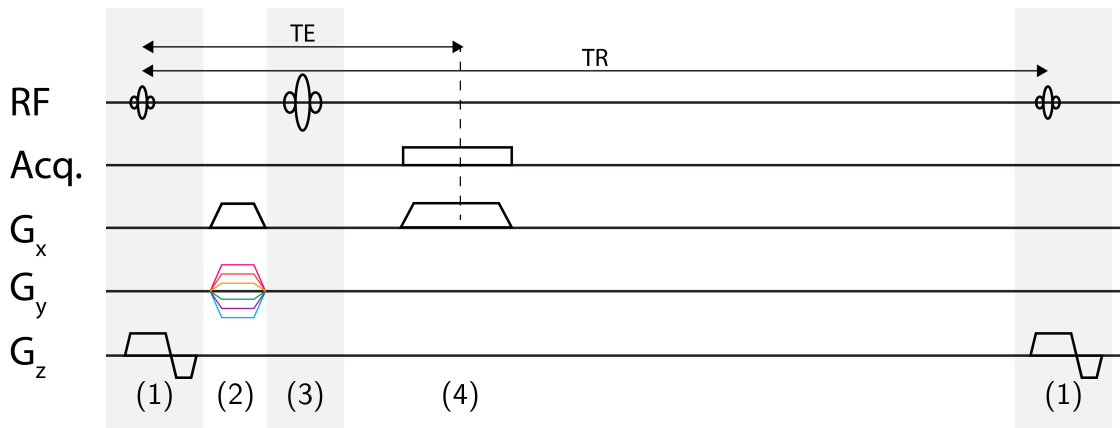


**Figure 2.4:** Schematic of a 2D spin echo pulse sequence. **(1)** Slice encoding along the  $z$  axis is followed by **(2)** phase encoding along  $y$ , the coloured lines indicate the gradient amplitude at subsequent repetitions with different amplitudes to traverse  $k$ -space along different frequency encoding lines. **(3)** At a time  $TE/2$ , a  $180^\circ$  refocusing pulse is played out to produce a spin echo at time  $TE$  **(4)** where data is acquired with a frequency encoding gradient along  $x$ .

repetitions of the pulse sequence, the reason for which is described later. In section (3), a  $180^\circ$  RF pulse, applied at time  $TE/2$ , refocuses the magnetisation to produce a spin echo in section (4) at time  $TE$  when data is acquired.

MRI data is acquired in the time domain, which in equation (2.15) was shown to correspond to sampling of a variable  $k$  in a domain known  $k$ -space [24], where the axes are  $k_x$ ,  $k_y$  and  $k_z$ . Thus,  $k$ -space can be used to visualise the acquired data in the time domain, where each data point corresponds to a spatial frequency. Figure 2.5 shows the  $k$ -space sampling pattern from the 2D spin echo sequence described in the previous section. In section (2) where gradients are applied in  $x$  and  $y$ , phase is accumulated proportional to the  $x$  and  $y$  position, resulting in a diagonal trajectory through  $k$ -space. The  $y$  gradient is here referred to as a *phase encoding* gradient. In section (4), when data is acquired, a gradient is applied along  $x$ , known as the *frequency encoding* gradient. During frequency encoding, phase is accumulated during the data acquisition along  $x$ , resulting in a trajectory along  $k_x$  in  $k$ -space. In the next repetition, the amplitude of the phase encoding gradient is reduced and the  $k$ -space trajectory during the frequency encoding will follow a different line along  $k_x$ , resulting in another set of acquired  $k$ -space points. After a number of repetitions, when all points in  $k$ -space have been acquired, the image can be reconstructed using the inverse Fourier transform.

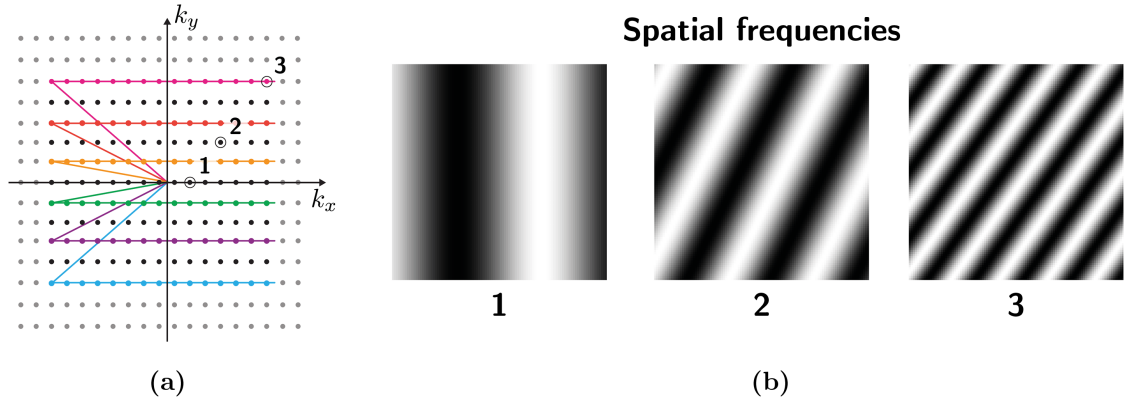


**Figure 2.5:** (a) K-space sampling diagram for the spin echo sequence shown in figure 2.4 with (b) examples of where different spatial frequencies are located in k-space.

### Readout Bandwidth and Nyquist Sampling

The bandwidth of the acquired signal  $s(t)$  is determined by the strength of the frequency encoding gradient, as this will modify the resonance frequency across the sample. If an object with size  $D$  is imaged with a readout gradient  $G_x$ , the bandwidth required along the readout direction to cover the whole object is given by  $BW = (\gamma/2\pi)G_x D$ . Different MR vendors use different notations for readout  $BW$ , here the convention used by GE,  $\Delta\nu = \pm BW/2$  is used. If a field of view (FOV)  $L$ , smaller than the size of the object  $D$  is desired, the analogue signal can be lowpass filtered to remove the signal from area outside  $L$ , resulting in an effective bandwidth of

$$\Delta\nu = \frac{1}{2} \frac{\gamma}{2\pi} G_x L. \quad (2.20)$$

According to the Nyquist sampling criterion, this signal has to be sampled with a rate of

$$\Delta t = \frac{1}{2\Delta\nu} \quad (2.21)$$

to avoid aliasing in the signal. The distance between samples in k-space is determined by the sampling time  $\Delta t$  and the gradient amplitude as

$$\Delta k_x = \frac{\gamma}{2\pi} G_x \Delta t. \quad (2.22)$$

Together with (2.21), the k-space Nyquist criterion in MRI can be expressed as

$$\Delta k_x = \frac{1}{L_x}. \quad (2.23)$$

The same requirement holds in the other spatial dimensions as well. However, there is an important difference between the readout direction and the phase encoding direction (in 3D imaging, slice selection is a special case of phase encoding, and thus the following derivation also applies in the same way). As previously mentioned, the analogue signal acquired during the frequency encoding can be lowpass filtered to remove signal from parts of the object outside the field of view (as determined by their resonant frequency) which otherwise would cause aliasing in the image domain. In the phase encoding direction, the phase variation generated by the applied gradient will affect all spins in the object that have been excited by the excitation pulse, thus potentially including points outside the desired imaging volume. These signals cannot be removed through lowpass filtering, as spins have a unique, position dependent, frequency only in the direction of the frequency encoding gradient. Therefore, the phase encoding direction has to encompass the whole object to avoid aliasing, or *phase-wrap*<sup>1</sup>.

So far, the process of how to obtain an image with a given field of view have been discussed, but not how to obtain a given resolution or voxel size. Note that while the terms are often used interchangeably, there is an important distinction between voxel size and image resolution in MRI. The voxel size is directly determined by the size of the sampled k-space. The voxel size along  $x$  ( $\Delta x$ ) for instance is given by

$$\frac{1}{\Delta x} = N_x \Delta k_x, \quad (2.24)$$

where  $N_x$  is the size of k-space in  $k_x$ . Analogous expressions hold for the other spatial dimensions as well. The image resolution on the other hand depends on the point spread function of the acquisition and is affected by other acquisition parameters. For instance, if the duration of the readout is on the time scale of  $T_2^*$ , then the signal will experience decay during the readout, effectively creating a filter in k-space, which will reduce the amplitude of the points in the edge of k-space, resulting in a wider point-spread function. This can be understood by studying the spatial frequencies corresponding to different parts in k-space,

---

<sup>1</sup>If the volume of the sample that is excited can be limited, using spatially selective RF excitation, then alias free imaging of a field of view smaller than the object in the phase encoding direction is possible.

shown in figure 2.5. Close to the centre of k-space contains the low spatial frequencies, while the edge of k-space contains high spatial frequencies, necessary to produce details in the image and thus determining the actual resolution, i.e. point spread function, of the acquisition.

### 2.1.3 Image Reconstruction

To reconstruct an image from k-space data, a matrix equation can be formulated describing the reconstruction problem as [25]

$$\mathbf{y} = \mathbf{E} \cdot \mathbf{x} \quad (2.25)$$

where  $\mathbf{y}$  and  $\mathbf{x}$  are vectors of the acquired k-space samples and the unknown image intensities, and  $\mathbf{E}$  is the Fourier encoding matrix which is fully determined from the k-space sampling scheme. To solve (2.25),  $\mathbf{E}$  needs to be inverted which in many situations is impractical. Instead, if the data points fall on a Cartesian grid, as is the case for spin warp imaging, the reconstruction problem is typically solved using the fast Fourier transform (FFT). The transformed data yields a complex valued image from which the magnitude and phase data can be calculated. In non-Cartesian imaging experiments, i.e. where data is not sampled on a Cartesian grid, the direct formulation in (2.25) can still be used [25, 26], but a more practical option is to grid the data onto a Cartesian grid and then reconstruct the image using the FFT [27]. Image reconstruction of non-Cartesian data will be described in further detail in chapter 3.

In the work presented in this thesis, reconstruction will in some cases be performed (in MATLAB [The MathWorks, Inc., Natick, Massachusetts, United States]), instead of online on the scanner, using open source reconstruction software such as the Berkeley Advanced Reconstruction Toolbox (BART) [28], to enable adoption of the latest advanced imaging reconstruction techniques. Details and background about the specific image reconstruction techniques used will be presented in the relevant chapters throughout this thesis.

## 2.2 MRI of the Brain

MRI is a whole body imaging technique capable of imaging everything from ankle joints to the brain. Each anatomical region in the body poses different unique technical challenges. The focus of this thesis is exclusively on *brain* MRI, and this section will therefore present a short overview of the tissue composition of the brain, in particular with respect to how this influences  $T_1$  and  $T_2$ , along with common technical difficulties in brain imaging.

**Table 2.1:**  $T_1$  relaxation values in the literature. (<sup>a</sup>Magnetisation Prepared Rapid Gradient Echo, <sup>b</sup>Variable Flip Angle, <sup>c</sup>Inversion Recovery)

Tissue	Field Strength [T]	Method	$T_1$	Ref.
White Matter	7	MPRAGE <sup>a</sup>	$1130 \pm 100$	[30]
White Matter	7	VFA <sup>b</sup>	$1500 \pm 100$	[31]
White Matter	3	MPRAGE <sup>a</sup>	$840 \pm 50$	[30]
White Matter	3	VFA <sup>b</sup>	1100	[32]
White Matter	3	VFA <sup>b</sup>	$933 \pm 15$	[33]
White Matter	3	IR <sup>c</sup>	$1084 \pm 45$	[34]
White Matter	1.5	MPRAGE <sup>a</sup>	$650 \pm 30$	[30]
White Matter	1.5	IR <sup>c</sup>	$884 \pm 50$	[34]
Gray Matter	7	MPRAGE <sup>a</sup>	$1940 \pm 150$	[30]
Gray Matter	7	VFA <sup>b</sup>	$2000 \pm 100$	[31]
Gray Matter	3	MPRAGE <sup>a</sup>	$1600 \pm 110$	[30]
Gray Matter	3	VFA <sup>b</sup>	1700	[32]
Gray Matter	3	VFA <sup>b</sup>	$1380 \pm 59$	[33]
Gray Matter	3	IR <sup>c</sup>	$1820 \pm 114$	[34]
Gray Matter	1.5	MPRAGE <sup>a</sup>	$1200 \pm 130$	[30]
Gray Matter	1.5	IR <sup>c</sup>	$1124 \pm 50$	[34]

**Table 2.2:**  $T_2$  relaxation values in the literature. (<sup>a</sup>Carr-Purcell-Meiboom-Gill spin echo sequence)

Tissue	Field Strength [T]	Method	$T_2$	Ref.
White Matter	1.5	CPMG <sup>a</sup>	$72 \pm 4$	[34]
Gray Matter	1.5	CPMG <sup>a</sup>	$95 \pm 8$	[34]
White Matter	3	CPMG <sup>a</sup>	$69 \pm 3$	[34]
Gray Matter	3	CPMG <sup>a</sup>	$99 \pm 7$	[34]

The brain is composed of 75-80% water [29], making it an excellent target for MRI examination because of the correspondingly high number of MR visible hydrogen nuclei. The three main tissue types (white matter (WM), gray matter (GM) and cerebrospinal fluid (CSF)) can be distinguished using MRI due to differences in PD,  $T_1$ , and  $T_2$  arising from differences in the tissue properties. Tables 2.1 and 2.2 show typical values of  $T_1$  and  $T_2$  found in white and gray matter, obtained at different field strengths and using different techniques. The influence of field strength on  $T_1$  will be discussed further in chapter 5 and the different measurement techniques will be described in this chapter in section 2.4.

### 2.2.1 White Matter

White matter has a high density of myelinated axons, giving it a white-ish colour under light microscopy. Myelin, a structure composed of several different lipids and proteins, is wrapped around the axons in a layered structure with water trapped between the myelin bi-layers [17]. This produces three distinct water compartments in white matter: intra-cellular, extra-cellular, and myelin water. The intra- and extra-cellular water is typically assumed to have the same relaxation time of  $T_1 \approx 800\text{ms}$  and  $T_2 = 70\text{--}80\text{ms}$ , while myelin water has a much shorter  $T_2 \approx 20\text{ ms}$  [16]. The signal fraction originating from the myelin water relative to the total water signal is around 11% in WM [16]. While considered separate compartments, exchange of magnetisation does take place between the compartments, which may result in averaging of the effective relaxation values, or more complex relaxation behaviour, depending on the time scale of the acquisition [35]. Because of the multiple water compartments,  $T_2$  measurements in white matter should include at least two components to account for the multi-exponential signal decay. Previous studies have applied multi-component  $T_1$  relaxometry in white matter across field strengths, finding a stronger short  $T_1$  component from myelin water at higher field [36]. However, the existence of multi-component  $T_1$  in vivo is not well established. An NMR study investigating  $T_1$  and  $T_2$  relaxation in bovine brain found that at body temperature ( $37^\circ\text{C}$ ), only a single  $T_1$  component could be identified [37].

MR signals from non-aqueous protons are typically considered MR invisible due to their very short  $T_2^*$ , on the sub millisecond scale. In white matter, this includes signal from the non-aqueous protons in the myelin. Recent studies have proposed that the signal from non-aqueous myelin protons can be observed using ultra-short and zero echo time (ZTE) acquisition methods [38, 39, 40, 41]. However, due to the ultrashort  $T_2^*$ , an extremely fast imaging system is required to capture the signal before it has decayed, so the applicability of such direct myelin imaging using clinical system remains debatable [42].

### 2.2.2 Gray Matter

In the brain, gray matter is found on the cerebral surface, the cortex, as well as in deep gray matter structures such as the thalamus and the basal ganglia. It has lower myelin content and higher water content than WM, resulting in a longer  $T_1$  [16]. Because of a lower fraction of macro-molecules in GM compared to WM, water molecules can move more freely, resulting in a longer  $T_2$  as well [16].

### 2.2.3 Cerebrospinal Fluid - CSF

CSF is found in the ventricles in the brain, as well as in the subarachnoid space surrounding the brain. Since CSF is mainly water, it has a very long relaxation times,  $T_1 \approx 4s$  and  $T_2 \approx 2s$ , almost equivalent to water [43], however in vivo measurements of these values are difficult in CSF due to pulsatile motion related to the cardiac cycle [44].

## 2.3 Contrast Weighted Imaging and Acquisition Parameters

One of the reasons MRI finds applications in many different areas is the range of imaging parameters that can be optimised to tune the image contrast for a specific application. The main tissue parameters that produce contrast in MRI are  $T_1$ ,  $T_2$  and PD, the influence of which on final image appearance are controlled by the acquisition parameters. Typically, images are referred to as being *weighted* by a particular contrast, i.e.  $T_1$ ,  $T_2$ , or PD, however all three factors will contribute to some degree to the obtained image intensity and contrast. In this section, examples of how different image contrast can be obtained by altering the acquisition parameters of a spin echo and gradient echo sequence will be shown.

To obtain a PD weighted image, influence of  $T_1$  is minimised using a long repetition time (TR) ( $\approx 3-5 \cdot T_1$ ), allowing for full  $T_1$  recovery, and the shortest possible TE to minimise  $T_2$  decay, example shown in figure 2.6a.  $T_2$  contrast is obtained by increasing the TE to be on the order of the  $T_2$  of interest to allow for  $T_2$  decay, while retaining a long TR to allow full  $T_1$  recovery, example shown in figure 2.6b and c. A  $T_1$  weighted image can be obtained by using an inversion pulse ( $180^\circ$ ) and wait a time inversion time (TI) to produce the desired  $T_1$  weighting, example shown in figure 2.6d. Again, a short TE would be used to minimise  $T_2$  weighting.

$T_1$  weighting can also be achieved by using a very short TR gradient echo acquisition, resulting in reduced  $T_1$  recovery between acquisitions. The lack of  $T_1$  recovery between acquisition results initially in a transient state where the available magnetisation for each repetition changes [46], after which a steady-state is reached. The signal in the steady-state depends on the excitation flip angle as well as  $T_1$  and PD. Therefore, the flip angle can be used to change the amount of  $T_1$  contrast in a steady state acquisition, which later will be shown to be the foundation of variable flip angle (VFA)  $T_1$  mapping [8]. To obtain pure  $T_1$  contrast, the transverse magnetisation between excitations needs to be fully spoiled, i.e. only having a longitudinal component [46]. Figure 2.7 shows examples of the change

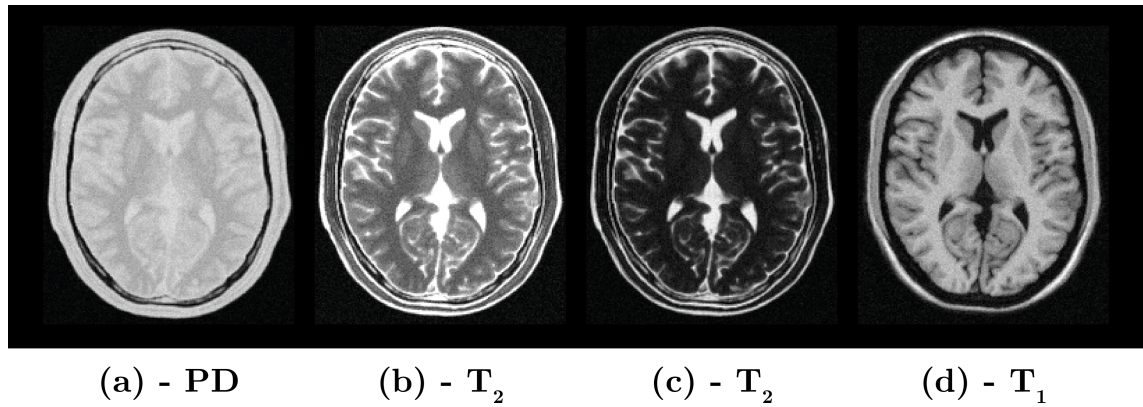


**Figure 2.6:** Example of contrast weighted images simulated by the BrainWeb platform [45]. (a) PD weighted spin echo (SE), TE/TR: 10/5000ms. (b)  $T_2$  weighted SE, TE/TR: 100/5000ms. (c) Stronger  $T_2$  weighted SE, TE/TR: 200/5000ms. (d)  $T_1$  weighted inversion recovery SE, TE/TI/TR: 3/1100/2530ms.

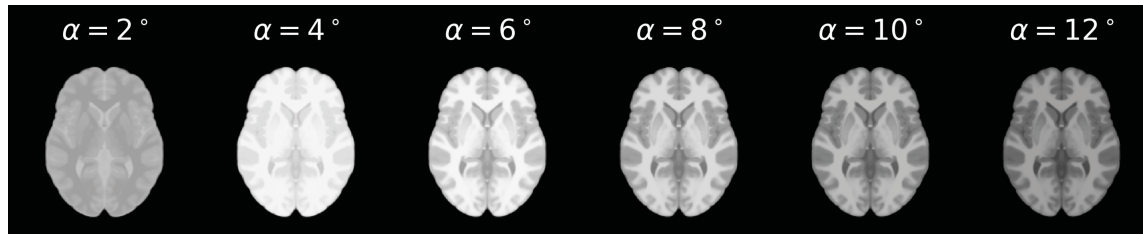


**Figure 2.7:** Example of short TR spoiled gradient echo images for different flip angles simulated using the BrainWeb platform [45]. (Simulation parameters: TE/TR=2/5ms)

in contrast with a spoiled gradient echo sequence as a function of flip angle where stronger  $T_1$  contrast is observed at higher flip angles.

## 2.4 Quantitative Parameter Mapping

In contrast weighted images, the signal intensity value in each voxel cannot be interpreted quantitatively. This is in contrast to quantitative imaging<sup>2</sup>, where the goal is to obtain an image where the voxel values can be interpreted and related to some physical property of the tissue. The field of Quantitative Magnetic Resonance Imaging (qMRI) encompasses all MRI techniques which provide quantitative measurement of tissue properties, for example: relaxation times, or perfusion, diffusion and flow velocities. In this thesis, the focus is on relaxometry techniques, i.e.  $T_1$  and  $T_2$  quantification. To obtain a quantitative parameter map, i.e. an image with the  $T_1$  or  $T_2$  time as the voxel values, multiple images with different

<sup>2</sup>Pun intended



degrees of  $T_1$  and or  $T_2$  weighting have to be obtained after a data fitting procedure is used to estimate  $T_1$  and  $T_2$ . A wide range of methods have been developed for  $T_1$  and  $T_2$  mapping, which will be briefly reviewed in this section.

### 2.4.1 $T_1$ mapping

$T_1$  mapping techniques can be divided into two main categories: magnetisation preparation techniques and steady state acquisitions. The former includes the simplest technique, inversion recovery, which is still considered a *gold standard*. By applying a  $180^\circ$  RF pulse and waiting a time TI before applying the  $90^\circ$  and  $180^\circ$  pulses of a standard spin warp spin echo sequence, a  $T_1$  weighted image can be acquired [47]. In practice, inversion recovery is more commonly coupled with a fast readout such as echo-planar imaging (EPI), or a spoiled gradient echo acquisition known as magnetisation prepared rapid gradient echo (MPRAGE) [48]. To quantify  $T_1$ , two or more images with different inversion times are acquired, from which a quantitative  $T_1$ -map can be calculated by measuring the change in contrast as a function of TI [49, 50].

The alternative to magnetisation prepared  $T_1$  mapping is steady state imaging using spoiled gradient echo images with different flip angles, a technique known as the VFA method, also sometimes referred to as Driven Equilibrium Single Pulse Observation of  $T_1$  (DESPOT1) [51, 52, 53, 8, 54]. In a spoiled gradient echo acquisition where a steady state has been reached in the longitudinal magnetisation, the transverse magnetisation can be expressed as

$$M_T(\alpha, TR, PD, T_1) = PD \cdot \frac{1 - e^{-TR/T_1}}{1 - \cos(\alpha)e^{-TR/T_1}} \cdot \sin \alpha \quad (2.26)$$

If data are acquired with two or more flip angles, the signal equation can be fitted for  $T_1$  and PD.

Measurements of  $T_1$  can, depending on the method, be affected by variations in the transmit RF field ( $B_1^+$ ). In magnetisation prepared methods with multiple readouts, variations in  $B_1^+$  can be corrected for [49], however the VFA method requires a separate acquisition to map the  $B_1^+$ . To resolve this issue, numerous methods have been developed for mapping the  $B_1^+$ , which will be discussed further in chapter 4.

### 2.4.2 $T_2$ mapping

The most commonly used method for obtaining  $T_2$  contrast is using spin echoes [20]. Following the excitation pulse, a  $180^\circ$  RF pulse is applied at a time  $\tau$ , producing a spin

echo at a time  $TE = 2\tau$ . The signal from images acquired with different TEs will follow an exponential decay with respect to TE, as shown in (2.10). In a system with only a single  $T_2$  component, only two TEs are required to fit for  $T_2$  using an exponential model. These two echo times can be acquired in two separate acquisition, or for higher efficiency in a multi-echo spin echo experiment, where a large number of TE values are acquired within a single series [55]. Note that in most biological samples, including brain WM, the assumption of a single  $T_2$  component is not valid, and additional measurements are needed to more fully characterise the complex relaxation behaviour [19].

$T_2$  weighting can also be obtained with a magnetisation preparation module, similar to a spin echo. A  $90^\circ$  pulse tips the magnetisation into the transverse plane, followed by a  $180^\circ$  pulse to refocus the magnetisation and finally a  $-90^\circ$  *tip-up* pulse to return the magnetisation to the longitudinal axis [56]. The end result is a longitudinal magnetisation which is reduced by a factor proportional to the  $T_2$  decay which occurred during the time between the tip down and tip up pulses. After the  $T_2$  preparation, a range of readout modules such as EPI, spin echo or gradient echo, can be used to read out the prepared magnetisation, and if multiple images with different preparation delays are collected, a  $T_2$  map can be calculated [56].  $T_2$  preparation can also be achieved using an adiabatic preparation pulse for reduced  $B_0$  and  $B_1$  sensitivity [57], which will be discussed further in chapter chapter 6.

A third method of  $T_2$  mapping is steady state imaging using balanced Steady-State Free Precession (bSSFP) [58], a technique sometimes referred to as Driven Equilibrium Single Pulse Observation of  $T_2$  (DESPOT2) [59]. Similar to the VFA method for  $T_1$  mapping, DESPOT2 uses a steady state acquisition but instead of spoiling the transverse magnetisation after each readout, it is deliberately refocused which leaves the magnetisation in the transverse plane, allow for  $T_2$  decay and thus  $T_2$  weighting.

### 2.4.3 Combined $T_1$ and $T_2$ Mapping Methods

The aforementioned techniques are all methods specialised to measure only  $T_1$  or  $T_2$ , individually. There has been an increasing interest recently in developing methods for quantifying  $T_1$  and  $T_2$  simultaneously, from data collected in the same acquisition, as the two parameters often are intertwined in the signal model describing the final image intensity. Two categories of techniques have emerged in this area: the so-called *MR-fingerprinting* method and non-fingerprinting methods. The idea behind MR-fingerprinting

is to use a pseudo-random pulse sequence, by changing for instance the flip angle of a gradient echo acquisition from  $TR$  to  $TR$ , causing each combination of  $T_1$  and  $T_2$  to produce a unique *finger print* [60]. Using dictionary fitting methods, the  $T_1$  and  $T_2$  corresponding to the signal evolution can be found.

Non-fingerprinting methods on the other hand typically employ a pulse sequence where  $T_1$  and  $T_2$  contrast is controlled. One example is Quantification of Relaxation Times and Proton Density by Multiecho acquisition of a saturation-recovery using Turbospin-Echo Readout (QRAPMASTER) which consists of a partial saturation pulse followed by a turbo spin echo readout [61].  $T_1$  is quantified by changing the slice order to acquire slices with different effective TI. Similarly,  $T_2$  is quantified by acquiring slices at different effective TE values in the spin echo train. More recent work by the same authors is the QuAntification using an interleaved Look-Locker Acquisition Sequence with T2 preparation pulse (QALAS) sequence [62] which utilises interleaved  $T_2$  preparation and inversion recovery with 3D spoiled gradient echo readout for simultaneous  $T_1$  and  $T_2$  mapping. A method for combined  $T_1$  and  $T_2$  mapping with RUFIS, similar to QALAS will be presented in chapter 6.

#### 2.4.4 Synthetic Imaging

With knowledge about  $T_1$ ,  $T_2$  and PD it is possible to generate, or synthesise, many of the standard contrast weighted images commonly acquired in clinical settings [63]. Synthesis of weighted MRI images from quantitative parameter maps was first proposed in 1984 by Riederer et al. [64], but it is only recently that the concept has been adopted widely [63, 65, 66, 67, 40]. The goal of these techniques is that the MR examination can be reduced to one scan, acquiring all the necessary information, and thus reduce scan time and costs.

#### 2.4.5 Theories, Models, and Representations

The aim of qMRI is to probe tissue properties using the MRI scanner, but due to the complexity of biological systems studied with qMRI, the list of confounding factors usually never ends. After years of efforts in the field of developing quantitative metrics for clinical use, very few have made it into clinical practice, why? A recent paper by Novikov et al. suggests that there might be fundamental problems that are still unresolved in the models [68]. The remainder of this section will summarise the highlights of the Novikov

et al. paper, as a foundation for discussions about development of qMRI techniques using RUFIS later in this thesis.

On the lowest level, a **theory** is constructed to describe how the system behaves, in this case the biophysics of the brain tissue in terms of MRI features such as  $T_1$ ,  $T_2$ , magnetisation transfer (MT) and diffusion. One important step in building the theory is determining the relevant degrees of freedom. For instance, in a  $T_1$  mapping experiment, the theory is built on spin-lattice relaxation ( $T_1$ ) which is assumed to be the main source of contrast in the acquisition. Spin-lattice relaxation can be explained through quantum mechanical concepts but for the scale of the measurement, these effects will average out and a classical description of the spin system can be used.  $T_2$  or diffusion effects do not need to be included but MT might be included in the theory for instance [69].

The second step involves developing a **model** for the system, which can be used to describe the outcome of a given measurement. In a single-component  $T_1$  measurement, the signal can be described using the Bloch equations. If exchange between multiple tissue compartments, or magnetisation transfer effects, are to be included, the model has to be expanded [70]. Different measurement techniques can then be used to measure  $T_1$  in vivo, such as VFA or inversion recovery. To obtain the  $T_1$  estimate, a **representation** of the signal, i.e. the signal equation, is developed, based on the type of measurement.

A signal representation that fits the data is only meaningful if it is rooted in a well defined model with a solid theory. As an example, the multi-component  $T_2$  relaxation model proposed by Mackay et al. has been shown to be a valid model for studying myelin in the brain [19]. However, if this model would be applied outside the central nervous system and multiple  $T_2$  components are identified through a good fit to a given signal representation, it does not mean that the tissue contains myelin. Models should be as specific as possible to the tissue characteristic that is measured, and the scope within which the model is valid needs to be defined.

#### 2.4.6 Metrology

Metrology, the scientific study of measurements, is crucial to the study of qMRI, but the existing literature on metrology from other fields is usually overlooked. In this section some of the fundamental metrological concepts that will be the foundation for the study of quantitative measurements later in this thesis are outlined. The definitions presented herein are taken from the National Institute of Standards and Technology (NIST) Technical

Note 1297 *Guidelines for Evaluating and Expressing the Uncertainty of NIST Measurement Results* [71].

The first and most important term is **accuracy**, defined in Appendix D of the NIST document as:

... **accuracy of measurement [VIM 3.5]**<sup>3</sup>: closeness of the agreement between the result of a measurement and the value of the measurand.

In MRI, the value of the measurand, sometimes referred to as the true value, is only known in experiments using calibrated phantoms. Alternatively, if a *gold standard* method exists as a comparison, the results of such a measurement could be considered the true value. Another term commonly mentioned together with accuracy is **precision**, commonly interpreted as the variability in repeated measurements obtained under certain conditions. There are many different conditions under which an experiment can be repeated, however. Taylor and Kuyatt therefore recommend the use of **repeatability** and **reproducibility** to distinguish between various factors of variability that affects the repeated measurement [71]. Repeatability is defined as:

... **repeatability (of results of measurements) [VIM 3.6]**: closeness of the agreement between the results of successive measurements of the same measurand carried out under the same conditions of measurement.

The following repeatability conditions need to apply: (1) the same measurement procedure, (2) the same observer, (3) the same measuring instrument used under the same conditions, (4) the same location, (5) repetition over a short period of time. Repeatability may be expressed quantitatively in terms of the dispersion characteristics of the results. Translating this into MRI terms, a repeatability measurement would be obtained if the same subject or sample is scanned more than once within the same scan session without repositioning, and preferably without retuning the spectrometer. If all other terms are kept constant, the repeatability would be inherently related to the SNR of the measurement. Reproducibility on the other hand is defined as:

... **reproducibility (of results of measurements) [VIM 3.7]**: closeness of the agreement between the results of measurements of the same measurand carried out under changed conditions of measurement

---

<sup>3</sup>ISO, International Vocabulary of Basic and General Terms in Metrology, second edition (International Organization for Standardization, Geneva, Switzerland, 1993), abbreviated as VIM in the NIST documentation.

It is therefore crucial to specify which conditions that changed between the repeated measurements. Example of reproducibility measurements in an MRI study include:

- Repositioning of the subject in the same session: After repositioning a new landmark position will usually need to be set and the scanner will typically both retune and reshim, thus changing the conditions of the measurements.
- Scans acquired on different days: Such measurements would incorporate the variability due to repositioning but now also longer term changes in the scanner such as variation in the scan room environment and potentially hardware or software updates. Day to day biological variations in the subject will also be another source of variability.
- Scans acquired on different scanners: This would introduce yet another source of variability, due to different hardware and software.
- Scans acquired with scanners from different vendors: Different implementation of the pulse sequence between vendors will introduce yet another source of variability.
- Different scanner operators: The operator running the scanner can potentially also influence the measurement from different positioning of the subject and the scan volume prescription.

## 2.5 Acoustic Noise in MRI

This chapter has mainly focused on theoretical aspects of MRI including contrast mechanisms, pulse sequences, and qMRI methods. There are however practical aspects of MRI experiments that are sometimes overlooked, one of them, which is at the core of this thesis, is the acoustic noise produced by the scanner. The acoustic noise is produced by rapid switching of the magnetic field gradients used for spatial localisation in the MRI scanner during data acquisition can reach levels far over 100 dB(A) [72, 73, 5, 1, 74, 75, 76]. The gradients are constructed of wires organised in specific patterns to produce the desired magnetic field gradient when currents are run through them. Since the coils are placed inside the main magnetic field, they will experience Lorentz forces proportional to the current and the strength of the magnetic field  $B_0$  [72]. The force  $\mathbf{F}$  experienced by a conductor with length  $|\mathbf{L}|$  in a magnetic field  $\mathbf{B}$ , with a current  $I$  running through it is given by

$$\mathbf{F} = \mathbf{L}I \times \mathbf{B}. \quad (2.27)$$

The gradient waveforms required for standard pulse sequences typically have a trapezoidal shape, and thus the amplitude of current through the coils is varying in time. From (2.27) it is seen that a time varying current produces time varying forces, which in turn produce vibrations in the system. Higher gradient amplitude and faster gradient slew rate, produce stronger forces and bigger vibrations, which in turn produce louder acoustic noise. For a thorough mathematical description of the mechanics behind the noise production in gradient coils, the reader is referred to the excellent work by Mansfield et al. [72]. The strength of the vibration also scales with the field strength, from the factor  $\mathbf{B}$  in (2.27), and thus stronger vibrations and higher acoustic noise is expected at higher field strengths. This has been observed experimentally, with studies showing increasing acoustic noise levels from 80 dB(A) at 0.2T, to 115 dB(A) at 3T [77]. In addition to vibrations of the gradient coils, one study found that induced eddy currents in metal structures in the scanner, including the inner bore of the cryostat and the RF body coil, also cause vibrations [78].

### 2.5.1 Common Notations and Descriptions of Acoustic Noise

Sound pressure level  $L_p$  is reported on a logarithmic scale in units of decibel as

$$L_p = 20 \log_{10} \left( \frac{p_{rms}}{p_{ref}} \right) \text{ dB} \quad (2.28)$$

where  $p_{rms}$  is the root-mean-square of the sound pressure, and  $p_{ref}$  is the standard reference sound pressure<sup>4</sup>. The human ear is not equally sensitive to all frequencies of sound, therefore a special weighting, the *A-weighting*, was developed to give an estimate of the loudness perceived by the human ear [79]. Most measurements related to human exposure are therefore A-weighted and given in the units of dB(A). Other commonly used weightings are: Z-weighting, as in zero or no weighting, and C-weighting which is considered a better choice for perceived loudness at high noise levels. To quantify exposure to noise over time, the *equivalent continuous sound level* is commonly used, defined as the mean squared sound pressure over a given time period. The A-weighted equivalent continuous sound level is written as LAeq.

---

<sup>4</sup>Sound pressure of 20μPa in air (ISO 1683:2015).

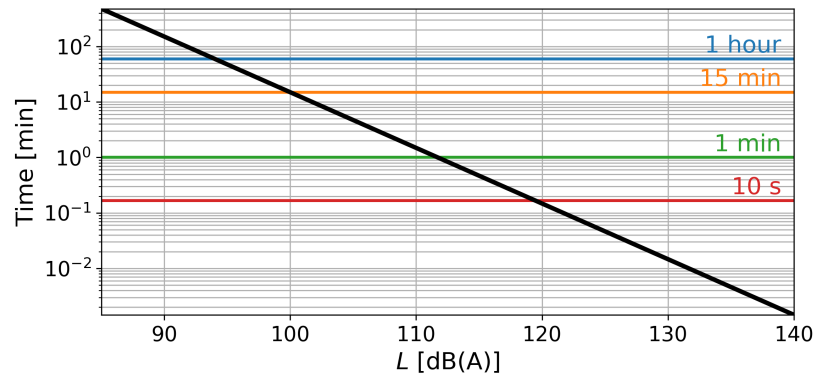


**Figure 2.8:** Maximum exposure time at different sound pressure levels.

### 2.5.2 Exposure Limits for Acoustic Noise and Hearing Protection

Exposure to loud acoustic noise can produce temporary hearing loss, quantified as a threshold shift in the sensitivity of hearing. Long term and/or repeated exposure to high acoustic noise however can lead to permanent hearing loss. In guidelines developed by National Institute for Occupational Safety and Health (NIOSH), the limit for exposure to acoustic noise over the course of an eight hour workday is set to 85dB(A) [80]<sup>5</sup>. For higher levels of noise, the maximum exposure time, in minutes, can be calculated by

$$T = \frac{480}{2^{(L-85)/3}} \quad (2.29)$$

where  $L$  is the sound pressure level, also shown graphically in figure 2.8.

If the sound pressure level exceeds 85dB(A), hearing protection should be used to reduce the noise to below 85dB(A). The most commonly used form of hearing protection in MRI is disposable earplugs. All hearing protections are rated with a number, the Noise Reduction Rating (NRR), which is a measure in dB of how much they reduce the noise on a C-weighted scale. If the noise exposure is given in dB(A), the NRR is reduced by 7 to given the A-weighted equivalent [80]. The effectiveness of hearing protection is only guaranteed if they are properly used, i.e. in the case of earplugs properly inserted, which cannot always be guaranteed. Numerous studies, summarised in a report by NIOSH [80], have found that the effective NRR typically is much less than that stated by the manufacturer. Based on these results, NIOSH recommend that the NRR should be adjusted by up to 75% for ear plugs. A more recent study found large variability in the effective NRR ranging from more

<sup>5</sup>This specific number was decided on after population level studies where exposure to 85dB(A) for 8 hours every day, over the course of 40 years, results in a 15% excess risk of hearing loss.



than half of the expected to almost no protection [81]. It is therefore crucial that hearing protection is correctly used to achieve the expected level of hearing protection to ensure patient safety.

### 2.5.3 Motivation for Reducing the Acoustic Noise

The sound pressure levels produced by a 3T MRI scanner during a typical exam can reach up to 110dB(A)[4], with extreme cases measuring up to 130dB(A) for EPI acquisitions [1]. The peak sound pressure limit of an MRI scanner is limited 140dB by the IEC standard [82], which also is the ceiling level of maximum sound pressure levels that humans should be exposed to [80]. At 100dB(A), the maximum exposure time without hearing protection is 1.5 min, given by (2.29), and seen in figure 2.8. Subjects are therefore highly recommended to wear hearing protection during MRI scans [2], to reduce the noise experienced by the patient. Earplugs with NRR=37<sup>6</sup> would reduce scan noise at 110dB(A) to 80dB(A), given that the earplugs are properly fitted and actually achieves the given NRR, which many studies have shown not to be the case [80]. If hearing protection is worn properly, it is assumed that no hearing damage will be sustained, although one study found decreased cochlear function in patients with suspected acoustic neuroma compared to controls following MRI scanning [83]. Similarly, a recent study (with subjects wearing earplugs with NRR=37) found a 5dB increase in the hearing threshold after MR examination, compared to a baseline assessment [4].

One patient group unable to be fitted with earplugs are fetuses in utero, although this appears to not be a significant issue. A 1995 study investigated the sound dampening effects of the uterus using a fluid filled stomach with a microphone in it as a phantom, and found a 30dB reduction in noise, enough to reduce a the noise from a typical MRI down to non-harmful levels [84]. This conclusion is supported by a 2010 study by Reeves et al. who found no neonatal hearing impairment after scanning on a 1.5T scanner during the second and third trimester [85]. The 2015 UK *Safety Guidelines for Magnetic Resonance Imaging Equipment in Clinical Use* concludes that pregnant patients can be scanned in normal mode<sup>7</sup> [2]. However, the studies described were all performed at 1.5T, which is associated with lower acoustic noise than 3T scanners. And even though their hearing is not permanently affected, a study of newborns undergoing MRI scanning observed changes in

<sup>6</sup>This is the specification of the ear plugs used at our centre (3M 1100B).

<sup>7</sup>Normal mode is an operation mode where the RF power, gradient switching rate, and maximum field strength is limited

blood pressure, heart rate, and/or oxygenation status, suggesting that they are nevertheless aware of the scanner noise [86].

A related area where reduction of the acoustic noise could be helpful is pediatric MRI, where deep sedation or general anaesthesia sometimes are used to minimise motion artefacts [87]. While the acoustic noise is only one aspect of the environment that can cause discomfort to the patient, it is believed that acoustic noise reduction can help with compliance during scanning, and reduction in motion artefacts [88].

The effects of exposure to the acoustic noise in the MR scanner is generally considered to not be an issue for most patient groups, as long as the required precautions, such as hearing protection, are followed. However, patients with *hyperacusis*, denoting increased sensitivity to sounds which would not trouble a normal individual [89, 90, 91], might not be able to tolerate the sounds from the scanner even with properly fitted hearing protection. Hyperacusis has been linked to several peripheral and central conditions including: Lyme disease, tinnitus, Williams syndrome, depression, migraine, post-traumatic stress disorder, autism, and chronic pain [91, 92, 93, 90]. Many of these conditions affect the central nervous system and investigation of changes in the brain are essential for understanding of the disease. Reduction of the acoustic noise during MR examination would thus be likely to increase accessibility to the MR scanner for these cohorts.

It is also known that the acoustic noise increase with field strength, as shown by Lorentz law, and observed in MRI studies [77]. A 2013 study on subject tolerance of 7T examinations found that the acoustic noise was the second most unpleasant feature of the scanning experience (reported by 33% of the subjects), after the dizziness moving in to the scanner (reported by 34% of the subjects) [94]. Acoustic noise reduction could therefore be particularly important for high field imaging.

#### 2.5.4 Methods for Reducing the Acoustic Noise

Methods for reducing the noise from the MRI scanner can be categorised by three main approaches. First, and most fundamentally, the construction and mounting of the gradient coils will affect the noise produced by the scanner [72, 78]. The second approach is software based, adjusting how the gradient coils are controlled, i.e. through the pulse sequence [95]. The third approach is passive noise reduction, such as ear-plugs, headphones, and in some cases foam padding inside the scanner [96]. The focus of this thesis is noise reduction through the pulse sequence modifications.

The strength of the magnetic field produced by the gradient coils is directly proportional to the current put through the coil, and thus stronger Lorentz forces are produced with higher gradient strength if the slew rate is kept constant. Reducing the amplitude of each gradient pulse, or the slew rate, are therefore two simple, although not efficient, approaches for reducing acoustic noise in any MRI sequence. To maintain the same field of view and voxel size, a reduction of the readout gradient amplitude can be achieved by reducing the bandwidth, although this will increase the acquisition time. Similarly, ramping up to the desired gradient amplitude more slowly, i.e. reduced slew rate, will also increase the overall acquisition time. An alternative to a constant reduction of the slew-rate is using a *soft* gradient pulse shape, where the rectangular waveforms are convolved with a smoothing function, resulting in smooth waveforms with plateaus [97]. This method effectively band limits the gradient waveform to frequency bands where the acoustic frequency response of the MR system is low. Further reduction can be achieved by removing the plateaus altogether and sample the data with sinusoidal gradients [95]. This method was shown to reduce the noise further and without reducing the performance of the scan, however, it leads to non-cartesian k-space data.

The method chosen in this thesis is a pulse sequence designed to have minimal gradient switching and thus inherently produces minimal acoustic noise. The pulse sequence Rotating Ultra-Fast Imaging Sequence (RUFIS) was introduced by Madio and Lowe in 1995 but has only recently been adopted for clinical systems due to the high demands put on the RF transmit system, which will be further discussed in the next chapter. With the RUFIS sequence (distributed on GE scanners as *Silent Scan*, part of their *Silent Scan* package), the noise level during scanning is increased by only a few dB compared to the background noise in the scan room [98]. Only a few studies have used RUFIS so far, likely due at least in part to the restricted range of contrast weightings currently available. Studies to date have mainly used RUFIS for  $T_1$ -weighted imaging, observing comparable image quality to conventional, noisy, pulse sequences [98, 99, 100]. The aim of this thesis was to increase the range of contrast types available within RUFIS, and to extend its use from qualitative to quantitative approaches.

## Chapter 3

# The Rotating Ultra-Fast Imaging Sequence - RUFIS

### Contents

---

<b>3.1</b>	<b>MRI with Zero Echo Time</b>	<b>61</b>
<b>3.2</b>	<b>The RUFIS Pulse Sequence</b>	<b>63</b>
<b>3.3</b>	<b>Image Reconstruction</b>	<b>69</b>
<b>3.4</b>	<b>Study A: Comparison of Gridding Methods</b>	<b>73</b>
<b>3.5</b>	<b>Study B: A Quantitative Signal Equation for RUFIS</b>	<b>77</b>
<b>3.6</b>	<b>Study C: A Rotating 3D Excitation Profile</b>	<b>82</b>
<b>3.7</b>	<b>Study D: Acoustic Noise</b>	<b>86</b>
<b>3.8</b>	<b>Chapter Discussion and Conclusions</b>	<b>90</b>
<b>3.9</b>	<b>Publications and Contribution</b>	<b>91</b>

---

### Summary

IN this chapter, the Rotating Ultra-Fast Imaging Sequence (RUFIS) is introduced and the core imaging parameters relevant to image acquisition with RUFIS are explained. It will be shown that RUFIS can be treated as a spoiled gradient echo sequence with zero echo time (ZTE). Constraints imposed by the ZTE readout are discussed and the image reconstruction methods used in this thesis are described. Four sub-studies are presented which investigate specific aspects of RUFIS including: gridding methods, a quantitative signal equation, non-selective excitation profile effects, and acoustic noise.

### 3.1 MRI with Zero Echo Time

#### 3.1.1 Reducing the Echo Time

In the previous chapter, a basic 2D spin echo sequence and its corresponding k-space diagram were discussed. In a spin echo sequence, an echo is produced by refocusing the magnetisation using a  $180^\circ$  pulse at the echo time (TE) after the excitation pulse, figure 3.1a. The minimum TE in a spin echo sequence is limited by the time it takes to play out the phase encoding gradient, the  $180^\circ$  refocusing radio frequency (RF) pulse, and the frequency encoding gradient, typically around 5 ms. In a gradient echo sequence, there is no refocusing RF pulse, instead, a gradient echo is produced by the frequency encoding gradient, figure 3.1b. The negative lobe on the readout gradient will de-phase the spins, the positive readout gradient will then refocus the spins in the middle of the readout, producing the gradient echo. The TE in a gradient echo sequence is limited only by the duration of the phase and frequency encoding gradients, plus half of the excitation pulse, thus a shorter TE than in a spin echo sequence can be achieved.

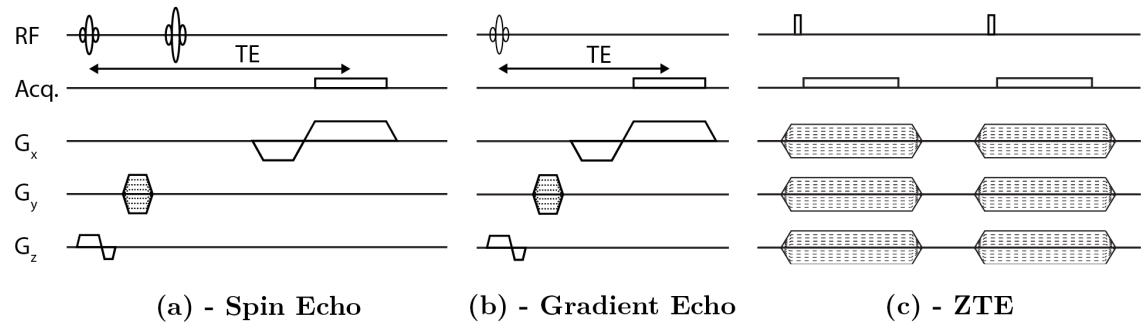


**Figure 3.1:** Comparison between spin echo (a), gradient echo (b), and zero TE (ZTE) (c) pulse sequences. These pulse sequence diagrams are simplified for illustration of the different concepts, practical implementations will differ to these sketches.

A further reduction in the TE can be achieved with zero echo time (ZTE) sequences, by performing RF excitation with the frequency encoding gradient already on and starting readout immediately after excitation, figure 3.1c [101]. ZTE can, therefore, be considered a special case of projection imaging. No spin or gradient echo is produced, instead, the free induction decay (FID) is acquired. Figure 3.1c shows a simplified ZTE sequence where the gradients are ramped up and down for each FID. Practical implementations of ZTE sequences, such as RUFIS, typically ramp only between the desired gradient amplitudes for subsequent readouts to reduce gradient switching, and thus acoustic noise, as will be

discussed later. Since readout is performed immediately after RF excitation, the effective TE is zero (ZTE), resulting in minimal signal decay, i.e.  $T_2^*$  decay, which is advantageous for several applications. With TE=0, there is no phase evolution before the readout which results in an acquisition that is robust to both flow and motion [102, 21, 7]. ZTE can also be used for imaging of tissues with low water content, and thus ultra-short  $T_2$ , which typically would be MR invisible, such as bone [103], tendons [104] and lung tissue [105].

With the gradient structure in ZTE, as shown in figure 3.1c, radial projections, originating from the centre of k-space are acquired. The repeated sampling of the centre of k-space leads to uneven sampling density in k-space, and thus less optimal sampling efficiency. In a direct comparison with Cartesian sequences, projection reconstruction methods are significantly slower than the Cartesian equivalent [106]. However, ZTE sequences can achieve much shorter TR than a Cartesian sequence and, will therefore, have higher efficiency per TR. In chapters 4 and 5, Cartesian gradient echo and ZTE sequences will be compared in more detail.

### 3.1.2 ZTE with RUFIS

The ZTE imaging sequence used in this thesis is the Rotating Ultra-Fast Imaging Sequence (RUFIS) [7]. The first works using RUFIS aimed at measuring turbulent flow using a 2D implementation [7, 107]. The first quantitative relaxometry work using RUFIS, to my knowledge, was  $T_1$  mapping using the transient state behaviour in RUFIS [108]. In these early publications, the silent aspect of RUFIS was not highlighted. Only more recent work, following the commercialisation of a 3D RUFIS sequence by General Electric Healthcare, did exploit the near-silent properties of RUFIS. Comparisons have been made between  $T_1$ -prepared RUFIS to standard  $T_1$  weighted imaging at both 3T and 7T, finding comparable image contrast with RUFIS but substantially reduced acoustic noise levels, at or just above the ambient noise in the scan room [98, 99, 104]. Using  $T_2$ -preparation Solana et al. used RUFIS for silent BOLD-fMRI [109], and recently diffusion prepared RUFIS has been demonstrated [110].

The ZTE feature in RUFIS is not directly beneficial in standard neurological exams, however, it is useful for studying tissues with short  $T_2$  outside the brain. Recent work has utilised high bandwidth (BW) RUFIS acquisitions for bone imaging in the head, showing that the resulting images can be transformed to produce attenuation maps useful for combined positron emission tomography (PET)/Magnetic Resonance Imaging (MRI) ac-

quisitions [103]. RUFIS has also been used for lung imaging, where its high sensitivity to tissue with short and rapid acquisition are attractive features [105]. Imaging using RUFIS outside the head typically requires high imaging bandwidth to avoid water-fat shift artefacts. Recent work by Engström et al. has shown that by acquiring two sets of data with different bandwidths the signal from fat can be separated from the water signal and a pure in-phase image can be reconstructed, free from water-fat shift artefacts [111].

### 3.2 The RUFIS Pulse Sequence

An overview of the RUFIS pulse sequence is shown in figure 3.2. The sequence consists of a segmented readout, with each segment consisting of a number of data acquisitions (each in the presence of a slightly different readout gradient), referred to as spokes. The segmented layout of the sequence allows for contrast preparation between segments [109]. Excitation is performed using an ultra-short ( $\approx 8\text{-}64\mu\text{s}$ ) hard RF pulse, which typically limits the flip angle to the range of  $1\text{-}10^\circ$  due to RF amplifier and specific absorption rate (SAR) constraints. The repetition time (TR) is defined as the time between two spokes, typically on the order of 1-4 ms, determined by the BW and the matrix size. Since the TR is only limited by the readout time, the imaging time scales almost linearly with the bandwidth. Increasing the bandwidth imposes constraints on other imaging parameters though, which will be discussed in section 3.6.

At the beginning of each segment, the gradients are slowly ramped up to the required amplitude and direction of the first spoke. RF excitation is performed with the gradients on, and the RF system switches from transmit to receive mode immediately, achieving an effective echo time of zero<sup>1</sup>. The k-space trajectory is designed such that the end points of the spokes trace a spiral on a sphere in k-space, minimising the gradient change between subsequent spokes, and thus ensuring a near silent acquisition. An example of a k-space trajectory (i.e. the spoke end-points) with 512 spokes for RUFIS is shown in figure 3.3. In this thesis, the *standard* RUFIS trajectory is a single path through k-space which produces a uniform distribution of points, similarly as described by Wong and Roos [112]. In chapter 7, another trajectory, the 3D spiral phyllotaxis trajectory, will be presented for the application of motion correction [113]. Unless stated otherwise, the k-space trajectory used in this work is the standard RUFIS trajectory.

<sup>1</sup>The switching time is finite which results in a deadtime gap where data can be missed; this is discussed further later in this chapter.

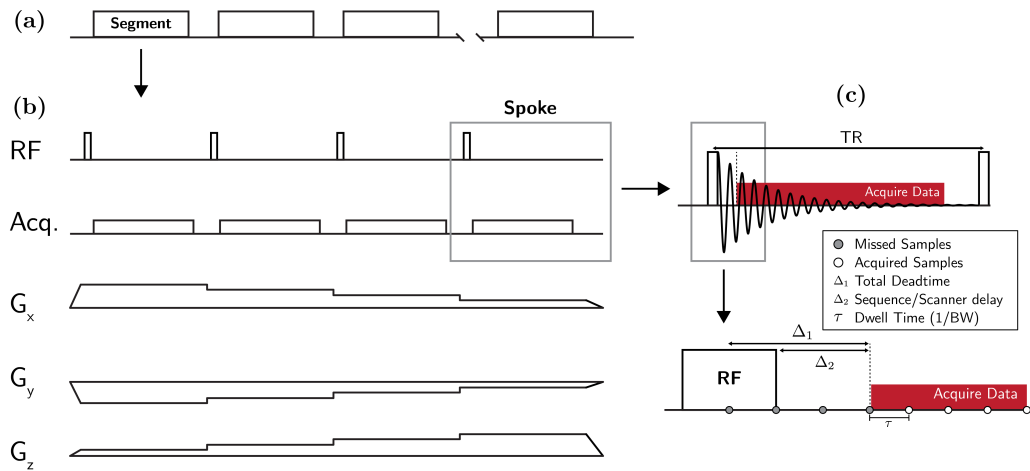


**Figure 3.2:** Overview of the RUFIS sequence. (a) The sequence is divided into segments, where each segment (b) consists of a number of spokes, i.e. collection of data along centre-out radial projections in k-space. (c) Each spoke comprises a single hard RF pulse and an FID readout. The time from the centre of the RF pulse (when the trajectory through k-space begins) to the beginning of data collection leads to a deadtime gap  $\Delta_1$ , resulting in missed k-space samples (gray dots in (c)). The number of samples missed depends on the dwell time  $\tau$ .

The phase of the excitation RF pulse is incremented between excitations to spoil the transverse magnetisation [114]. Additional spoiling is achieved from dephasing of the signal by the gradients during readout. If residual transverse magnetisation remains after the readout, it will be refocused when the time integral of the applied gradients is zero<sup>2</sup>. Coherences excited at the beginning of the acquisition, with strong positive  $z$ -gradient will not be refocused until the end of the acquisition. Spokes in the middle of the trajectory on the other hand, where  $G_z \approx 0$  (i.e. around the equator), can be rapidly refocused. The spoiling behaviour of the RUFIS sequence is therefore not trivial. For Cartesian spoiled gradient echo (SPGR), numerical methods have been developed for studying effects of imperfect spoiling [116, 117]. These techniques are not directly translatable to RUFIS, as they assume dedicated gradient spoiling along one axis, which is not true for the 3D gradients applied in RUFIS. Recent work has studied spoiling behaviour in radial SPGR [118], suggesting that a random RF phase increment provides the best spoiling behaviour. The RUFIS implementation used in this thesis uses a  $117^\circ$  phase increment [114]. It was outside the scope of this thesis to do a thorough study of the optimal phase increment.

<sup>2</sup>It was accidental refocusing in a RUFIS in a lung imaging experiment using a phyllotaxis trajectory that sparked the idea of *Looping Star*, a variation of RUFIS where the signal is purposefully refocused to obtain a gradient echo and thus produce  $T_2^*$  weighted images [115] (Personal communication with Florian Wiesinger).



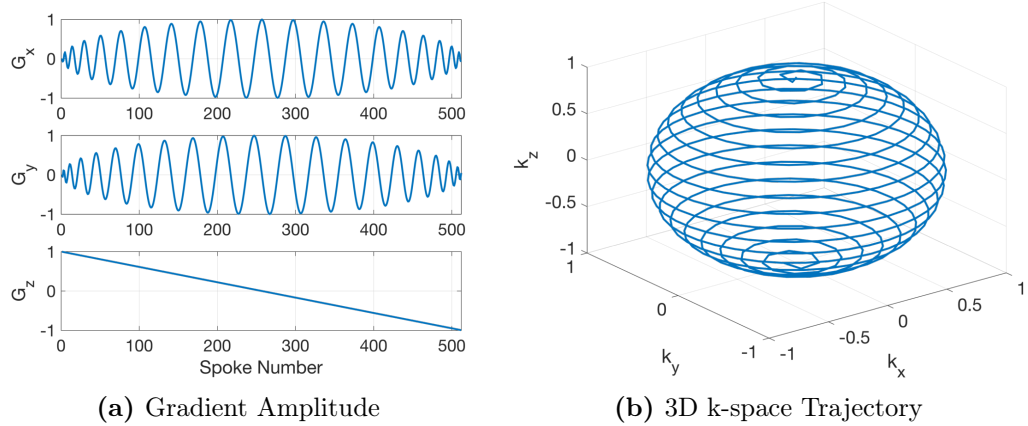


**Figure 3.3:** Example of a RUFIS k-space trajectory. **(a)** Gradient waveforms ( $G_x, G_y, G_z$ ) showing the spiral trajectory in  $x$  and  $y$  while the  $z$  gradient is linear. **(b)** 3D view of the k-space trajectory showing the end-points of the spokes connected by a line, demonstrating the smooth changes between subsequent spokes, and thus near-silent readout.

While the spoiling behaviour in RUFIS is still not fully understood, no evidence of imperfect spoiling was noted in the images collected for this thesis and the transverse magnetisation after each FID is therefore assumed to be fully spoiled. The sequence can thus be treated as a segmented SPGR, also known as fast low angle shot (FLASH) [119], sequence, with optional magnetisation preparation, similar to as described by Haase et al. [120], or more recently in pulse sequences such as magnetisation prepared rapid gradient echo (MPRAGE) and MP2RAGE [48, 49]. In an MPRAGE experiment, the contrast can be manipulated both by changing the inversion time (TI) but also the view ordering of the rapid gradient echo (RAGE) readout, as the k-space line closest to the centre of k-space determines the image contrast. In RUFIS, each spoke originates in the centre of k-space, thus the effective image contrast is the average of the signal from all spokes in the segment and is not affected by the order in which these are collected.

### 3.2.1 Radial Sampling

The Nyquist criterion for Cartesian imaging requires  $\Delta k = 1/L$  to avoid aliasing. In centre-out 3D radial imaging, each readout originates in the centre of k-space, figure 3.4a, resulting in a sampling density proportional to the square of the radial distance  $k_r$  from the centre of k-space. To satisfy the Nyquist criterion in radial imaging, both the radial and angular sampling density need to be considered, figure 3.4b. The readout along the spoke can be compared to the frequency encoding in Cartesian imaging, with the data

being low-pass filtered to satisfy Nyquist. In the angular direction, it is typically considered that the distance between the endpoints of the spokes has to satisfy the relationship  $\Delta k_\phi = 1/L$  [121]. The following derivation will be based on this assumption, after which the implication of non-uniform sampling, and the effect on the Nyquist criterion will be discussed.

The endpoints of the spokes all lie on the same spherical shell in k-space at the radius  $k_{r,max}$  spaced  $\Delta k_\phi$  apart in each direction to satisfy Nyquist, figure 3.4c and d. The area of the sphere at the end of the spokes is given by  $A_{max} = 4\pi k_{r,max}^2 = 4\pi(\Delta k \cdot N_{pts})^2$ , where  $N_{pts}$  is the number of points along the spoke. If the surface of the sphere is approximated by squares, each sample occupies an area  $A_{samp} = \Delta k^2$ . The total area covered by  $N_{spokes}$  spokes is thus given by  $A_N = N_{spokes} \Delta k^2$ . To satisfy the Nyquist criterion, the following relationship should therefore hold

$$A_N = A_{max} \rightarrow 4\pi \Delta k^2 N_{pts}^2 = N \Delta k^2 \rightarrow N = 4\pi N_{pts}^2 \quad (3.1)$$

Since the spokes are sampled from centre out,  $N_{pts}$  is half the matrix size  $MAT$ , which yields

$$N_{nyquist} = \pi \cdot MAT^2. \quad (3.2)$$

The definition of the Nyquist criterion  $\Delta k_\phi = 1/L$  is derived for uniform sampling and does therefore not strictly apply in the same sense for radial acquisitions where the sampling density scales with  $1/k_r^2$ . The requirement  $N_{spokes} = \pi \cdot MAT^2$ , which is typically quoted for 3D radial acquisitions [121], will ensure that Nyquist is satisfied at the very edge of k-space, which means that it is more than well satisfied in the centre where the density is higher. It was shown by Landau that for non-uniform sampling, it is the average sampling density that has to satisfy the Nyquist criterion [122, 123]. Therefore, the number of spokes required to satisfy Nyquist for average sampling density is lower than  $N_{nyquist} = \pi \cdot MAT^2$ , and the exact number will depend on the trajectory.

Undersampling in the angular direction in a radial acquisition by reducing the number of spokes, will not produce coherent aliasing artefacts as observed in undersampled Cartesian acquisitions [124, 125]. The undersampled radial acquisition will produce aliasing artefacts manifesting in all directions, resulting in blurring or, depending on the level of undersampling, streaking, artefacts [104, 126]. It is therefore common to undersample 3D radial acquisitions by a factor  $\pi$  as long as the signal to noise ratio (SNR) is suffi-

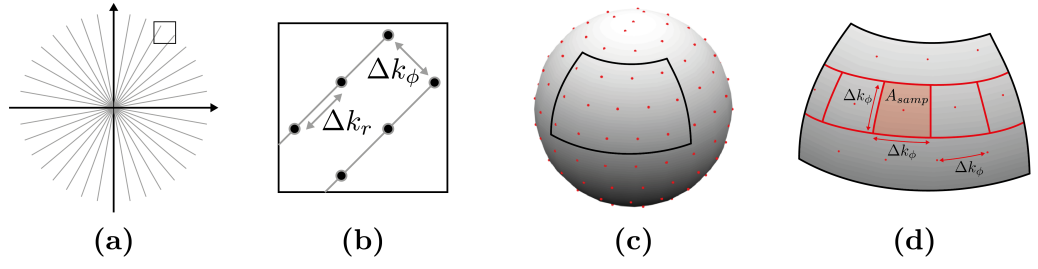


**Figure 3.4:** (a) Schematic 2D view of a radial trajectory showing the spokes originating from the centre of k-space. (b) To satisfy Nyquist, the samples are spaced  $\Delta k$  apart in the radial direction, and  $\Delta k$  in the angular direction at the end of the spokes. (c) The endpoints of the spokes fall onto the same spherical shell in k-space, where each spoke occupies an area  $A_{samp} = \Delta k^2$  (d).

cient [104]. In the implementation of RUFIS used in this work, undersampling with a factor  $\pi$  is considered fully sampled, i.e. number of excitations (NEX)=1. The inherent non-uniform sampling in 3D radial acquisitions lends itself well to compressed sensing (CS) reconstruction where non-uniform, pseudo-random, sampling with radially increasing sampling density is preferred [127].

### 3.2.2 The Deadtime Gap

Since the readout gradients are already on during excitation, the radial-out trajectory in k-space starts immediately. Due to the finite switching time from transmit to receive mode, a number of samples may be missed during this time, as shown in figure 3.2 and referred to as the deadtime gap [128]. This results in region in the centre of k-space without acquired k-space samples, with the number of samples missed directly proportional to the readout bandwidth and the switching time of the transmit/receive chain.

Figure 3.5 shows examples of the type of image artefacts that appears when samples in the centre of k-space are missed, and how artefact free images can be recovered by filling the deadtime gap, as explained below, in this case using the WASPI method. At 7.8kHz readout BW, the number of samples missed is negligible and an image can be reconstructed without filling the deadtime gap. Increasing the BW, and thus the number of samples missed, results in severe image artefacts. The data shown in figure 3.5 were collected using a single channel transmit/receive coil<sup>3</sup> which has a much longer deadtime gap compared to transmission on the body coil and a dedicated head receive coil. The artefacts are the same using a different setup, but the deadtime artefacts will appear at

<sup>3</sup>The GE phantom only fits in this coil

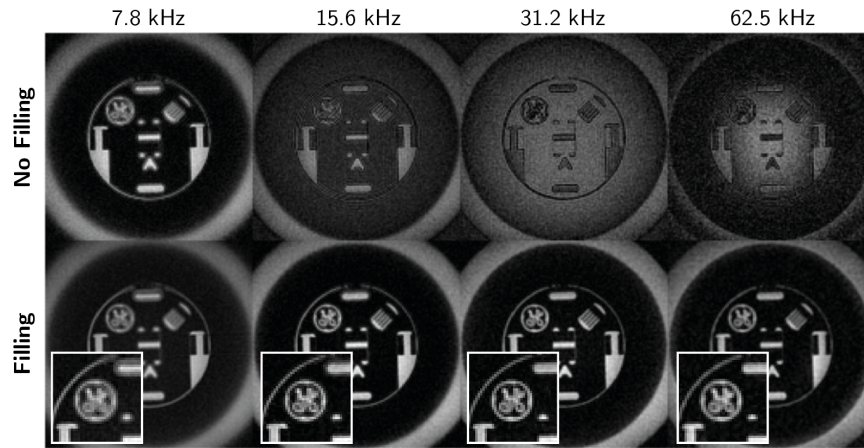


**Figure 3.5:** Example of images acquired with four different readout bandwidths (7.8, 15.6, 31.2, 62.5 kHz) with and without centre k-space filling using WASPI. The effect of missing samples in the centre of k-space is seen in the top row.

higher bandwidths. For example, using a 32 channel Nova Medical head receive coil it is possible to acquire artefact free images at 15.6 kHz without filling the centre of k-space.

Various methods have been developed to fill the deadtime gap [128], which can be categorised as either acquisition or interpolation based. One of the earliest interpolation methods, co-authored by the authors who originally introduced RUFIS, is referred to as algebraic reconstruction [25]. It requires a k-space trajectory in which each spoke is paired up with another spoke with the opposite direction, forming a complete 1D projection through k-space. The missing samples in the centre can be interpolated by requiring that the data has finite support in image space, i.e. the image is zero around the edge of the field of view. The algebraic reconstruction works well as long as the number of missed samples is low [128]. Alternatively, a separate acquisition for the centre of k-space can be used, which is an approach taken by two main methods: Water- and Fat-Suppressed Solid-State Proton Projection Imaging (WASPI) and Pointwise Encoding Time Reduction with Radial Acquisition (PETRA) [129, 130]. In WASPI, a second acquisition is performed, with k-space trajectory and other parameters similar to the main sequence but with a lower gradient amplitude (and accordingly less number of spokes), which results in a longer dwell time and fewer missed samples, as illustrated in figure 3.2. In PETRA on the other hand, individual points are acquired on a Cartesian grid in the region of k-space where points were missed due to the deadtime gap.

The choice of deadtime gap filling method depends on the acquisition requirements [128]. Algebraic reconstruction requires no additional acquisition, but imposes additional con-

straints on the k-space trajectories. With WASPI, near silent acquisition can be maintained since a similar k-space trajectory as the main acquisition is used, except fewer spokes. Using a gradient reduction factor  $k$ , the WASPI acquisition requires a factor  $k^2$  fewer spokes compared to the nominal number of spokes. PETRA is the preferred method for imaging of samples with ultra-short  $T_2^*$ , as each k-space sample is collected separately and therefore produces no  $T_2$  apodisation, i.e. weighting of the k-space samples as a function of radius from the centre. However, this is at the expense of increased acoustic noise as the k-space trajectory is no longer silent. In this thesis, the deadtime gap was addressed using the WASPI method [129].

### 3.3 Image Reconstruction

Data acquired with RUFIS are encoded in non-Cartesian, radial, coordinates, along spokes originating from the centre of k-space. Since the sampling points do not fall onto a Cartesian grid, a direct inverse Fourier transform can not be used to obtain the image. Instead, the data is interpolated onto a Cartesian grid, a process called gridding, after which an inverse Fourier transform can be applied [131]. Alternatively, the reconstruction can be done in one step using the non-uniform fast Fourier transform (NUFFT) [27]. In this thesis, the method of gridding and inverse Fourier transform is used. The following sections outline typical steps in non-Cartesian image reconstruction and common problems that have to be solved.

#### 3.3.1 Gridding

Interpolating non-cartesian data onto a Cartesian grid is a non-trivial problem both from the theoretical and practical point of view. The gridding algorithm calculates the contribution of the data from each non-Cartesian point to each Cartesian grid point using a gridding kernel. Generally, the non-Cartesian data is interpolated onto a twice oversampled Cartesian grid, resulting in twice the field of view in image space, compensated for by cropping the image after the reconstruction. In this thesis, two different gridding methods are used: Kaiser-Bessel, and nearest neighbour gridding, both in 3D.

The k-space sampling trajectory, or pattern, can be described by k-space coordinates for each sample point  $(k_x, k_y, k_z)$ . In nearest-neighbour gridding, the trajectory coordinates for each point are rounded to the nearest integer value [132], and assigned to the corresponding Cartesian grid point (assuming that the Cartesian grid points have integer

coordinates). A more sophisticated, commonly used, gridding method is the Kaiser-Bessel method, where the non-Cartesian data are convolved with a 3D Kaiser-Bessel kernel onto a twice oversampled Cartesian grid [131]. The Kaiser-Bessel method is more computationally intensive but can produce less artefacts. Convolution by a kernel in k-space is equivalent to multiplication of the fast Fourier transform (FFT) of the same kernel in image space, which must be corrected for by dividing the image by the FFT of the convolution kernel, a process referred to as apodisation.

In nearest-neighbour gridding, the gridding kernel can be approximated as a shifted delta function, with a unique shift for each data point (although the gridding process is not strictly a convolution). The FFT of a delta function is a uniform function and results only in a change of the (already arbitrary) scaling of the data [132]. However, since the delta function has a different shift for each sample point, the gridding kernel will have a unique phase ramp for each sample point in image space, according to the Fourier shift theorem. In contrast to Kaiser-Bessel gridding, apodisation is not required after nearest-neighbor gridding, since the gridding kernel is uniform in image space. See section 3.4 for a comparison between the two methods, and further discussion on the implications on the image quality.

With non-Cartesian sampling, it is common to end up with variable sampling density in k-space, which has to be accounted for in the reconstruction to avoid artefacts. If the data are sampled along straight radial spokes, evenly distributed radially in k-space, the sampling density will be proportional to the square of the radius from the centre of k-space, as shown in section 3.2.1. The radial density compensation (DC) for a 3D acquisition  $DC_{radial}$ , which is applied before gridding to each spoke, is calculated as

$$DC_{radial}(r) = \frac{1}{r^2}. \quad (3.3)$$

### 3.3.2 Self-calibrated Sensitivity Maps

A coil sensitivity map is an image quantifying the sensitivity of the receive coil, which is a prerequisite for image-based parallel imaging methods such as SENSE [124], and can also improve the reconstruction of un-accelerated multi-coil data. Sensitivity maps are spatially smooth and thus typically obtained through a separate, fast, low-resolution, acquisition. It can also be extracted from the image data of a given acquisition if a non-aliased low-

resolution image can be reconstructed from the centre part of k-space [133], known as *self calibration*. With RUFIS, such a low resolution image can always be reconstructed as each spoke originates in the centre of k-space, as shown in figure 3.6 and outlined below.

An image acquired from a single receive coil,  $c_i$ , can be described as the true proton density  $\rho$  multiplied by the coil sensitivity  $C$ .

$$I_{coil}(x, y, z, c_i) = \rho(x, y, z) \cdot C(x, y, z, c_i) \quad (3.4)$$

Reconstruction of an image from the centre of k-space yields a low resolution representation of the proton density multiplied by the coil sensitivity. However, the coil sensitivity image is spatially smooth and thus accurately described even by such a low resolution image.

$$I_{acq}^{low}(x, y, z, c_i) = (\rho(x, y, z) \cdot C(x, y, z, c_i))^{low} = \rho(x, y, z)^{lowres} \cdot C(x, y, z, c_i) \quad (3.5)$$

A low resolution estimate of the proton density can be obtained by calculating the root sum of squares of all coil images as

$$\rho_{RSS}^{lowres}(x, y, z) = \rho(x, y, z)^{lowres} = \sqrt{\sum_{i=1}^N |I_{acq}^{low}(x, y, z, i)|^2} \quad (3.6)$$

The coil sensitivities can thus be calculated as

$$C(x, y, z, c_i) = \frac{I_{acq}^{low}(x, y, z, c_i)}{\rho_{RSS}^{lowres}(x, y, z)} \quad (3.7)$$

Using these coil sensitivity maps, a high resolution coil-combined image can be obtained by summing the individual coil images, weighted by the complex conjugate of the coil sensitivity

$$I_{comb}(x, y, z) = \sum_{i=1}^N I_{coil}(x, y, z, i) \cdot C^*(x, y, z, i). \quad (3.8)$$

### 3.3.3 Full Reconstruction Pipeline

An example of a multi-channel RUFIS reconstruction pipeline is outline in figure 3.7. The dimensions of the input data are  $n_{pts}, n_{spk}, n_{coils}$ , where  $n_{pts}$  is the number of readout points along the spoke,  $n_{spk}$  is the number of spokes in the acquisition and  $n_{coils}$  is the number of receiver channels. First, the radial density compensation  $DC_{radial}$  is applied to

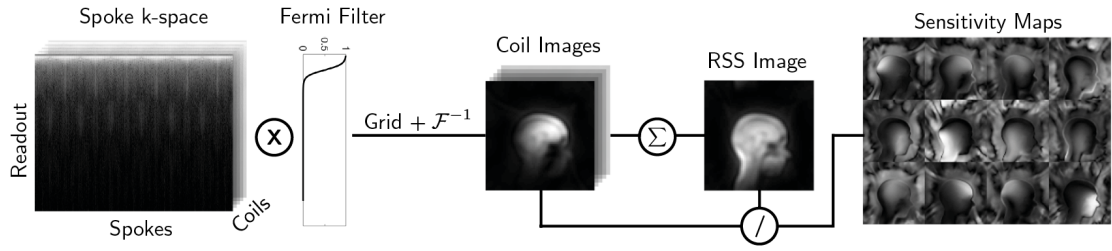


**Figure 3.6:** Example of how a low resolution reconstruction of RUFIS data can be used to produce sensitivity maps. Radial data is Fermi filtered and gridded to produce a low resolution image. Image from each coil is divided by the root-sum-of-squares (RSS) image to produce complex valued coil sensitivity maps.

the raw data. If density compensation is not performed, the image will appear blurry, as shown in 3.7, as this is equivalent to convolving the image with the Fourier transform of the  $DC$ . After gridding the data, a Cartesian k-space with dimensions  $(n_x, n_y, n_z, n_{coils})$  is obtained where, in the case of isotropic voxel size,  $n_x = n_y = n_z = 2n_{pts}$ . After inverse Fourier transform of the density compensated k-space, individual coil images are obtained from which the magnitude image can be calculated using a root-sum-of-squares (RSS) combination or complex valued coil combination using (3.8)<sup>4</sup>. Due to the standard two fold oversampling, an image with the prescribed FOV is obtained by cropping the final image to half the image size, indicated by the white rectangle.

In many standard image reconstruction pipelines, an apodization filter is applied to smooth the transition in the edge of k-space. If the k-space samples in the edge of k-space have high intensity, the sharp transition at the edge can lead to artefacts such as Gibbs ringing. In radial imaging, a Fermi filter can be applied in the radial direction, calculated as

$$f(r) = \frac{1}{1 + e^{(r-r_f)/w_f}} \quad (3.9)$$

where  $r_f$  and  $w_f$  is the filter radius and width respectively.

<sup>4</sup>There are numerous other methods for coil combination, in particular iterative methods which may have better noise-propagation. Here, a simple root-sum-of-square is used for simplicity and illustrating the concept.



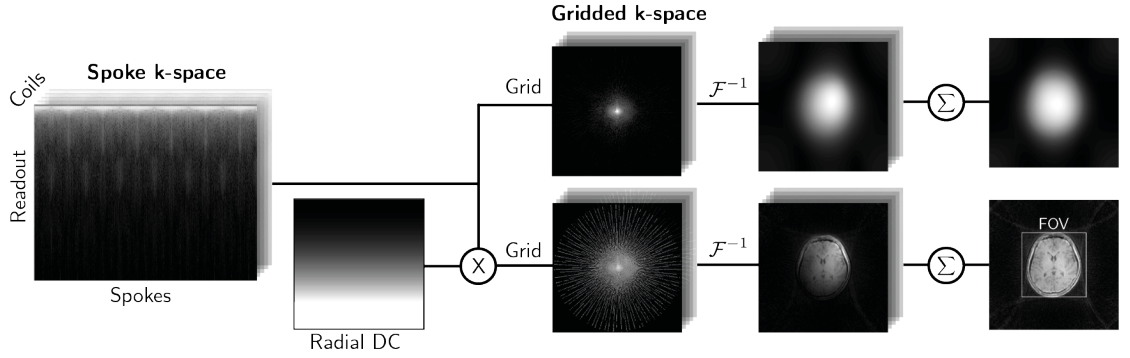


**Figure 3.7:** Example of RUFIS multi-coil reconstruction pipeline. In the top row, DC compensation is not applied resulting in significant blurring of the image.

### 3.4 Study A: Comparison of Gridding Methods

#### 3.4.1 Study A: Purpose

To compare the Kaiser-Bessel (KB), and Nearest-Neighbor (NN) gridding methods and evaluate how the choice of method influences the point spread function (PSF) and image artefacts.

#### 3.4.2 Study A: Methods

Three experiments were carried out: (1) an investigation of the point spread function (PSF) using simulated data, (2) reconstruction of simulated phantom data, and (3) reconstruction of in vivo data. To study the PSF, a point source was simulated by creating a k-space data set of ones, assuming no deadtime gap. To study gridding artefacts, k-space data for a 3D Shepp-Logan phantom were produced using the Berkeley Advanced Reconstruction Toolbox (BART) [28]. A trajectory with  $N_1 = 16384$  spokes, 128 readout points along each spoke, and two-fold oversampling was generated, resulting in a nominal matrix size of  $128 \times 128 \times 128$ . The data were density compensated using a radial *DC* filter, gridded using both the Kaiser-Bessel and Nearest-Neighbor gridding methods, and inverse Fourier transformed. The same procedure was then also performed with  $N_2 = 3 \cdot N_1$  number of spokes to study the effect of higher sampling density in k-space.

The in vivo data were collected on a 3T GE MR750 scanner with a 12 channel head coil, using a modified RUFIS sequence. Acquisition parameters: field of view (FOV)=  $192 \times 192 \times 192 \text{ mm}^3$ , voxel size= $1.5 \times 1.5 \times 1.5 \text{ mm}^3$ , TR=4.4 ms,  $\alpha = 12^\circ$ , BW= $\pm 7.8 \text{ kHz}$ . The data were reconstructed using the procedure outlined above, with addition of radial

Fermi filtering. Reconstruction was performed using in house developed scripts in MATLAB (The Mathworks, Natick, MA).

### 3.4.3 Study A: Results

There was a clear difference in the PSF between the two gridding methods, as shown in figure 3.8. The most visible difference was that KB gridding produced less structured artefacts in the final image. Studying the line profiles in the bottom row of figure 3.8 shows that the drop-off from the main peak was smoother with KB compared to NN. The line profiles in the three spatial dimensions showed different patterns, most clearly visible with KB where the  $z$  direction showed the widest drop-off, but similar behaviour in  $x$  and  $y$ . Using NN gridding, the difference in the PSF is smaller between the three dimensions. With  $N_1$  spokes, the PSF artefacts are right at the border of the nominal field of view. Increasing the number of spokes by a factor of 3 widens the smooth drop-off region of the PSF, most clearly visible in the KB images and PSF, but also apparent, to a lesser degree, with NN gridding.

The full width half max (FWHM) of the PSF, which can be interpreted as an estimate of image resolution, was comparable for KB and NN. At  $N_1$  number of spokes the FWHM was 1.48 and 1.51 for KB and NN respectively. Increasing the number of spokes to  $3 \cdot N_1$  did not change the FWHM of the PSF.

The results from the phantom experiment are shown in figure 3.9. Visual inspection shows that both methods produced good quality images. Visualising the data on a logarithmic intensity scale, however, shows artefacts in the NN image outside the object that are not present in the KB image. Studying the line profile through the phantom, 3.9c, shows less structured noise-like artefacts with the KB method and a sharper drop-off in intensity outside the object, especially with  $N_{spokes} = 3 \cdot N_1$ .

The in vivo data showed similar results to the phantom, with an initial visual inspection indicating comparable image quality from both methods within the central portion of the image, figure 3.10. With NN gridding, however, there was a gridding artefact around the brain, similar to that seen in the phantom data visualised on the logarithmic scale. Again, the artefact appeared along the border of the prescribed FOV indicated by the dashed white lines in the figure, but was not present with KB gridding. Studying the line profiles in 3.10c shows differences in intensity in the middle of image, indicating a brightening

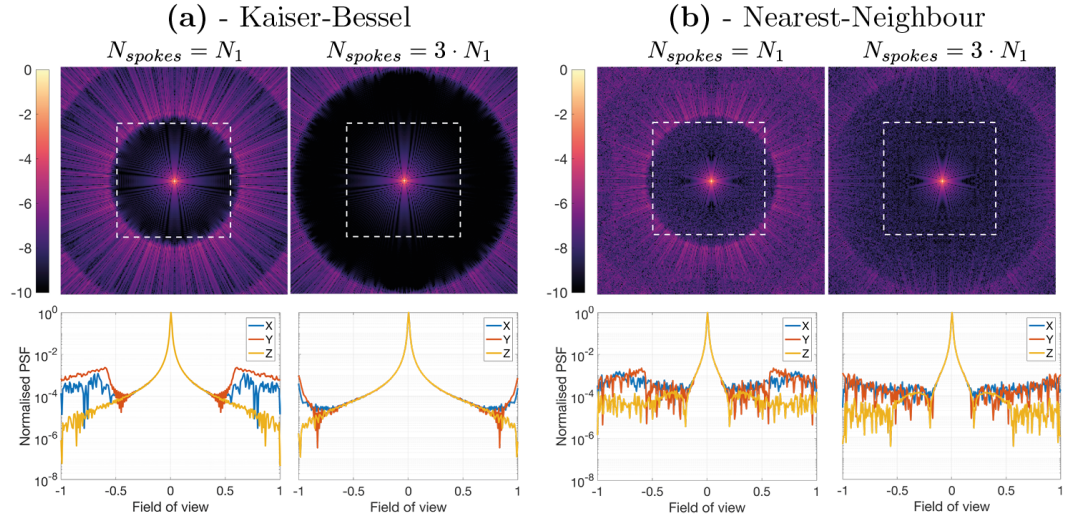


**Figure 3.8:** Comparison of point spread functions obtained using (a) Kaiser-Bessel and (b) Nearest-Neighbour gridding. Top row shows the point function in image space, and bottom row the line profile through isocentre along each of the three axes. The data is visualised on a logarithmic scale. The dashed white rectangle in the top row outlines the nominal field of view.

artefact which could be due to imperfect density compensation. This was also observed in the line profiles from the phantom experiment, shown in figure 3.9c.

#### 3.4.4 Study A: Discussion and Conclusion

The results from simulations and in vivo experiments presented in this sections shows the difference in image quality and artefacts that arise from using different gridding methods. The Kaiser-Bessel gridding method produced images with less structured and noise-like artefacts. It should be noted that while the NN gridding appears to be noisier, there was no noise introduced in these simulations, and thus it is not noise in the final image either. Rather, it should be interpreted as structured artefacts that appears noise-like. Oesterle et al. showed that the image quality with NN gridding improves as the oversampling factor in the gridding is increased [132]. Here, a factor of 2 was used, increasing this further would likely exceed the memory limits available on a typical workstation. A likely origin of the structured, noise-like, artefacts observed in the NN gridding is the variability in the phase of the gridding kernel. With NN gridding, the gridding kernel is a shifted delta function, with a unique shift for each point. This produces a kernel with a uniform intensity in image space, but with a unique phase ramp for each point. Due to variable direction and amplitude of these phase ramps, interference patterns can be produced in image space, producing the artefacts observed as here.

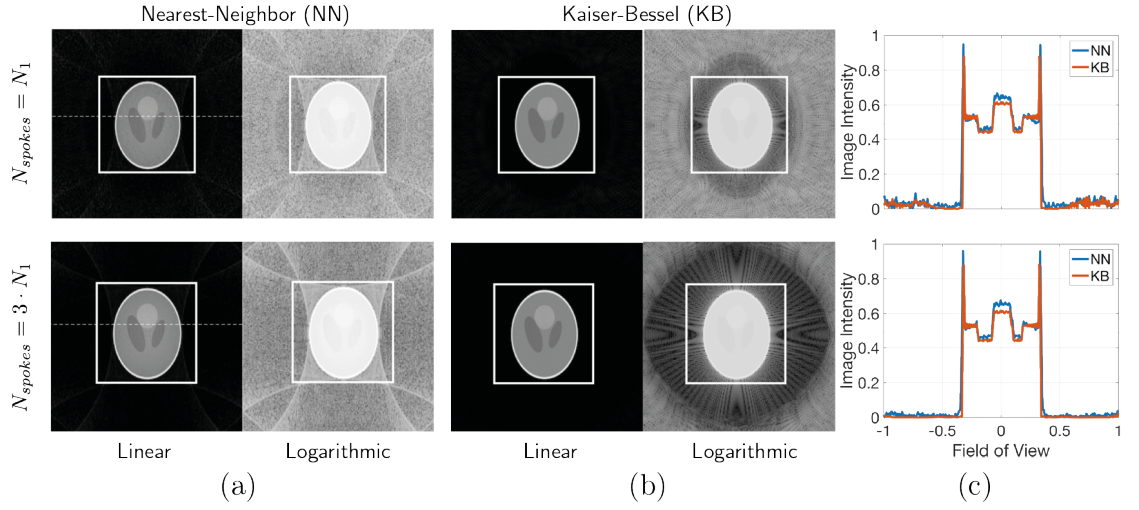


**Figure 3.9:** Shep-Logan phantom after gridding using KB (a) and NN (b) visualised on linear scale and logarithmic scale, together with line profile (c) along the white dashed line. Top row shows data with  $N_1$  number of spokes, and bottom row  $3 \cdot N_1$  number of spokes. Solid rectangle indicates the nominal field of view.

The 1D PSF shown in figure 3.8 showed different patterns in the three spatial dimensions, even though the sampling is uniform over the sphere. This highlights the fact that even though this is a 3D acquisition with cubic FOV, the choice of scan plan should still be considered. The specific pattern of the PSF in the three dimensions require more detailed analysis of the sampling trajectory which will be the goal of further work.

Increasing the number of spokes pushed the radial gridding artefacts further away from the centre of the FOV, as seen in the PSF and phantom experiments. The width of the PSF did not change with increasing number of spokes, as the resolution depends on the sampling radius in k-space and not the sampling density.

Based on these results, KB is the preferred method for reconstructing high quality images with RUFIS. However, there was a substantial difference in computation time; gridding the in vivo data presented here using the Nearest-Neighbour method took 11s, while the Kaiser-Bessel method took 77 s seconds (calculations performed on a MacBook Pro with 2.5 GHz Intel Core i7 and 16 GB of DDR3 RAM). Thus, when fast reconstruction is required, NN is the preferred choice, but when time is not of essence, KB gridding is the recommended method. Further acceleration could be achieved with more efficient implementations in for instance C++. In this work, both methods were implemented in MATLAB, with the KB gridding as compiled MEX code, but there is still overhead time for interfacing with MATLAB.

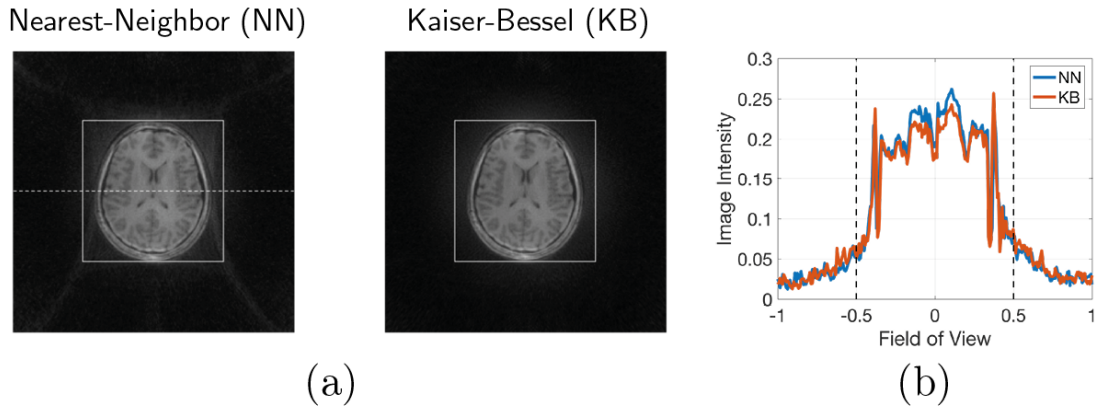


**Figure 3.10:** Comparison of KB and NN gridding in vivo. Brain slices in (a) shows less gridding artefacts with NN compared to KB. Line profiles in (b) shows difference in image intensity in the middle of the brain, similar to the phantom examples. Solid rectangles in (a) and dashed black lines in (b) indicate the nominal field of view.

### 3.5 Study B: A Quantitative Signal Equation for RUFIS

#### 3.5.1 Study B: Purpose

This thesis aims to develop quantitative methods for RUFIS, and thus a quantitative signal representation for RUFIS is required. In this section, an analytical signal equation for the acquired signal from an individual RUFIS segment is derived. A semi-iterative signal equation for a complete magnetisation prepared RUFIS acquisition will also be investigated.

#### 3.5.2 Study B: Method

##### Analytical Method

The segmented structure of the RUFIS sequence, and repeated sampling from the centre of k-space, requires the calculation of the average magnetisation of all spokes in a segment, given an initial longitudinal magnetisation. The first part of the derivation outlined here can also be found in previous works such as Hsu and Lowe [108]. However, the focus here is on calculating the average magnetisation within a segment which is the effective magnetisation that is observed in the resulting images.

The acquired signal is given by the transverse magnetisation, which given a longitudinal magnetisation  $M_z$  and excitation flip angle  $\alpha$  is calculated by  $M_T = \sin \alpha \cdot M_z$ . Each RF pulse acts on the longitudinal magnetisation, decreasing it by a factor of  $\cos \alpha$ ,

while the time required for the spoke readout results in  $T_1$  recovery. Since the transverse magnetisation is spoiled, only the longitudinal magnetisation is considered here.

Consider two RF pulses in a given segment. The longitudinal magnetisation before RF pulse  $n + 1$  depends on the time since RF pulse  $n$  (i.e. the TR) as well as the flip angle  $\alpha$  as

$$M_z(n + 1) = M_z(n) \cdot \cos \alpha \cdot E_1 + \rho(1 - E_1). \quad (3.10)$$

where  $E_1 = e^{-TR/T_1}$ . The solution to this recursive expression can be written as

$$M_z(n) = M_z(0) \cdot \cos^n \alpha \cdot E_1^n + \rho(1 - E_1) \cdot \frac{1 - \cos^n \alpha \cdot E_1^n}{1 - \cos \alpha \cdot E_1} \quad (3.11)$$

where  $M_z(0)$  is the magnetisation at the beginning of the segment, prior to any RF excitation. As  $n \rightarrow \infty$ , (3.11) reduces to the standard SPGR equation [51]

$$\lim_{n \rightarrow \infty} M_z(n) = M_{z,SPGR} = \rho \cdot \frac{1 - E_1}{1 - \cos \alpha \cdot E_1} \quad (3.12)$$

Equation (3.11) can be simplified by substituting  $\xi = \cos \alpha \cdot E_1$  and the expression for  $M_{z,SPGR}$ , which yields

$$M_z(n) = M_z(0) \cdot \xi^n + (1 - \xi^n) \cdot M_{z,SPGR}. \quad (3.13)$$

The acquired signal from a segment  $M_{seg}$  with  $N$  spokes is given by the average signal of all  $N$  spokes

$$M_{seg} = \sin \alpha \cdot \frac{1}{N} \sum_{i=0}^{N-1} [M_z(0) \cdot \xi^i + (1 - \xi^i) \cdot M_{z,SPGR}] \quad (3.14)$$

$$= \sin \alpha \cdot (M_z(0) \cdot f_N + (1 - f_N) \cdot M_{z,SPGR}) \quad (3.15)$$

where

$$f_N = \frac{1 - \xi^N}{N(1 - \xi)}. \quad (3.16)$$

and  $M_z(0)$  is the longitudinal magnetisation before the first spoke. Due to the inter-segment delay in RUFIS, a perfect steady state will never be reached, due to  $T_1$  recovery between segments. If an inter-segment steady state has been reached, however, such that the  $M_z(0)$  is the same for each segment, here called  $M_{z,SS}$ , then the magnetisation at the

beginning of each segment can be described as

$$M_{z,SS}(0) = M_z(N) \cdot e^{2\tau/T_1} + \rho(1 - e^{-2\tau/T_1}) \quad (3.17)$$

$$= (M_{z,SS}(0) \cdot \xi^N + (1 - \xi^N) \cdot M_{z,SPGR}) \cdot e^{-2\tau/T_1} + \rho(1 - e^{-2\tau/T_1}) \quad (3.18)$$

where  $2\tau$  is the delay between segments, typically on the order of  $2\tau = 20\text{ms}$ . Solving for  $M_{z,SS}(0)$  yields

$$M_{z,SS} = \frac{1}{1 - e^{-2\tau/T_1} \xi^N} \left( (1 - \xi^N) \cdot M_{z,SPGR} \cdot e^{-2\tau/T_1} + \rho \cdot (1 - e^{-2\tau/T_1}) \right). \quad (3.19)$$

If  $\tau \rightarrow 0$ , and  $N \rightarrow \infty$  then  $M_{z,SS} \rightarrow M_{z,SPGR}$ .

### Iterative Method

The analytical method presented above provides an efficient calculation of the quantitative signal in a RUFIS acquisition, but it is only suitable for a steady state acquisition. For more complicated sequences with magnetisation preparation modules in place of, or in addition to the inter-segment delay, e.g.  $T_1$  and  $T_2$  preparation which will be described in chapter 6, the magnetisation evolution is difficult to describe analytically. An iterative method provides a more flexible framework for describing the magnetisation quantitatively, albeit at the cost of being more computationally expensive.

Consider a magnetisation prepared RUFIS sequence as outlined in the figure 3.11. Here, a  $T_1$  preparation in the form of an inversion pulse is applied, followed by four RUFIS segments,  $T_2$  preparation with a given TE, and another RUFIS segment. Each RUFIS segment is defined by its TR, flip angle ( $\alpha$ ), number of spokes  $N$ , and gradient ramp up time  $\tau$ . Since the transverse magnetisation is continuously spoiled in RUFIS, only the longitudinal magnetisation needs to be tracked through the sequence.



**Figure 3.11:** Example of RUFIS sequence with multiple magnetisation preparation modules.

Let the acquired signal in RUFIS segment  $i$  be given by  $y_i$ . To reach a steady state, a number of dummy repetitions ( $dda$ ) of the sequence are applied before acquiring data. This is accounted for in the simulation by running a loop  $dda + 1$  times and only saving

the signal from the last iteration. The algorithm outlined in Algorithm (1) can be used to calculate the magnetisation evolution.

---

**Algorithm 1** Iterative RUFIS Algorithm

---

```

 $M_z \leftarrow 1$ 
 $k \leftarrow 0$ 
 $E_\tau \leftarrow e^{-\tau/T_1}$ 
 $\xi \leftarrow \cos \alpha \cdot e^{-TR/T_1}$ 
for  $k \leq (dda + 1)$  do                                 $\triangleright$  Repeat loop for dummy acquisitions
     $M_z \leftarrow -M_z$                                      $\triangleright$  Inversion pulse

     $l \leftarrow 0$ 
    for  $l < 4$  do                                 $\triangleright$  Acquire RUFIS segments
         $M_z \leftarrow M_z \cdot E_\tau + \rho(1 - E_\tau)$          $\triangleright$  Ramp up gradient(s)
         $y_{k,1} \leftarrow \sin \alpha \cdot (M_z \cdot f_N + (1 - f_N) \cdot M_{z,SPGR})$      $\triangleright$  Segment Average
         $M_z \leftarrow M_z \cdot \xi^N + (1 - \xi^N) \cdot M_{z,SPGR}$      $\triangleright$  Effect of  $N$  RF pulse
         $M_z \leftarrow M_z \cdot E_\tau + \rho(1 - E_\tau)$          $\triangleright$  Ramp down gradient(s)
    end for

     $M_z \leftarrow M_z \cdot e^{-TE/T_2}$                      $\triangleright$  T2-preparation

     $M_z \leftarrow M_z \cdot E_\tau + \rho(1 - E_\tau)$          $\triangleright$  Ramp up gradient(s)
     $y_{k,1} \leftarrow \sin \alpha \cdot (M_z \cdot f_N + (1 - f_N) \cdot M_{z,SPGR})$      $\triangleright$  Segment Average
     $M_z \leftarrow M_z \cdot \xi^N + (1 - \xi^N) \cdot M_{z,SPGR}$      $\triangleright$  Effect of  $N$  RF pulse
     $M_z \leftarrow M_z \cdot E_\tau + \rho(1 - E_\tau)$          $\triangleright$  Ramp down gradient(s)
end for

```

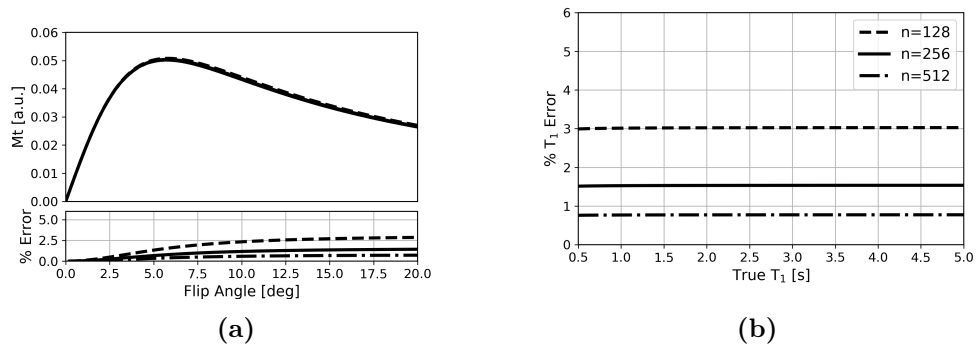
---

### 3.5.3 Study B: Results

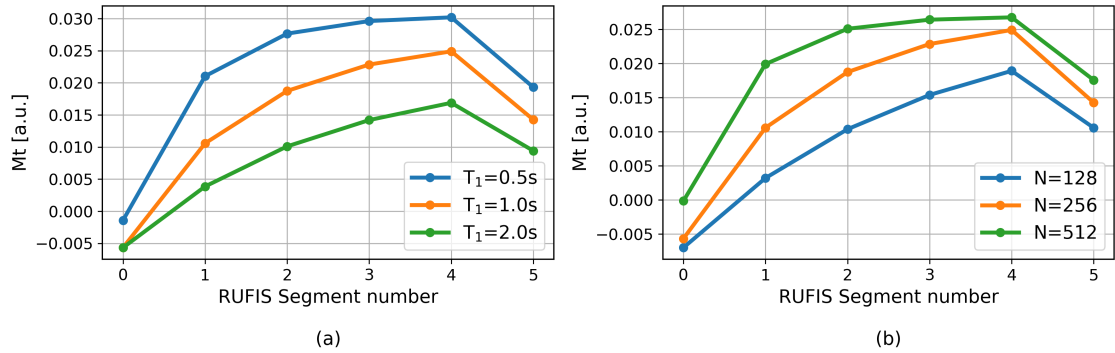
In a steady state RUFIS experiment, the steady state is slightly disturbed by inter-segment delays. Figure 3.12a shows the transverse magnetisation in a RUFIS experiment for different number of spokes, compared to the conventional SPGR equation. With 512 spokes per segment, as would typically be used for a steady state experiment, there is  $\approx 1\%$  difference between the two signal representations at high flip angles. If the SPGR equation is used for quantifying  $T_1$  with data simulated by the RUFIS equation, the error in  $T_1$  is thus small, with a error of  $< 1\%$  over a large range of  $T_1$ , as seen in figure 3.12b.

Figure 3.13 shows an example of the iterative method, calculating the signal of a contrast prepared RUFIS sequence. The RUFIS readout produces  $T_1$  weighting from the repeated excitation and  $T_1$  recovery. At longer  $T_1$ , 3.13a, there is less  $T_1$  recovery. Increasing the number of spokes per segment increases the  $T_1$  weighting, 3.13b. The iterative simulation method will be further validated in chapter 6 where it is used in the context of  $T_1$  and  $T_2$  mapping.





**Figure 3.12:** (a): Example of steady state signal simulations of the RUFIS sequence for different number of spokes per segment. With 512 spokes per segment (maximum), the error between the SPGR equation and analytical RUFIS equation is negligible. (b): Error in quantitative  $T_1$  fitting using the SPGR equation with simulated RUFIS data



**Figure 3.13:** Simulation of contrast prepared RUFIS acquisition simulated using the iterative method. (a) 256 spokes per segment,  $T_2=80\text{ms}$ ,  $TE=80\text{ms}$ . (b)  $T_1=1\text{s}$ ,  $T_2=80\text{ms}$ ,  $TE=80\text{ms}$ .

### 3.5.4 Study B: Discussion and Conclusions

In this section, it was shown that RUFIS imaging in the steady state, with a high number of spokes per segment, is well approximated by the SPGR equation. Given the small flip angles and short TR used in RUFIS, the SPGR equation could also be simplified with a first order approximation as

$$M_{z,RUFIS} = \frac{\rho}{1 + \frac{T_1}{TR} \cdot \frac{\alpha^2}{2}}. \quad (3.20)$$

The iterative signal representation method presented in here is a powerful method for describing any type of contrast-prepared RUFIS acquisition. The key difference between contrast-prepared RUFIS and a segmented gradient echo readout is the signal averaging over the readout segment. With a contrast prepared FLASH acquisition, the contrast is set

by the k-space line acquired closest to centre of k-space, thus if the k-space is filled centre-out then the contrast is dominated by the first readout, at the beginning of the segment. With RUFIS, the segment averaging results in additional  $T_1$  weighting in the signal from the repeated nutation and recovery periods. To maintain the prepared contrast, the number of spokes per segment must be low, although this will reduce the overall efficiency of the sequence (because of increased number of preparation periods needed and the "wasted" time for gradient ramps up and ramp down) and will thus increase acquisition time.

## 3.6 Study C: A Rotating 3D Excitation Profile

### 3.6.1 Study C: Purpose

In RUFIS, excitation is performed with a non-selective, hard, RF pulse which is applied in the presence of the readout gradients, resulting in a sinc shaped excitation profile<sup>5</sup>, similar to slice or slab selection, but here in the direction of the current readout spoke [130]. In this substudy, a theoretical framework for simulating the excitation profile will be presented, together with data showing the excitation profile effect in a spherical phantom.

### 3.6.2 Study C: Theory

The width of the main lobe of the sinc shaped excitation profile is proportional to the gradient amplitude (i.e. the bandwidth), and the width of the excitation pulse  $\tau_{rf}$  as

$$E(\vec{r}) = \text{sinc}(\tau_{rf} \cdot \gamma \cdot \vec{G} \cdot \vec{r}) \quad (3.21)$$

where  $\vec{r}$  is the position in the field of view and  $\vec{G}$  is a vector describing the direction of the applied gradient. The excitation profile is the spatial profile of the  $B_1$  efficiency, i.e. the effective flip angle across the field of view. To obtain uniform signal intensity over the field of view, the shortest possible pulse width should therefore be used. As the spoke direction constantly changes, so does the excitation profile. With a large number of spokes, the excitation profile will average out to a radially symmetric shape.

---

<sup>5</sup>With a linear gradient, and for the low flip angles typical of RUFIS, the excitation profile is given by the Fourier transform of the excitation pulse which here is a rectangular pulse, resulting in a sinc shaped excitation profile.

### 3.6.3 Study C: Methods

To simulate the excitation profile an iterative method was developed in MATLAB (The Mathworks, Natick, MA). Let  $T$  be the sampling trajectory with size  $[3, n_{spokes}]$  containing unit vectors describing the direction of each spoke. In an acquisition with matrix size  $[n_x, n_y, n_z]$ , a readout bandwidth of  $\pm BW$ , and a RF excitation with a pulse width  $pw$ , the excitation profile  $SP$  for spoke  $i$  can be simulated using the code in listing 3.1. Using this approach, a 3D excitation profile was generated for each of the gradient directions in a given trajectory, averaged and normalised.

**Listing 3.1:** Excitation profile MATLAB code

```

1  fx = linspace(-BW, BW, nx);
2  fy = linspace(-BW, BW, ny);
3  fz = linspace(-BW, BW, nz);
4  [X,Y,Z] = meshgrid(fx,fy,fz);
5  SP = sinc(pw*(T(1,i)*X + T(2,i)*Y + T(3,i)*Z));

```

An MR experiment was carried out with a spherical fluid filled phantom on a 3T GE MR750w using the head section of a GE 24 channel head neck spine (HNS) array coil. Data were acquired with voxel size  $3 \times 3 \times 3 \text{ mm}^3$ , matrix size  $64 \times 64 \times 64$ ,  $1^\circ$  flip angle and  $\pm 7.8 \text{ kHz}$  readout bandwidth. Eight different datasets were acquired with the RF pulse width set to: 8, 16, 32, 48, 64, 80, 96 and  $128 \mu\text{s}$ .

### 3.6.4 Study C: Results

#### Simulations

The direction of the excitation profile changes with the trajectory, therefore the effective flip angle in every spatial location within in the sample, except iso-centre, will also change over time. An example of this phenomenon is shown in figure 3.14a, showing the  $B_1$  efficiency, for spins in two different locations  $\bar{r}_1 = \sqrt{1/3} \cdot [1, 1, 1]$  and  $\bar{r}_2 = [0, 0, 1]$ . These two spins are the same distance from iso-centre, i.e.  $|\bar{r}_1| = |\bar{r}_2|$ , which means the effective  $B_1$ -efficiency is the same as can be found by calculating the average  $B_1$  efficiency over all spokes, shown by the dashed line in 3.14a. However, the spin history is very different, a phenomenon that will not be captured with the proposed correction.

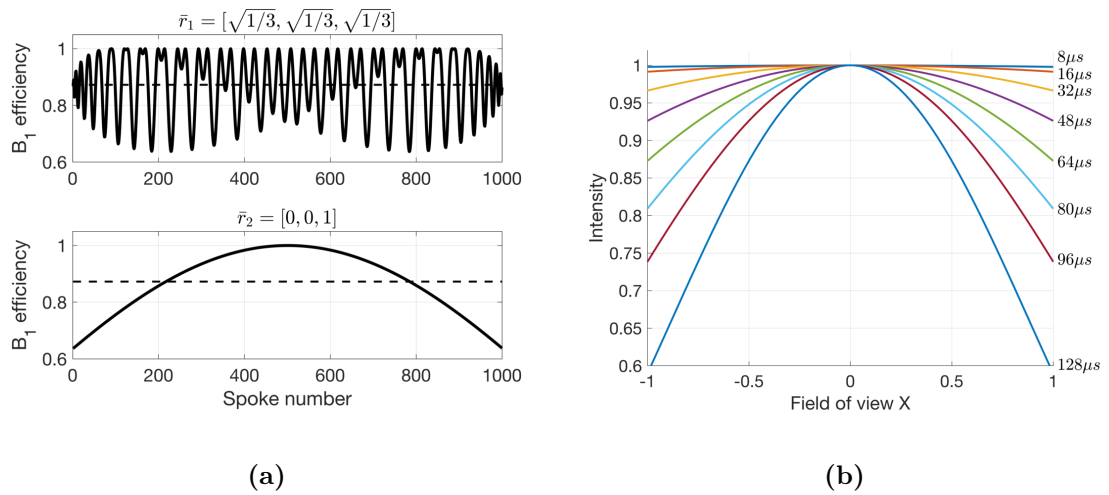


**Figure 3.14:** (a) Effect of the rotating excitation profile at two different positions, on the same radius from iso-centre, over 1000 spokes for  $\tau_{rf} = 64\mu\text{s}$  at  $\pm 7.8\text{kHz}$  readout bandwidth. (b) Effective excitation profile for different pulse widths at  $\pm 7.8\text{kHz}$  readout bandwidth, after averaging the excitation profile for all spokes.

Simulating the excitation profile for all spokes in the trajectory and calculating the average excitation profile produce a sinc-like shape, as shown in figure 3.14b. With increasing pulse width, the excitation profile becomes narrower, i.e. less homogeneous flip angle across the field of view. The excitation profile is radially symmetric, and therefore it is here shown on a radial x-axis.

### Phantom Data

The results from the simulations are mirrored in the acquired phantom data. Figure 3.15 shows an increased "doming" effect for longer pulse widths. The line profiles through the phantom, bottom row of figure 3.15, clearly show the effect of the excitation profile. There is also some additional B<sub>1</sub>-inhomogeneity visible, most evident in the profile for the shortest pulse width, which can be attributed to the receive and transmit sensitivity of the coil. With longer pulse width, the effect of the sinc excitation profile becomes more prominent, and at  $\tau_{rf} = 64\mu\text{s}$  there is substantial doming occurring. As the pulse width is further increased, the excitation profile effect becomes stronger, but effects from the increased deadtime gap associated with longer pulses are also observed, resulting in apparent increased signal intensity outside the phantom.

When data is collected in a steady state, the image intensity is not only proportional to the flip angle but also dependent on the T<sub>1</sub> and TR of the acquisition, as shown in

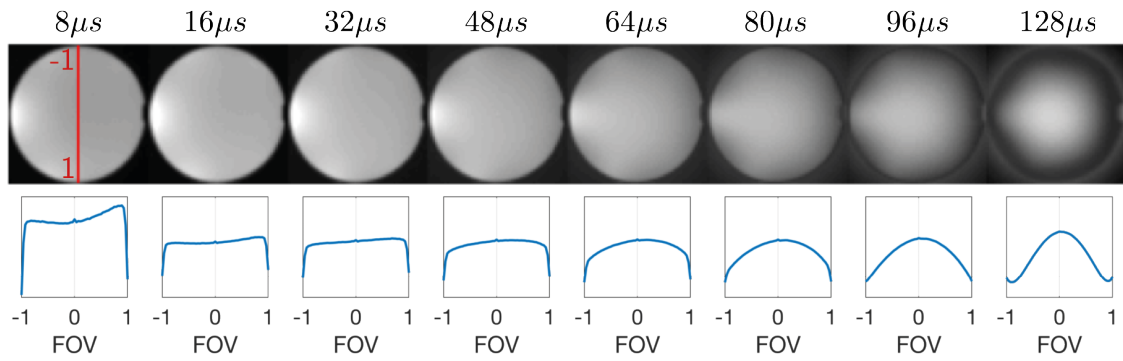


**Figure 3.15:** Example of phantom data showing the effect of changing the width of the excitation pulse. Data obtained from spherical phantom with different pulse widths (top) and the corresponding line profiles through the phantom (bottom).

equation (3.12) and (3.20). Therefore, the spatial variations in flip angle caused by the excitation profile cannot be corrected for by a simple division by the simulated excitation profile. Therefore, only visual comparison of the excitation profiles is presented here.

### 3.6.5 Study C: Discussion and Conclusion

The excitation profile arising from application of the RF pulse in the presence of the readout gradient can produce a substantial reduction in  $B_1$ -efficiency, in particular at the edge of the FOV. For qualitative imaging, the excitation pulse width needs to be short relative to the readout bandwidth, to ensure that the contrast is constant across the FOV. For quantitative imaging reliant on the  $B_1$  field for the fitting, such as the variable flip angle method for  $T_1$ -mapping, a simulated excitation profile can be incorporated into the fitting procedure, as further described in chapter 4.

With prior knowledge of the excitation profile, it is also possible to incorporate it into the reconstruction process [130]. However, the method presented by Grodzki et al. for excitation profile correction requires direct inversion of the encoding matrix, which is difficult for a 3D acquisition with multiple coils [130]. An alternative to matrix inversion is to use iterative methods, which have been shown to be very powerful for a range of image reconstruction problems [134, 135, 136], albeit at the expense of computational time. It is also possible to reduce the excitation profile effect within the acquisition itself, by using shaped RF pulses, although this results in lower flip angle for the same pulse duration [137].

## 3.7 Study D: Acoustic Noise

### 3.7.1 Study D: Purpose

To measure the acoustic noise produced by the RUFIS sequence and study the effects of changing resolution and readout bandwidth on the acoustic noise profile.

### 3.7.2 Study D: Theory

Acoustic noise is produced by the MRI scanner from the vibrating gradient coils, as described in chapter 2. The level of the acoustic noise is a function of the acoustic properties of the system [138], the magnetic field strength (Lorentz Law) [77], and the rate of change of the gradient amplitude [95]. In RUFIS, the gradient amplitude is gradually switched between spokes, resulting in minimal change in the gradients, and thus minimal acoustic noise. The noise that is produced by the sequence is determined by the size of the gradient steps and the duration of the readout. The size of the gradient steps are determined both by the maximum gradient amplitude and the number of spokes in the trajectory, as fewer spokes require larger gradient steps.

### 3.7.3 Study D: Methods

Acoustic noise measurements were performed on a GE MR750 3T MRI scanner, using an MR safe microphone (Casella, CEL-495), mounted on a cylindrical phantom placed in the centre of a 32-channel head coil (Nova Medical). The microphone was calibrated before the measurements using the provided calibration unit. Measurements were taken for a period of 20s. The microphone was connected to a sound meter (Casella, CEL-63X) which performed the processing of the sound recordings. The A-weighted equivalent continuous sound level (LAeq) and the C-weighted peak sound level (LCpeak) as well as the A-weighted sound levels at 11 octave bands from 16Hz to 16kHz were recorded.

A RUFIS acquisition was set up with FOV= $192 \times 192 \times 192 \text{ mm}^3$  and flip angle  $1^\circ$ . The standard trajectory was used with twice the nominal number of spokes, i.e.  $N = 2 \cdot MAT^2$ . The acquisition was performed at three different bandwidths  $\pm 7.8/15.6/31.2 \text{ kHz}$  and two different resolutions  $1 \times 1 \times 1 \text{ mm}^3$  and  $1.5 \times 1.5 \times 1.5 \text{ mm}^3$ . As a comparison, measurements were also taken from a standard SPGR sequence with  $1.5 \times 1.5 \times 1.5 \text{ mm}^3$  resolution, TR=10.6ms, BW= $\pm 16.67 \text{ kHz}$ . A measurement was also taken of the background noise before the start of the scan as a reference.

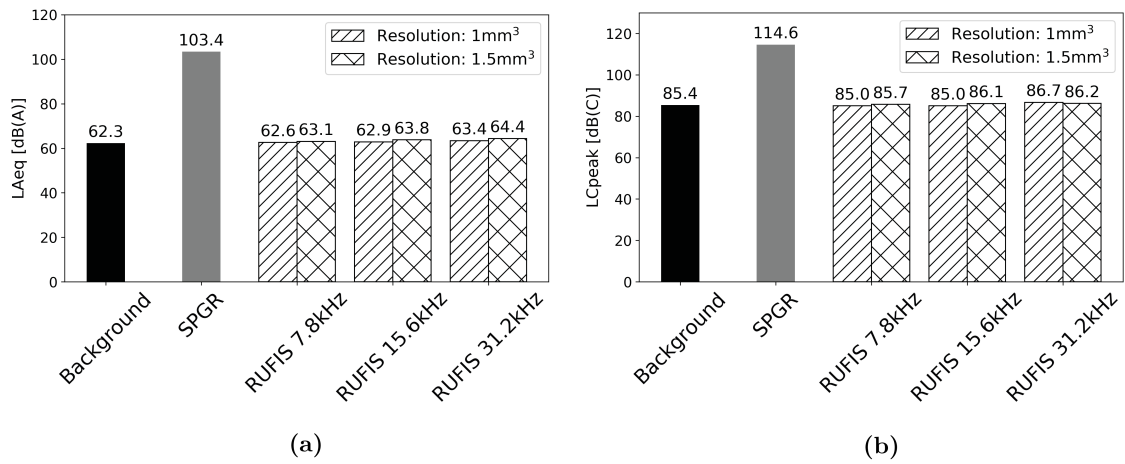


**Figure 3.16:** Average sound pressure levels, (a) LAeq and (b) LCpeak, from the 20s measurement period, comparing RUFIS at different bandwidths and resolutions, to SPGR and background noise levels.

### 3.7.4 Study D: Results

The average acoustic noise levels with RUFIS was less than 3dB(A) higher than the background noise for all sequence settings tested here, compared to SPGR which was 41.1 dB(A) louder, figure 3.16a. Similarly, the LCpeak was less than 3dB(C) higher than the background for all settings, compared to SPGR which was 29.2dB(C) louder, figure 3.16b. The acquisitions with higher resolution produced lower acoustic noise, while higher bandwidth produced higher acoustic noise, both in terms of LAeq and LCpeak.

The frequency profile of the sound from RUFIS was distinctly different from SPGR, as expected from the different gradient waveforms. Figure 3.17a shows a comparison of the sound levels at different frequencies, between: RUFIS, SPGR and the background noise. SPGR has a wide frequency distribution which diverges from the background noise around 30Hz, and with a peak at 500Hz. RUFIS on the other hand traces the background noise up to 4kHz after which it has a higher sound pressure level at the higher frequency bands. Comparison of RUFIS acquisitions at different bandwidths, figure 3.17b, shows an increased sound pressure at the high frequency content with higher bandwidth at all frequency bands above 500Hz.

Figure 3.18 shows a breakdown of how the frequency content of the noise changes with resolution at the three different bandwidths. At  $\pm 7.8$ kHz, the difference is minimal between the two resolutions, while at  $\pm 31.2$ kHz there is a noticeable difference in the frequency bands between 1-4kHz.

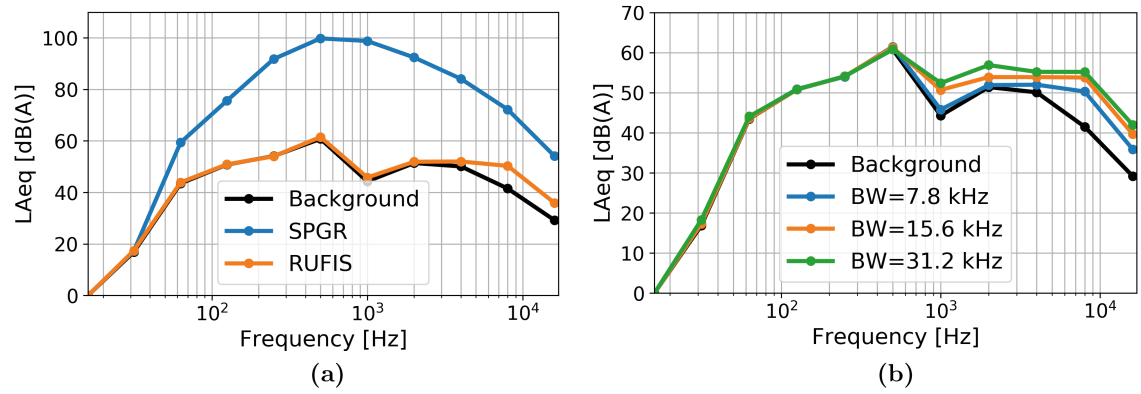


**Figure 3.17:** Acoustic noise levels (LAeq [dB(A)]) across 11 octave bands from 16Hz to 16kHz. (a) Comparison between RUFIS ( $1.5 \times 1.5 \times 1.5 \text{ mm}^3$  and BW=7.8kHz), SPGR, and background noise levels. (b) Comparison of RUFIS acquisitions different readout bandwidths at resolution of  $1.5 \times 1.5 \times 1.5 \text{ mm}^3$

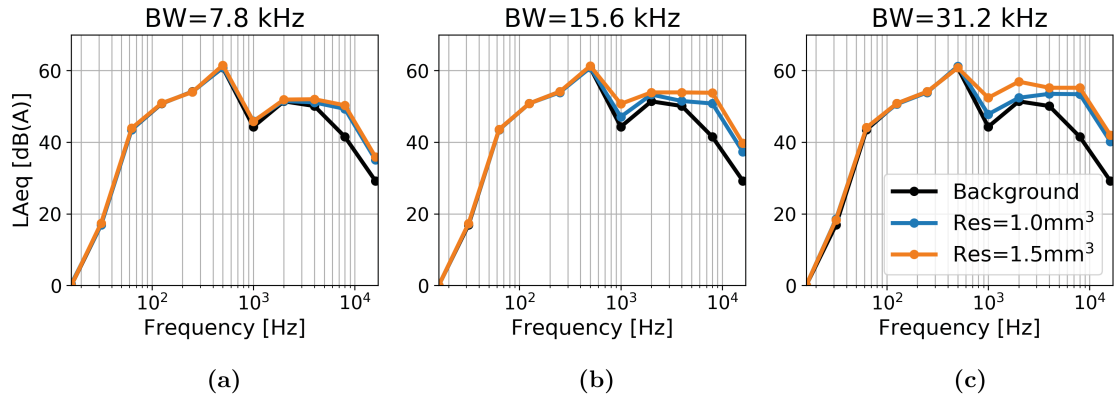


**Figure 3.18:** Acoustic noise levels (LAeq [dB(A)]) across 11 octave bands from 16Hz to 16kHz comparison RUFIS acquisitions with different resolutions at bandwidths of (a) 7.8kHz, (b) 15.6kHz, (c) 31.2kHz.

### 3.7.5 Study D: Discussion and Conclusion

The acoustic noise produced by RUFIS was within 3dB(A) of the background noise levels for the range of sequence parameters tested here. The high resolution RUFIS image acquired at  $\pm 31.2\text{kHz}$  bandwidth, which would be a commonly used setting, was only 1.1dB(A) louder than the background noise levels in the scan room. This is in comparison to the SPGR sequence which here was 41.1dB(A) louder than the background noise. Changing the readout bandwidth and resolution in the RUFIS acquisition altered both the acoustic noise levels and frequency profiles. Increasing the bandwidth, which reduces the TR, i.e. the time between spokes, and thus shorter time between gradient updates, increased the acoustic noise across all frequencies above 500Hz. The subjective experience



of this is thus a higher pitched sound from the scanner. Changing the resolution changes both the number of spokes in the acquisition and the length of the spokes. Lower resolution would therefore be expected to produce higher acoustic noise, which also was measured here, with the largest difference at high bandwidths.

Subjective accounts from MR acquisitions using RUFIS have reported changes in the acoustic noise when changing the flip angle. In a VFA experiment, a subject reported the noise to decrease with decreasing flip angle. This could be explained by a phenomenon known in the literature as *RF hearing* [139]. The first studies on this phenomenon was published by Alan Frey in the 1960s, where subjects reported hearing buzzing, clicking, or knocking inside or just behind their head, while being exposed to pulsed electromagnetic radiation in the RF frequency range from radars [140]. It was also reported that the perceived loudness of the sound was mainly affected by peak power in the RF pulses, rather than the average power [141]. While both of these studies operated in a frequency range outside that of the carrier frequency of an MR scanner, similar findings have been reported in the MRI literature [142]. Röschmann described the outcome of a failed MR experiment where the gradient system broke down during scanning, but there was still an audible sound produced by the scanner [142]. After investigation, it was concluded that it originated from the RF system. A study was therefore conducted with several healthy volunteers using different RF coils and results similar to those reported by Frey was observed. Röschmann used pulse trains with 100 $\mu$ s pulses at a repetition rate between 1Hz and 5kHz. In the 300 Hz range, i.e. inter pulse spacing of 3ms which is the range expected with RUFIS, the sound was described as buzzing or hissing, similar to the subjective report from this thesis. The biophysical phenomenon behind this is believed to be thermoelastic expansion in the tissue, caused by a  $\approx 5 \cdot 10^{-6}$ °C temperature increase[139]. The expansion of the tissue produces a pressure wave which propagates through the tissue and is observed as sound by the ear. For most MR sequences, the contribution of RF hearing to the acoustic noise is minimal as it is masked by the sound produced by the gradients. With silent sequences, such as RUFIS however, this sound could be an important component of the perceived noise during the acquisition and warrants further investigation.

In conclusion, this experiment have shown that the acoustic noise produced by the RUFIS sequence is very low and the sequence can be considered to be near silent with noise levels less than 3dB(A) above the background noise in the scan room, which measured 62.3dB(A). At the sound levels reported here, hearing protection would not be needed. In

practice however, hearing protection should still be used at all times in the scanner as there currently are no safety systems in place to limit the acoustic noise, similar to operation modes for SAR and peripheral nerve stimulation.

### 3.8 Chapter Discussion and Conclusions

This chapter have presented a detailed study of a range of features of the RUFIS sequence which will be important for the development of quantitative parameter mapping methods. One of the key parameters in a RUFIS experiment is the readout BW which determines duration of the readout and thus the TR. It also determines the number of missed points during the deadtime gap. Increasing the bandwidth increases the gradient amplitude, which also results in a stronger excitation profile effect and thus limits the maximum width of the excitation pulse, and therefore also directly the maximum achievable flip angle. The BW also changes the water-fat shift, but in contrast to a Cartesian sequences, the fat-water chemical shift difference manifest as out-of-phase spherical blurring artefacts, especially at tissue interfaces [143, 111]. In chapter 5, interactions between acquisition parameters are discussed in further detail in the context of RUFIS imaging across field strengths.

The segmented readout in RUFIS is similar to a FLASH readout, used in many magnetisation prepared sequences such as MP2RAGE [49]. In a Cartesian MPRAGE sequence, it is common to order the phase encoding steps such that the first phase encode is in the centre of k-space, thus determining the main image contrast. In RUFIS, all spokes originate from the centre of k-space and the image contrast is therefore an average of all spokes, as shown in section 3.5. Higher number of spokes will lead to faster acquisition, but will also introduce  $T_1$  weighting from the repeated nutation and  $T_1$  recovery, as described by (3.14). If  $T_1$  is known, it can be corrected for to obtain the desired prepared contrast [110], but otherwise it is advisable to minimise the number of spokes per segment to maintain the desired contrast weighting.

The unique feature of RUFIS motivating this thesis, is the low acoustic noise achieved by small gradient steps between subsequent readouts, here measured to be less than 3dB(A). Shorter spoke duration, i.e. a faster readout as a result of high bandwidth or small matrix size, will result in faster gradient updates, and higher acoustic noise. The number of spokes in the acquisition will change the gradient step size between spokes, with fewer spokes producing larger steps and thus higher acoustic noise. However, while

the variations in acoustic noise with acquisition parameters is observable to the ear, the variations are still within 3dB(A) of the background noise levels.

## 3.9 Publications and Contribution

### 3.9.1 Publications

The analytical signal equation and excitation profile correction presented in here have been presented in a conference presentation and journal article

- **Ljungberg E**, Wood T, Solana AB, Kolind S, Williams SCR, Wiesinger F, et al. *Silent  $T_1$  mapping using the variable flip angle method with  $B_1$  correction*. Magn Reson Med. 2020;(December 2019):1–12. DOI:10.1002/mrm.28178
- **Ljungberg E**, Beatriz A, Sanchez S, Wood TC, Kolind S, Wiesinger F, et al. *Silent  $T_1$ -Mapping Using the Variable Flip Angle Method with Zero Echo Time*. In: Proc Intl Soc Mag Reson Med 26. Paris; 2018. p. 0270.

### 3.9.2 Contribution

The theory presented in this chapter was mainly developed by me, with support from my supervisors. The gridding methods used here were provided by collaborators at GE Healthcare. The Nearest-Neighbor (NN) gridding method was implemented by one of my supervisors, Dr. Wiesinger. The KB gridding method was implemented internally at GE Healthcare and provided by Dr. Wiesinger.

## Chapter 4

# $T_1$ Mapping Using the Variable Flip Angle Method

### Contents

---

4.1	Introduction	93
4.2	Considerations for VFA $T_1$ Mapping with RUFIS	94
4.3	Silent $B_1^+$ Mapping	96
4.4	Reproducibility and SPGR Comparison Study	102
4.5	Chapter Discussion and Conclusion	115
4.6	Publications and Contribution	116

---

### Summary

IN this chapter, a method for  $T_1$  mapping with RUFIS using the variable flip angle method is introduced. A novel, silent,  $B_1^+$  mapping method based on magnetisation prepared RUFIS is developed and combined with VFA RUFIS for a unified, silent  $T_1$  mapping framework. The technique is evaluated in a quantitative phantom and a small group of healthy volunteers, and compared to standard Cartesian SPGR VFA  $T_1$  mapping.

## 4.1 Introduction

In chapter 3 it was shown that, theoretically, the Rotating Ultra-Fast Imaging Sequence (RUFIS) can be treated as a spoiled gradient echo (SPGR) sequence as long as the number of spokes per segment is high, and the delay between segments is kept to a minimum. The longitudinal magnetisation in a steady state SPGR sequence is described by the SPGR equation as [51]

$$M_{z,spgr} = \rho \cdot \frac{1 - E_1}{1 - \cos \alpha \cdot E_1}, \quad E_1 = e^{-TR/T_1} \quad (4.1)$$

where  $\rho$  is the proton density (PD),  $\alpha$  is the flip angle, and TR the repetition time. For small flip angles and short TRs, this can be simplified to [144, 145]

$$M_{z,spgr} = \frac{\rho}{1 + \frac{T_1}{TR} \cdot \frac{\alpha^2}{2}}. \quad (4.2)$$

The acquired signal is only proportional to  $T_1$  and PD since the transverse magnetisation is spoiled between excitations. If multiple volumes are acquired with different excitation flip angles, it is possible to fit for  $T_1$  and PD, a method referred to as the variable flip angle (VFA) method, or sometimes DESPOT1 [51, 52, 53, 146, 8, 54]. This is a highly efficient method for  $T_1$  mapping as data are acquired in the steady state, i.e. very high sampling efficiency compared to, for instance, inversion recovery  $T_1$  mapping [59].

To describe a  $T_1$  measurement using the VFA method, it is useful to reiterate the concepts behind *Theories, Models and Signal Representations* presented in chapter 3 [68]. The model used here is the VFA method with a RUFIS acquisition, and the signal representation is the SPGR equation 4.1. The relevant degrees of freedom in the theory only includes PD and  $T_1$ .

In a VFA experiment, the flip angle  $\alpha$  is the independent variable and must, therefore, be known with high accuracy to obtain an unbiased  $T_1$  estimate. However, at magnetic field strengths  $B_0 \geq 3T$ , the transmit RF field,  $B_1^+$ , is not homogenous over the imaging volume, but has a spatial profile which largely depends on the dielectric properties of the sample [147]. In equation 4.2 it can be seen that the flip angle is directly coupled to  $T_1$ , the dependent variable, and can therefore not be estimated from the measured data, but has to be measured independently. Measurements of the effective flip angle across the sample is obtained from a  $B_1^+$  map, for which there are numerous dedicated methods,

none of which are silent, however. A fully silent VFA  $T_1$  mapping protocol using RUFIS, therefore, requires a novel  $B_1^+$  mapping technique.

#### 4.1.1 Outline of Chapter

This chapter will describe a method for performing a VFA  $T_1$  mapping experiment with RUFIS. First, a description of relevant acquisition parameters and constraints imposed by the RUFIS acquisition is presented, followed by protocol recommendations. Excitation profile effects are investigated and a method for correction is presented. Secondly, a novel  $B_1^+$  mapping technique using magnetisation prepared RUFIS is developed, implemented and tested. Third, the fully silent RUFIS VFA  $T_1$  mapping protocol, including  $B_1^+$  correction, is compared to a Cartesian SPGR protocol, in a small group of healthy volunteers and a quantitative phantom. Reproducibility and repeatability of both protocols are investigated. Finally, the chapter is concluded with a discussion on future improvements and applications of the technique.

### 4.2 Considerations for VFA $T_1$ Mapping with RUFIS

#### 4.2.1 Flip Angle Selection

The primary design consideration in a VFA experiment is the choice of flip angles. For a single  $T_1$ , the optimal sampling scheme consists of a pair of flip angles on either side of the Ernst angle  $\alpha_e$  [148, 149], which is the flip angle that gives the highest transverse magnetisation, given by [150]

$$\cos \alpha_e = E_1 \rightarrow \alpha_e = \cos^{-1}(\exp(TR/T_1)) \quad (4.3)$$

To balance the signal to noise ratio (SNR) in the two data points, the two flip angles should produce equal signal intensity. The low flip angle image will have mainly PD contrast, while the high flip angle will have  $T_1$  contrast. Wood showed that the pair of optimal flip angles for minimum variance in the  $T_1$  estimates are given by [149]

$$\cos \alpha_{1,2} = \frac{E_1 \pm \sqrt{2(1 - E_1^2)}}{2 - E_1^2}. \quad (4.4)$$

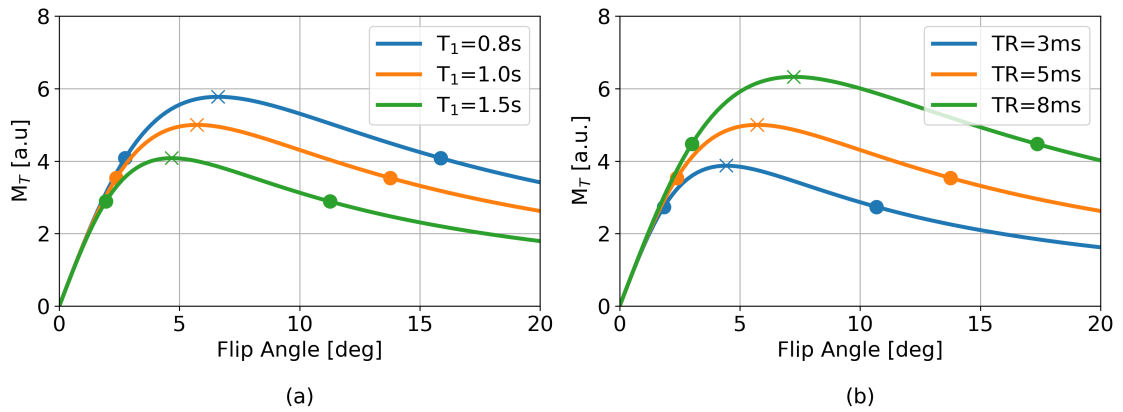


**Figure 4.1:** Examples of SPGR curves showing the transverse magnetisation with the optimal pair of flip angles, indicated with dots, and the Ernst angle, crosses, for different  $T_1$  (a) and TR (b)

Figure 4.1 shows SPGR signal curves for different  $T_1$  and TRs, together with the pair of optimal flip angles, and the Ernst angle. The Ernst angle, and thus the high optimal flip angle, increase with TR but decrease with  $T_1$ .

#### 4.2.2 Flip Angle Limitations with RUFIS

In a conventional SPGR acquisition, the flip angles are mainly limited by SAR constraints, but in RUFIS there are additional constraints to consider. For a hard, i.e. rectangular, RF pulse used in RUFIS, the flip angle is given by

$$\alpha = \gamma B_1 \tau \quad (4.5)$$

where  $\gamma$  is gyromagnetic ratio,  $B_1$  is the amplitude of the RF pulse, and  $\tau$  is the RF pulse width. Since RF excitation is performed using hard pulses with the readout gradient on, the excitation profile will have a sinc shape across the field of view, as described in chapter 3, *Study C: A Rotating 3D Excitation Profile*. To maintain an acceptable excitation profile, the bandwidth of the RF pulse, which is inversely proportional to the pulse width, has to encompass the readout bandwidth across the field of view. Therefore, the RF pulse width has to scale with the readout bandwidth, which means that also the flip angle will scale with the readout bandwidth. The achievable flip angle for a given pulse width is determined by the peak  $B_1$  of the RF system, which is limited by both hardware and safety constraints. Empirical tests on our scanner (3T GE MR750) showed that  $\approx 0.25^\circ/\mu s$  is achievable for most subjects. At a readout bandwidth of  $BW = \pm 15$  kHz, the maximum pulse width would

be 32 $\mu$ s, which gives a maximum flip angle of 8°. Even if the RF bandwidth encompasses the readout bandwidth, there will be a noticeable excitation profile across the field of view (FOV), affecting the actual flip angle. An excitation profile correction should, therefore, be simulated, as described in chapter 3, and treated as a  $B_1^+$  map in the  $T_1$  estimation.

It should be noted here that the flip angle limitations are not strict rules, but rather recommendations for optimal image quality. Longer pulse width, and thus higher flip angles, is possible but image quality will be degraded due to increased excitation profile effects. Furthermore, differences in patient weight and coil loading will set different limits to the peak  $B_1$ , which will affect the pulse width. It is therefore recommended to have a conservative approach when deciding on a maximum flip angle to ensure that the same protocol will be applicable across a wide range of subjects.

## 4.3 Silent $B_1^+$ Mapping

### 4.3.1 Principles of $B_1^+$ Mapping

The term  $B_1$  includes both  $B_1^+$ , the profile of the transmit field, and  $B_1^-$ , the profile of the receive field. Variations in the  $B_1^+$  are largely due to spatial variations in the dielectric properties of the sample being imaged [147]. The  $B_1^+$  field is therefore unique for each scan prescription and has to be measured. The  $B_1^-$  field is affected by the same properties as  $B_1^+$ , and at low field strengths, the principle of reciprocity can be used to calculate  $B_1^-$  directly from  $B_1^+$  [151]. However, at higher field strengths, this relation is no longer valid and dedicated  $B_1^-$  techniques have to be used [152, 153]. With multi-channel coils,  $B_1^-$  will also include the sensitivity of the coil elements.

Techniques for  $B_1$  mapping typically refers to quantification of the  $B_1^+$  field as it affects the spin dynamics by changing the flip angle, while the  $B_1^-$  field affects the received signal only by a scaling factor. In a VFA  $T_1$  mapping experiment, the  $B_1^-$  affects each measurement point as a constant scale factor, and does therefore not affect the  $T_1$  quantification, but it does affect the PD map [153]. The  $B_1^+$ , on the other hand, has a non-linear effect as it affects the flip angle directly.  $B_1$  correction in a VFA  $T_1$  mapping experiment therefore only focus on  $B_1^+$ . The  $B_1^+$  field is a smoothly varying field which can be sufficiently sampled with a low resolution acquisition. It is therefore common to acquire  $B_1^+$  maps with low resolution and to smooth the  $B_1^+$  field in post-processing to avoid noise propagation into the calculated  $T_1$  maps [154].



**Table 4.1:** Summary of commonly used  $B_1^+$  mapping techniques. (<sup>†</sup> Number of citations obtained from Google Scholar on January 28<sup>th</sup> 2020)

Name	Ref.	Data Type	Citations <sup>†</sup>
Actual Flip Angle Method (AFI)	[154]	3D, Magnitude	841
Bloch-Siegert Shift	[157]	2D, Phase	423
Double Angle Method (DAM)	[9]	2D, Magnitude	316
Saturated Double angle	[162]	2D, Magnitude	357
Dual Refocusing Echo Acquisition Mode (DREAM)	[158]	2D, Magnitude	202
Phase Imaging	[163]	3D, Phase	158
180° Null	[160]	3D, Magnitude	141
Turbo Saturated Flash	[164]	2D, Magnitude	116
Stimulated Echo	[159]	3D, Magnitude	84

There is a wide range of  $B_1^+$  mapping techniques available, briefly summarised in table 4.1. The main difficulty with  $B_1^+$  mapping methods is that the effects of  $T_1$ ,  $T_2$ , and PD have to be removed. It is outside the scope of this thesis to give a thorough review of  $B_1^+$  mapping techniques. The interested reader is referred to original articles cited in table 4.1 or reviews such as Ref [155] and [156]. Instead, the more relevant question here is if any existing method can be adapted to work with RUFIS to achieve silent  $B_1^+$  mapping. For an existing technique to be directly applicable to RUFIS, it has to use a segmented readout. This excludes popular methods such as AFI [154], Bloch-Siegert Shift [157], DREAM [158] or stimulated echoes [159]. The 180° Null method [160] is not possible either as it requires flip angles that are outside the possible range for RUFIS. One of the oldest, and most basic,  $B_1^+$  mapping method is the double angle method (DAM) [9]. Two images are acquired with flip angles  $\alpha$  and  $2\alpha$  from which the  $B_1^+$  field can be calculated. However, the method is very time consuming as it requires  $T_1$  recovery between readouts and in the original implementation, the readout was performed with a gradient echo readout. The acquisition can be accelerated using an EPI readout instead (EPI-DAM) [161], which makes it resemble a magnetisation prepare RUFIS acquisition. The next section will describe a  $B_1^+$  mapping technique based on magnetisation preparation, similar to EPI-DAM.

### 4.3.2 Silent Magnetisation Prepared $B_1^+$ Acquisition - SIMBA

#### Theory

The lack of directly translatable methods for  $B_1^+$  mapping with RUFIS necessitated development of a new method. One of the issues with RUFIS is that the readout produce  $T_1$  weighting and therefore methods such as the double angle method cannot be used directly, as it would results in signal changes that depend not only on  $B_1^+$  but also  $T_1$ . Instead, the method proposed here produces  $B_1^+$  contrast by a magnetisation preparation module, similar to EPI-DAM. In the following calculations, the  $B_1^+$  efficiency will be denoted by  $\lambda$  where  $\lambda = 1$  is the prescribed  $B_1^+$ , i.e. flip angle.

In chapter 3 it was shown that the acquired signal in a RUFIS segment is given by

$$M_{seg} = \sin \alpha \cdot (M_z(0) \cdot f_N + (1 - f_N) \cdot M_{z,SPGR}). \quad (4.6)$$

If a preparation RF pulse with flip angle  $\alpha_{prep}$  is applied before the RUFIS segment, assuming fully spoiled transverse magnetisation after the preparation, then

$$M_z(0) \propto \cos(\lambda \cdot \alpha_{prep}). \quad (4.7)$$

If multiple volumes are acquired with different  $\alpha_{prep}$ , assuming full  $T_1$  recovery between preparations, it is possible to fit for  $\lambda$  as

$$M_{seg,i} = \cos(\lambda \cdot \alpha_{prep,i}) \cdot A + B \quad (4.8)$$

where  $A$  and  $B$  are constants which contain  $T_1$  and PD information. The important part is that  $A$  and  $B$  do not change with  $\alpha_{prep,i}$ . Similarly, the factor  $\sin \alpha$  can be removed as the readout flip angle is the same for each volume. This method can thus be described as a magnetisation preparation version of the classic double angle method [9]. More than two flip angles (as in double) are required though since  $\lambda, A, B$  all have to be fit for.

The  $B_1^+$  preparation can be done with any type of RF pulse. In this work, a composite pulse consisting of a series of hard RF pulses, similar to those used in the RUFIS readout, are used. This was motivated by initial experiments with the RUFIS sequence suggesting that the hard RF pulses are not perfectly rectangular, as this would require infinitely fast ramping of the RF amplifier. Imperfections in the RF pulse shape will result in a reduction

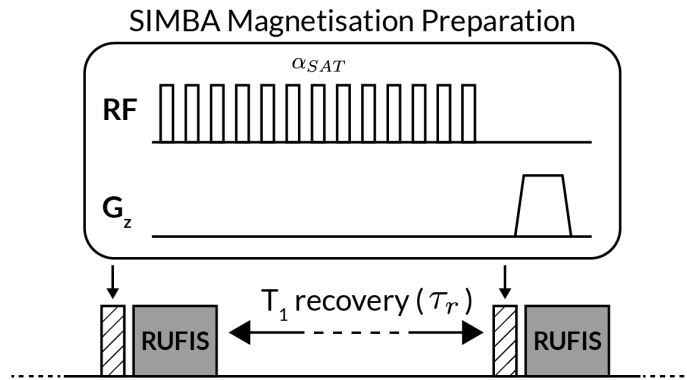


**Figure 4.2:** Pulse sequence diagram of the SIMBA sequence showing the composite magnetisation preparation module before the RUFIS readout. (Reproduced from my publication [166] with permission from Wiley and Sons.)

of the effective flip angle, without any spatial pattern. By using the same RF pulses in the preparation as in the readout, the aim is to capture RF imperfections in the  $B_1^+$  map and thus incorporating these into the  $B_1^+$  correction. A train of  $n$  RF pulses each with flip angle  $\alpha_{SAT}$  will act as a single pulse with flip angle  $\alpha_{prep} = n \cdot \alpha_{SAT}$  as long as each pulse has the same phase and that the spacing between the pulses is short. This resembles a DANTE pulse train used for selective excitation or tagging [165], however, the tagging or selective excitation features will not be present given tight spacing and no variation in phase.

Since each new MR pulse sequence needs its catchy own name for referencing, this method is named *SIMBA* - **S**ilent **M**agnetisation prepared  $B_1^+$  map **A**cquisition. Figure 4.2 shows the outline of the SIMBA sequence with the composite preparation module before the RUFIS readout. After the preparation, a crusher gradient is applied on the  $z$  axis to destroy any transverse magnetisation. After the readout, there is a delay  $\tau_r$  for  $T_1$  recovery. Figure 4.3A shows simulations of the SIMBA pulse sequence for different values of  $\lambda$ , i.e.  $B_1^+$  error, and 4.3B shows the effect of different number of spokes in the readout.  $B_1^+$  error shows as a change in the "wavelength" of the signal curve, while more spokes per segment increase  $T_1$  saturation and thus decreases the dynamic range of the measurement.

### Pulse Sequence Implementation

The SIMBA sequence was implemented using the GE pulse programming environment EPIC. The main difficulty in implementing this pulse sequence is the generation of the preparation module. To ensure that the accumulated flip angle of the preparation module is the sum of all the individual RF pulses, they have to be spaced as tightly as possible.

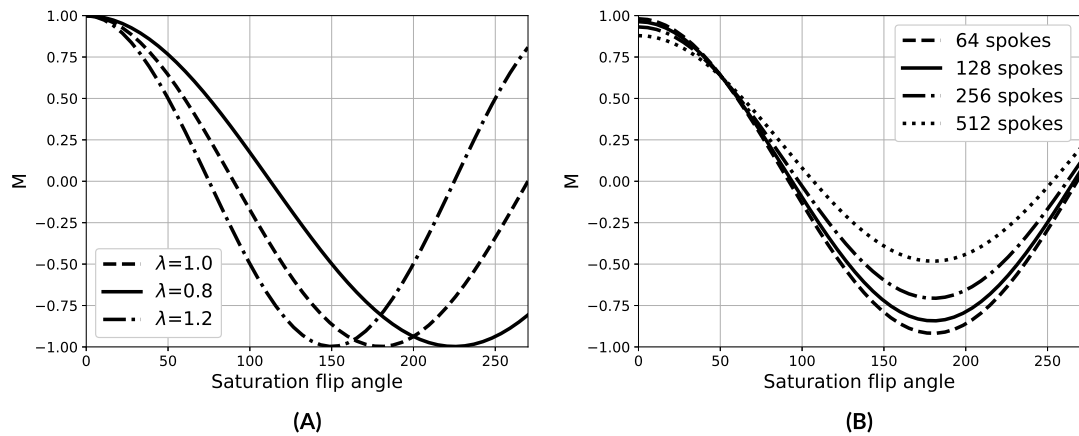


**Figure 4.3:** Simulations showing the effects of **(A)** different  $B_1^+$  efficiency ( $\lambda$ ) and **(B)** number of spokes in the RUFIS readout (Simulations parameters  $\lambda = 1$ ,  $T_1 = 1$  s, RUFIS  $\alpha=2^\circ$  and  $TR=1$  ms. (Reproduced from my publication [166] with permission from Wiley and Sons.)

Typically, when RF pulses are added into an MR sequence there is a minimum spacing between subsequent pulses of  $\approx 300\mu\text{s}$  to unblank the RF power amplifier. With an RF pulse width of  $6\text{--}64\mu\text{s}$ , as used in RUFIS,  $300\mu\text{s}$  spacing is proportionally very long and would increase the length of the pulse train significantly as well as potentially introducing unwanted relaxation effects. To avoid this, a custom preparation module was written where the RF power amplifier is unblanked before the pulse train, each hard RF pulse is added manually, spaced  $4\mu\text{s}$  apart, and then the amplifier is unblanked afterwards again<sup>1</sup>. The preparation module was programmed such that the flip angle and number of pulses in the preparation could be controlled during the acquisition, enabling multiple volumes with different  $\alpha_{prep}$  to be acquired in quick succession.

## MR Experiment

To demonstrate the SIMBA method, a single healthy volunteer was scanned on a 3T GE MR750 with the SIMBA sequence. The acquisition was performed with  $\alpha_{prep}=(0, 90, 180 \text{ and } 270)^\circ$ ,  $\alpha_{SAT}=5^\circ$ , 256 spokes per segment,  $TR=1.2$  ms,  $\alpha=1^\circ$ , voxel size= $6 \times 6 \times 6$  mm<sup>3</sup>, FOV= $192 \times 192 \times 192$  mm<sup>3</sup> and  $\tau_r=3$  s. Images were reconstructed offline in MATLAB with Kaiser-Bessel gridding. Coil sensitivity maps were estimated from the centre of k-space using Berkeley Advanced Reconstruction Toolbox (BART) [133, 28]. Real data was used for the fitting to distinguish negative signals based on the signal phase. The SIMBA

<sup>1</sup>For those using EPIC, this involves generating manual SSP packets and writing the RF pulses into the waveform memory directly.

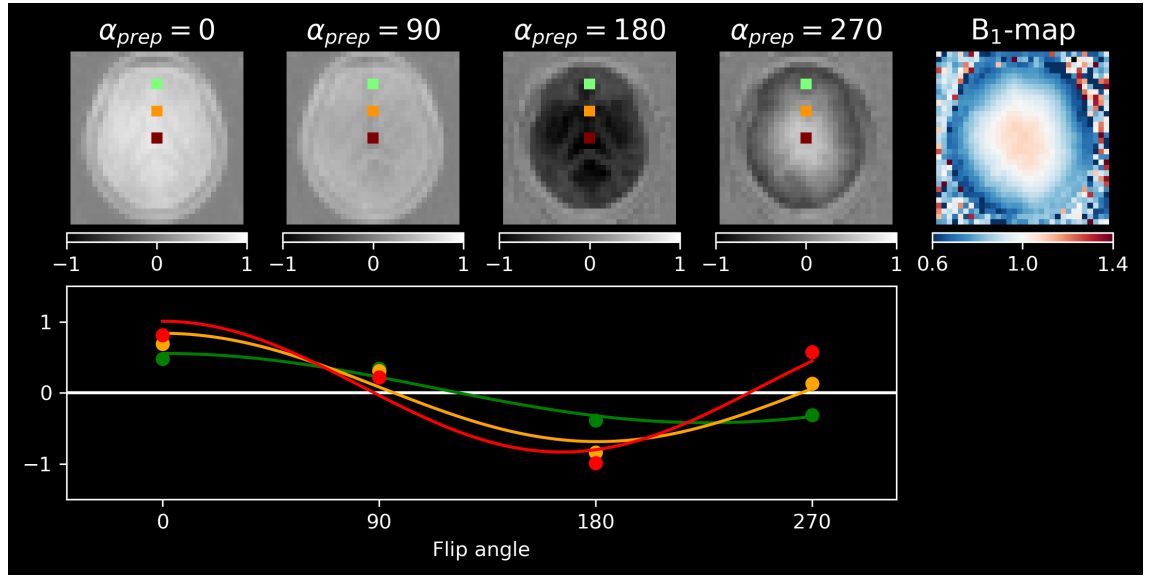


**Figure 4.4:** Example of SIMBA acquisition showing axial slices from four volumes, the calculated  $B_1^+$  map as well as signal curves from three regions of interest (ROI). (Reproduced from my ISMRM abstract [167])

$B_1^+$  map was obtained by fitting the acquired data to equation 4.8. The standard  $B_1^+$  map available on the GE platform, 2D Bloch-Siebert  $B_1^+$  mapping [157], was also acquired as a comparison.

Figure 4.4 shows the four images acquired with the SIMBA acquisition with different preparation flip angles, together with the resulting  $B_1^+$  map from the fitting. The signal intensity across the brain changes in a cosine pattern as expected, as shown by the signal curves from isolated regions of interest. The best fit curve for each ROI, solid line, shows a good, but not perfect, fit to the data. It is clear though that the "wavelength" of the curve is increased for areas with low  $B_1^+$ , i.e. the green ROI.

The  $B_1^+$  map from SIMBA compared well to the standard  $B_1^+$  map with Bloch-Siebert, shown in figure 4.5. The resolution of the SIMBA acquisition was lower than Bloch-Siebert, thus the map appears slightly smoother. The key features of this comparison are: (1) there is no tissue contrast in either of the maps, indicating that  $T_1$ ,  $T_2$ , or PD do not affect the maps; (2) both maps shows the same  $B_1^+$  pattern, i.e. higher  $B_1^+$  in the centre of the brain and drop-off toward the edges. The utility of SIMBA  $B_1^+$  mapping will be demonstrated in the next section where it is combined with VFA RUFIS for silent  $T_1$  mapping.

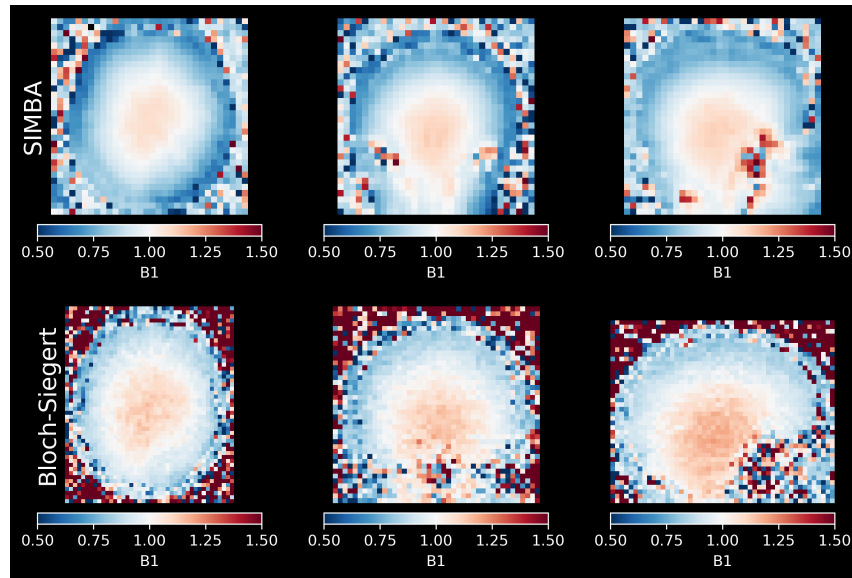


**Figure 4.5:** Comparison of  $B_1^+$  maps from SIMBA and the standard  $B_1^+$  map on the GE platform, 2D Bloch-Siebert. The same patterns of the  $B_1^+$  field are observed with both sequences. SIMBA was acquired with lower resolution and is therefore appearing less noisy. (Reproduced from my ISMRM abstract [167])

## 4.4 Reproducibility and SPGR Comparison Study

### 4.4.1 Introduction

In this section, RUFIS is compared to Cartesian SPGR for VFA  $T_1$  mapping, comparing quantitative results between the two techniques as well as repeatability and reproducibility. This is a feasibility study, demonstrating that RUFIS can be used for silent  $T_1$  mapping together with  $B_1^+$  correction using SIMBA.

### 4.4.2 Methods

#### MR Acquisition

Four healthy volunteers were scanned on a 3T GE MR750 using the body coil for transmit and a Nova Medical 32 channel head receive coil. VFA  $T_1$  mapping using RUFIS was compared to a Cartesian SPGR sequence. The two acquisitions were matched in resolution ( $1.5 \times 1.5 \times 1.5 \text{ mm}^3$ ), field of view ( $192 \times 192 \times 192 \text{ mm}^3$ ), and acquisition time ( $\approx 2 \text{ min}$  per flip angle). Because of the different structures of the pulse sequences, the TR will be different and thus the optimal flip angles are different. The sampling flip angles were calculated as the optimal pair for  $T_1=1\text{s}$ , given the TR for each sequence. RUFIS data was acquired with  $\alpha=2^\circ$  and  $12^\circ$ , while Cartesian data was acquired with  $\alpha=3.5^\circ$  and  $20^\circ$ . Acqui-

sition details for RUFIS: TR=4.4 ms, TE=0 ms, readout bandwidth= $\pm 7.8$  kHz, 512 spokes per segment, 24576 readout spokes in total, and RF spoiling phase increment= $117.0^\circ$ , RF pulse width fixed to 64 $\mu$ s. Similarly, for the Cartesian data: TR=10.6 ms, TE=3.4 ms, parallel imaging factor=1.5 (ASSET), and RF spoiling increment= $115.4^\circ$ . A relative low bandwidth ( $\pm 7.8$  kHz) was used with RUFIS to allow for high sampling flip angles ( $12^\circ$ ), as required for the optimal sampling scheme, while still maintaining an acceptable excitation profile. At  $\pm 7.8$  kHz readout bandwidth, the deadtime gap is negligible, and therefore no dedicated deadtime gap compensation was required. The fixed RF pulse width of 64 $\mu$ s was a conservative choice but required in order to use the same setting for all subjects in this study.

Similarly to the VFA acquisition, two sets of  $B_1^+$  maps were acquired: SIMBA, based on RUFIS; and 2D Bloch-Siegert, based on SPGR. Bloch-Siegert data was collected with a 2D multi-slice sequence using an 8 ms Fermi pulse applied 4 kHz off resonance, readout parameters: FA= $15^\circ$ , TE/TR=13.1/18ms, in-plane resolution= $4 \times 4$  mm<sup>2</sup>, FOV= $256 \times 256$  mm<sup>2</sup>, 40 slices with 4 mm slice thickness, duration=1:40 min. SIMBA data was collected using the protocol described in section 4.3.2.

Each subject was scanned twice, on average 50 days between the two scans (range 48-52 days). In each scan session, the full  $T_1$  mapping acquisition (VFA and  $B_1^+$  map) was acquired twice for RUFIS and the Cartesian protocol respectively, without repositioning between scans. Each session also included a high resolution  $T_1$ w scan (GE BRAVO) which was used for tissue segmentation. BRAVO acquisition parameters: TE/TR/TI=3/7/400ms, FOV= $270 \times 270 \times 240$  mm<sup>3</sup>, slice thickness=1.2 mm, in-plane resolution= $1.05 \times 1.05$  mm<sup>2</sup>, FA= $11^\circ$ , BW= $\pm 31.25$  kHz, and ASSET=1.75.

The two sequences were also compared in a quantitative phantom (EUROSPIN test object TO5) [168]. The phantom consisted of 12 vials of doped agarose gel mounted in a Styrofoam holder, see appendix B.1 for further details. The same sequences were used for the phantom, as in vivo, except for the SIMBA acquisition where the voxel size was decreased to  $4 \times 4 \times 4$  mm<sup>3</sup> to accurately map  $B_1^+$  in the small vials. Higher resolution results in larger matrix size, longer TR and thus more  $T_1$  saturation during the readout. This was compensated for by reducing the number of spokes per segment to 176.

Acoustic noise measurements were performed by mounting an MR safe microphone (Casella, CEL-495, IDEAL Industries, Ill) to a phantom and placing it in the middle of the bore. The sound from each sequence was measured for 40s with a sampling rate of 1

sampled every 2s using a sound meter (Casella, CEL-63X), from which the average LAeq and LCpeak values were calculated.

### Image Reconstruction

Cartesian SPGR data were reconstructed online on the scanner using the manufacturer’s standard reconstruction methods. RUFIS data were reconstructed offline in MATLAB. Gridding was performed using the Kaiser-Bessel method, after which coil sensitivity maps were obtained using the ESPIRiT method, implemented in BART [169, 28]. Final reconstruction was performed using an iterative SENSE reconstruction method with 3D total variation regularisation  $\lambda = 0.001$ , implemented in BART. SIMBA data were reconstructed using the method outlined in section 4.3.2.

### Image Analysis

The RUFIS and Cartesian VFA data were motion-corrected using mcFLIRT [170] and the two VFA scans within each session were co-registered using an affine transformation [171]. The SIMBA and Bloch-Siegert  $B_1^+$  maps were then registered to the respective VFA dataset using an affine transformation [171] and smoothed with a Gaussian kernel with a full width half max (FWHM) of 8 mm to reduce the noise.

The first RUFIS and Cartesian SPGR acquisition in each session were registered to the high resolution  $T_1$  weighted image using a combined affine and non-linear transformation, implemented in the ANTs toolbox [171]. Minor differences in distortions were observed between the different acquisitions and therefore a non-linear transformation was used to improve the registration.

The high resolution  $T_1$ w volume (BRAVO) was processed using FreeSurfer to obtain unbiased regions of interest (ROI) [172]. From the FreeSurfer analysis, the following ROIs were used: Pallidum (ID: 13+52), Thalamus (ID: 10+49), Caudate (ID: 11+50), Putamen (ID: 12+51), Corpus Callosum (CC) posterior (ID: 255), CC anterior (ID: 251), cerebral white matter (WM) (ID: 2+41), cerebral cortex (ID: 3+42). The average  $T_1$  value was calculated within each ROI, bi-lateral ROIs were averaged. The analysis pipeline was implemented into the `nipype` framework [173], including the  $T_1$  estimation, described in the next section.



## T<sub>1</sub> Estimation

Quantitative T<sub>1</sub> and PD maps were obtained through a linear fit implemented in QUIT [174]. For the Cartesian data, the Bloch-Siegert map was used for B<sub>1</sub><sup>+</sup> correction. For RUFIS, the SIMBA B<sub>1</sub><sup>+</sup> map was multiplied by the simulated excitation profile generated from a trajectory of 1024 spokes, using the method outlined in chapter 3 "*Study C: A Rotating 3D Excitation Profile*". The combined SIMBA and excitation profile B<sub>1</sub><sup>+</sup> map was then used for B<sub>1</sub><sup>+</sup> correction.

## Statistical Analysis

In this study, there were three goals of the statistical analysis:

1. Compare the quantitative T<sub>1</sub> values between RUFIS and Cartesian SPGR
2. Compare the repeatability
3. Compare the reproducibility

All of these goals were accomplished using the methods described by Bland and Altman [175]. Comparison between the two techniques was performed using Bland-Altman plots (i.e. plotting the difference vs. mean of the two methods), as well as histogram analysis from whole brain white matter and cortical gray matter. Repeatability was previously defined in chapter 2 as [71, 176]

**...repeatability (of results of measurements) [VIM 3.6]:** closeness of the agreement between the results of successive measurements of the same measurand carried out under the same conditions of measurement.

In this study, this refers to the repeated scans within the same session where it is assumed that nothing has changed. The only possible change is variability in the pre-scan settings of the scanner which is assumed to not influence the measurement. This is in contrast to reproducibility which was defined as [71, 176]

**...reproducibility (of results of measurements) [VIM 3.7]:** closeness of the agreement between the results of measurements of the same measurand carried out under changed conditions of measurement

which here are the repeated visits, where day to day biological variability, changes in the scan room environment, and positioning inside the scanner are factors that can change.

Bland and Altman described a framework for quantifying both repeatability and reproducibility using the coefficient of reproducibility/repeatability, abbreviated COR [175]. Subscript  $w$  is here used for repeatability, as in *within* session, and subscript  $b$  for reproducibility, as in *between* sessions. The  $COR_w$  was calculated as  $CoR_w = 2s_d$  where  $s_d$  is the standard deviation of  $T_1$  across subjects for a given ROI, sequence, and visit. The  $CoR_b$  was calculated as  $COR_b = 2s_c$  where  $s_c = \sqrt{s_D^2 + \frac{1}{4}s_{d,1}^2 + \frac{1}{4}s_{d,2}^2}$ , where  $s_D$  is the standard deviation of the difference of the average  $T_1$  values at each session, and  $s_{d,x}$  is the within session standard deviation as used in the calculation of  $COR_w$ . In addition to the ROI analysis,  $T_1$  histograms were calculated from the whole brain white matter and cortical gray matter masks.

#### 4.4.3 Results

##### $B_1^+$ Mapping

Figure 4.6 shows a comparison of the calculated  $B_1^+$  maps from SIMBA (4.6A) and the Bloch-Siegert method (4.6B). The maps have been processed by registration to the VFA volume and smoothed, as described in the methods. The  $B_1^+$  estimates from SIMBA were lower across the whole brain compared to Bloch-Siegert, appearing to be a global scaling. To study the impact of using different  $B_1^+$  maps, the RUFIS VFA data from one subject was analysed using both the SIMBA and Bloch-Siegert  $B_1^+$  maps. The comparison, shown in figure 4.6C, shows clear improvements using any of the  $B_1^+$  maps compared to no  $B_1^+$  correction. The difference between using SIMBA or Bloch-Siegert appears to be small, and again, more of a global scaling. In this figure,  $R_1 = 1/T_1$  is shown instead of  $T_1$  as it highlights the  $B_1^+$  errors more clearly. Figure 4.6D shows a quantitative comparison of the  $T_1$  values obtained from RUFIS VFA data using SIMBA and Bloch-Siegert correction. The relative error in  $T_1$  shows up as a global scale factor, with no tissue contrast, indicating again that there is a global difference in the  $B_1^+$  maps and that it does not affect the tissue specific  $T_1$  quantification.

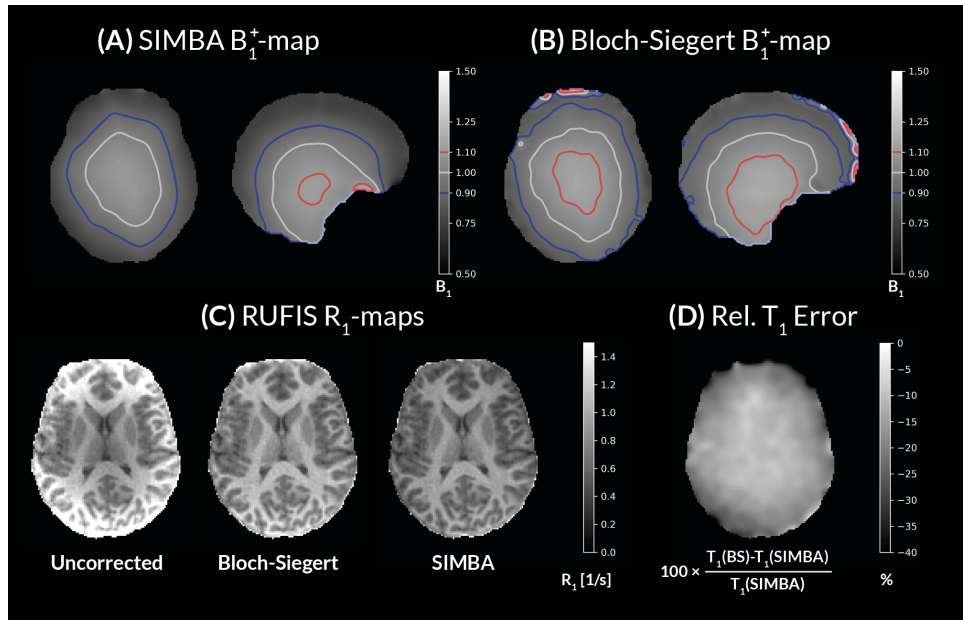


**Figure 4.6:** Comparison of B<sub>1</sub><sup>+</sup> maps between (A) SIMBA and (B) Bloch-Siegert. (C) R<sub>1</sub> maps (1/T<sub>1</sub>) calculated from RUFIS data without B<sub>1</sub><sup>+</sup> correction and with correction using the two different methods. (D) Relative T<sub>1</sub> error in RUFIS VFA when processed using the two different B<sub>1</sub><sup>+</sup> maps. (Reproduced from my publication (Ref [166]) with permission from Wiley and Sons.)

## T<sub>1</sub> Mapping

Representative quantitative T<sub>1</sub> and PD maps from one subject, presented in figure 4.7, show excellent image quality from both acquisitions. There are a few noticeable differences though. In the SPGR data, there are regions where the T<sub>1</sub> estimation failed, particularly around the brain, showing up as noise in the T<sub>1</sub> map. The RUFIS T<sub>1</sub> map is much more uniform with almost no areas where the fitting appears to have failed. This is due to the effective TE=0 in the RUFIS acquisition which enhances sensitivity to tissues with short T<sub>2</sub><sup>\*</sup>, in this case most clearly the cortical bone, indicated with white arrows in figure 4.7. The same is observed in the PD map where a higher PD is estimated in the cortical bone with RUFIS, compared to SPGR.

T<sub>1</sub> histograms comparing the two acquisitions in all four subjects are shown in figure 4.8. The T<sub>1</sub> values in WM correspond well between the two sequences, while larger deviations were observed in GM. The average difference between the peak T<sub>1</sub> values were  $\Delta WM_{peak} = 70 \pm 40\text{ms}$  and  $\Delta GM_{peak} = -180 \pm 70\text{ms}$ . Even though there are some differences, the T<sub>1</sub> distributions in WM and GM show the same shape indicating that the same tissue feature is being quantified.

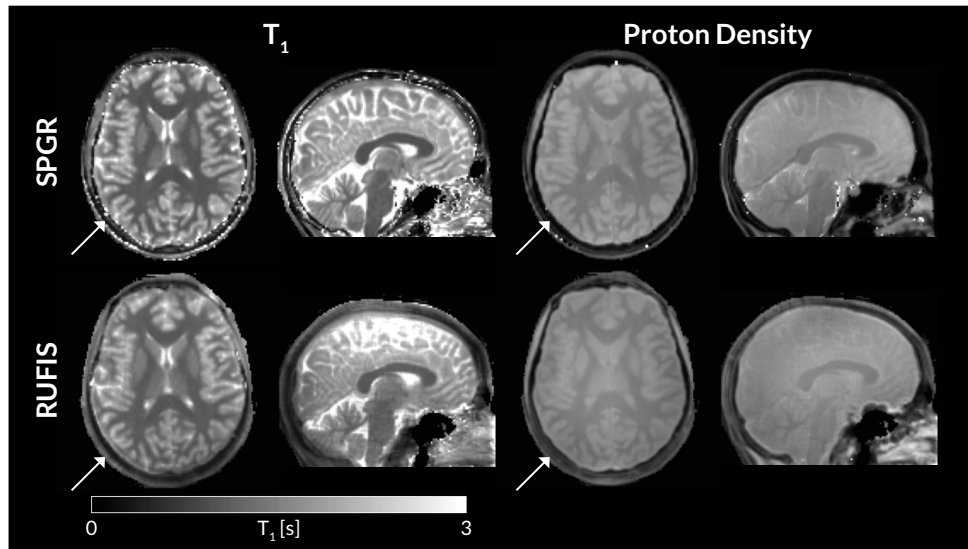


**Figure 4.7:** Representative  $T_1$  and PD maps from one subject, acquired with RUFIS and SPGR. With RUFIS a  $T_1$  and PD estimate can be obtained in the cortical bone (white arrow) due to effective  $TE=0$ . (Reproduced from my publication (Ref [166]) with permission from Wiley and Sons.)

Comparison of isolated ROIs, figure 4.9A, shows the same results as the histogram analysis;  $T_1$  estimates with RUFIS are lower in GM compared to SPGR, but higher in WM. Results from the quantitative phantom, figure 4.9B, further support these results, also showing lower estimated  $T_1$  with RUFIS compared to SPGR in the vials with long  $T_1$ . However, in the phantom data, RUFIS consistently produce lower  $T_1$  values compared to SPGR, compared to the in vivo data where RUFIS estimated higher  $T_1$  in WM.

The average repeatability, i.e. variability within session, across ROIs was comparable between RUFIS  $CoR_{w,1}/CoR_{w,2} = 0.06/0.02$  and SPGR  $CoR_{w,1}/CoR_{w,2} = 0.05/0.08$ . The average reproducibility, i.e. variability between session, was better with RUFIS ( $CoR_b = 0.07$ ) compared to SPGR ( $CoR_b = 0.2$ ). The full breakdown of repeatability and reproducibility estimates are presented in table 4.2.

### Acoustic Noise

The results from the acoustic noise measurements are presented in table 4.3. RUFIS showed no measurable increase in the acoustic noise, compared to a 33dB(A) increase with Cartesian SPGR, relative to the ambient noise levels in the scan room. There was a 5dB(A) increase in the noise with SIMBA created by the crusher gradient after the SIMBA preparation pulse. This noise could be reduced by reducing the slew rate of the crusher gradient.

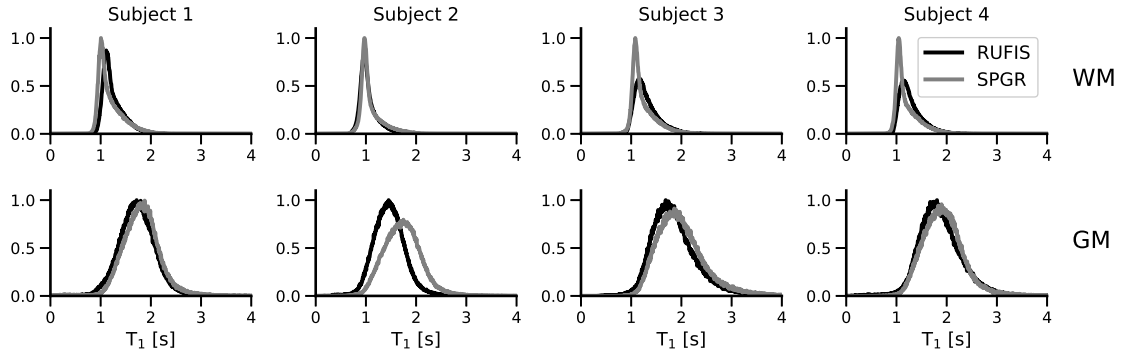


**Figure 4.8:**  $T_1$  histograms from WM and GM from each subject, obtained with RUFIS (black) and SPGR (gray). With RUFIS,  $T_1$  is slightly higher in WM but lower in GM. Histograms calculated from the average of the two scans in the first visit. (Reproduced from my publication (Ref [166]) with permission from Wiley and Sons.)

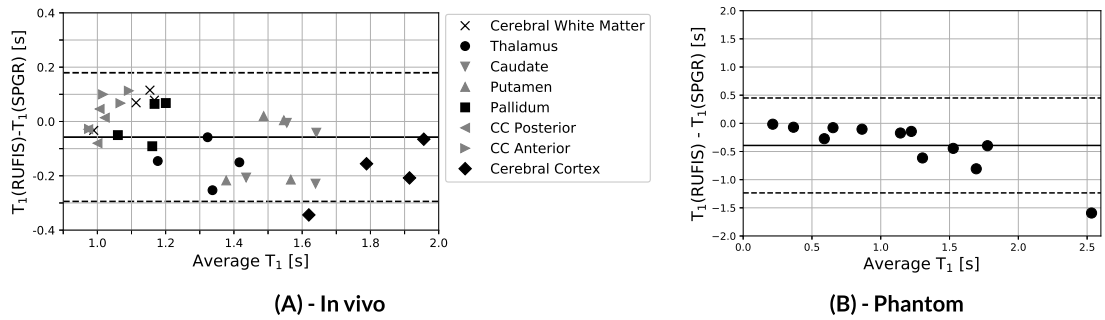


**Figure 4.9:** Comparison of  $T_1$  estimates between RUFIS and SPGR within (A) in vivo ROIs and (B) the quantitative phantom. Both experiments shows similar results with lower estimates for longer  $T_1$  with RUFIS. Data is from first scan in first visit. (Reproduced from my publication (Ref [166]) with permission from Wiley and Sons.)

**Table 4.2:**  $T_1$  values in isolated ROIs averaged between the two scans in the first visit together with within session repeatability estimates ( $COR_w$ ) from the first visit and between sessions reproducibility measurements ( $COR_b$ ). Lower values of  $COR$  are better

ROI	RUFIS			SPGR		
	$T_1[s]$	$CoR_{w,1}$	$CoR_b$	$T_1[s]$	$CoR_{w,1}$	$CoR_b$
Cerebral WM	$1.13 \pm 0.09$	0.07	0.07	$1.08 \pm 0.04$	0.01	0.08
Thalamus	$1.23 \pm 0.09$	0.05	0.05	$1.38 \pm 0.08$	0.09	0.2
Caudate	$1.5 \pm 0.1$	0.06	0.09	$1.63 \pm 0.08$	0.05	0.2
Putamen	$1.4 \pm 0.1$	0.05	0.05	$1.55 \pm 0.08$	0.04	0.2
Pallidum	$1.15 \pm 0.07$	0.04	0.04	$1.16 \pm 0.04$	0.02	0.1
CC Posterior	$0.99 \pm 0.03$	0.05	0.05	$1.01 \pm 0.03$	0.04	0.1
CC Anterior	$1.07 \pm 0.06$	0.06	0.04	$1.01 \pm 0.03$	0.08	0.1
Cerebral Cortex	$1.7 \pm 0.2$	0.1	0.1	$1.92 \pm 0.08$	0.04	0.2
<b>Mean</b>	-	0.06	0.07	-	0.05	0.2

**Table 4.3:** Summary of acoustic noise measurements from each sequence. Values are reported as  $\text{mean} \pm \sigma$  noise levels over a 40 s period. The large standard deviation in the noise levels for SIMBA is due to the periodic spoiling gradients. (LAEQ - A-weighted equivalent continuous sound level, LCPEAK - C-weighted peak sound level)

Sequence	LAEQ [dB(A)]	LCPEAK [dB(C)]
Ambient	$70.0 \pm 0.2$	$89.7 \pm 0.7$
RUFIS	$70.0 \pm 0.2$	$89.6 \pm 0.7$
SIMBA	$75.2 \pm 4.0$	$102.5 \pm 9.5$
SPGR	$103.3 \pm 0.04$	$116.2 \pm 0.1$
Bloch-Siebert	$98.8 \pm 0.04$	$111.0 \pm 0.1$

#### 4.4.4 Discussion

##### Silent $T_1$ Mapping

The  $T_1$  values estimated in this study are within the expected range from the literature, such as those reported in the study by Stanisiz et al. who measured  $T_1=1084\pm45/1820\pm114$  in WM/GM [34]. There is however great variability in the  $T_1$  mapping literature with regards to what the "normal"  $T_1$  is in WM and GM, where results seem to depend on which technique is used. But even with the VFA method, different flip angle schemes and  $B_1^+$  mapping methods have been shown to affect the results [177, 69].

Both RUFIS and SPGR showed high repeatability and reproducibility in this study, although RUFIS had slightly better reproducibility, i.e. between session performance. Given the small number of subjects ( $N = 4$ ) and only two visits, only limited statistical conclusions can be drawn. I chose to use the coefficient of reproducibility (COR) as it is a directly applicable measure for this type of small study [175]. This is in contrast to the coefficient of variation (COV) and intra class correlation coefficients (ICC) which have been used in larger studies to quantify repeatability and reproducibility. For example, Deoni et al. calculated voxel wise intra-site CoV=6.4 in whole brain white matter [178]. Similarly, Weiskopf et al. calculated intra-site CoV of  $R_1$  in the corpus callosum and caudate nucleus of 3.9 and 4.7 [179].

No increase in acoustic noise was measured using RUFIS compared to the ambient background noise levels, similar to Alibek et al. [98]. The acoustic noise measurements presented in chapter 3 were lower than those presented here, which can be explained by the much higher background noise here, 70dB(A) compared to 62db(A) in chapter 3.

The  $T_1$  values from RUFIS and SPGR in the current study were in the same range in WM and GM. However,  $T_1$  values from RUFIS were slightly higher in WM compared SPGR, but lower in GM, as seen in figure 4.8 and 4.9. The biggest difference was observed in subject 2 while the difference was smaller for the three other subjects. This pattern of difference in  $T_1$  between tissue types cannot be explained simply by an overall  $B_1^+$  error as this would result in a scaling of all  $T_1$  values. The following sections will discuss the potential influence of ZTE effects, magnetisation transfer, and spoiling on the quantitative  $T_1$  estimates.

### ZTE Effects

The effect of the zero echo time (ZTE) readout appears most clearly in the cortical bone, which has a very short  $T_2^*$  and thus the signal decays too quickly for the SPGR acquisition to capture any signal. Using RUFIS, a  $T_1$  and PD fit could be obtained in the cortical bone, which resulted in a more homogeneous  $T_1$  and PD map, see figure 4.7. One issue that could arise from this, however, is reduced performance of brain extraction algorithms which rely on the difference in image intensity between brain tissue, CSF, and the skull [180]. Conversely, one application for which this aspect of the ZTE readout could find applications is outside the brain, e.g. for imaging of joints as recently demonstrated by Engström et al. who used VFA ZTE for  $T_1$  mapping in the knee [111].

The contribution from ultra-short  $T_2$  components in WM and GM, macromolecules such as myelin, is believed to be negligible in this study. Firstly, the relative proton density of the macromolecular pool is very small compared to the free water pool. Secondly, if the signal indeed could be measured, it would have decayed within the first few samples of the readout, resulting in extremely poor localisation of the signal. Seifert et al. performed measurements at 3T and 9.4T and quantified the observable fraction of the signal from solid myelin [41]. Their analysis showed that with the range of flip angles used here, less than 2% of the total signal from myelin can be measured. The observable fraction can only be increased by decreasing the deadtime and increasing the sampling rate in the experiment. Preliminary work by Weiger et al. showcased a custom built 3T system with a deadtime of 15  $\mu$ s, and readout bandwidth of 2000 kHz [181]. By subtracting two images with different deadtimes, Weiger et al. produced a "myelin image" with very strong WM contrast.

### Magnetisation Transfer

One potential contribution to the discrepancies in the quantitative  $T_1$  values observed in this study between RUFIS and SPGR is magnetisation transfer (MT) [182]. The magnitude of the MT effect in an experiment is driven both by the type of RF pulses used and the power delivered by the pulses. In this work, there is a clear difference between the approaches investigated: RUFIS uses ultra-short hard RF pulses with close to peak  $B_1^+$ , while SPGR uses shaped pulses, with lower  $B_1^+$ , for slab selection. If the bound pool (i.e. the non aqueous protons) is fully saturated in an MR experiment, the effective  $T_1$  will approach  $T_{1SAT}$  ( $T_1$  observed when the bound pool is fully saturated) [183, 184], which is shorter than  $T_1$  in the absence of MT. The effect is typically observed in MT experiments



where off-resonance pulses are applied to saturate the bound pool [182], but it can also be observed with on-resonance excitation pulses as they will also partly saturate the bound pool [184]. Recently, Teixeira et al. showed that the estimated  $T_1$  decreases in both WM and GM with increasing peak  $B_1$  of the excitation pulse, when other acquisition parameters were kept constant, due to MT effects [69]. In the context of the present experiment, RUFIS has a higher peak  $B_1$  due to the ultra-short hard RF pulses, but RUFIS also used much lower flip angles than SPGR. Further quantitative analysis of the RF pulses used in the experiment is required to estimate the MT effect produced by the excitation pulse. Another contributing factor is the TR; RUFIS has a much shorter TR than SPGR which leads to less time for recovery of the bound pool, and thus likely higher saturation.

If MT was the main contributing effect to the difference observed in  $T_1$  in this experiment, then the largest difference should be observed in WM, under the assumption that the  $T_1$  estimates would correlate perfectly in the absence of MT. However, the biggest difference is here observed in GM, suggesting that even in the absence of MT, there is a difference between the techniques. This is further supported by the phantom experiment, figure 4.9b, which has very low macromolecular content, where the same pattern of larger difference for longer  $T_1$  was observed. There will be some MT effect in vivo, affecting the  $T_1$  results, but it is more likely that the discrepancies in  $T_1$  between RUFIS and SPGR is a complex combination of several factors, one of them being MT. Overall, a more detailed, quantitative, analysis is required to fully understand the influence of MT in the RUFIS.

## Spoiling

The signal equation used to model the signal in the VFA experiment assume complete spoiling of the transverse magnetisation between excitations [114]. In SPGR, this is achieved through a dedicated spoiling gradient and cycling the phase of the RF pulse. In RUFIS on the other hand, only RF spoiling (phase cycling) can be used to maintain a silent readout<sup>2</sup>.

Incompletely spoiled signals will refocus whenever the integral of the accumulated gradient trajectory on all three axes crosses zero, i.e. the zeroth-moment  $m_0$  is zero. Assume that excitation of spoke  $s_0$  in the trajectory produce unspoiled transverse magnetisation. The relevant question is then, at which spoke  $s_i$ , later in the acquisition, will the signal refocus? The integral of the gradients on axis  $k$  between spoke  $s_0$  and  $s_1$  (equivalent to

<sup>2</sup>Some spoiling will be produced by the readout gradient in RUFIS, but this will be similar to the spoiling achieved by the readout gradients in SPGR.

the zeroth moment  $m_0$ ) can be written as

$$m_{0,k}(s_0, s_1) = \int_{s_0}^{s_1} G_k(s) ds \quad (4.9)$$

If  $m_{0,k} = 0$ , the signal has refocused on the given axis. Only if  $m_{0,k} = 0$  on all three axes for the same pair of spokes, however, will the signal completely refocus and produce a spoiling artefact.

Figure 4.10 shows a simulation where the magnitude of  $m_{0,k}$ , i.e. the zeroth moment, is visualised on a grayscale for pairs of spokes in a 1024 spoke trajectory. White color indicates  $m_{0,k} = 0$ , i.e. refocused on the given axis, and black indicates out of phase. For the X and Y gradient, which have sinusoidal shapes,  $m_{0,x}$  and  $m_{0,y}$  crosses zero repeatedly, while  $m_{0,z}$  is only zero at equidistant points from the equator. In a trajectory with  $N$  spokes, spoke  $s_i$  will refocus on the  $z$ -axis at spoke  $N - s_i$ . Therefore, the complete refocusing is limited by the  $z$ -axis, shown in figure 4.10D where the shading is most white in middle around spoke  $N/2$ . Overall, this suggests that if refocusing occur with RUFIS, it is most likely to appear around the  $k$ -space equator, which would produce spoiling artefacts that appearing in the scan plane (i.e. axial plane for an axial acquisition).

In practice, RUFIS uses a segmented readout where the gradient amplitude is slowly ramped up to the required amplitude for the first spoke, resulting in additional spoiling *between* segments. The discussion of accidental refocusing can thus be limited to *within* a single segment. Refocusing is therefore most likely to occur in low resolution acquisitions where a small number of spokes is used, and a single segment covers both sides of the  $k$ -space equator. The extent to which these potential artefacts affect the image quality needs to be investigated further, but from visual inspection there was no sign of spoiling artefacts in the acquired data presented in this chapter.

Insufficient spoiling is known to affect quantitative  $T_1$  results [116]; this has been studied thoroughly for Cartesian sequences, and correction methods have been developed to account for the effects [117]. Studies investigating spoiling in radial sequences, have mainly focused on image quality rather than the effects on quantitative measurements, but have found that a random RF phase increment is the optimal approach [185, 118]. In the current study no corrections for insufficient spoiling were applied, mainly because the available correction methods are designed for Cartesian sequences with gradient spoiling. Future work will further investigate the spoiling behaviour of RUFIS, and in particular

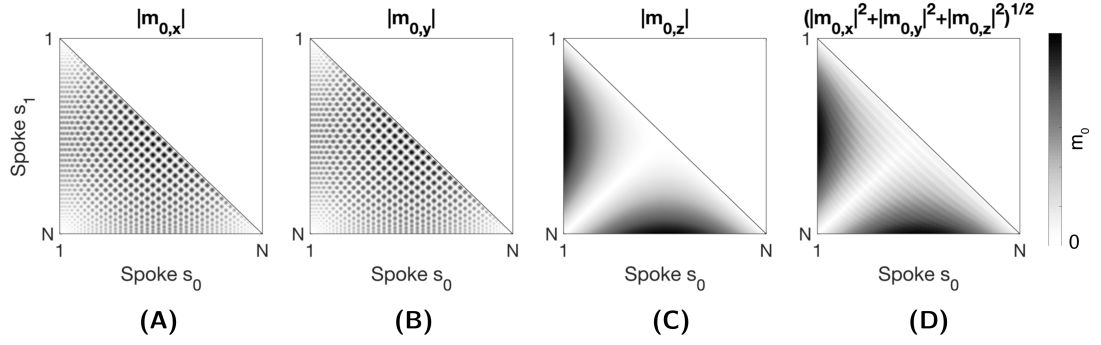


**Figure 4.10:** Simulation demonstrating the refocusing behaviour of the RUFIS trajectory with 1024 spokes, showing the integral of the X, Y, and Z gradient (**A-C**), as well as the magnitude of the gradient along all three axes (**D**) (i.e. square root sum of squares), calculated using equation 4.9.

whether a random RF phase increment can improve image quality and to which extent it affects the quantitative results.

## 4.5 Chapter Discussion and Conclusion

In this chapter, VFA  $T_1$  mapping using RUFIS has been studied. It was first shown, through theoretical derivations, that the flip angles that can be achieved with RUFIS are tightly linked to the readout bandwidth. To achieve high flip angles, as required for VFA  $T_1$  mapping, a low readout bandwidth must be used, here  $\pm 7.8\text{kHz}$ . Higher bandwidth could accelerate the acquisition and improve image quality by reducing chemical shift artefacts. However, a higher bandwidth will reduce the maximum flip angle possible and thus, depending on the TR of the acquisition, the optimal flip angles might not be achievable. In the next chapter, the VFA experiment is extended to 1.5T and 7T scanners, and it will be demonstrate that higher readout bandwidths are required at high field strengths, requiring these interactions to be investigated further.

To enable VFA  $T_1$  mapping with RUFIS, a new  $B_1^+$  mapping technique, SIMBA, was developed. The SIMBA  $B_1^+$  map showed similar  $B_1^+$  profile but overall lower estimated  $B_1^+$  compared to a standard Bloch-Siegert  $B_1^+$  acquisition. Future work will investigate whether the global scaling factor in  $B_1^+$  between the sequences originates from imperfections in the hard pulses used in the preparation, and is thus a feature that should be captured, or reflects an error in the model used. It is also possible that the RF pulses in the preparation module are spaced too tightly relative to the ringdown time of the RF transmit chain, leading to erros in the total flip angle achieved. Further experiments could be carried out

to investigate this in which the composite preparation pulse is replaced with a single long hard pulse of equivalent flip angle.

Combining SIMBA with a RUFIS VFA resulted in a near silent VFA  $T_1$  mapping protocol (within 5dB(A) of the background noise levels). The silent  $T_1$  mapping protocol was compared to a standard Cartesian SPGR acquisition, showing that the estimated  $T_1$  values from the two methods compared well in WM but that there was a larger difference in GM. The underlying cause for the discrepancy in  $T_1$  is unknown, but hypothesised to be driven by a combination of different spoiling behaviour, and different magnetisation transfer effects, between the sequences. Further work will extend the simulation framework presented by Malik et al. for studying and modelling the MT effects in RUFIS [70].

With a two flip angle protocol, as used here, the acquisition is optimised for a single  $T_1$ , here  $T_1=1s$  (approximate  $T_1$  in WM). An alternative approach would be to acquire a larger number of flip angles over a wider range, in order to optimise the acquisition for a range of  $T_1$ . If the number of flip angles is high enough, and each volume is sampled with a unique k-space pattern, low-rank reconstruction methods could be used in the flip angle dimension [186, 187]. This could improve precision of the  $T_1$  measurement over a larger range of  $T_1$ .

## 4.6 Publications and Contribution

### 4.6.1 Publications

This work has previously been published in

1. **Ljungberg E**, Wood T, Solana AB, Kolind S, Williams SCR, Wiesinger F, et al. *Silent  $T_1$  mapping using the variable flip angle method with  $B_1$  correction*. Magn Reson Med. 2020;(December 2019):1–12. DOI:10.1002/mrm.28178
2. **Ljungberg E**, Wiesinger F, Solana AB, & Barker G J, (2019). *Silent Magnetization Prepared  $B_1$ -map Acquisition - SIMBA*. In Proc. Intl. Soc. Mag. Reson. Med 27 (p. 0448). Montreal.
3. **Ljungberg E**, Sanchez AB, Wood TC, Kolind S, Wiesinger, F, & Barker GJ, (2018). *Silent  $T_1$ -Mapping Using the Variable Flip Angle Method with Zero Echo Time*. In Proc. Intl. Soc. Mag. Reson. Med 26 (p. 0270). Paris.

### 4.6.2 Contribution

Collaborator at GE Healthcare had investigated the idea of VFA  $T_1$  mapping with RUFIS prior to me starting the PhD. The study presented here was formed through discussions with my supervisor Dr. Wiesinger at GE Healthcare, and thus influenced by their early developments. I performed all the pulse programming in this chapter, with advice from Prof. Barker. The idea to use a train of hard pulses for the SIMBA technique came from Prof. Barker. All modelling and data analyses were developed and performed by me.

## Chapter 5

# T<sub>1</sub> Mapping Across Field Strengths

### Contents

---

5.1	Introduction	119
5.2	A Theoretical Perspective on RUFIS Across Field Strengths	120
5.3	RUFIS T <sub>1</sub> Mapping at 1.5, 3, and 7T	130
5.4	Chapter Discussion and Conclusion	148
5.5	Publications and Contribution	149

---

### Summary

IN this chapter, the utility of using RUFIS for quantitative T<sub>1</sub> mapping using the variable flip angle method across three field strengths (1.5, 3, and 7T) is demonstrated. A single subject is scanned at all three field strengths with RUFIS and a Cartesian spoiled gradient echo sequence for comparison. Recommendations for implementation of VFA T<sub>1</sub> mapping with RUFIS at each field strength are presented.

## 5.1 Introduction

Development of scanners with higher magnetic field strength is largely driven by the increased spin polarisation at high field, resulting in more available magnetisation for imaging, and thus increased signal to noise ratio (SNR). However, with higher field strength, many imaging artefacts and issues faced at lower field strengths are amplified. Some of the main issues, affecting most imaging sequences include:

- Specific absorption rate (SAR), which increases quadratically with field strength
- Off-resonance effects, both from susceptibility differences and chemical shift, which increase linearly with field strength
- $B_1$  inhomogeneity which increases with field strength due to the decreased RF transmit wavelength.
- Increase in  $T_1$  and decrease in  $T_2^*$  relaxation times.

Ultra-high field scanners ( $\geq 7\text{T}$ ) have, to date, mainly found applications within research, due to high costs and regulatory issues [188], and as many of the needs of clinical Magnetic Resonance Imaging (MRI) can be satisfied with 1.5T or 3T scanners. A survey by the Clinical Imaging Board (CIB) in the U.K., representing approximately 42% of the MR systems in the U.K., showed that 1.5T scanners make up 79% of the clinical scanners, and 17% are 3T [189]. Given the interest in pushing MRI technology to ultra-high field as well as utilising the large number of 1.5T scanners currently available, it is of interest to study the utility of the Rotating Ultra-Fast Imaging Sequence (RUFIS) across field strengths. Most of the work to date (at the time of writing this thesis) has been focused on 3T, with some applications described at 7T, but no work at 1.5T. In this chapter, the limitations on the RUFIS acquisition with regards to field strength are investigated. A theoretical study is presented, investigating how factors such as SNR, contrast to noise ratio (CNR), SAR and acoustic noise change with field strength. Field-strength specific interactions are investigated and presented as corollaries. Finally, an in vivo study of  $T_1$ -mapping at 1.5, 3, and 7T is presented, demonstrating the performance of variable flip angle (VFA)  $T_1$ -mapping across field strengths.

## 5.2 A Theoretical Perspective on RUFIS Across Field Strengths

A change in field strength ( $B_0$ ) does not directly necessitate changing any of the imaging parameters, except the frequency of the RF transmit and receive systems. It is common, though, to adjust parameters such as: readout bandwidth, to reduce off-resonance effects; echo time and repetition time, to account for change in relaxation times; and RF pulse types, to stay within the SAR limits. The following sections will describe how the imaging parameters in RUFIS are affected by the field strength by analysing constraints imposed by the RUFIS sequence.

### 5.2.1 Readout Bandwidth

The readout bandwidth determines sampling rate and thus the duration of the signal readout, given a fixed matrix size. It is the primary acquisition parameter that can be adjusted to reduce off-resonance effects, produced by variation in the local precession frequency. Off-resonance effects can be caused by variation in magnetic susceptibility, or differences in chemical shift, most commonly between water and fat. The absolute difference in resonance frequency between water and fat is

$$\Delta f = \gamma \cdot B_0 \cdot \delta_{fat} \quad [Hz]. \quad (5.1)$$

where  $\delta_{fat} = 3.5\text{ppm}$ . At the out of phase time ( $T_{op} = 1/2\Delta f$ ), the phase of the fat signal relative to water is  $\pi$ , causing destructive interference and a reduction of the signal at any water-fat interfaces encoded by the specific k-space location being sampled at this time [111]. The influence of off-resonance effects depends on the duration of the readout, which for a fixed matrix size is adjusted via the readout bandwidth. Figure 5.1 shows the in and out of phase behaviour of water and fat at 1.5, 3, and 7T along the k-space readout for a spoke with 64 readout points [111]. In the brain, where fat is mainly located in a small area around the skull, i.e. represented by a high spatial frequency component, water and fat need to be in phase at the edge of k-space in order to accurately localise this signal. This can be achieved by setting acquisition time equal to  $T_{ip} = 1/\Delta f$ . This is equivalent to achieving a water-fat shift of 1 voxel. Figure 5.1 shows that for a 64 point spoke, this corresponds to a readout bandwidth of  $\approx 15$  kHz at 3T and  $\approx 31$  kHz at 7T. Figure 5.1 shows that a 15 kHz readout bandwidth at 7T will also put water and fat



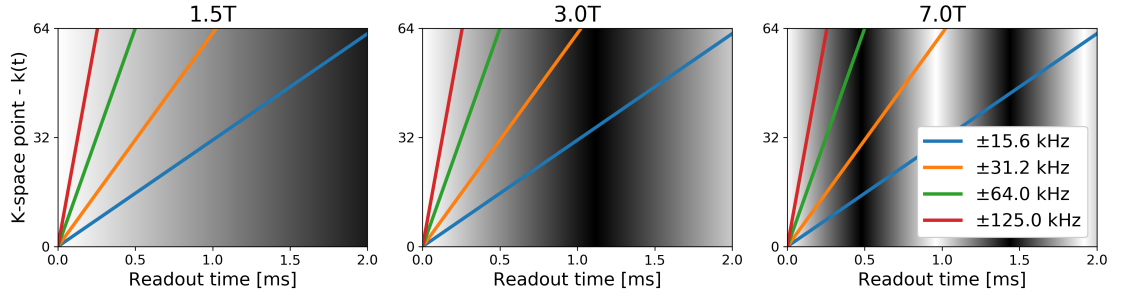


**Figure 5.1:** Demonstration of the in- and out-of-phase behaviour at 1.5, 3, and 7T. Lines shows k-space readout timings for different readout bandwidths. Greyscale background shows the in- and out-of-phase behaviour of water and fat, with white being in-phase and black out of phase.

in phase, however this would increase the water-fat shift to 2 voxels, i.e. result in more obvious image artefacts. This leads to the first corollary, stating the relationship between bandwidth and field strength

**Corollary 1** *For an acquisition with  $N_p$  points along the spoke, the readout bandwidth should scale with  $B_0$ , to maintain the same level of susceptibility artefacts, as*

$$BW = \Delta f \cdot \frac{N_p}{2} = \gamma B_0 \cdot \delta_{fat} \cdot \frac{N_p}{2} \quad \rightarrow \quad BW \propto B_0 \quad (5.2)$$

Since the RUFIS readout is mainly limited by the duration of data acquisition, the repetition time (TR) is proportional to the bandwidth (BW), leading to the second corollary

**Corollary 2** *To a very good approximation, the TR is inversely proportional to the readout bandwidth BW*

$$TR \approx \frac{N_p}{2 \cdot BW} = \frac{2}{2\gamma B_0 \delta_f} \quad \rightarrow \quad TR \propto \frac{1}{B_0} \quad (5.3)$$

### 5.2.2 RF Systems

The peak  $B_1$  achievable on a given scanner, and thus the maximum flip angle possible, depends on the radio frequency (RF) transmit system. It is impossible to make a generalised argument across field strengths regarding RF performance, as amplifier performance varies greatly between scanners. For the sake of making an argument here, two different assumptions are considered in order to develop a better understanding of the likely range of possible  $B_1$ . If a fixed peak  $B_1$  is assumed to be achievable across field strengths, this would require more powerful RF amplifiers at high field since the absorbed power in tissue

scales with  $B_0^2$ . To achieve the same peak  $B_1$  as a 15 kW amplifier delivers at 1.5T would therefore require a 70 kW amplifier at 7T (this is the most realistic scenario). Alternatively, it could be assumed that the same RF amplifier is used across field strength with fixed power output. Since the absorbed power scales with  $B_0^2$ , this results in a decrease in peak  $B_1$  with field strength proportional to  $1/B_0$ . In reality, this would not be the case as the RF system then would be the limiting factor of a very expensive high-field MR system. It is still useful though to consider this situation as it builds an understanding of how a change in field strength influences other factors of the MR system

In reality, stronger RF amplifier are typically used in higher field scanners, in order to achieve sufficient  $B_1$  power, but the increased power deposition also results in higher SAR which can become the limiting factor instead. The type of transmit coil will also make a difference; at 7T, it is common to utilise local transmit coils which reduce the SAR by only irradiating a small part of the body, as well as reducing the power required from the amplifier.

**Corollary 3** *The peak  $B_1$  achievable at a given field strength will be generalised as a function of field strength as*

$$B_1 = q(B_0). \quad (5.4)$$

*Two cases can be considered. Either the peak  $B_1$  is assumed to be constant across field strength*

$$q(B_0) = B_{1,peak} \quad (5.5)$$

*or as the amplifier performance is constant which gives*

$$q(B_0) \propto \frac{1}{B_0} \quad (5.6)$$

### 5.2.3 Excitation RF Pulse Width

In RUFIS, RF excitation is performed in the presence of a readout gradients, resulting in a sinc shaped excitation profile in the readout direction [130], as discussed in chapter 3. To maintain  $B_1^+$  uniformity, the bandwidth of the RF pulse has to encompass the readout bandwidth, i.e.  $BW_{RF} > BW_{acq}$ . The bandwidth  $\Delta f$ , defined as the full width half max

(FWHM), of a hard pulse with duration  $\tau_{rf}$  is given by [121]

$$\Delta f = \frac{1.21}{\tau_{rf}}, \quad (5.7)$$

leading to the following relation between RF pulse width  $\tau_{rf}$  and readout bandwidth  $BW$

$$\tau_{rf} \cdot BW \leq \frac{1.21}{2}. \quad (5.8)$$

The flip angle ( $\alpha$ ) of a hard RF pulse with width  $\tau_{rf}$  and amplitude  $B_1$  is given by

$$\alpha = \gamma B_1 \tau_{rf}. \quad (5.9)$$

To reach the highest possible flip angle with RUFIS, the maximum RF amplitude ( $B_1$ ) is used with the maximum pulse width, given by (5.8). From equations (5.3), (5.9), (5.8) and corollary (3), it can be seen that the maximum flip angle is limited by  $B_0$ , leading to the third corollary:

**Corollary 4** *The maximum obtainable flip angle  $\alpha_{max}$  is inversely proportional to  $B_0$  as*

$$\alpha = \gamma B_1 \tau_{rf} = \frac{1.21 \cdot \gamma B_1}{2 \cdot BW} = \frac{1.21 \cdot \gamma B_1}{\gamma B_0 \Delta f N_p} \rightarrow \alpha \propto \frac{q(B_0)}{B_0} \quad (5.10)$$

#### 5.2.4 Acoustic Noise

The acoustic noise produced during an MRI scan originates from vibrations of the gradient coils and vibrations from induced eddy currents in other parts of the scanner [78]. A conductor  $\mathbf{L}$ , with length  $|\mathbf{L}|$ , carrying a current  $I$  inside a magnetic field  $\mathbf{B}$  will experience a Lorentz force  $\mathbf{F}$  given by [72]

$$\mathbf{F} = I \cdot \mathbf{L} \times \mathbf{B}. \quad (5.11)$$

If the magnetic field is oriented along  $z$  and the conductor along  $x$ , then the force, along  $y$  is  $F_y = I \cdot B_z$ . During an MRI experiment, the current through the gradient coils will vary over time, according to the k-space trajectory, causing a change in this force and thus inducing vibrations. The force on the gradient coils are proportional both to the strength of the gradients ( $I$ ) and the main magnetic field ( $B$ ). As the field strength is increased, the gradient amplitude is also increased to maintain the same chemical shift for equivalent image quality, corollary (1). Therefore, the Lorentz force will increase approximately as  $B_0^2$ .

That does not mean though that the acoustic sound pressure will increase quadratically with field strength, however, as the acoustic noise produced by the scanner is also heavily influenced by the construction of the system [78]. Higher field strength scanners are typically bigger, producing a larger resonant body, compared to lower field strength. However, studies have found an increase in acoustic noise levels with increasing field strength [77].

### 5.2.5 Change in Relaxation Times

Relaxation times ( $T_1$  and  $T_2$ ) change with the resonance frequency, i.e. with field strength. The theory presented by Bloembergen, Purcell and Pound (commonly abbreviated BPP theory) can be used to predict  $T_1$  and  $T_2$  in liquids. The relaxation times depends on the correlation time  $\tau_c$  and the Larmour frequency  $\omega_0$  as [190]

$$\frac{1}{T_1} = K \left( \frac{\tau_c}{1 + (\omega_0 \tau_c)^2} + 4 \cdot \frac{\tau_c}{1 + (2\omega_0 \tau_c)^2} \right) \quad (5.12)$$

$$\frac{1}{T_2} = K \left( \frac{3}{2} \cdot \tau_c + \frac{5}{2} \cdot \frac{\tau_c}{1 + (\omega_0 \tau_c)^2} + \frac{\tau_c}{1 + (2\omega_0 \tau_c)^2} \right) \quad (5.13)$$

The correlation time  $\tau_c$  is a measure of the molecular tumbling rate, i.e. how quickly molecules reorient themselves. This tumbling produces fluctuations in the dipolar field, which in turn causes spin transitions between energy states, and thus  $T_1$  and/or  $T_2$  relaxation.  $T_1$  is most sensitive to transitions at  $\omega$  and  $2\omega$ , as seen in (5.12), while  $T_2$  is dominated by the constant term (5.13), equivalent to transition between spin states without energy difference<sup>1</sup>. BPP theory therefore predicts that  $T_1$  changes with  $B_0$  while  $T_2$  remains relatively constant. In practice, the apparent transverse relaxation time  $T_2^*$  does change with  $B_0$  however, as it is also influenced by magnetic field inhomogeneities, which increase with field strength.

It is not possible to directly predict relaxation times in tissues using BPP theory as it only valid for liquids, however studies have confirmed that the theoretically predicted trends in relaxation times still hold. Stanisiz et al. studied  $T_1$  and  $T_2$  relaxation at 1.5T and 3T in various tissues and found clear increases in  $T_1$ , while the changes in  $T_2$  where within the margin of the measurement error [34]. Several studies have investigated changes in  $T_1$  across field strength confirming that it increases with field strength [191, 14, 30].

<sup>1</sup>e.g. in a two spin system this would be  $\uparrow\downarrow$  to  $\downarrow\uparrow$

Attempts have been made to develop simplified analytical models for approximating  $T_1$  and  $T_2^*$  as a function of field strength for white and gray matter based on in vivo measurements [192, 191]. The models for  $T_1$  and  $T_2^*$  used here, in (5.14) and (5.15) (below), were proposed by Bottomley et al. [191]. Each model takes two tissue specific design parameters, shown in table 5.1, obtained from Rooney et al. [14]. Figure 5.2 shows the two models evaluated from 0.5-7T in white and gray matter, showing an increase in  $T_1$  and decrease in  $T_2^*$  with increasing field strength.

**Corollary 5** *The longitudinal relaxation time  $T_1$  increases with field strength,  $T_2^*$  decreases, and  $T_2$  stays constant.*

$$T_1(B_0) = a \cdot (\gamma B_0)^b \quad [ms] \quad (5.14)$$

$$T_2^*(B_0) = c \cdot e^{-dB_0} \quad [ms] \quad (5.15)$$

**Table 5.1:** Tissue specific design parameters for analytical models of  $T_1$  and  $T_2^*$  relaxation in white and gray matter.

Tissue	T <sub>1</sub> Model		T <sub>2</sub> <sup>*</sup> Model	
	<i>a</i>	<i>b</i>	<i>c</i>	<i>d</i>
White Matter	0.71	0.382	90	0.142
Gray Matter	1.16	0.376	64	0.132

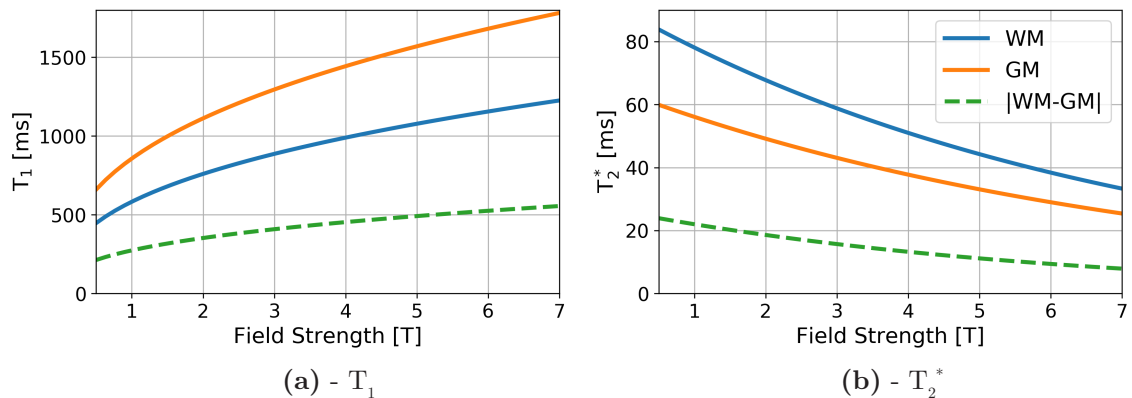


**Figure 5.2:** Simulation of (a)  $T_1$  and (b)  $T_2^*$  as a function of field strength in white and gray matter.

### 5.2.6 Signal to Noise Ratio - SNR

The signal in an nuclear magnetic resonance (NMR) experiment is proportional to both the magnetisation and the Larmour frequency, which results in a quadratic increase with field strength [193]

$$S \propto \omega M \rightarrow S \propto B_0^2 \quad (5.16)$$

while the noise in the acquired signal scales linearly with field strength [193]

$$\nu \propto B_0. \quad (5.17)$$

Together this results in an intrinsic SNR that scales linearly with field strength

$$SNR = \frac{S}{\nu} \rightarrow SNR \propto B_0. \quad (5.18)$$

These calculations assume that the main contributor to reduction of the signal is in the sample. At low field strength, the resistance in the coils become a significant contributor to the noise, and the SNR instead scales by  $SNR \propto B_0^{7/4}$ . At the field strengths relevant to the work in this thesis, a linear increase in SNR will be assumed.

**Corollary 6** *The SNR scales linearly with field strength, with all other parameters held constant*

$$SNR \propto B_0 \quad (5.19)$$

### 5.2.7 Specific Absorption Rate

The SAR is calculated as the average power deposition across the duration of the acquisition, taking the different RF pulses and delays into account. For a single hard RF pulse, as used in RUFIS, the SAR can be approximated as [121]

$$SAR_{pulse} \propto B_0^2 \cdot (B_1 \tau_{RF})^2 \cdot \Delta f \quad (5.20)$$

where  $\tau_{RF}$  is the duration,  $B_1$  is the amplitude and  $\Delta f$  is the bandwidth of the RF pulse. For a hard RF pulse with duration  $\tau_{rf}$ , this can be expanded using equation (5.9) and (5.7) to

$$SAR_{pulse} = B_0^2 \cdot B_1^2 \cdot \gamma^2 \cdot \tau_{RF}^2 \cdot \frac{1.21}{\tau_{rf}}. \quad (5.21)$$

To achieve the maximum flip angle, which would yield the highest SAR, the  $B_1$  is kept constant and the flip angle is only changed by changing  $\tau_{RF}$ . However,  $\tau_{RF}$  also change with field strength, corollary (4), which yields

$$SAR_{pulse} \propto B_0^2 \cdot \tau_{RF} \propto \frac{B_0^2}{B_0} = B_0 \quad (5.22)$$

Assuming that the whole acquisition is performed using identical RF pulses and the TR is changed to keep the off-resonance artefacts constant, the time average SAR ( $SAR_{ave}$ ) is given by

$$SAR_{ave} \propto \frac{SAR_{pulse}}{TR} \propto \frac{B_0}{1/BW} \propto \frac{B_0}{1/B_0} = B_0^2. \quad (5.23)$$

The results of equation (5.23) shows that the time average SAR ( $SAR_{ave}$ ) does not depend on the TR or flip angle, if the maximum achievable flip angle is used. If the flip angle was kept constant, the  $SAR_{ave}$  would increase if TR is decreased. However, as the TR is decreased by increasing the bandwidth in RUFIS, the maximum flip angle will be decreased as a result, which decreases the SAR.

**Corollary 7** *For an acquisition with constant TR, determined by the BW, and identical RF pulses, with maximum amplitude at the given BW, the time average SAR increase quadratically with  $B_0$*

$$SAR_{ave} \propto B_0^2. \quad (5.24)$$

### 5.2.8 Effective Contrast to Noise Ratio

Given the linked constraints described in the previous sections concerning the RUFIS acquisition across field strength, the relevant question for most clinical applications, and qualitative research studies, is how the contrast to noise ratio (CNR) in the acquired data changes with field strength. The CNR will be affected by change in relaxation times, flip angle and TR limitations, as well as the SNR. Since this chapter focuses on VFA  $T_1$  mapping, only the CNR of a steady-state RUFIS acquisition will be studied here. The CNR between two tissue types  $A$  and  $B$  is here defined as

$$CNR = SNR_A - SNR_B = B_0 \cdot [S(\alpha, TR, T_{1,A}, PD_A) - S(\alpha, TR, T_{1,B}, PD_B)] \quad (5.25)$$

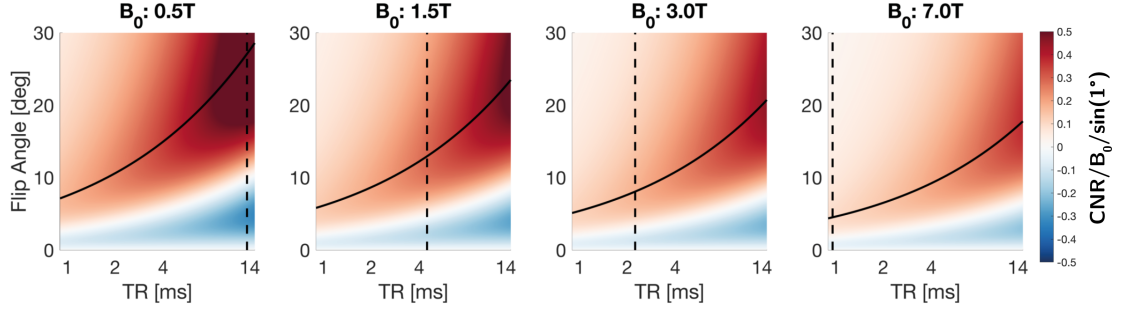


**Figure 5.3:** Relative CNR ( $CNR/B_0$ ) at four different field strength as a function of TR and flip angle. The relative CNR is shown to highlight the effects of the change in  $T_1$  over field strengths. Solid line indicates maximum  $T_1$  contrast, dashed vertical line indicates the in-phase TR ( $TR_{ip}$ )

where  $S(\cdot)$  is the acquired signal given the acquisition and tissue parameters. For a steady state acquisition,  $S$  is the spoiled gradient echo (SPGR) equation

$$S(\alpha, TR, T_{1,A}, PD_A) = \sin \alpha \cdot \frac{1 - e^{-TR/T_1}}{1 - e^{-TR/T_1} \cos \alpha}. \quad (5.26)$$

In the brain, the most relevant contrast is between white and gray matter, for which the  $T_1$  values can be found using the analytical expression described in Equation (5.14). The proton density is assumed to be fixed across field strengths; here  $PD_{WM} = 0.70$  and  $PD_{GM} = 0.81$  will be used [194].

Figure 5.3 shows the CNR scaled by  $B_0$  at four different field strengths, as a function of the TR and flip angle of the acquisition. The increase in  $T_1$  at higher field strength reduces the difference in signal between white matter (WM) and gray matter (GM) resulting in reduced CNR. Additionally, this figure also indicates the maximum readout time, i.e. TR, that can be used at each field strength while ensuring that the fat and water signal are in phase at the edge of k-space, i.e.  $TR < T_{ip}$ . At 0.5T this is 13.42ms compared to 0.96ms at 7T. The reduction in TR, corollary (2), further reduces the possible contrast at high field strengths.

To maintain a  $TR < T_{ip}$  across field strengths, the bandwidth has to be increased proportionally. With increased BW the maximum pulse width is reduced and consequently the flip angle, corollary (4). The achievable flip angle is a function of the maximum pulse width and the achievable peak  $B_1$ , the latter being a complex function of RF amplifier performance, transmit coil design, and SAR limitations. To enable some conclusions to be drawn, constant  $B_1$  amplitude across field strength is assumed here. Figure 5.4 shows



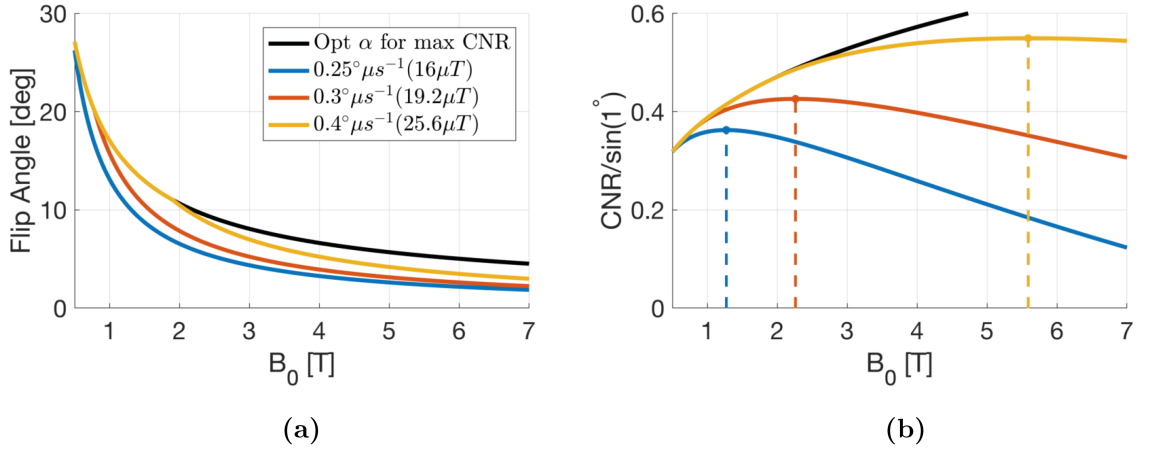


**Figure 5.4:** (a) Achievable flip angle for different RF amplifier specifications together with the flip angle for optimal CNR. (b) Maximum CNR as a function of field strength for the same RF amplifier specifications. Dashed vertical lines indicate field strength for the maximum CNR.

the achievable flip angle for maximum contrast for three different peak  $B_1$  levels, assuming  $TR = T_{ip}$  and  $T_1$  changing with field strength. The flip angle for optimal contrast (black line) decreases with  $B_0$  since the TR also decreases. At high field strengths, the optimal flip angle cannot be achieved and thus the maximum WM-GM contrast can not be achieved. The achievable flip angle directly affects the CNR shown in figure 5.4. With high  $B_1$  power, the CNR increase steadily with field strength but for low  $B_1$  power, the CNR reaches a maximum and then decrease with  $B_0$ , Figure 5.4. The reduction in CNR shows that the linear increase in SNR with field strength is not enough to compensate for the reduced signal difference between WM and GM as the maximum flip angle is reduced.

From figure 5.4 it is clear that the performance of the RF system strongly determines the maximum  $T_1$  contrast that can be achieved. Through scans carried out in this study (presented later), it was found that  $0.25^\circ \mu s^{-1}$  was feasible across field strengths (1.5, 3 and 7T), i.e. the blue line in figure 5.4. While high field scanners can produce higher peak  $B_1$ , at high flip angles the SAR limit can become an issue which was not included in this comparison. Furthermore, this is only a measure of CNR for  $T_1$  contrast using steady state RUFIS and there are other ways of producing  $T_1$  contrast at 7T, using for instance inversion or saturation pulses. The overall conclusion that can be drawn from this simplified analysis is that it is more difficult to produce strong  $T_1$  contrast at high field strengths with RUFIS, given the flip angle limitations imposed by the excitation profile.

### 5.2.9 Conclusion

Imaging at high field greatly improves the SNR but for most approaches it is associated with a slew of issues related to image acquisition, and RUFIS is no exception. There are a series of linked constraints which limit the acquisition parameters. In this section, these constraints were analysed theoretically to build a theory which experiments can be developed from.

To maintain acceptable image quality with low off-resonance effects, the BW has to be linearly increased with field strength, which reduces the maximum flip angle that can be achieved. While the SNR increases linearly with field strength, due to the simultaneous required change in other acquisition parameters (mainly reduced max flip angle), the maximum contrast between white and gray matter is reduced at higher field strength. Theoretically, the CNR will increase at higher field strength, but due to RF amplifier limitations, the CNR reaches a maximum which depends on the peak  $B_1$ . The results presented from this theoretical study shows that the  $T_1$  contrast with RUFIS is limited by the flip angle at higher field strength, while at low field strengths, optimal  $T_1$  contrast can be achieved.

The following in vivo study will follow and confirm some these theoretical results through VFA  $T_1$ -mapping at 1.5, 3, and 7T.

## 5.3 RUFIS $T_1$ Mapping at 1.5, 3, and 7T

### 5.3.1 Introduction

Translation of imaging techniques across field strength enables adoption in both clinical settings, commonly performed on lower field scanners, as well as cutting edge research using (ultra)-high field scanners. The previous section outlined some of the issues related to implementation of RUFIS at higher field strength. Following the successful implementation of RUFIS VFA  $T_1$  mapping at 3T, presented in chapter 4, the current study aimed to extend the method to both 1.5T and 7T, acquiring data at 1.5, 3, and 7T.

### Pilot Study

The most challenging part of this study was the translation of RUFIS to 7T, mainly due to the increased  $B_1$  and off-resonance effects. To investigate these issues, a small pilot study was conducted together with collaborators at University of California, San Francisco.

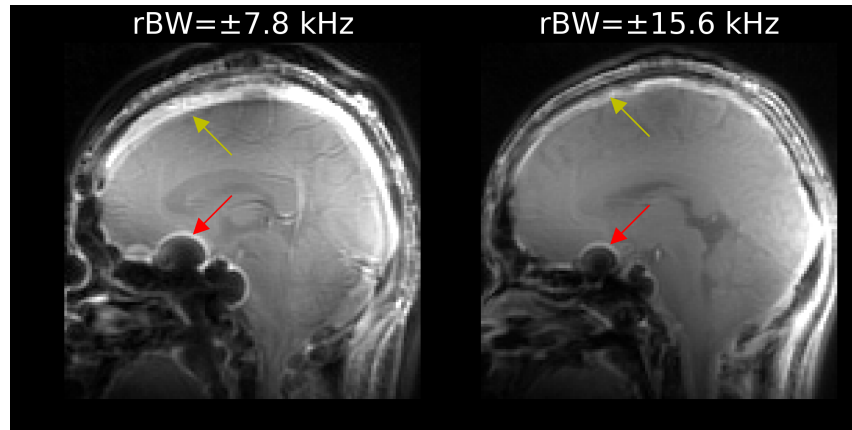


**Figure 5.5:** Comparison of steady state RUFIS data collected at 7T with  $\pm 7.8$  and  $\pm 15.6$  kHz readout bandwidth. Severe off-resonance artefacts are seen around the sinuses (red arrow) and chemical shift artefacts around the skull (yellow arrow).

From the 3T VFA  $T_1$  mapping study, it was found that a relatively low readout bandwidth ( $\pm 7.8$  kHz) was required to reach high enough flip angles for accurate  $T_1$ -mapping. Data were therefore collected on the 7T system with readout bandwidth  $\pm 7.8$  and  $\pm 15.6$  kHz to study, mainly, the off-resonance effects. The results of this study, shown in figure 5.5, clearly show that a readout bandwidth of  $\pm 7.8$  kHz is, as expected, not feasible at 7T. Doubling the readout bandwidth to  $\pm 15.6$  kHz clearly reduced the artefacts, but there are still some visible, shown by the red and yellow arrows. According to corollary (1), to achieve the same level of off-resonance artefacts at 7T as with  $\pm 7.8$  kHz bandwidth at 3T, a bandwidth of  $(7/3 \cdot 7) = \pm 18.2$  kHz is required, i.e. slightly higher than  $\pm 15.6$  kHz which was used here.

### Design of Main Study

Following the pilot study, a second study was undertaken, with a primary aim of performing VFA  $T_1$  mapping at 1.5, 3, and 7T using RUFIS and comparing the results to conventional SPGR. There are numerous options for designing a field strength comparison study such as this. One option, as in the theoretical study above, is to scale bandwidth with field strength to reduce the chemical shift to 1 voxel. This option was rejected for the current study, however, as it results in the maximum flip angle at 7T being at or below the Ernst angle. Taking normal  $B_1^+$  variation at 7T into account (50-150%) [195], the highest flip angle would be far below the Ernst angle, which would not allow reliable  $T_1$  maps to be produced. Instead, it was decided to acquire data at the same two bandwidths at each field

strength, which results in the same acquisition time for each scan, enabling comparison of the inherent SNR difference across field strengths. This choice also makes it easier to study changes in  $T_1$  across field strengths as the sampling scheme remains the same.

### 5.3.2 Methods

#### Scanners

This study was carried out on three different GE MRI scanners:

- 1.5T GE MR450w on software version DV26, at GE Research Centre, Stanford Research Institute, Menlo Park, CA, US. Body coil for transmission and GE 12 channel receive head coil.
- 3T GE MR750 on software version DV25, at King's College London, London, UK. Body coil for transmission and Nova Medical 32 channel receive head coil.
- 7T GE MR950 on software version 7T23, at University of California, San Francisco, CA, US. Combined head 2 channel transmit and 32 channel receive head coil, Nova Medical.

#### Pulse Sequence Development

The same base RUFIS sequence was used across all three scanners (initially developed at DV25) and only modified where necessary to comply with the requirements at each software level. This was done to ensure that any differences between scanners were due to field strength and not the pulse sequence code. For each scanner, the default ("product") SPGR sequence for the scanner's particular software level was used for the VFA comparison. These were all based on the same original sequence (efgre3d), and to our knowledge there were no major differences between software versions.

The RUFIS sequence was modified to acquire all flip angles sequentially by reading in the flip angle scaling factors from a text file stored on the scanner. This allowed all data to be collected following a single prescan, and avoided potential changes in transmit and/or receive settings between flip angles. Multiple flip angles were acquired manually with SPGR by performing a manual prescan for the first image (highest flip angle), and then changing the variable within the pulse sequence which directly controls the scaling of the amplitude of the excitation RF pulse for subsequent acquisitions, keeping the same prescan settings (and thus again avoiding changes to transmit and/or receive settings).

## An Optimal Set of Flip Angles

An integral part of the design of a VFA experiment is the choice of flip angles, which depends on the TR of the acquisition and the  $T_1$  for which the acquisition is optimised. An optimum acquisition protocol is a pair of flip angles, one on each side of the Ernst angle, which result in images of the same intensity (ideally equal to  $\sqrt{2}$  of the intensity at the Ernst angle) [149]. The two point measurement has some limitations though: (1) it is only optimised for a single  $T_1$ , (2) it is not possible to estimate the quality of the fit since there is always a perfect fit with only two data points, and (3) with large  $B_1^+$  variation the actual flip angles may be far from the optimal pair at some positions within the imaging volume. Therefore, in this study a measurement protocol with five points was chosen, spanning the available range of flip angles.

In this study, RUFIS acquisitions were performed with  $\pm 15.6$  and  $\pm 31.2$  kHz readout bandwidths. Initial piloting showed that the RF amplifiers in all the scanners could generate  $0.25^\circ/\mu s$ , which resulted in maximum flip angles of  $8^\circ$  at  $\pm 15.6$  kHz and  $4^\circ$  at  $\pm 31.2$  kHz. At 7T, the minimum flip angle was set to  $0.5^\circ$  to achieve sufficiently low flip angle in areas where the  $B_1^+$  efficiency  $> 1$ . At 1.5T and 3T, the minimum flip angle was set to  $1^\circ$  as the  $B_1^+$  errors are less extreme at lower field strengths.

Given the minimum and maximum flip angles  $(\alpha_{min}, \alpha_{max})$  there are several methods for determining the 3 intermediate flip angles in the 5 flip angle protocol; here, the method presented by Helms et al. was used [148]. The SPGR equation, normally written as

$$M(\alpha) = \sin \alpha \cdot \rho \frac{1 - E_1}{1 - E_1 \cos \alpha} \quad E_1 = e^{-TR/T_1} \quad (5.27)$$

can be rewritten with two substitutions<sup>2</sup>

$$\tau = 2 \cdot \tan \alpha / 2 \approx \alpha \quad \text{if } \alpha \text{ is small} \quad (5.28)$$

$$\phi = 2 \frac{1 - E_1}{1 + E_1} = 2 \cdot \tan(R_1 \cdot TR/2) \quad (5.29)$$

which transforms the SPGR equation into a lower order polynomial as

$$S(\tau) = \rho \cdot \frac{\tau}{1 + \tau^2/(2\phi)}. \quad (5.30)$$

---

<sup>2</sup>Helms et al. use  $\rho_1$  instead of  $\phi$ , the substitution was made here to avoid confusion with  $\rho$  being used to refer to proton density.

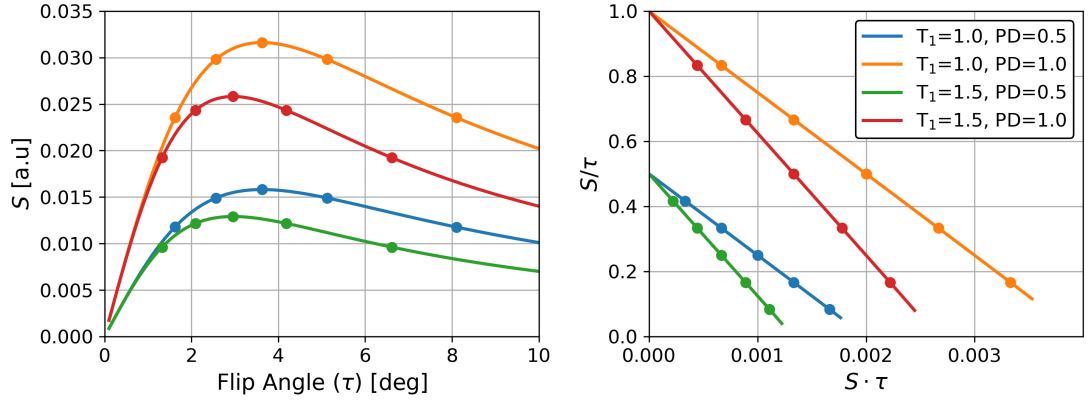


**Figure 5.6:** Comparison of the standard and linearised version of the SPGR equation, as proposed by Helms et al. [148], with an example 5 point sampling scheme. (Curves simulated with  $TR=2$  ms and  $T_1=1$  s)

To visualise this linearised version of the SPGR equation,  $X = S \cdot \tau, Y = S/\tau$  can be plotted, as shown in figure 5.6. The linearised SPGR equation has several other elegant features. Firstly, the Ernst angle is given by

$$\tau_E = \alpha_E = \sqrt{2\phi}. \quad (5.31)$$

Secondly, an optimal flip angle scheme with  $n$  points, centred around the Ernst angle can be calculated by

$$\tau_i = \alpha_i = \sqrt{\frac{n+1-i}{i}} \cdot \tau_E. \quad (5.32)$$

Figure 5.6 shows an example 5 point flip angle scheme calculated using (5.32), clearly demonstrating that the flip angles are equally spaced along the *linearised* SPGR curve, but not when plotted in the conventional form. Additionally, the middle flip angle is the Ernst angle and the four others are on equal signal level on either side of the Ernst angle. The motivation for distributing the flip angles evenly on the linearised version of the SPGR equation is to improve the fit by balancing the SNR in the data; points on equal signal level, on different sides of the Ernst angle will have the same SNR. The 5 point sampling scheme therefore consists of 5 points with pairs of images having the same signal intensity.

With RUFIS, there are restrictions on the minimum and maximum flip angles, and the optimal sampling scheme might not be feasible. Equation (5.32) can be modified to include the RUFIS flip angle constraints. Given the minimum flip angle  $\tau_0$  and the maximum  $N^{th}$  flip angle  $\tau_N$ , a flip angle distribution for  $N$  points, evenly distributed on the linearised

SPGR equation, is given by

$$\tau_i = \tau_E \sqrt{\frac{1 - y(\tau_0) + i \cdot \Delta y}{y(\tau_0) - i \cdot \Delta y}} \quad (5.33)$$

$$y(\tau) = S(\tau)/\tau \rightarrow \Delta y = \frac{y_0 - y_N}{N - 1} \quad (5.34)$$

where  $y_0 = S(\tau_0)/\tau_0$ . See appendix C for full derivation.

In the present study where RUFIS is compared to SPGR for VFA  $T_1$  mapping, an equivalent sampling scheme for each sequence is required to produce comparable acquisitions. Since the TR is different between the two scans, the same flip angle scheme cannot be used, as it would result in a different distribution of sampling points over the SPGR curve. To produce an equivalent flip angle scheme between RUFIS and SPGR, the RUFIS flip angles were scaled by the ratio of the Ernst angle for RUFIS and SPGR.

$$FA_{SPGR} = FA_{RUFIS} \cdot \frac{\alpha_{E,SPGR}}{\alpha_{E,RUFIS}} \quad (5.35)$$

### Scan protocol

A single healthy volunteer was scanned on each scanner, after giving written consent under the relevant local ethical approval procedures. In each scan session, VFA data were collected with RUFIS and SPGR using the respective 5 flip angle protocols. The flip angles for RUFIS were calculated using equation (5.33) given the TR of the acquisition at each field strength (outlined below) and  $T_1$  values of: 1.5T=875 ms, 3T=1000 ms, 7T=1500 ms, corresponding to  $T_1$  values intermediate to those of WM and GM [14, 49]. The SPGR flip angles were then calculated through scaling by the Ernst angle, as shown in (5.35). As described above, for RUFIS, the flip angles were changed dynamically in the acquisition by repeating the acquisition 5 times and automatically scaling the instruction amplitude of the excitation RF pulse. With SPGR, the acquisition was repeated 5 times and the instruction amplitude of the excitation RF pulse was manually changed by the operator.

The field of view was fixed to  $192 \times 192 \times 192 \text{ mm}^3$  and resolution  $1.5 \times 1.5 \times 1.5 \text{ mm}^3$ , resulting in a matrix size of  $128 \times 128 \times 128$ . RUFIS data were acquired with two fold radial oversampling, resulting in a full field of view of  $384 \times 384 \times 384 \text{ mm}^3$ . At 1.5T, data were collected at  $\pm 15.6 \text{ kHz}$  readout bandwidth resulting in a TR for RUFIS and SPGR of 2.4/6.9ms respectively, with TE in SPGR of TE=2.8ms. The same parameters were

used at 3T, with only a change in the SPGR TR, to TR=6.7ms. At 7T, the  $\pm 15.6$  kHz RUFIS acquisitions used the same TR as at 3T, while the SPGR acquisition had TE/TR of 1.78/5.8 ms. An additional acquisition with bandwidth 31.2 kHz was also acquired at 7T, resulting in RUFIS and SPGR TR of 1.3/4.6ms respectively and SPGR TE=1.8ms. Since the SPGR sequence only accepts integer values for the flip angle, the maximum flip angle was set to  $13^\circ$  and  $8^\circ$  for the  $\pm 15.6$  and  $\pm 31.2$ kHz bandwidths respectively. The SPGR flip angle schemes were rescaled to these maximum flip angles (which are very close to the calculated ones), resulting in a small change ( $<1^\circ$ ) to the final flip angles. The  $T_1$ -analysis was performed using the actual flip angles used during data acquisition.

When the bandwidth was increased in the RUFIS acquisitions at 7T, twice the number of spokes were acquired in order to balance the SNR. Due to limitations in the number of NEX available with SPGR, however, 1 NEX data were acquired at both  $\pm 15.6$  and  $\pm 31.2$ kHz. The acquisition time was 1:50 min per flip angle for SPGR  $\pm 15.6$ kHz and 1:16 min for SPGR  $\pm 31.2$ kHz, equivalent to 1 NEX. For RUFIS the acquisition time was 1:05 and 1:12.

At 3T, a high resolution inversion recovery prepared SPGR (IR-SPGR/BRAVO) was also acquired for tissue segmentation (TE/TR/TI=3/7/400 ms, FOV= $270 \times 270 \times 240$  mm<sup>3</sup>, slice thickness=1.2mm, in-plane voxel size= $1.05 \times 1.05$  mm<sup>2</sup>, FA= $11^\circ$ , BW= $\pm 31.25$  kHz, and ASSET=1.75).

At 1.5T, due to time restrictions, only four flip angles could be acquired, for both RUFIS and SPGR data. A five flip angle scheme was calculated in the same way as at the other field strengths, but data from the middle flip angle of the five were not collected. (This point was chosen as it contains the least amount of  $T_1$  information).

$B_1^+$  mapping was performed at 3T and 7T, using the Bloch-Siegert method [157]. At 1.5T the  $B_1^+$ -inhomogeneity can be considered negligible and  $B_1^+$ -mapping is not required [59]. The SIMBA  $B_1^+$  mapping method presented in chapter 4 was not used in this study, partly due to time constraints but also to isolate potential differences between results to the VFA acquisition itself, avoiding additional confounds due to any implementation effects in the  $B_1^+$  mapping method used.

## Image Reconstruction

RUFIS data were reconstructed offline in MATLAB using Kaiser-Bessel gridding with density compensation and radial Fermi filtering. Reconstructed images from each coil



were combined with sum-of-squares combination and the combined image was cropped to the nominal field of view (FOV). The  $\pm 15.6\text{kHz}$  data from 1.5T was also reconstructed using the full FOV to demonstrate the potential for large FOV  $T_1$  mapping. Using the full FOV, it was not possible to apply the manufacturers gradient non-linearity correction. SPGR data were reconstructed online on the scanner.

### Image Processing

VFA data were motion corrected using mcFLIRT in FSL [196]. For the 3T and 7T data, the  $B_1^+$  maps were transformed to the space of the VFA data using a linear registration implemented in ANTs [171] and fitted to a 6<sup>th</sup> order polynomial to reduce noise in the  $B_1^+$  map [174], based on the assumption that  $B_1$  is smoothly varying [154]. For the RUFIS acquisition, the radial excitation profile was simulated and used in the fitting as an additional  $B_1^+$  correction, at all field strengths. The quantitative  $T_1$  and proton density (PD) maps were calculated using a linear fit implemented in QUIT [174]. From the  $T_1$  fit, the residuals were calculated as the root mean square error (RMSE) across all flip angles. Since the RMSE is proportional to the magnitude of the signal (i.e. the PD) the RMSE was divided by PD to obtain a metric that was quantitatively comparable between acquisitions and field strengths.

The BRAVO data, acquired at 3T, were processed using the **recon-all** pipeline in FreeSurfer to obtain an accurate brain mask and subcortical tissue masks (the **aseg** output) [172]. The VFA images acquired at each field strength were registered to the 3T BRAVO image using an affine registration, and tissue masks were subsequently transformed using the inverse transformation with multilabel interpolation.

### 5.3.3 Results

#### Qualitative Cross Field Comparison

Results from the 1.5T acquisition are shown in figure 5.7. Visually, the  $T_1$  maps from RUFIS and SPGR appear very similar, with slightly less WM to GM contrast in the RUFIS data. On the sagittal slice it is clear how the ZTE readout in RUFIS increases sensitivity to short  $T_2$  species, such as the cortical bone which shows a measurable  $T_1$  and higher PD than SPGR (pink arrows in 5.7). Another bone that is visible with RUFIS is the clivus, indicated by yellow arrows in fig 5.7. From the PD maps, it can be seen that there is much less contrast between tissue and CSF in RUFIS than SPGR. In the sagittal

view, there is almost no contrast around the cerebellum with RUFIS, while there is a clear difference in the SPGR image. The residuals in the  $T_1$  fit from RUFIS and SPGR both show a uniform noise distribution within the brain, indicating that the data fit the  $T_1$  model well in all brain tissues. However, the residuals were slightly higher with RUFIS than SPGR. This could be due to higher SNR in the SPGR acquisition from using higher flip angles. Although difficult to see in figure 5.7, the SPGR  $T_1$  maps are slightly sharper than RUFIS, which could be a result of the difference in k-space sampling density between Cartesian and radial sampling.

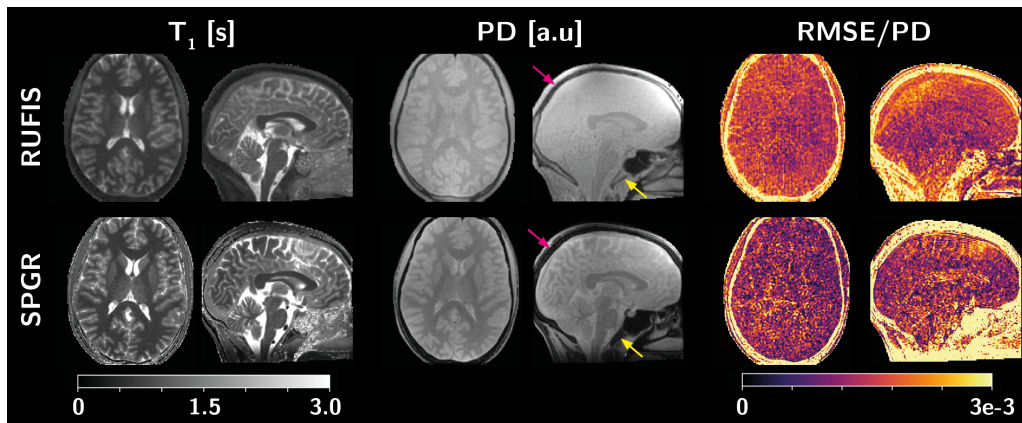


**Figure 5.7:** Quantitative maps from the 1.5T experiment, comparing the results from RUFIS and SPGR. Arrows indicate regions with short  $T_2$  species where a good fit was obtained with RUFIS but not SPGR (pink: cortical bone, yellow: the clivus)

The results obtained at 3T, shown in figure 5.8, shows similar patterns to the results from 1.5T, with  $T_1$  and PD maps appearing similar between RUFIS and SPGR. Again, the main difference between the two sequences is the signal from short  $T_2$  species, such as bone. In the PD maps, the CSF contrast is lower with RUFIS than SPGR. However the fit residuals show clear tissue contrast for both SPGR and RUFIS, suggesting that there are additional parameters which need to be included in the signal model. With RUFIS, the residuals are higher in CSF than in tissue, while with SPGR the opposite is true. Furthermore, compared to 1.5T, the PD maps at 3T shows signs of stronger  $B_1^-$  effects around the skull.

At 7T, two  $T_1$  experiments were performed, with  $\pm 15.6$  and  $\pm 31.2$  kHz readout bandwidths respectively. The results, presented in figure 5.9 in axial slices and 5.10 in sagittal slices, show very similar  $T_1$  and proton density maps at both readout bandwidths, for both RUFIS and SPGR. The quantitative maps have been brain masked, since at 7T the

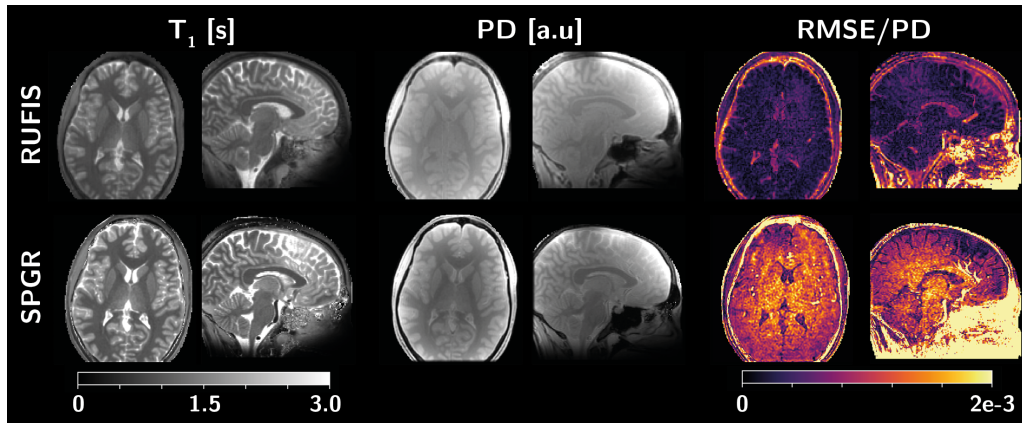


**Figure 5.8:** Quantitative maps from the 3T experiment, comparing the results from RUFIS and SPGR.

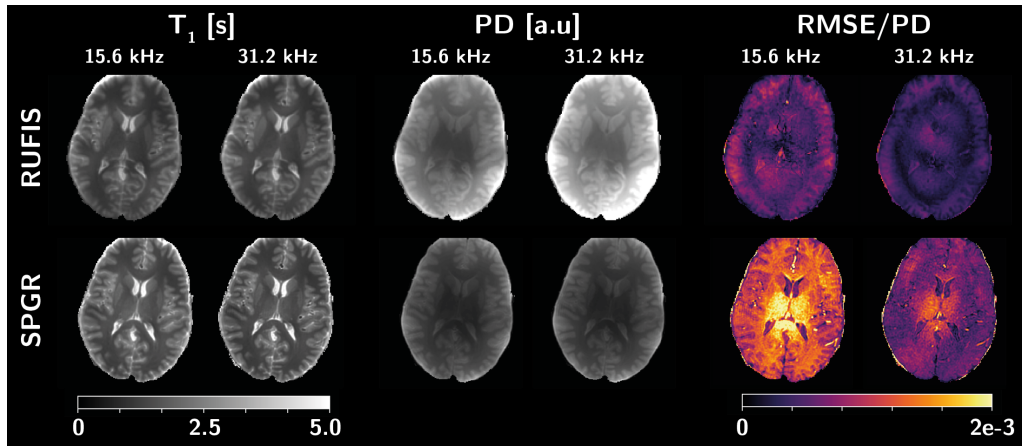


**Figure 5.9:** Quantitative maps in axial slices from the 7T experiment, comparing the results from RUFIS and SPGR at both  $\pm 15.6$  and  $\pm 31.2$  kHz readout bandwidths.

$B_1^+$  map did not provide an accurate  $B_1^+$  correction outside the brain, resulting in large fit errors. For both RUFIS and SPGR, the fit residuals were lower at higher bandwidth. Compared to the 1.5 and 3T data, there is a clear spatial pattern in the RUFIS residuals, and potentially a similar but smaller pattern in the SPGR data, indicating another effect. The pattern resembles the  $B_1^+$  field, and thus the flip angle variation across the brain. The ring in the RUFIS data with the lowest residuals could be where the nominal flip angle is achieved (discussed more later), and thus the model fit is optimal. However, variation in the flip angle should result in a direct scaling of the  $T_1$  values. It is also not clear why the effect would be different between RUFIS and SPGR. Additionally, the PD maps here also show stronger effects of  $B_1^-$  as expected at high field strengths.

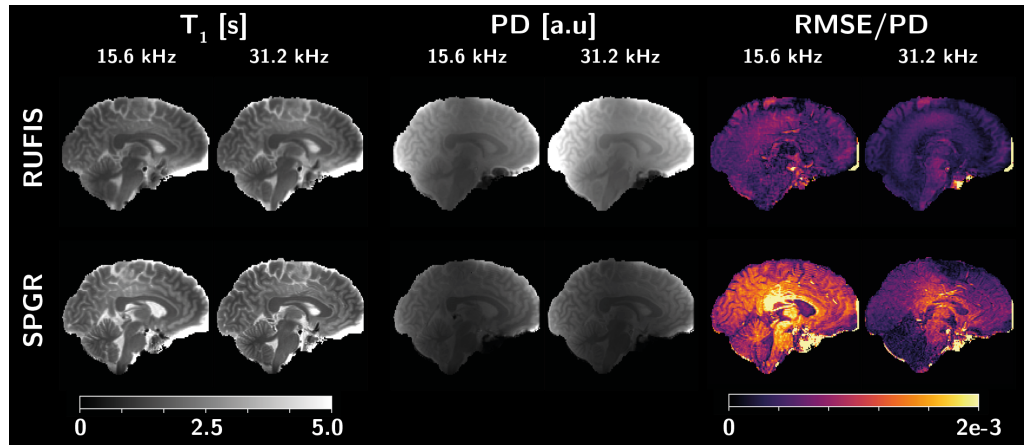


**Figure 5.10:** Quantitative maps in sagittal slices from the 7T experiment, comparing the results from RUFIS and SPGR at both  $\pm 15.6$  and  $\pm 31.2$  kHz readout bandwidths.

### Quantitative Cross Field comparison

Using the whole brain white and gray matter masks from the FreeSurfer segmentation,  $T_1$  histograms were calculated for RUFIS and SPGR across the three field strengths, figure 5.11. Comparing RUFIS and SPGR across field strengths showed an increasing in the difference between the sequences at higher field strength, although this difference was reduced when the bandwidth was increased at 7T. There was also a clear broadening in the  $T_1$  histograms for both sequences with higher field strength.

Comparing  $T_1$  histograms across field strengths for each sequence showed a clear increase in  $T_1$  with field strength for both RUFIS and SPGR (figure 5.12), as predicted by the theory. At 7T, increasing the bandwidth resulted in increased  $T_1$  for RUFIS but decreased  $T_1$  with SPGR.

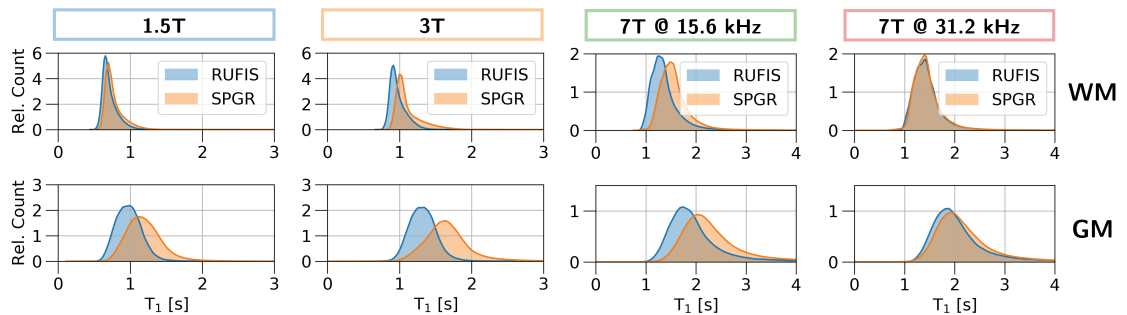


**Figure 5.11:** Comparison of  $T_1$  histograms between RUFIS and SPGR across field strengths.

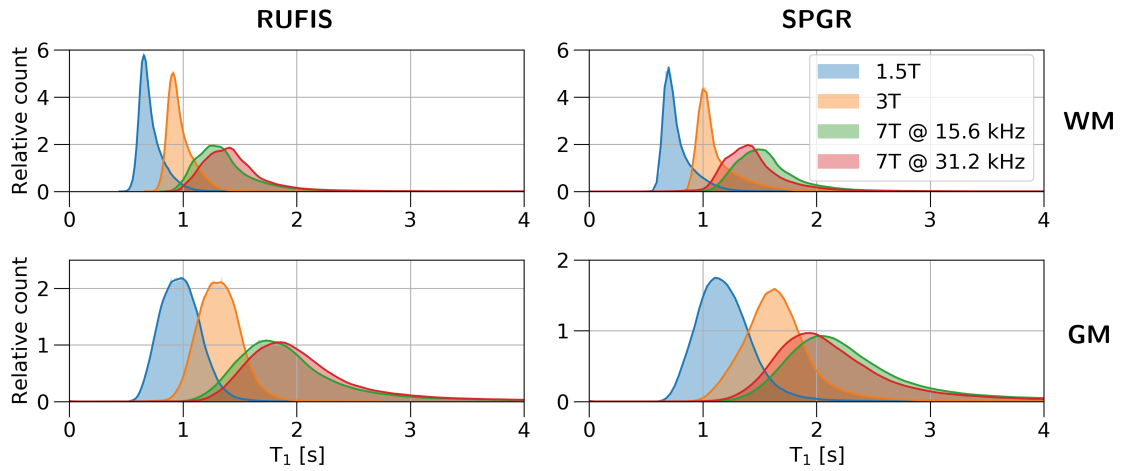


**Figure 5.12:** Comparison of  $T_1$  histograms across field strengths for RUFIS and SPGR in white matter (top) and gray matter (bottom).

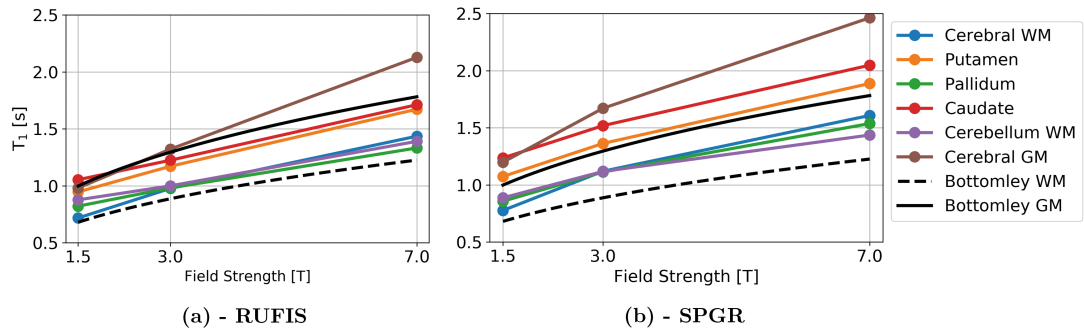


**Figure 5.13:** Change in  $T_1$  with field strength for within isolated ROIs for (a) RUFIS and (b) SPGR. 7T data point is the 15.6 kHz data.

Studying  $T_1$  values from individual ROIs (figure 5.13) showed similar patterns between RUFIS and SPGR. For all ROIs, there was a clear increase in  $T_1$  between 1.5T and 3T and again between 3T and 7T. The measured  $T_1$  values followed the pattern of predicted change in  $T_1$  described by the model of Bottomley et al., however SPGR produced higher  $T_1$  than the theoretical model in both WM and GM, while RUFIS produced higher  $T_1$  in WM but lower in GM [191].  $T_1$  values obtain at the three different field strengths in the present are similar to those obtain in previous studies, as shown in table 5.2.

Histograms of the fit residuals (RMSE) from cerebral white matter, shown in figure 5.14, display distinct differences in patterns between RUFIS and SPGR. With RUFIS, the RMSE was lowest at 3T and highest at 1.5T. High RMSE at low field is indicative of low SNR, as expected. With higher field strength, the SNR increases and the residuals decrease. Higher RMSE at 7T compared to 3T could indicate that the model does not fit

**Table 5.2:**  $T_1$  values in white matter (WM) and (GM) obtained from the current study and compared to previous studies. (Abbreviations, LL: Look-Locker, IR: Inversion Recovery)

Sequence	$B_0$ [T]	WM	GM	Ref.
RUFIS	1.5	$0.72 \pm 0.01$	$0.98 \pm 0.02$	This study
SPGR	1.5	$0.78 \pm 0.01$	$1.12 \pm 0.01$	This study
LL	1.5	$0.656 \pm 0.16$	$1.188 \pm 0.069$	Rooney et al. [14]
MPRAGE	1.5	$0.650 \pm 30$	$1.197 \pm 0.135$	Wright et al. [30]
IR	1.5	$0.884 \pm 0.05$	$1.124 \pm 0.05$	Stanisz et al. [34]
RUFIS	3	$0.98 \pm 0.02$	$1.32 \pm 0.01$	This study
SPGR	3	$1.119 \pm 0.002$	$1.670 \pm 0.004$	This study
MPRAGE	3	$0.840 \pm 0.05$	$1.607 \pm 0.112$	Wright et al. [30]
IR	3	$1.084 \pm 0.045$	$1.820 \pm 0.045$	Stanisz et al. [34]
RUFIS	7	$1.44 \pm 0.05$	$2.13 \pm 0.08$	This study
SPGR	7	$1.61 \pm 0.04$	$2.46 \pm 0.06$	This study
LL	7	$1.22 \pm 0.036$	$2.132 \pm 0.103$	Rooney et al. [14]
MPRAGE	7	$1.130 \pm 0.100$	$1.939 \pm 0.150$	Wright et al. [30]
SPGR	7	$1.256 \pm 0.089$	$1.867 \pm 0.164$	Olsson et al. [197]
IR-EPI	7	$1.253 \pm 0.082$	$1.928 \pm 0.158$	Olsson et al. [197]

the data well, i.e. that there are other factors affecting the measurement besides  $T_1$ . For SPGR, however, the central peak of the RMSE plots overlap for 1.5T, 3T and the 15.6 kHz acquisition at 7T.

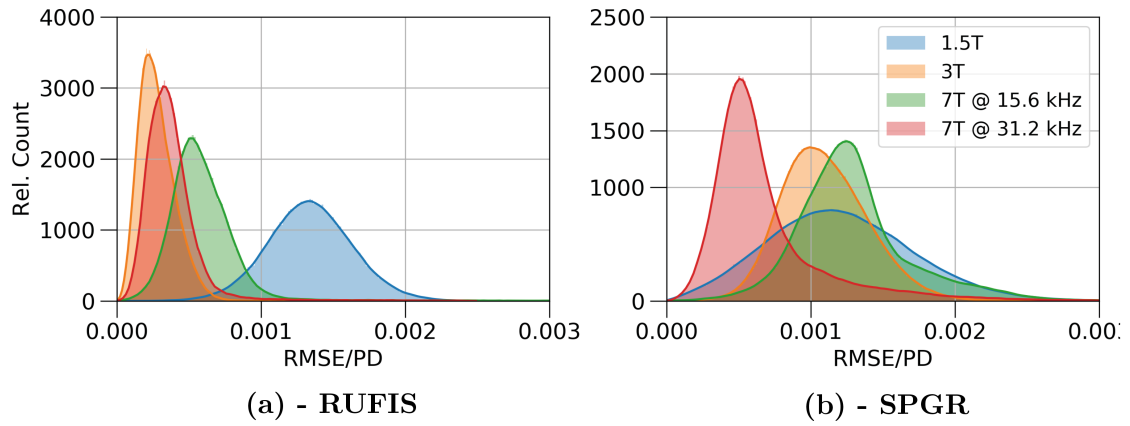


**Figure 5.14:** Comparison of residual histograms across field strengths for **(a)** RUFIS and **(b)** SPGR calculated within the cerebral WM mask.

### **B<sub>1</sub> and Off-Resonance Artefacts**

Higher field strength results in larger off-resonance artefacts, as shown in figure 5.15, where off-resonance artefacts appear stronger around the sinues at 7T than 1.5T. Similarly, B<sub>1</sub> inhomogeneity increases with field strength, both on the transmit and receive side. Maps of the B<sub>1</sub><sup>+</sup> field acquired at 3T and 7T (figure 5.16a) show substantially larger B<sub>1</sub><sup>+</sup> variation at 7T compared to 3T. At 7T, the effective flip angle is between 50% to 150% of the prescribed. For the  $\pm 15\text{kHz}$  RUFIS acquisition, this means that the lowest flip angle varied between 0.25° and 1.5°, while the highest flip angle varied between 4° and 12°. This should be compared to the Ernst angle which, at the given TR=2.4ms and T<sub>1</sub> measured in WM at 7T T<sub>1</sub>=1.44s, was  $\alpha_E = 3.3^\circ$ , i.e. the range of flip angles covered both sides of the Ernst angle.

The B<sub>1</sub><sup>-</sup> field is also more inhomogeneous at 7T, as seen in the low flip angle images at each field strength, figure 5.16b. The two fields produce a compound effect in the images, but since two different coils are used for transmit (2 channel) and receive (32 channels), the effect of the two can be seen separately in some regions of the data. This is especially evident around the skull, where areas close to coil elements are brighter than other areas (figure 5.16b).



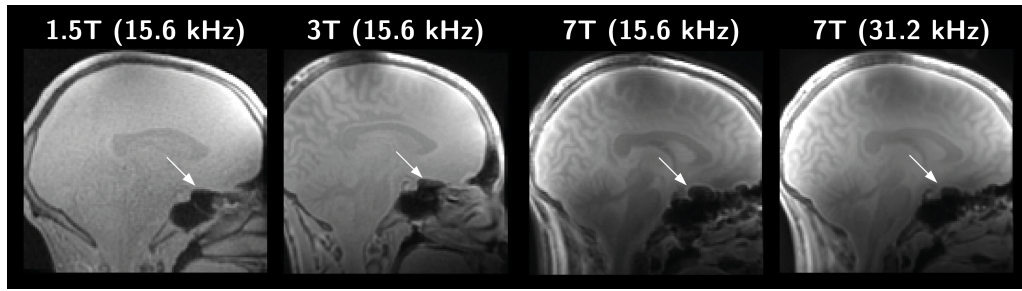


**Figure 5.15:** Off resonance effects with increasing bandwidth seen around the sinuses (white arrow) on the raw low flip angle images at each field strength. By doubling the bandwidth at 7T to 31.2 kHz, the artefact is reduced.

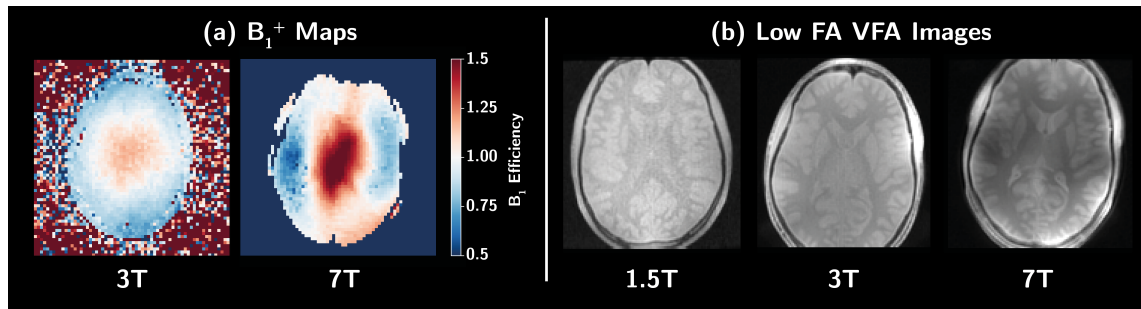


**Figure 5.16:**  $B_1$  inhomogeneity increase at higher field strength, both on the transmit and receive side. (a)  $B_1^+$  maps acquired at 3T and 7T, showing substantially higher  $B_1^+$  variation at 7T. (b) Low flip angle RUFIS images at all three field strengths showing the compound effect of  $B_1^+$  and  $B_1^-$ . The effect of  $B_1^-$  is most clearly seen around the skull where there are localised areas of higher signal, which are strong at 7T but almost non-existent at 1.5T.

### 5.3.4 Discussion

#### $T_1$ Across Field Strengths

This study demonstrated that RUFIS VFA  $T_1$  mapping can be successfully implemented across field strengths (1.5, 3, and 7T), making it the first cross field strength study using RUFIS. Qualitatively,  $T_1$  maps from RUFIS were of similar quality to those from SPGR at all field strengths. Quantitatively, the  $T_1$  histogram results were similar to those in the  $T_1$  mapping study presented in chapter 4, with lower  $T_1$  in GM with RUFIS compared to SPGR. The results from this study agree with the literature showing increase in  $T_1$  with field strength, table 5.2 [191, 192, 14, 30]. In figure 5.13,  $T_1$  values from this study are compared to the model presented by Bottomley et al., showing a very similar pattern in the increase of  $T_1$ , but with global offsets [191]. In the study by Rooney et al., the width of whole brain  $T_1$  histograms were shown to increase at higher field strength, which was also observed in the current study, see figure 5.12. These results align with the



theoretical model for  $T_1$  presented in this chapter, which shows larger difference in  $T_1$  with field strength, figure 5.2a.

The  $T_1$  values measured with RUFIS and SPGR increased across field strengths as expected, but there were clear differences between the techniques. One potential cause of this is magnetisation transfer (MT) effects, which are driven by RF irradiation, and are therefore proportional to the  $B_1^+$  field. In this study, the peak  $B_1$  was kept approximately constant across field strengths, i.e. the same pulse width was used to obtain the same flip angles. The saturation of the bound pool would thus be equivalent across field strengths, and with all other parameters constant, the MT effect would not change. However,  $T_1$  of both the free and bound pool change with field strength, as shown in the theory section, which will affect the MT effect [198]. Duvvuri et al. observed a 26% change in MTR between 1.5T and 4T, believed to be driven mainly by changes in  $T_1$ , although this was not proved in the study [199]. The difference in  $T_1$  across field strengths in this study is mainly observed in WM, which has a much higher macromolecular content than GM, and thus expected to produce a stronger MT effect. A recent study by Teixeira et al. found that quantitative  $T_1$  estimates obtained with SPGR VFA were decreased with increasing  $B_1^+$  as a result of MT effects [69]. Further work is needed to investigate these effects more fully.

Another effect that can drive differences in  $T_1$  is insufficient spoiling. In a study by Olsson et al., where VFA  $T_1$  mapping was performed at 7T, spoiling errors were observed for the highest flip angles in areas with  $B_1^+$  efficiency  $>1$  [197]. Insufficient spoiling could thus potentially contribute to the spatial profile of the residual maps at 7T which resembles the patterns of the  $B_1^+$  map. At 3T, there is a similar pattern in the SPGR residuals, although not as strong. At 1.5T the residuals appear as uniform noise for both RUFIS and SPGR, indicating that neither spoiling nor MT effects are resulting in poor fit to the signal equation.

In chapter 4, where  $T_1$  mapping using VFA was compared between RUFIS and SPGR at 3T, the two techniques showed good agreement in WM but the RUFIS  $T_1$  estimates were lower in GM. In this study, the  $T_1$  estimates from RUFIS were consistently lower than SPGR, although at 3T, the difference in  $T_1$  was larger in GM than in WM. The discrepancy to the results in chapter 4 could have multiple explanations. First, looking at the data from 1.5T, the correspondence between RUFIS and SPGR was good in WM, but with lower  $T_1$  from RUFIS in GM, similar to chapter 4. At 1.5T, variations in the

$B_1^+$  field are assumed to be negligible and thus no correction was made. At 3T, where the same  $B_1^+$  correction was applied to both techniques, a longer  $T_1$  was measured in WM with SPGR, suggesting that the differences could be driven by  $B_1^+$ . The same pattern was observed at 7T. Additionally, as discussed previously, potential MT effects are stronger in WM than GM, and thus if MT effects are more dominant in RUFIS from higher peak  $B_1$  and shorter TR, this would lead to decrease in  $T_1$  as observed here. Furthermore, the RUFIS and SPGR protocols used in this study at 3T are not the same as those used in chapter 4 (different TR and flip angles), which is known to produce different  $T_1$  values [69]. In conclusion, it is likely that the difference between RUFIS and SPGR in this chapter, and the difference to the results in chapter 4, are driven by a combination of  $B_1^+$  and MT effects.

### **Change in $T_1$ with Bandwidth at 7T**

Increasing the readout bandwidth at 7T changed the  $T_1$  values for both RUFIS and SPGR, but in opposite directions, resulting in almost perfect agreement between the two sequences. The exact cause of this apparent change in  $T_1$  with bandwidth is not fully understood but again, this could be due to MT or spoiling effects effects. When the bandwidth was changed in the 7T experiment, both the bandwidth and flip angles were changed. Changing in flip angles will change the RMS of the  $B_1^+$ , thus affecting the MT effect, and changing the TR will reduce the  $T_1$  recovery of bound pool, which again will affect the MT effect. Again, further work is needed in order to fully understand the effects of MT in VFA RUFIS.

### **$B_1$ Inhomogeneity**

Translation of MRI techniques across field strengths require adjustments of acquisition parameters because of changes in the imaging environment at each field strength, including  $B_1$  inhomogeneity, off-resonance effects and change in relaxation times. For VFA  $T_1$  mapping, the increased  $B_1$  inhomogeneity at high field is a major issue that has to be accounted for. At 1.5 and 3T it is common to perform a two point measurement as this results in optimal noise propagation into the  $T_1$  estimates [149]. With large  $B_1^+$  inhomogeneity however, the actual flip angles across the brain will deviate from the optimal scheme. In this study, this was addressed at 7T by acquiring 5 flip angles from 0.5 up to the maximum permissible flip angle given the readout bandwidth, in an attempt to achieve near optimal sampling across the whole brain, or at least flip angles on both sides of the Ernst angle. Olsson

et al. took an alternative approach where they mapped the Ernst angle across the brain, estimated the median Ernst angle, and calculated the optimal pair of flip angles based on this estimate [197]. They did however reduce the high flip angle from  $23^\circ$  to  $16^\circ$  to reduce effects of incomplete spoiling.

The pattern in the  $B_1^+$  map in figure 5.16a is similar to the pattern in the residuals observed in the 7T RUFIS data, suggesting that the quality of the fit depends on the flip angle. The scheme that was derived for the acquisition was based on 5 flip angles distributed around the Ernst angle. In areas where the flip angle is higher than prescribed, the lowest actual flip angle is much closer to the Ernst angle, thus reducing the dynamic range of the measurement and leading to a poorer  $T_1$  fit. Similarly, in areas with flip angles lower than prescribed, the highest flip angle will approach the Ernst angle and again the dynamic range of the measurement is reduced, leading to a poorer fit of the data.

$B_1$  inhomogeneity is not only an issue in terms of optimising acquisition parameters, it also requires accurate mapping of the  $B_1^+$  field for the  $T_1$  estimation, which can be difficult at high field. In the current study, the Bloch-Siegert method was used for  $B_1^+$  mapping [157]. Signal drop-out was observed in the temporal lobes, however, which resulted in poorly quantified  $B_1^+$ , which propagated into the  $T_1$  and PD maps. Further work will implement the SIMBA technique at 7T.

## SAR

At 7T, SAR is one of the main issues [200] and this was also noticed in the current study. For both sequences, the SAR was not an issue at neither 1.5 nor 3T. However, at 7T, the flip angles had to be interleaved (high-low-high-low) in order to avoid reaching the SAR limit with both RUFIS and SPGR. High resolution VFA acquisition, with long acquisition times, could therefore be difficult with RUFIS or SPGR at 7T due to SAR restrictions.

### 5.3.5 Conclusion

The VFA method is a highly efficient method for  $T_1$  mapping, with minimal deadtime in the acquisition [59]. The technique is well suited for low field imaging, but at higher field strengths ( $>1.5T$ ), the  $B_1^+$  inhomogeneity needs to be measured using a separate sequence, as has been shown here. Incorporating such  $B_1^+$  maps into the  $T_1$  fitting process can, however, produce uniform  $T_1$  maps across field strengths, as demonstrated here.

In summary, in the current study we have shown that RUFIS can be used for quantitative  $T_1$  mapping at 1.5, 3, and 7T, and that the quantitative values follow theoretical predictions of increased  $T_1$  with field strength.

## 5.4 Chapter Discussion and Conclusion

In this chapter, the utility of RUFIS for VFA  $T_1$  mapping across field strengths have been demonstrated, building on the results at 3T in chapter 4. The unique constraints on RUFIS for VFA  $T_1$  mapping related to the readout bandwidth was here shown to also have an indirect field strength dependency. Common features of low and high field imaging such as  $B_1$  inhomogeneity and chemical shift artefacts apply to RUFIS in the same way as other sequences. The main difference with RUFIS, as discussed in previous chapters, is the relation between bandwidth and flip angles. To reduce off-resonance effects at high field, the readout bandwidth must be increased proportional to the change in field strength. Since the bandwidth of the excitation pulse has to encompass the readout bandwidth, this introduces a unique field strength constraint on the excitation flip angle with RUFIS. This constraint results in lower maximum flip angles at high field, and thus a less optimal  $T_1$  mapping sampling scheme.

The RUFIS acquisition presents unique advantages and disadvantages at each field strength which do not exist in Cartesian SPGR. At high field strength, the flip angle in RUFIS is limited by both SAR and bandwidth constraints. Therefore, RUFIS might not be optimal choice for  $T_1$  mapping with the VFA method at 7T. These issues are further exacerbated by severe  $B_1^+$  inhomogeneity. Magnetisation preparation methods such as MP2RAGE might therefore be a better choice for  $T_1$  mapping at 7T [49, 201]. In collaboration with my colleague Tobias Wood, I have previously shown an implementation of the MP2RAGE formalism with a RUFIS readout with successful results at 3T [202]. Symms et al. have shown results at 7T, also using the MP2RAGE formalism with RUFIS, but using two separate acquisition, with images showing excellent white and gray matter contrast [203]. At low field strengths on the other hand, the flip angle constraints with RUFIS are more relaxed, and given the low  $B_1$  inhomogeneity, the VFA method is a very useful method for  $T_1$  mapping. It could even be consider that VFA  $T_1$  mapping could replace conventional  $T_1$  weighted imaging, such as MP(2)RAGE, as VFA has very high sampling efficiency. With low  $B_1$  inhomogeneity, synthetic  $T_1$  weighted images can easily be generated from the  $T_1$  and PD maps [64].

An advantage of RUFIS at all field strengths, but especially at 7T, is the silent readout. Studies have reported that acoustic noise from the scanner is one of the most unpleasant features of the 7T scan experience compared to being scanned at 1.5T [200]. Further development and implementation of silent structural and functional imaging techniques at 7T would therefore directly benefit research subjects and patients.

Several theoretical corollaries describing the field strength dependency of RUFIS acquisition parameters were presented in the beginning of this chapter. Some of these were validated in the present study, such as the linear increase in bandwidth to reduce off-resonance effects. However, further work is required to experimentally validate the corollaries relating SAR and acoustic noise, to the magnetic field strength.

In conclusion, RUFIS can be used across field strengths with results comparable to an equivalent spoiled gradient echo acquisition. This motivates further applications at both 1.5 and 7T, such as  $T_2$  prepared RUFIS for quantitative imaging [204],  $T_1$  prepared RUFIS for MP2RAGE imaging [202], and functional imaging using  $T_2$  prepared RUFIS [109] or the closely related Looping Star sequence [115].

## 5.5 Publications and Contribution

### 5.5.1 Publications

This work has been presented previously in:

1. **Ljungberg E**, Burns B, Wood TC, Solana AB, Larson PEZ, Barker GJ, & Wiesinger F, (2019). *ZTE Imaging Across Field Strengths; Opportunities for Low-Field Imaging*. Accepted to Proc. Intl. Soc. Mag. Reson. Med 28, Sydney
2. **Ljungberg E**, Burns B, Larson PEZ, Kolind S, Symms M, Wiesinger F, & Barker GJ, (2019). *Silent  $T_1$ -Mapping at 7T Using the Variable Flip Angle Method*. In Proc. Intl. Soc. Mag. Reson. Med 27 (p. 4976). Montreal.

### 5.5.2 Contribution

This work could not have been accomplished without the collaboration and help from Dr. Peder Larson and Dr. Brian Burns at UCSF/GE, who performed a large number of scans on the UCSF 7T scanner and also provided the pulse sequence code and offline reconstruction routines for the 7T RUFIS pulse sequence. The idea for the cross field strength comparison of  $T_1$  mapping was proposed by Dr. Wiesinger and further developed by me. Dr. Wiesinger

also helped developed the theoretical analysis of the  $B_0$  dependency of RUFIS imaging. I planned, executed, and performed all the analyses reported in the study.

## Chapter 6

# Multi-Contrast Magnetisation Prepared RUFIS

### Contents

---

<b>6.1</b>	<b>Introduction</b>	<b>152</b>
<b>6.2</b>	<b>T<sub>2</sub> Contrast Using Magnetisation Preparation</b>	<b>152</b>
<b>6.3</b>	<b>A T<sub>2</sub> Prepared RUFIS Sequence</b>	<b>158</b>
<b>6.4</b>	<b>Combined T<sub>1</sub> and T<sub>2</sub> Mapping with RUFIS</b>	<b>166</b>
<b>6.5</b>	<b>Simulating MT Effects in Multi-Contrast RUFIS</b>	<b>185</b>
<b>6.6</b>	<b>Chapter Discussion and Conclusion</b>	<b>191</b>
<b>6.7</b>	<b>Publications and Contribution</b>	<b>193</b>

---

### Summary

IN this chapter a multi-parametric sequence for quantitative T<sub>1</sub> and T<sub>2</sub> mapping with RUFIS is introduced. An adiabatic T<sub>2</sub> preparation module is presented and it is demonstrated how it can be integrated into the RUFIS sequence to obtain T<sub>2</sub> weighted images. Using a combination of inversion recovery and T<sub>2</sub> preparation, a multi-contrast RUFIS sequence for simultaneous T<sub>1</sub> and T<sub>2</sub> mapping is developed.

## 6.1 Introduction

In this chapter, a modification of the Rotating Ultra-Fast Imaging Sequence (RUFIS) sequence for silent quantitative  $T_1$  and  $T_2$  mapping is presented. It was shown in previous chapters, that RUFIS can be used for quantitative  $T_1$  mapping using the variable flip angle (VFA) method. However, RUFIS can not produce  $T_2$  contrast, and therefore contrast preparation pulses are required. Previous studies have used  $T_2$  prepared RUFIS for functional Magnetic Resonance Imaging (fMRI) studies [109] as well as for quantitative imaging [205]. The work presented here is an extension, and deeper exploration, of the work by Wiesinger et al. [115] to which I made contributions during the initial development.

The development of the multi-parametric RUFIS sequence, referred to here as MUPA, is divided into three parts. First, an adiabatic  $T_2$  preparation pulse, the modified  $B_1$ -insensitive rotation (mBIR)4 pulse, is introduced and Bloch simulations are performed to study the behaviour of this preparation pulse under different  $B_0$  and  $B_1^+$  inhomogeneity conditions. The mBIR4 pulse is then incorporated into the RUFIS sequence, in order to demonstrate that it can produce  $T_2$  weighting in vivo. It is shown that the RUFIS acquisition inherently produces  $T_1$  contrast from the segment readout, and thus for quantitative  $T_2$  mapping (rather than simple  $T_2$  weighting), information on  $T_1$  is also required. The  $T_2$  prepared RUFIS sequence is therefore combined with an inversion recovery module in order to quantify  $T_1$  and  $T_2$  simultaneously. The resulting MUPA sequence is evaluated in a quantitative phantom and in a healthy volunteer.

## 6.2 $T_2$ Contrast Using Magnetisation Preparation

To produce  $T_2$  contrast, the magnetisation has to decay in the transverse plane, which typically is achieved with a spin echo sequence [20], from which images acquired at different echo times can be used to quantify  $T_2$  [19]. To introduce  $T_2$  contrast into RUFIS, a magnetisation preparation module is used to encode  $T_2$  contrast in the longitudinal magnetisation prior to the RUFIS readout [204]. This preparation approach can also be used to introduce magnetisation transfer contrast [206],  $T_1$ -weighting using inversion or saturation recovery [207, 202], or diffusion weighting [110]. The following two sections will describe two methods for producing  $T_2$  contrast using magnetisation preparation: a spin echo preparation using hard pulses, and an adiabatic  $T_2$  preparation module [208, 209, 210, 211].



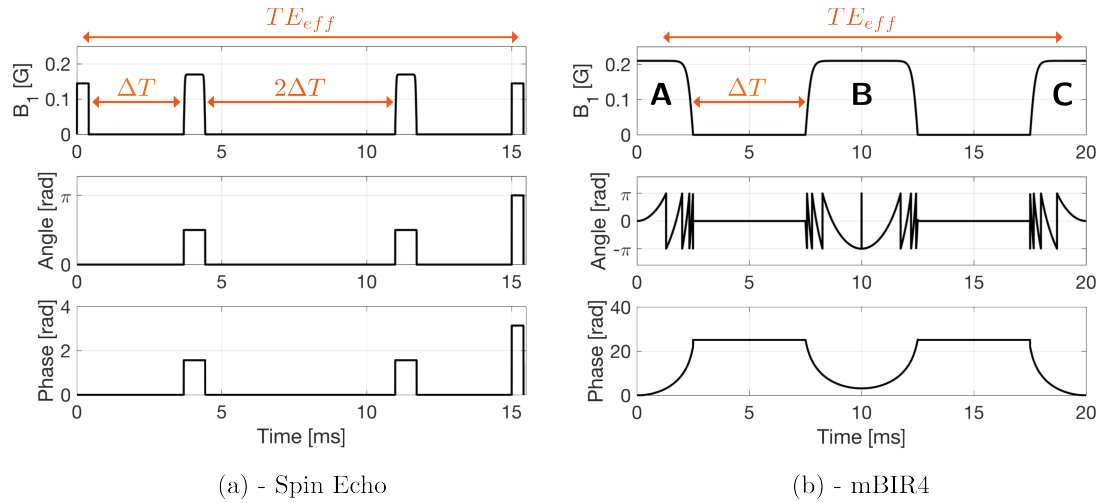


**Figure 6.1:** Examples of  $T_2$  preparation using (a) a spin echo and (b) the adiabatic mBIR4 pulse. The inter pulse spacing  $\Delta T$  which can be adjusted to change the TE is indicated with red arrows, along with the resulting effective TE.

### 6.2.1 Spin Echo Preparation

$T_2$  contrast preparation can be achieved using a spin echo module, figure 6.1a, comprising a series of radio frequency (RF) pulses:  $90_x - (180_y)_n - (-90)_x$ , i.e. the magnetisation is tipped into the transverse plane and refocused by  $n$   $180^\circ$  pulses (applied on an axis orthogonal to the excitation pulse) and finally tipped back up along the longitudinal axis [212, 213, 214, 56]. The TE is controlled by changing the inter-pulse spacing  $\Delta T$ , demonstrated for two  $180^\circ$  pulses in figure 6.1a. For long TEs, larger number of refocusing pulses can be used together with the MLEV phase cycling scheme to reduce sensitivity to  $B_0$  variations [215]. The available magnetisation at the beginning of the RUFIS readout is then proportional to the degree of  $T_2$  weighting achieved during the preparation module.

A preparation module using hard pulses enables short minimum echo time, and is simple to model as the pulses can be considered to act instantaneously. However, this type of  $T_2$  preparation is very sensitive to inhomogeneities in  $B_0$  and  $B_1^+$  [211]. The robustness of the preparation can be improved using adiabatic pulses, which will be described in the next section.

### 6.2.2 The Adiabatic mBIR-4 Pulse

Adiabatic RF pulses have a time varying amplitude and phase, and therefore the effective flip angle is not simply determined by the integral of the RF amplitude. In general, adiabatic RF pulses can be designed to achieve a desired flip angle over a wide range of  $B_1^+$

and  $B_0$ , thus improving the robustness of imaging experience in presence of experimental imperfections [209]. In this work, the mBIR4 pulse is used for  $T_2$  preparation [208, 216], which has previously been demonstrated at 3T [217, 218] and 7T [219, 220], as well as for quantitative  $T_2$  mapping [221, 211, 222].

The mBIR4 pulse is a composite pulse, consisting of four adiabatic half-passage (AHP) pulses [223], two forward (F-AHP) and two time-reversed (TR-AHP). The amplitude  $f_B(t)$  and frequency modulation  $f_\omega(t)$  functions for the AHP are given by [224]

$$f_B(t) = A \tanh(\lambda t) \quad (6.1)$$

$$f_\omega(t) = \Delta\omega \frac{\tan(\beta(t-1))}{\tan(\beta)} \quad (6.2)$$

where  $0 < t < 1$ , and  $(\lambda, \beta, A, \Delta\omega)$  are design parameters. It is common to choose  $\beta = \tan^{-1}(10)$ , and  $\lambda = 10$ , which is also used here. The critical design parameters are therefore  $A$  and  $\Delta\omega$  which control the peak  $B_1$  amplitude and frequency sweep respectively. The phase  $\phi(t)$  of the RF pulse is calculated by integrating the frequency modulation function, as

$$\phi(t) = \int_0^t d\tau f_\omega(\tau). \quad (6.3)$$

An example of an mBIR4  $T_2$  preparation pulse is shown in figure 6.1b, showing the amplitude, phase and wrapped phase (angle). The first TR-AHP, segment A, performs a  $90^\circ$  nutation from the longitudinal axis to the transverse plane. A combined F-AHP and TR-AHP, segment B, then acts as a refocusing pulse, followed by a F-AHP, segment C, to tip up the magnetisation along the longitudinal axis again.

### 6.2.3 Pulse Design

Thorough optimisation of the design parameters of the mBIR4 pulse is outside the scope of this thesis. Instead, the parameters determined by Nguyen et al. ( $A = 0.21\text{G}$ ,  $\Delta\omega = 9\text{kHz}$ , total duration of 10 ms without delays) are used in this work [211]. Nguyen et al. used the mBIR4 pulse for multi-component  $T_2$  mapping at 3T using a spiral readout, which is similar to the objective of this project. Bloch simulations were carried out to evaluate the effective TE of the preparation pulse and to evaluate the  $B_0$  and  $B_1^+$  profiles.

### Effective Echo Time

The TE of the mBIR4 pulse is set by changing the inter pulse spacing  $\Delta T$ , as shown in figure 6.1b. If the RF (sub-)pulses could be considered instantaneous then the TE of the preparation would be  $TE = 2\Delta T$ . The mBIR pulse used in this work has a total duration of 10ms (2.5+5+2.5 ms) which cannot be considered instantaneous, however, and therefore the relaxation behaviour during the pulse has to be understood in order to determine the effective TE [225].

The relaxation behaviour during the pulse was studied for a range of inter-pulse spacings  $2\Delta T = 10 \cdot 2^i$  with  $i = 0..5$ , using Bloch simulations with 20 linearly spaced  $T_2$  values from 10 to 200ms, assuming nominal  $B_1$  amplitude and no  $B_0$  error. The magnetisation at the end of the mBIR4 pulse, i.e. the prepared magnetisation  $M_{prep}$  at a given  $\Delta T_i$ , can be modelled as

$$M_{prep}(\Delta T_i, T_2) = a \cdot e^{-2\Delta T_i/T_2} \cdot e^{-\tau_{eff}/T_2} = a \cdot e^{-TE_{eff}/T_2} \quad (6.4)$$

where  $\tau_{eff}$  is the effective relaxation time in the transverse plane during the mBIR4 pulse, and  $TE_{eff} = 2\Delta T_i + \tau_{eff}$  is the overall effective TE. Figure 6.2a shows the simulated  $T_2$  prepared signal for each value of  $2\Delta T_i$ , together with the best fit line to equation 6.4, obtained using a non-linear fitting algorithm. The  $TE_{eff}$  was then plotted against  $2\Delta T$ , and a linear fit was calculated to find the slope and offset, shown in figure 6.2b. For the 10ms pulse used here,  $TE_{eff} = 2\Delta T + 7.4\text{ms}$ , i.e. the effective echo time is, to a very good approximation, the time from the middle of segment A to the middle of segment C, as outlined in figure 6.1b.

### $B_0$ and $B_1^+$ Profiles

Using Bloch simulations, the behaviour of the CPMG and mBIR4  $T_2$  preparation modules, shown in figure 6.1, were simulated for  $T_2=80$  ms,  $B_0$  variation -500 Hz to 500 Hz, and  $B_1^+$  variation of 0.75-1.25 of the nominal value. (Details of the Bloch simulation can be found in appendix D). The effective TE was set to 80 ms (longer than that shown in figure 6.1) in order to achieve  $T_2$  weighting similar to that typically used in vivo. Figure 6.3 shows the relative error in the prepared magnetisation, relative to preparation performed on resonance with nominal  $B_1^+$ , as a function of  $B_0$  and  $B_1^+$ . These results clearly show the high sensitivity to variation in  $B_0$  and  $B_1^+$  of the CPMG preparation sequence and

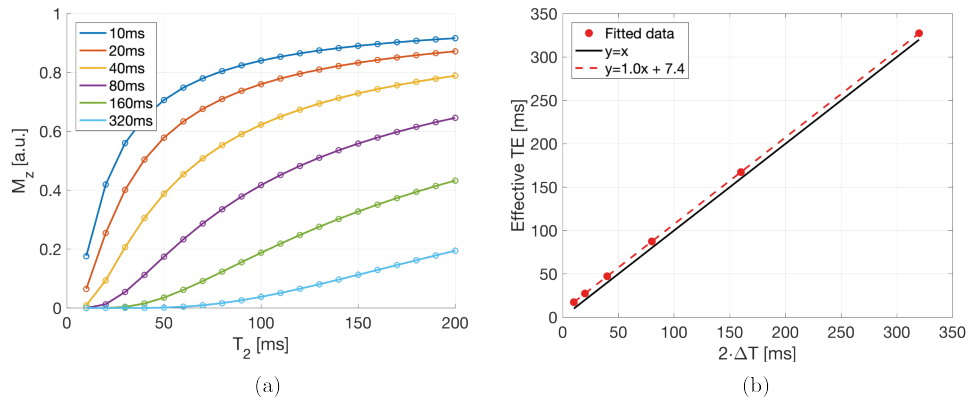


**Figure 6.2:** (a) Plot of prepared magnetisation (circles) for 6 different mBIR4 pulses with different inter pulse spacing (in legend), and the best exponential fit to equation 6.4 (solid line). (b) Effective TE as a function of  $2\Delta T$  in ms.

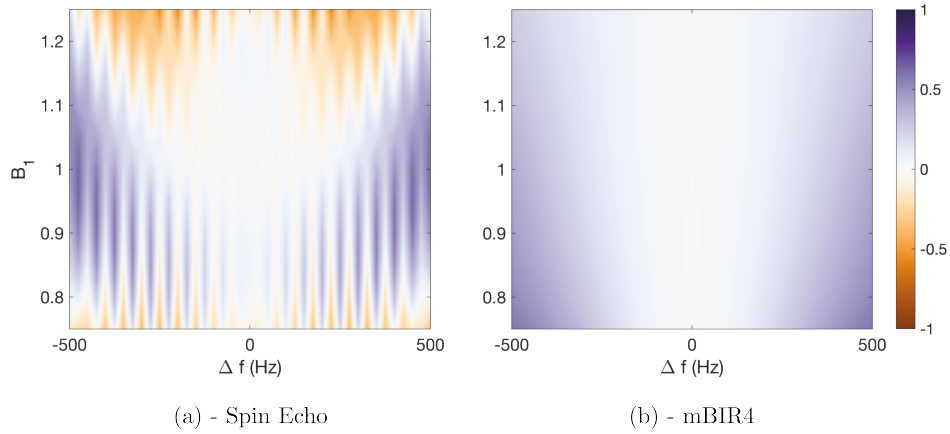


**Figure 6.3:** Off-resonance and  $B_1^+$  profiles of (a) the spin echo preparation and (b) mBIR4 pulse at  $T_2=80\text{ms}$  and  $TE_{eff} = 80\text{ms}$ . The colour shows the relative error of the prepared magnetisation at a given off-resonance frequency and  $B_1^+$ -error relative to the magnetisation on-resonance at nominal  $B_1^+$ .

the improved robustness with the adiabatic mBIR4 pulse. Figure 6.4 shows additional examples of the prepared magnetisation for different effective TEs, ranging from 10 to 200 ms. Longer TEs are more affected by off-resonance and  $B_1^+$  effects than short TEs, which appear very stable across the range of simulated  $B_0$  and  $B_1^+$ .

The magnetisation evolution of the mBIR4 pulse, shown in figure 6.5, demonstrates the behaviour of the magnetisation in the presence of  $B_0$  and  $B_1$  variations. At nominal  $B_1$  and on resonance, figure 6.5a, segment A puts the magnetisation in the transverse plane, segment B brings it up along the longitudinal axis and back into the transverse plane, and finally segment C puts it up back along the longitudinal axis again. At 250Hz off resonance, figure 6.5b, segment A will produce negative longitudinal magnetisation, segment B will

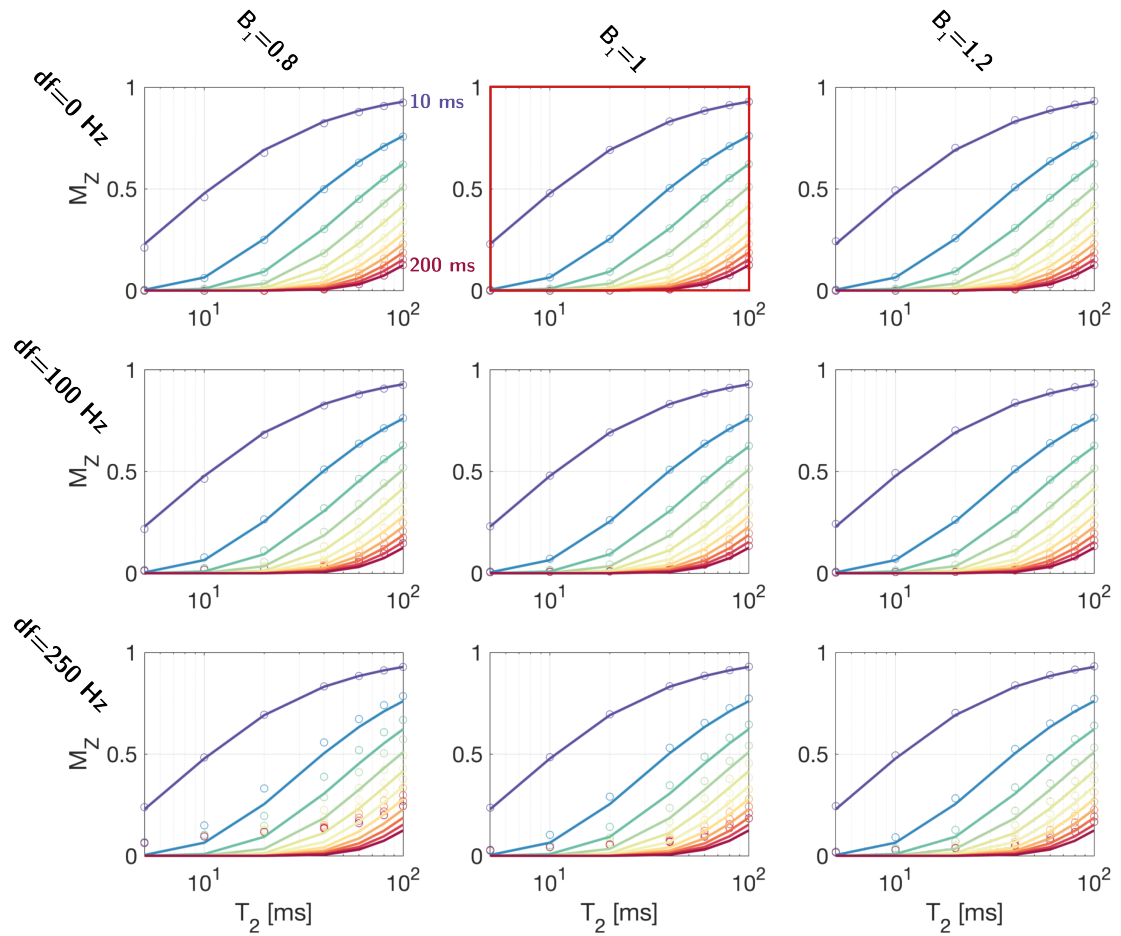


**Figure 6.4:** Curves showing the prepared magnetisation (dots) as a function of  $T_2$  for 11 different TEs, for combinations of three different off-resonance frequencies and three values of  $B_1^+$  error. Solid lines indicate the expected magnetisation under nominal conditions. The results for the combination that is on-resonance and with nominal  $B_1^+$  are indicated with a red frame.

again bring it back up along longitudinal axis but will then generate positive longitudinal magnetisation, and finally segment C will put it back along the longitudinal axis. If the  $B_1$  efficiency is lower than the nominal  $B_1$ , as shown in figure 6.5c, the behaviour of the magnetisation remains very similar to figure 6.5a, with only minor changes in the oscillations in each segment.

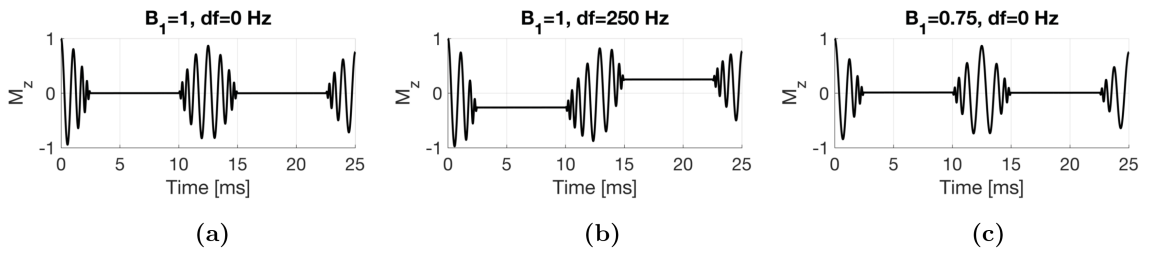


**Figure 6.5:** The mBIR4 pulse creates a complex magnetisation evolution, which can be partly understood by studying it under different conditions. Here the evolution is shown **(a)** on resonance and at nominal  $B_1$ , **(b)** at 250Hz off resonance (at nominal  $B_1$ ), and **(c)** on resonance but with 0.75 nominal  $B_1$ .

### $T_1$ Sensitivity

Ideally, the  $T_2$  preparation pulse should only produce contrast proportional to  $T_2$ , and not be influenced by  $T_1$ . To study the effect of  $T_1$  on the mBIR4  $T_2$  preparation pulse, the mBIR4 pulse was simulated for 100 linearly spaced  $T_1$  values between 0.5s to 3s and 100 linearly spaced  $T_2$  between 30ms and 200ms, with nominal  $B_1$  and on resonance. Four different effective TEs were investigated: 40, 80, 160, and 320 ms. Figure 6.6 shows the magnetisation following the  $T_2$  preparation pulse, and clearly indicates that (as desired) there is no influence of  $T_1$  during the preparation.

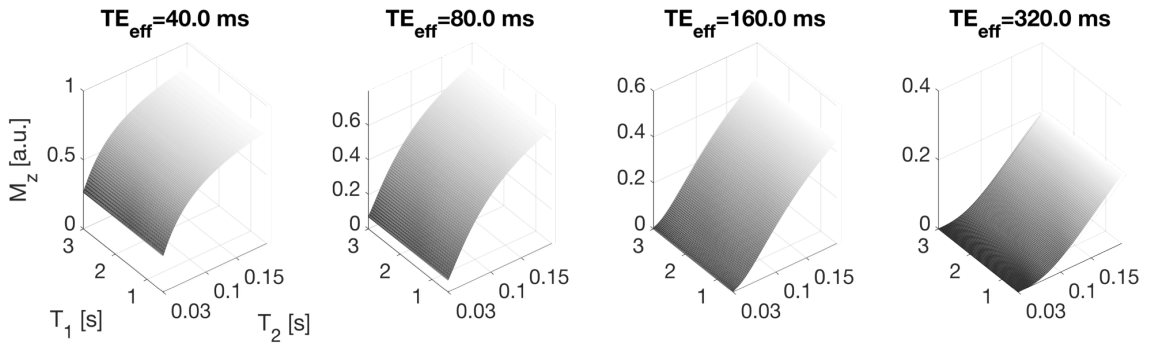


**Figure 6.6:** Simulation of the mBIR4 pulse over a range of different  $T_1$  and  $T_2$ , demonstrating that the preparation produces weighting proportional to  $T_2$  and is not influenced by  $T_1$ .

## 6.3 A $T_2$ Prepared RUFIS Sequence

### 6.3.1 Introduction

In this section a  $T_2$  prepared RUFIS sequence using an adiabatic mBIR4 pulse will be presented. The most basic layout of a  $T_2$  prepared RUFIS sequence is to apply the preparation, acquire a RUFIS segment, and then wait for  $T_1$  recovery, typically on the order

of 1-3 seconds. This results in lengthy acquisition times, and it will be shown that the acquisition can be accelerated using interleaved  $T_2$  preparation and RUFIS readouts.

A  $T_2$  prepared RUFIS acquisition will inherently produce  $T_1$  contrast from the readout, as shown by the signal equations in chapter 3. This makes  $T_2$  prepared RUFIS different from previous work using  $T_2$  prepared acquisitions for  $T_2$  mapping such as Nguyen et al. who used the mBIR4 pulse together with a spiral readout for multi-component  $T_2$  mapping [211]. With a spiral acquisition, only a single excitation pulse is used followed by a long readout, resulting in perfect  $T_2$  weighting, other than any  $T_2$  or  $T_2^*$  decay during the readout. The influence of the  $T_1$  contamination in the RUFIS acquisition will here be demonstrated through simulations and phantom experiments.

### 6.3.2 Pulse Sequence Design and Development

The mBIR4  $T_2$  preparation pulse was implemented into the RUFIS sequence as a separate and flexible preparation module. The time between segment A-B and B-C in the pulse was set through a variable which could be changed during scanning to enable different TEs to be acquired in the same run. After the mBIR4 pulse, a trapezoidal crusher gradient with an area of  $54\text{mT s m}^{-1}$  was applied to destroy any residual transverse magnetisation. The rise time was increased and maximum amplitude of the crusher gradient reduced by a factor of 5 relative to the minimum rise time ( $248\mu\text{s}$  to max amplitude) and maximum amplitude ( $50\mu\text{T m}^{-1}$ ) to reduce the acoustic noise.

The  $T_2$  preparation was implemented as a multi TE acquisition consisting of  $N$  repeated  $T_2$  preparations and RUFIS readout pairs, followed by a recovery period, see figure 6.7. Each RUFIS segment encoded the same part in k-space and data were stored as separate "volumes", thus producing  $N$  volumes with different  $T_2$  contrasts. The TEs of the  $T_2$  preparations were varied to achieve different degrees of  $T_2$  weighting in each volume.

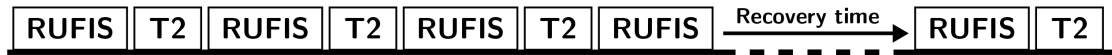


**Figure 6.7:** Schematic of the multi TE  $T_2$  prepared RUFIS pulse sequence. Each RUFIS segment, except the first, is coupled with a  $T_2$  preparation module. After the repeated  $T_2$  preparation and RUFIS readout, there is a wait period for  $T_1$  recovery.

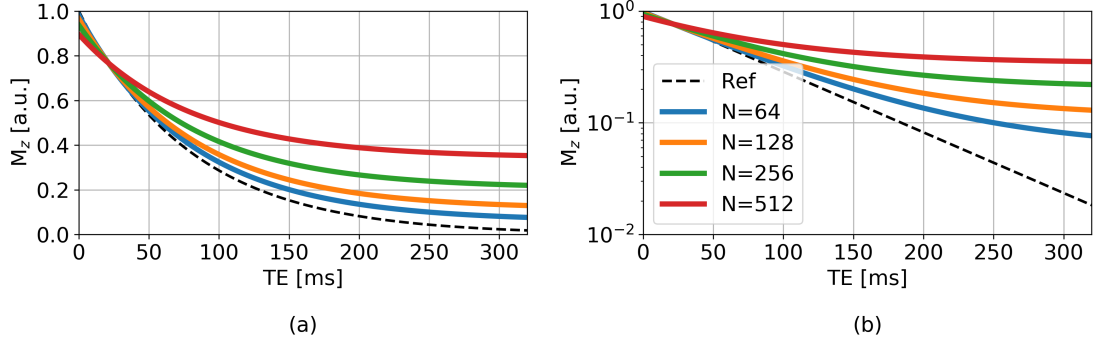


**Figure 6.8:** Effect of the RUFIS readout on  $T_2$ -prepared RUFIS for different number of spokes in the readout, compared to pure single exponential  $T_2$  decay (dashed line), as would be observed in a spin echo sequence. In **(a)**, the curves are shown on a linear scale, and in **(b)** on a logarithmic scale. With increasing number of spokes, the RUFIS curves deviates more from the reference. (Simulation parameters:  $TR=2\text{ms}$ ,  $\alpha=2^\circ$ ,  $T_1=1000\text{ms}$ ,  $T_2=80\text{ms}$ )

### 6.3.3 Simulations

#### Single TE

A simulation framework, based on the analytical signal equation in chapter 3 was developed to study the effect of a single RUFIS readout on the  $T_2$  weighting obtained from the preparation module.  $T_2$  decay was simulated with TEs from 0 to 320 ms, with a  $T_2$  of 80ms. The effect of a single RUFIS readout was modelled using the signal equation from chapter 3

$$M_{z,seg} = M_z(0) \cdot f_N + (1 - f_N) \cdot M_{z,SPGR} \quad (6.5)$$

$$f_N = \frac{1 - \xi^N}{N(1 - \xi)} \quad (6.6)$$

where  $M_z(0) = \exp(-TE/T_2)$  and  $\xi = \cos \alpha \cdot e^{-TR/T_1}$ . Figure 6.8 shows the results of the simulation, clearly demonstrating that with increasing number of spokes in the RUFIS readout, the signal deviates further from the standard  $T_2$  decay signal. The RUFIS signal appears to decay with a longer  $T_2$  with increasing number of spokes, which on a logarithmic scale would appear as a different slope. However, in figure 6.8b where the  $T_2$  prepared RUFIS signal is plotted on a logarithmic scale, it is seen that the signal can not be modelled as a single exponential.



### Multiple TEs

The simulation framework was expanded to simulate interleaved  $T_2$  preparation and RUFIS readouts. With a single  $T_2$  preparation, the signal can be calculated with equation (6.5). With multiple  $T_2$  preparations, the  $T_2$  preparation before segment  $i$  is applied to the signal at the end of segment  $i - 1$ , i.e. spoke  $N$

$$M_z^i(0) = e^{-TE_i/T_2} \cdot M_z^{i-1}(N) \quad (6.7)$$

where

$$M_z^{i-1}(N) = M_z^{i-1}(0) \cdot \xi^N + (1 - \xi^N) \cdot M_{z,SPGR}. \quad (6.8)$$

If the effect of the readout is ignored, the effective TE of segment  $i$  is the accumulated TE of the preceding preparation modules as

$$M_z^i(0) = M_z^0(0) \prod_{k=0}^i \exp\left(\frac{-TE_k}{T_2}\right) = M_z^0(0) \cdot \exp\left(\frac{-\sum_{k=0}^i TE_k}{T_2}\right) \quad (6.9)$$

and this will thus be the TE assigned to volume  $i$  in a multi-TE  $T_2$  prepared RUFIS acquisition.

Figure 6.9 shows simulation of an interleaved  $T_2$  prepared RUFIS acquisition, plotted against the accumulated TE, with preparation periods of TR=10, 40, 80, 160 and 320ms. With a single spoke readout, figure 6.9a, the  $T_2$  prepared RUFIS follows the reference spin echo signal. With increasing number of spokes, the acquisition deviates more strongly from the reference as expected due to  $T_1$  effects. In figure 6.9b, it is shown that the  $T_2$  prepared RUFIS sequence is inherently sensitive to  $T_1$ . Shorter  $T_1$  results in more longitudinal recovery during the readout, and thus stronger deviation from the reference. However, most importantly, as shown in figure 6.9c, the multi-TE  $T_2$  prepared RUFIS sequence does remain sensitive to changes in  $T_2$ .

#### 6.3.4 Experiments

A multi TE  $T_2$  prepared RUFIS experiment was performed on the EUROSPIN quantitative test object [168] and a single healthy volunteer. The acquisition consisted of 5 RUFIS readouts coupled with  $T_2$  preparation TEs: 0, 10, 20, 40 and 90ms, i.e. the first volume had no  $T_2$  preparation. There was a 1.5s recovery period after the last RUFIS segment. The  $T_2$  preparation module consisted of a mBIR4 preparation pulse with the parameters outlined

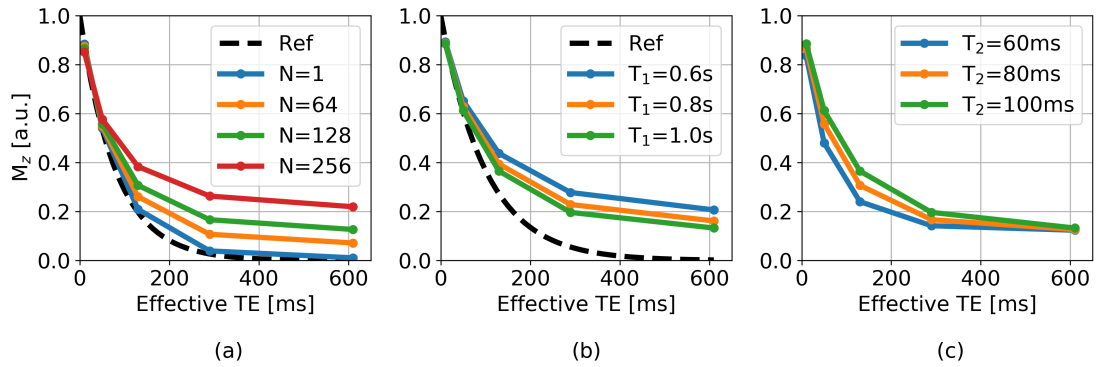


**Figure 6.9:** Example of the effects of interleaved  $T_2$  preparation and RUFIS readouts. The repeated excitation in the RUFIS readout produces both  $T_1$  and  $T_2$  contrast. **(a)**: Higher number of spokes increases the deviation from the reference spin echo curve. **(b)**: Shorter  $T_1$  results in more  $T_1$  recovery during the RUFIS readout and larger deviation from the reference. **(c)** Signal curves obtained with different  $T_2$ . (Simulation parameters:  $TR=2ms$ ,  $\alpha=2^\circ$ , 128 spokes per segment.  $T_2=80ms$  when  $T_1$  is changed.  $T_1=1s$  when  $T_2$  is changed.)

in section 6.2.3. The RUFIS readout consisted of 384 spokes,  $\alpha=2^\circ$  and  $TR=1.6ms$ . The field of view (FOV) was  $192 \times 192 \times 192 mm^3$  with voxel size  $1.2 \times 1.2 \times 1.2 mm^3$ .

A 2D, multi slice multi-echo fast spin echo (FSE) was also acquired, for comparison to the  $T_2$  prepared RUFIS, with acquisition parameters: 16 echoes,  $TE=10ms$ , 1.5s recovery period,  $1.5 \times 1.5 mm^2$  in-plane voxel size, and 3mm slices. All data were acquired on a GE MR750 3T scanner using the body coil for RF transmission and a head only 32-channel receive coil (Nova Medical). Acoustic noise from the RUFIS and FSE acquisitions were measured using an MR safe microphone (Casella, CEL-495) placed inside the bore and connected to a sound meter (Casella, CEL-63X).

In the volunteer data, two ROIs were defined in posterior WM and putamen GM. The size of the ROI was  $3 \times 3 \times 3$  voxels in the RUFIS data (volume  $46.7cm^3$ ), and  $3 \times 3$  voxels in a single slice on the FSE data ( $60.7cm^3$ ).

## Phantom Results

Figure 6.10 shows signal decay curves from the  $T_2$  prepared RUFIS in two different vials of the EUROSPIN phantom. The two vials have similar  $T_2$  ( $\approx 90ms$ ) but different  $T_1$  (464ms and 623ms). The spin echo experiment, dashed curves, showed almost identical signal curves for the two vials, as expected. With RUFIS, the vial with the shorter  $T_1$  shows less apparent  $T_2$  decay, due to the increased  $T_1$  recovery. Plotting the curves on a logarithmic y-

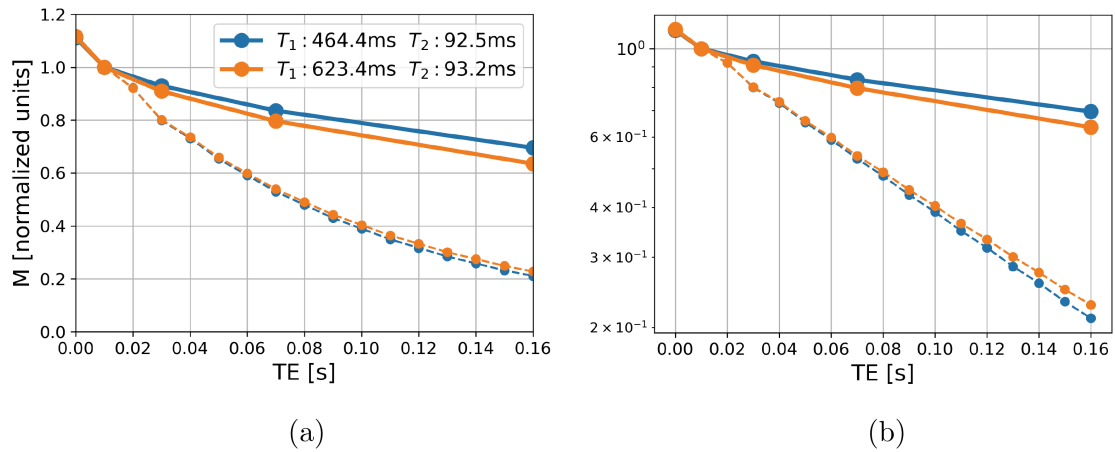


**Figure 6.10:** Signal curves from two vials in the EUROSPIN phantom with similar  $T_2$  but different  $T_1$  plotted on (a) linear and (b) logarithmic scale. Solid lines is data acquired with  $T_2$  prepared RUFIS and dashed lines is FSE. The vial with shorter  $T_1$  shows greater  $T_1$  recovery and thus less apparent  $T_2$  decay.

axis shows the single exponential behaviour of the spin echo acquisition. While the RUFIS acquisition shows a non-single exponential signal curve, this does not indicate multi  $T_2$  component decay but rather a complex combination of  $T_1$  and  $T_2$  relaxation. What does show though is that the complex combination of  $T_1$  and  $T_2$  relaxation cannot be modelled simply as an "effective TE" based on the number of spokes in the acquisition, as this would appear as a straight line in figure 6.10b but with a different slope compared to the spin echo acquisition.

The first volume in the RUFIS acquisition has an effective  $TE=0$ , because of both the lack of  $T_2$  preparation and the zero echo time (ZTE) readout. In figure 6.10 the signal curves from RUFIS and spin echo were normalised to their respective values at  $TE=10\text{ms}$ , to aid direct comparison. On the logarithmic scale, the spin echo signal can be linearly extrapolated back to zero, which clearly aligns with the RUFIS  $TE=0$  point.

### In Vivo Results

Similar contrast changes with  $TE$  were observed in vivo using the  $T_2$  weighted RUFIS and spin echo brain acquisitions, figure 6.11. The  $TE=0\text{ms}$  RUFIS volume has very low soft tissue contrast, as expected from an almost pure proton density (PD) weighted image. With increasing accumulated  $TE$ , the  $T_2$  weighting in the RUFIS acquisition increases similarly to the spin echo acquisition. At longer echo times ( $TE=70\text{ms}$  and above), it becomes clear

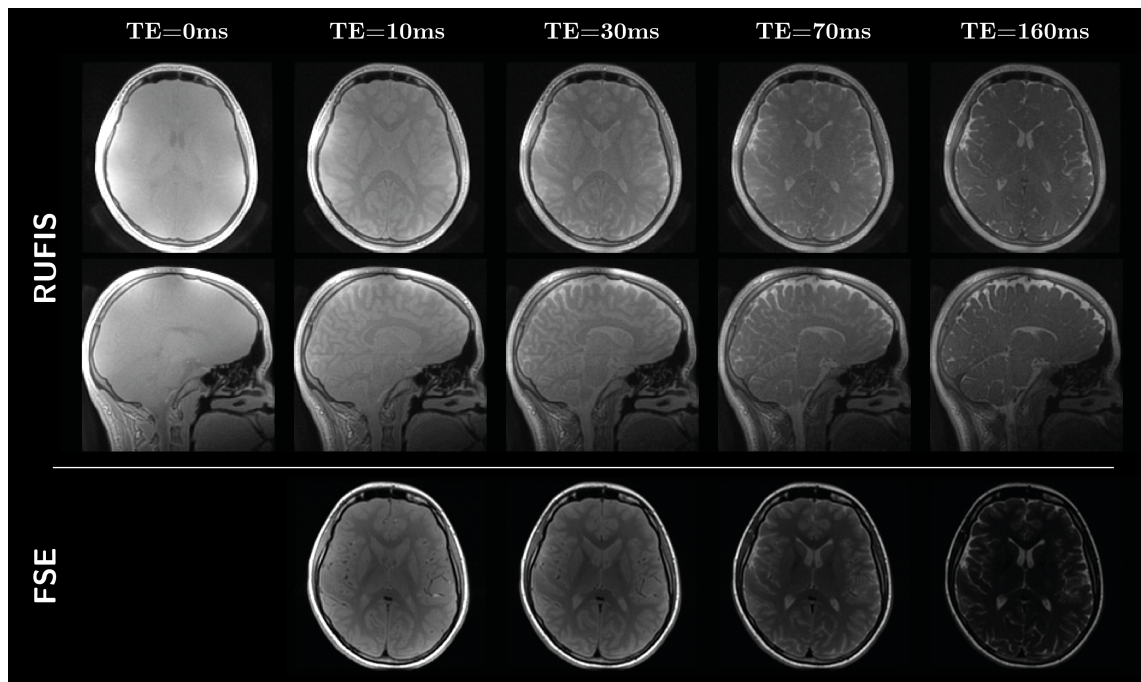


**Figure 6.11:** In vivo brain images, comparing  $T_2$  prepared RUFIS at different effective TEs to fast spin echo (FSE) at the same TEs. Only axial slices shown with FSE as data were collected in 2D slices. Image intensity was normalised to 1 for the WM ROI in the  $TE=10ms$  image, the window levels are the same for all slices.

that the RUFIS acquisition has lower  $T_2$  contrast than the spin echo, however, due to  $T_1$  contamination as demonstrated in the phantom experiment.

Signal curves from isolated WM and GM ROIs for RUFIS and FSE are shown in figure 6.12. Similarly to the simulations and phantom experiment, the signal curves from RUFIS shows less apparent  $T_2$  decay and a non-single exponential signal decay. There is however a clear difference in the observed  $T_2$  decay between WM and GM with  $T_2$  prepared RUFIS.

The in vivo results also demonstrate the  $B_0$  and  $B_1$  robustness of the mBIR4 pulse. If present,  $B_1$  inhomogeneity would manifest as loss of  $T_2$  weighting around the edge of the brain where the  $B_1$  efficiency is low, but here uniform contrast is observed across the brain. The spatial variation of the signal inhomogeneity in the  $TE=0ms$  image (brighter in spots around the skull) suggest that it is due to the receive profile of the coil, i.e.  $B_1^-$ .

The acoustic noise measurements showed low acoustic noise with RUFIS, as reported previously. Ambient background noise was 66dB(A),  $T_2$  prepared RUFIS 68dB(A), and FSE measured 104dB(A).

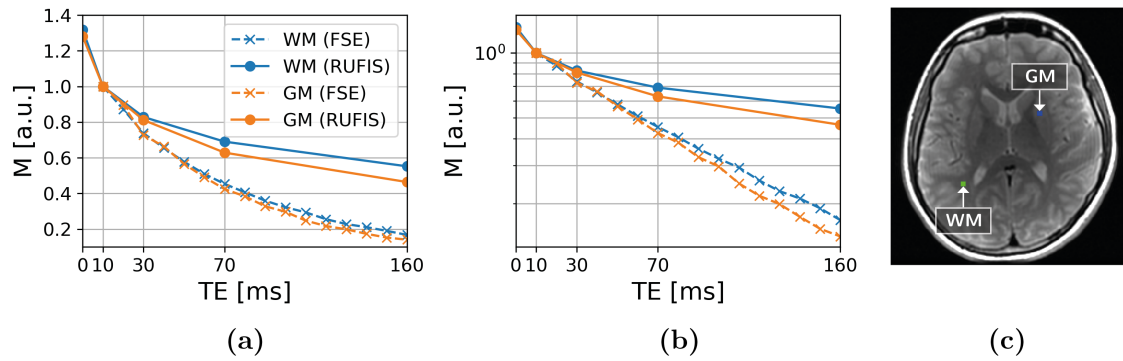


**Figure 6.12:** Signal curves from isolated WM and GM ROIs acquired with  $T_2$  prepared RUFIS and FSE shown on (a) linear and (b) logarithmic scale.  $T_1$  contamination from the RUFIS readout results in less apparent  $T_2$  decay in  $T_2$  prepared RUFIS. ROIs used are shown in (c)

### 6.3.5 Discussion

Using  $T_2$  preparation, images with  $T_2$  weighting can be acquired with RUFIS. The mBIR4 pulse provides a  $B_0$  and  $B_1$  robust  $T_2$  preparation, with inter-pulse spacing that easily can be adjusted to change the effective TE. The RUFIS readout inherently produces  $T_1$  weighting which contaminates the  $T_2$  weighting in the multi-TE  $T_2$  prepared RUFIS acquisition, thus preventing direct quantitative  $T_2$  mapping.

For neuroimaging applications, the  $T_1$  contamination from the RUFIS readout results in loss of contrast between WM and GM. White matter has shorter  $T_2$  than GM, resulting in faster  $T_2$  decay, producing the desired, albeit weak,  $T_2$  contrast seen in the brain. However, WM also has a shorter  $T_1$  than GM which results in a more  $T_1$  recovery during the RUFIS readout, resulting in an increase in the signal relative to the case with pure  $T_2$  decay, and thus reduced contrast to GM. For clinical purpose though, the most relevant contrast is that between WM/GM and pathology, such as lesions in Multiple Sclerosis (MS). MS lesions typically show up as hyperintense on  $T_2$  weighted images, i.e. they have a longer  $T_2$  than the surrounding tissue. A  $T_2$  hyperintense MS lesion will appear hyperintense also on a  $T_2$  prepared RUFIS image, however the overall contrast will also depend on the  $T_1$  of the lesion [226, 227]. This is relevant as a proportion of  $T_2$  hyperintense MS lesions will also appear hypointense on  $T_1$  weighted images, i.e. have a longer  $T_1$ , and are referred to as "black-holes". These lesions will therefore have stronger  $T_2$  contrast on a  $T_2$  weighted RUFIS acquisition due to reduced  $T_1$  recovery during the RUFIS readout, and thus stronger pure  $T_2$  weighting.

Because of the mixed  $T_1$  and  $T_2$  contrast described above, quantitative  $T_2$  mapping with a  $T_2$  prepared RUFIS requires knowledge of  $T_1$  to account for  $T_1$  recovery during the readout. The next section will describe a pulse sequence design which combines  $T_2$  prepared RUFIS with inversion recovery to simultaneously quantify  $T_1$  and  $T_2$ .

## 6.4 Combined $T_1$ and $T_2$ Mapping with RUFIS

### 6.4.1 Introduction

To enable quantitative  $T_2$  mapping with RUFIS, knowledge of  $T_1$  is required. This can be obtained through a separate experiment, such as a VFA acquisition described in chapter 4, or  $T_1$  data collection can be combined in the same acquisition as the  $T_2$  mapping experiment. The pulse sequence described in the previous section required a delay period after the last RUFIS readout to allow for  $T_1$  recovery, similar to a spin echo acquisition. This delay period can be used to acquire additional RUFIS segments with  $T_1$  contrast, in a manner similar to a Look-Locker acquisition [228], adding  $T_1$  information without extending the total acquisition time [205]. If the recovery period is fully occupied by RUFIS segments, the magnetisation will converge towards a steady state and thus the available magnetisation for the  $T_2$  preparation will be lower than with free  $T_1$  recovery. The sequence combining  $T_1$  and  $T_2$  weighting with RUFIS is here referred to as MUPA. Figure 6.13 shows a schematic of the MUPA pulse sequence diagram outlining the sequence "modules", i.e. preparation pulses and ZTE readout segments. The first four RUFIS segments (ZTE 1-4), will have variable different  $T_1$  contrast as the magnetisation approaches the steady state.  $T_2$  preparation modules are then used to produce  $T_2$  contrast, acquired by segment 5 and 6.

Similar approaches for integrated multi-contrast acquisitions using magnetisation preparation have been proposed previously. The method used here resembles the QuAntification using an interleaved Look-Locker Acquisition Sequence with  $T_2$  preparation pulse (QALAS) method, which utilises a rapid gradient echo (RAGE) readout with centre out elliptical k-space ordering [62]. By acquiring the centre of k-space in the first excitation, the  $T_2$ -weighting is not affected by  $T_1$  recovery during the RAGE readout. Cao et al. used contrast-prepared (mBIR4) RAGE at 7T to obtain  $T_1$ ,  $T_2$  and diffusion weighting [216]. The common principle of these approaches, and the method presented here, is to exploit the, sometimes complex, combination of  $T_1$  recovery and  $T_2$  decay in an MR acquisition.

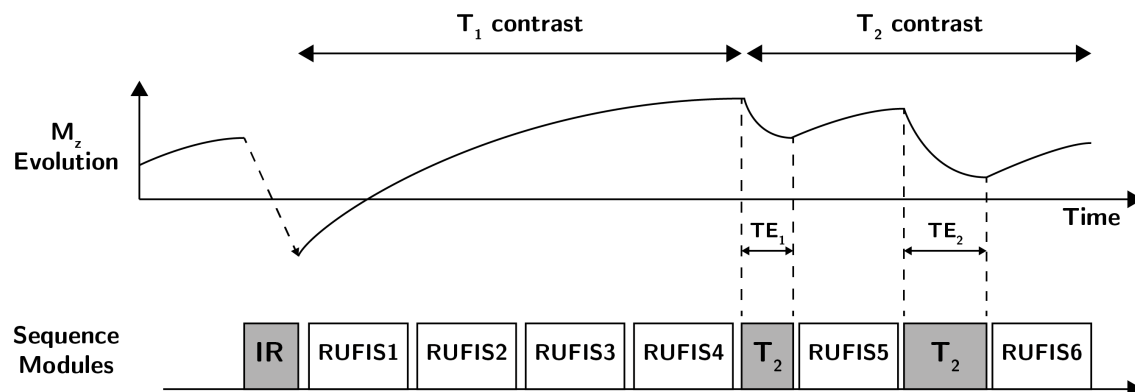


**Figure 6.13:** Schematic of the proposed multi-contrast RUFIS acquisition (MUPA). An inversion pulse (IR) is played out followed by a series of RUFIS segments (RUFIS 1-4), similar to the Look-Locker method.  $T_2$  preparation modules followed by RUFIS readouts are used to produce  $T_2$  contrast (RUFIS 5-6).

### 6.4.2 Purpose

To develop a pulse sequence which introduces controllable  $T_1$  preparation into a  $T_2$  prepared RUFIS acquisition for combined  $T_1$  and  $T_2$  mapping. Different acquisition strategies will be compared, and quantitative parameter mapping analysis methods will be described.

### 6.4.3 Pulse Sequence Design and Development

The  $T_2$  prepared RUFIS sequence was modified to include adiabatic inversion recovery for  $T_1$  contrast, described in detail below. For rapid prototyping of different acquisition protocols, the pulse sequence was modified to allow user input through a text file, specifying the outline of the sequence (i.e. the order of the preparation and readout modules to be used), example shown in table 6.1 corresponding to the layout in figure 6.13. Preparation pulses and RUFIS readouts are treated as modules with two parameters: **time** and **scale**. For preparation pulses, the **time** parameter sets the TI or TE. The **scale** parameter controls the  $B_1$ , providing a method for changing the excitation flip angle, as demonstrated in table 6.1 where the second to last RUFIS segment has a flip angle scaled by 0.7.

## T<sub>1</sub> Preparation

An adiabatic inversion pulse, with Silver Hoult design, was used for  $T_1$  preparation [229]. The pulse has a total duration of 8.6ms and a peak  $B_1$  of 0.12G at nominal flip angle of  $180^\circ$ . Increasing the flip angle of an adiabatic inversion pulse will improve its adiabatic performance, i.e. decreased sensitivity to  $B_0$  and  $B_1$  variation, and it is therefore common to use a flip angle higher than the nominal one. Figure 6.14a shows the waveform of the

**Table 6.1:** Example of what the file input to multi-contrast RUFIS sequence looks like. Duration of preparation pulses are controlled by the **Time** parameter, and the flip angle by the **Scale** parameter.

Type	Time	Scale
T1	30	1
RUFIS	0	1
RUFIS	0	1
RUFIS	0	1
RUFIS	0	1
T2	40	1
RUFIS	0	0.7
T2	80	1
RUFIS	0	1

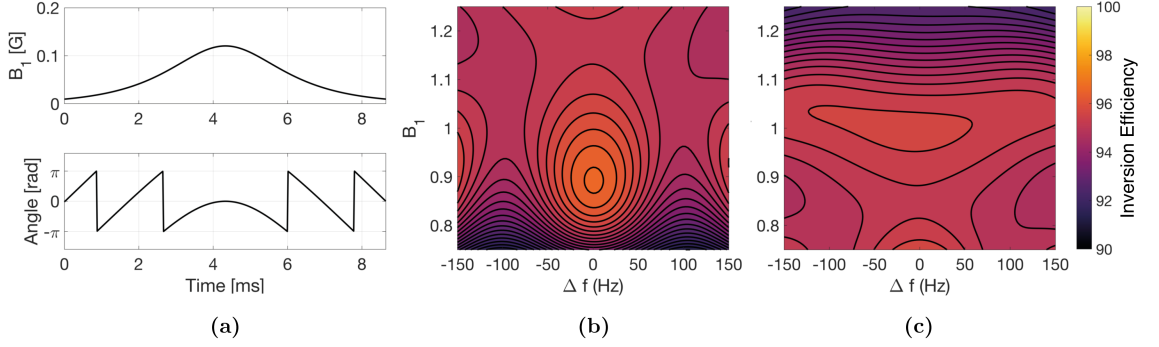


**Figure 6.14:** (a): Plot of the adiabatic inversion pulse with  $\alpha = 180^\circ$ . The  $B_0$  and  $B_1$  profiles shown in (b) and (c) showed decreased sensitivity to off-resonance and  $B_1$  variation with higher flip angle, at the cost of slightly reduced inversion efficiency.

inversion pulse at nominal flip angle of  $180^\circ$ , together with the  $B_0$  and  $B_1$  profiles of the inversion efficiency at  $180^\circ$  (figure 6.14b) and  $250^\circ$  (figure 6.14c). Increasing the flip angle to  $250^\circ$  reduces the  $B_0$  and  $B_1$  sensitivity, at the expense of higher peak  $B_1$  and thus higher specific absorption rate (SAR).

The adiabatic inversion pulse has a total duration of 8.6ms and can therefore not be considered instantaneous, so  $T_1$  and  $T_2$  relaxation are expected during the pulse. The relaxation behaviour during the pulse is modelled here as combined  $T_1$  and  $T_2$  relaxation during effective times  $\tau_1$  and  $\tau_2$ , making the inverted magnetisation  $M_1$  a function of  $T_1$  and  $T_2$ , given initial magnetisation  $M_0$  as

$$M_1(T_1, T_2) = \left( M_0 \cdot e^{-\tau_1/T_1} + \rho(1 - e^{-\tau_1/T_1}) \right) \cdot e^{-\tau_2/T_2} \quad (6.10)$$



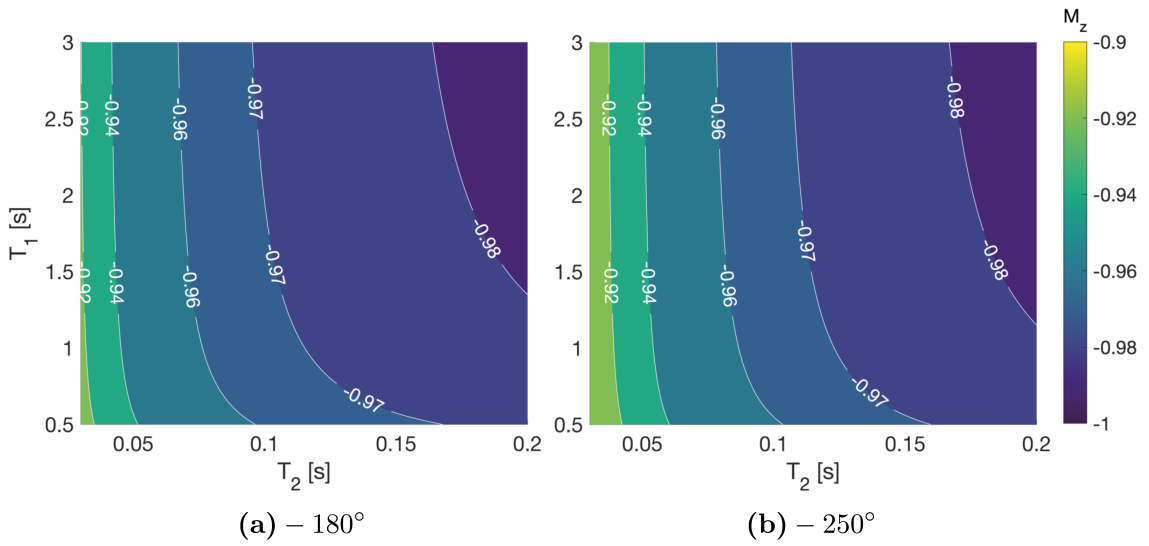


**Figure 6.15:** Inversion efficiency as a function of  $T_1$  and  $T_2$  at nominal  $B_1$  and on resonance for effective flip angle of (a) 180° and (b) 250°.

Using Bloch simulations, the effective  $T_1$  and  $T_2$  relaxation during inversion pulse were simulated over 100 linearly spaced  $T_1$  values between 0.5s to 3s and 100 linearly spaced  $T_2$  values between 30ms and 200ms. The results of this simulation are shown in figure 6.15. The simulated signal was then fitted to equation (6.10) using a non-linear least squares fit. With a nominal flip angle of 180°, the effective relaxation delay parameters were  $\tau_1 = 4.4\text{ms}$  and  $\tau_2 = 2.5\text{ms}$  with  $R^2 = 0.9918$ . Increasing the flip angle to 250° resulted in  $\tau_1 = 2.9\text{ms}$  and  $\tau_2 = 3\text{ms}$  with  $R^2 = 1.0$ . With a higher peak  $B_1$  of the RF pulse, the magnetisation spends a longer time in the transverse plane, resulting in more  $T_2$  decay, as indicated by the increase in  $\tau_2$ .

The effective  $T_1$  and  $T_2$  relaxation during the inversion pulse is small, but it should be included in the fitting procedure to produce accurate quantitative  $T_1$  and  $T_2$  estimates. However, even though the efficiency of the inversion pulse is robust with change in  $B_1$ , the effective relaxation behaviour will change with  $B_1$ , as evident from the change in  $\tau_1$  and  $\tau_2$  between 180° and 250° effective flip angle. A change from 180° to 250° would require a relative increase in  $B_1$  efficiency of 39% which is higher than expected at 3T. Nevertheless, while the values of  $\tau_1$  and  $\tau_2$  only apply on resonance and at nominal  $B_1$ , it is a good approximation, for an effect that is already small.

#### 6.4.4 Quantitative Parameter Mapping Fitting Methods

Quantitative parameter fitting procedures for  $T_1$ ,  $T_2$  and PD mapping were developed in Python. For rapid prototyping of different acquisition scheme, a semi iterative signal equation was used, sacrificing speed for flexibility. The multi-parametric sequence can be split up in separate modules, where the relationship between the initial and final magnetisation ( $M_0/M_1$ ) can be described analytically. For the RUFIS segments, the final and acquired magnetisation, given some initial magnetisation were calculated from equation (6.5) and (6.8).  $T_1$  preparation, was modelled using equation (6.10), and  $T_2$  preparation using equation (6.4). Off-resonance and  $B_1$  effects were ignored as the preparations use adiabatic pulses and the hard pulses have low  $B_0$  sensitivity. Five loops of the sequence were simulated to achieve steady state and only the magnetisation from the last loop was used for the fitting. The whole signal evolution was used to simultaneously fit for  $T_1$  and  $T_2$ .

Calculation of the signal equation was accelerated using the `jit` decorator in Numba [230]. The fitting was performed using `lmfit` [231] with least squares optimisation using the Trust Region method.

#### 6.4.5 Sequence Optimisation

Optimisation of sequence acquisition parameters is a difficult process due to the large search space of possible parameters, and the choice of cost function: should the sequence be optimised for speed, signal to noise ratio (SNR) or SNR efficiency? In most cases, the latter cost function is used, but there can still be many possible options. It was outside the scope of this chapter to perform a thorough investigation of optimal acquisition parameters for multi-parametric RUFIS, instead, guidelines for choosing appropriate parameters are presented here.

#### $T_1$ Contrast During Approach to Steady State

The transient approach towards the steady state from the RUFIS readouts after the inversion pulse depends on the readout TR and the flip angle, as well as the  $T_1$  of the tissue of interest. In chapter 3 it was shown that the magnetisation of spoke  $n$  in a RUFIS segment can be described by

$$M_z(n) = M_0 \cdot \xi^n + M_{z,spgr}(1 - \xi^n) \quad (6.11)$$

where  $M_0$  is the initial magnetisation,  $\xi = \cos \alpha \cdot e^{-TR/T_1}$ , and  $M_{z,spgr}$  the longitudinal steady state magnetisation of a spoiled gradient echo (SPGR) acquisition. If the delays between segments during the inversion recovery period are ignored, the approach to steady state can be modelled as one long segment. Once steady state has been reached, acquiring additional segments does not provide additional  $T_1$  information. Steady state can be considered to be reached when  $\xi^n < \epsilon$ , where  $\epsilon$  is an arbitrary tolerance. The number of spokes  $n$  required to reach steady state given  $\epsilon$  is thus

$$n = \frac{\log(\epsilon)}{\log(\xi)} = \frac{\log(\epsilon)}{\log(\cos \alpha \cdot e^{-TR/T_1})} \quad (6.12)$$

Figure 6.16a shows how the value of  $\epsilon$  influences on the number of spokes required to reach steady state. Reducing the TR will reduce the amount of  $T_1$  recovery during the readout, but it will also result in a faster readout. Figure 6.16b shows that reducing the TR always leads to reduction in the total time it takes to reach steady state, even though it requires more spokes. This can also be shown analytically by calculating the total time to steady state from (6.12) as  $TR \cdot n$ . Therefore, the TR should be minimised and the flip angle maximised to reduce the time it takes to reach steady state.

In RUFIS, the TR is directly proportional to the bandwidth, and therefore the bandwidth should be set as high as possible to reduce the TR. However, to achieve the highest possible signal, the acquisition should also be performed at the Ernst angle, as this will produce the highest steady state transverse magnetisation. Given the interaction of the bandwidth and RF pulse width in RUFIS, the bandwidth must be limited to ensure that the Ernst angle, or close to this, can be achieved.

A practical example is useful for gaining an appreciation of the likely range of the acquisition parameters. From previous experiments, it has been found that the maximum flip angle at a bandwidth of  $\pm 7.8\text{kHz}$  is about  $12^\circ$ . To maintain homogeneous excitation, the maximum flip angle must scale inversely with bandwidth, which means that at  $\pm 15.6\text{kHz}$ , the maximum flip angle is  $6^\circ$ . A typical acquisition would use a FOV of  $200 \times 200 \times 200 \text{ mm}^3$  and resolution of  $1 \times 1 \times 1 \text{ mm}^3$ . With a readout bandwidth of  $\pm 15.6\text{kHz}$ , the TR is approximately  $TR \approx 100 \cdot 1 / (2 \cdot 15.6 \cdot 10^3) = 3.2\text{ms}$ . Optimising the acquisition for  $T_1=1\text{s}$  yields an Ernst angle of  $4.6^\circ$ , which is below the maximum  $6^\circ$ . Increasing the bandwidth to  $\pm 31.25\text{kHz}$  gives  $TR \approx 1.6\text{ms}$ , and an Ernst angle of  $3.2^\circ$ .

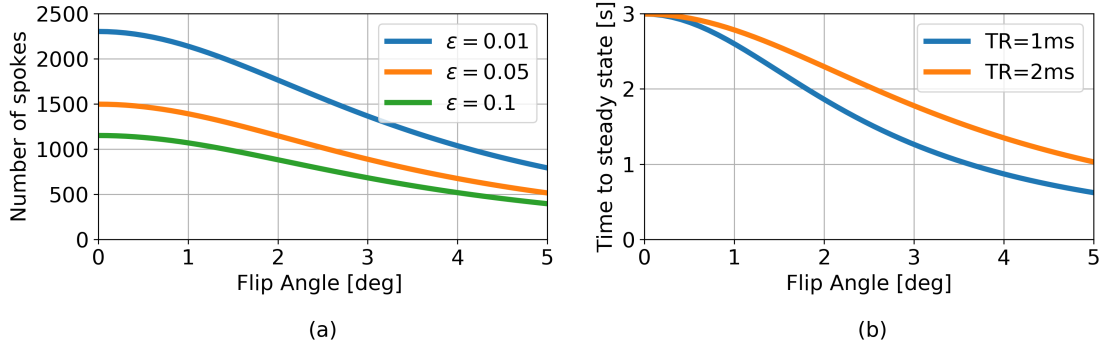


**Figure 6.16:** Simulation of the transient approach to steady state. **(a)** Comparison of different values of  $\epsilon$  ( $T_1=1s$ ,  $TR=2ms$ ) **(b)** Time required to reach steady state with different TRs ( $T_1=1s$ ,  $\epsilon=0.05$ ). A shorter TR will, even though it produces less  $T_1$  recovery, lead to a quicker approach to the steady state.

which is just beyond the maximum  $3^\circ$ . A good compromise for a  $1mm^3$  protocol might therefore be a readout bandwidth of  $\pm 32kHz$  and a flip angle of  $3^\circ$ .

### Optimal $T_2$ Contrast

In a typical spin echo experiment used for  $T_2$  mapping, a large number of TEs are used to accurately capture the  $T_2$  decay [232]. Given a maximum desired TE, shorter TEs can be acquired without additional acquisition time using repeated spin echoes. In a  $T_2$  prepared RUFIS experiment on the other hand, each TE is acquired individually and therefore the TE of the  $T_2$  preparation has to be tuned for optimal  $T_2$  quantification. Optimal measurement for a single component  $T_2$  measurement consists of two echo times [233, 234]. While the existence of multiple  $T_2$  components in WM is well established [19], multi-component  $T_2$  mapping requires a large number of echo times which is not feasible with RUFIS. Therefore, despite the demonstration of multi-TE  $T_2$  imaging with RUFIS, the discussion will be limited to optimisation of a single TE. Here, the optimisation method presented by Shrager et al. will be used [235], ignoring the effects off  $T_1$  relaxation from the RUFIS readout.

The optimal set of acquisition parameters in a  $T_2$  mapping experiment should minimise the normalised variance of the estimated  $T_2$  ( $\hat{T}_2$ )

$$\bar{\sigma} = \frac{\sigma(\hat{T}_2)}{T_2} \quad (6.13)$$

**Table 6.2:** Optimised TEs ( $TE_{opt}$ ) for single TE measurement of  $T_2$  in WM, GM and both WM and GM, together with the  $T_2$  range used for the optimisation ( $T_{2,A}$  to  $T_{2,B}$ ). Reference  $T_2$  at 3T values taken from Stanisiz et al. [34]

Tissue	$T_{2,A}$ [ms]	$T_{2,B}$ [ms]	$TE_{opt}$ [ms]
WM	59	79	75
GM	89	109	108
WM+GM	59	109	87

To find the set of TEs that minimize  $\bar{\sigma}$ , Shrager et al. used linearised least squares analysis, assuming a single exponential decay. Let  $\tau_i = TE_i/T_2$ , then equation (6.13) can be expressed as

$$\bar{\sigma}^2 = \left( \frac{\sigma}{M_0} \right)^2 \cdot g^2(\tau_1, \tau_2, \dots, \tau_n) \quad (6.14)$$

$$g^2 = \frac{a}{ac - b^2}, \quad a = \sum_{i=1}^n e^{-2\tau_i}, \quad b = \sum_{i=1}^n \tau_i e^{-2\tau_i}, \quad c = \sum_{i=1}^n \tau_i^2 e^{-2\tau_i}. \quad (6.15)$$

where  $\sigma/M_0$  is the SNR of the acquisition, which does not depend on the TE. Finding the optimal TEs is thus reduced to finding the set of  $\tau_i$  which minimize  $g$ . Optimising the acquisition for  $T_{2,A} < T_2 < T_{2,B}$  can be formulated as

$$g^* = \min_{\{t_i\}} \left[ \max_{T_A \leq T_2 \leq T_B} g \left( \frac{t_1^*}{T_2}, \frac{t_2^*}{T_2}, \dots, \frac{t_n^*}{T_2} \right) \right] \quad (6.16)$$

where  $\tau_i^*$  are the optimal sampling times. This optimisation problem can be expressed in words as: find the set of  $t_i$ s which minimises the maximum of  $g$  over the range of  $T_2$ s of interest, i.e. minimise the maximum possible variance in the  $T_2$  estimate over a given range.

In  $T_2$  mapping in the brain, white and gray matter are usually the tissues of interest. The acquisition should therefore be optimised for  $T_{2,WM} \approx 70\text{ms}$  and/or  $T_{2,GM} \approx 100\text{ms}$  (at 3T) [34]. With  $T_2$  prepared RUFIS,  $t_1 = 0$  corresponding to the RUFIS segment before the  $T_2$  preparation. Here, the optimal TE for a single  $T_2$  preparation is calculated. Figure 6.17 shows maximum value of  $g^2$  for three different ranges of  $T_2$ s: WM, GM, and WM+GM. The  $T_2$  range for each tissue was set to  $T_2 \pm 10$  ms to account for normal variability and partial volume effects. The optimal TEs, presented in table 6.2, were 75ms for WM, 108ms for GM, and 87ms for WM and GM combined.

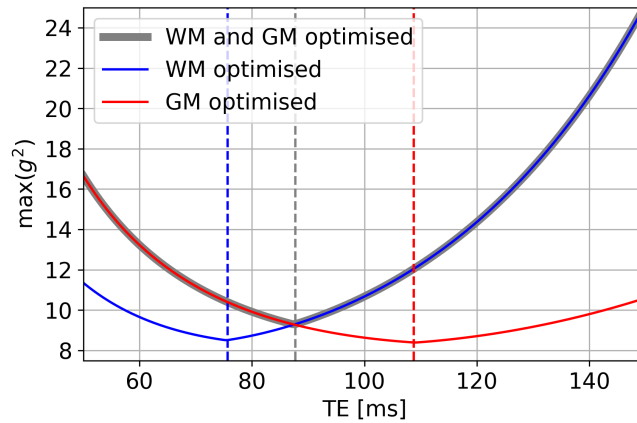


**Figure 6.17:** Maximum value of  $g^2$  for different range of  $T_2$ . The minimum of each curve, indicated with vertical dashed line, is the optimum TE for the given range of  $T_2$ .

The theory presented by Shrager et al. assumes a spin echo acquisition, and does not account for  $T_1$  saturation effects in RUFIS. The theory should therefore only be used to provide guidance, and will not be directly applicable to multiple  $T_2$  preparations.

Another consideration for  $T_2$  quantification is the difference in SNR between the two echo times. In a two point measurement, as described here, the two data points should have equal SNR for optimal parameter quantification, as in the case for VFA  $T_1$  mapping described earlier where the two flip angles were chosen to result in the same signal intensity [149]. The same applies for  $T_2$  mapping as well [233]. This can either be achieved through additional averaging, but in a combined sequence like MUPA, it would instead be better to change the flip angles between the segments to balance the SNR. For the  $T_2$  quantification this results in a higher flip angle after the  $T_2$  preparation to balance the SNR for the  $T_2$  decay.

#### 6.4.6 Sequence Validation - Phantom Experiment

Phantom experiments were carried out to validate the sequence design and development, by showing that change in acquisition parameters can be properly modelled and do not change the quantitative results. In addition, the phantom experiment also allowed the accuracy of MUPA to be compared to calibrated  $T_1$  and  $T_2$  values.

## Method

The quantitative EUROSPIN phantom was scanned on a GE 3T MR750 scanner using the multi-parametric RUFIS sequence. Four different acquisition schemes were evaluated, shown in figure 6.18. Scheme S.1 and S.2 were used to ensure that the TE can be changed during the scan and to evaluate whether the inclusion of two  $T_2$  preparation periods improves the quantification of  $T_2$ . Scheme S.3 was designed test whether changing the flip angle of the excitation RF pulse during the scan improves the  $T_2$  quantification, to balance SNR as described in section 6.4.5. Finally, scheme S.4 was design to study the effect of changing flip angle and addition of a third  $T_2$  preparation module.

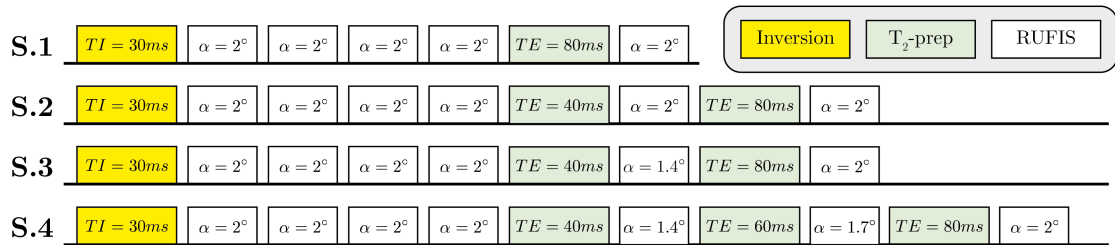


**Figure 6.18:** Outline of the MUPA schemes used for the phantom experiment.

The experiment used the body coil for RF transmit and a 32 channel head coil (Nova Medical) for receive.  $FOV = 192 \times 192 \times 192 \text{ mm}^3$ ,  $resolution = 1.5 \times 1.5 \times 1.5 \text{ mm}^3$ ,  $TR = 2.3ms$ ,  $FA = 2^\circ$ ,  $NEX = 1.25$ ,  $BW = \pm 15.6kHz$ , 256 spokes per segment. Acquisition time was 4:47min for scheme S.1, 5:47min for scheme S.2 and S.3, and 6:48 for scheme S.4. The acquisition used the standard RUFIS k-space spoke trajectory.

Image reconstruction was performed offline in MATLAB, using the KB gridding method. Coil sensitivity maps were generated from the 4<sup>th</sup> image (i.e. just before the  $T_2$  preparation), which has the highest SNR, using the method outlined in chapter 3 for self-calibrated sensitivity maps. Individual coil images were linearly combined, weighted by the conjugate of the coil sensitivity. The real part of the data was used for the fitting, to allow for the negative signal amplitudes which can occur after the inversion pulse.

## Results

The quantitative  $T_1$  and  $T_2$  results from the phantom experiment are presented in figure 6.19 and 6.20, compared to the calibrated  $T_1$  and  $T_2$  values for each vial, as provided by the phantom manufacturer. Overall, the  $T_1$  and  $T_2$  values obtained with MUPA correspond well to the calibrated phantom values. While there are some differences between the four

protocols, it can be concluded that the sequence was successfully implemented and that variations in the protocol are correctly accounted for in the fitting process.

In terms of  $T_1$  estimation, the four schemes perform almost identically, as seen in the correlation and Bland-Altman plots. This is expected, since most of the  $T_1$  information comes from the inversion recovery part of the sequence, which is unchanged between the four protocols. The main difference is in the  $T_2$  measurements, where figure 6.20 shows an improvement in  $T_2$  estimation (for the vial with the longest  $T_2$ ), with scheme S.3 and S.4. The improvement between S.1 and S.4 appears marginal for  $T_2$  values in the range expected in the brain, i.e.  $<200$  ms, however, it could help with quantification of  $T_2$  in regions with partial volume effects close to cerebrospinal fluid (CSF) spaces.

### Discussion and Conclusion

The results from the phantom experiments show that the sequence implementation and parameter fitting model both work as expected, and that the TE and flip angles can be changed and correctly modelled in the parameter fitting.  $T_1$  accuracy remained the same between the different protocols, as expected given equivalent sampling scheme after the inversion pulse up until the  $T_2$  preparation. Accuracy in the  $T_2$  estimation was improved for the vial with long  $T_2$  when two TEs were used, S.1 vs S.2, and using flip angle modulation in the  $T_2$  part of the sequence, S.2 vs S.3. Adding in a third echo time, S.4, did improve the fitting slightly, but at the expense of further increased acquisition time.



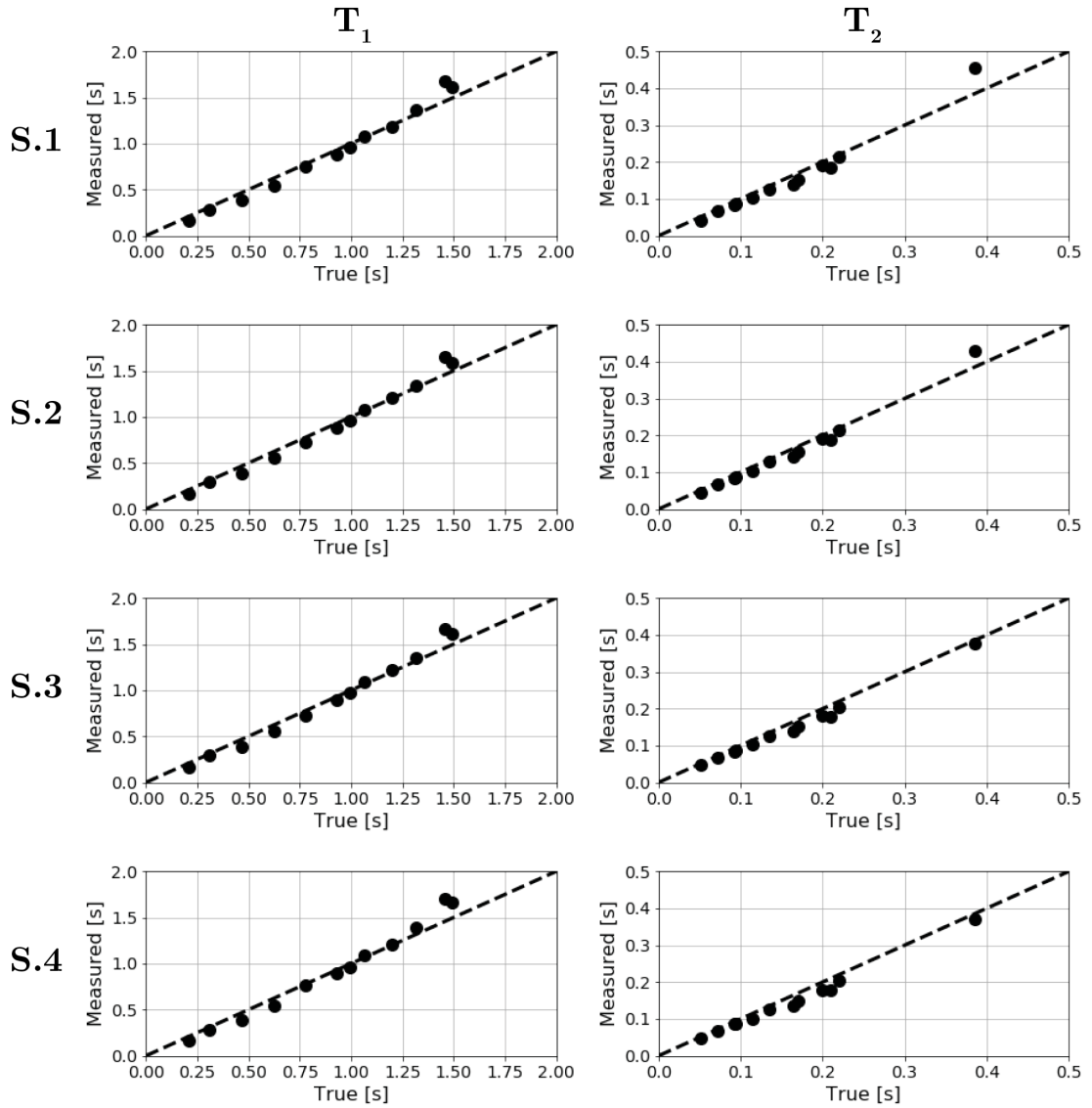


**Figure 6.19:** Results from MUPA phantom experiment showing the estimated  $T_1$  and  $T_2$  values in each vial for the four different acquisition schemes. The true  $T_1$  and  $T_2$  values were provided by the phantom manufacturer. Dashed line is the identity line, i.e. a perfect 1 to 1 correspondence.

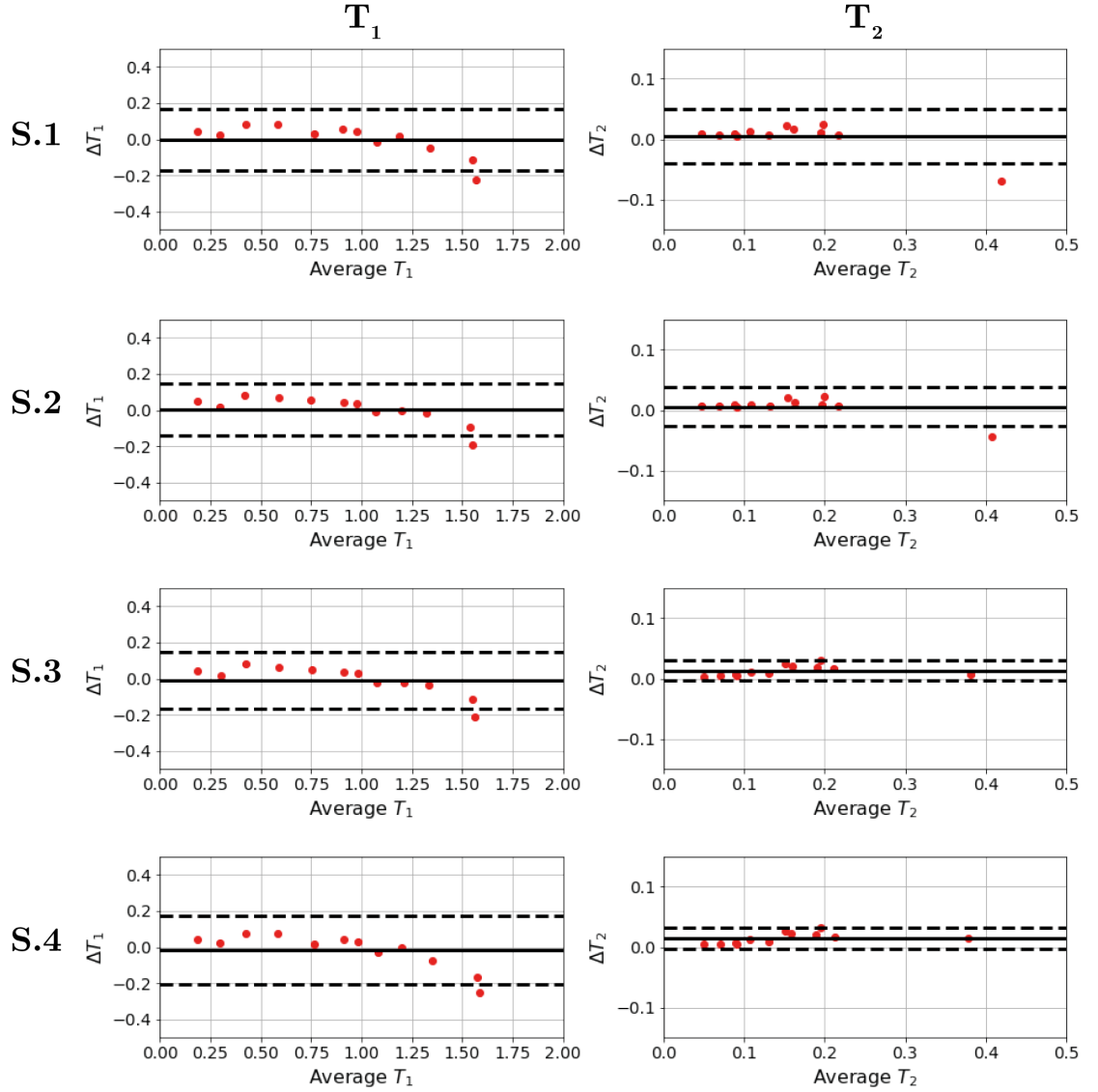


**Figure 6.20:** Results from MUPA phantom experiment visualised as Bland-Altman plots, showing the  $T_1$  and  $T_2$  estimation error in each vial for the four different acquisition schemes. Solid line indicate the average difference and dashed lines the 95% confidence interval (i.e. mean  $\pm 1.96\sigma$ ).

### 6.4.7 Optimised Protocol - Phantom and In Vivo

After validating that the sequence and quantitative fitting methods worked as expected, a second experiment was carried out with an optimised protocol.

#### Method

The EUROSPIN quantitative phantom and a single healthy volunteer were both scanned on a GE MR750 3T scanner using the body coil for transmit and a 32 channel Nova head receive coil. Two protocols were evaluated, a fast and a slow protocol. The following parameters were common for both protocols: BW= $\pm 32$ kHz, FOV= $200 \times 200 \times 200$  mm<sup>3</sup>, voxel size= $1 \times 1 \times 1$  mm<sup>3</sup>, TR=1.88ms, NEX=1.5. The T<sub>2</sub> preparation TE was set to the optimised value for WM and GM, TE=87 ms, as described in section 6.4.5. The number of spokes required to reach steady state was calculated using equation 6.12 with  $\epsilon = 0.02$  which yields  $n = 1029$  spokes. The flip angle was set to the Ernst angle given TR=1.88ms and T<sub>1</sub>=1s, giving  $\alpha = 3.5^\circ$  (RF pulse width 16 $\mu$ s).

The slow protocol was acquired with four segments after the inversion pulse, each with 256 spokes, for a total of 1024 spokes. The fast protocol was acquired with three segments after the inversion, each with 384 spokes, for a total of 1152 spokes. Both protocols had a single T<sub>2</sub> preparation with TE=87ms, as the phantom experiments showed that this resulted in good T<sub>2</sub> estimation for the range of T<sub>2</sub> values expected in the brain, but also to keep the acquisition time around 10 min. Total acquisition time was 11:04 and 8:48 min for the slow and fast protocols, respectively.

A 2D multi-slice multi-echo spin echo acquisition was also acquired as a reference for the T<sub>2</sub> values. The acquisition was performed with TR=2s, TE=10ms, 16 echoes, 3 mm slices with 3 mm gaps. Large gaps between slices were chosen to avoid slice "crosstalk" effects from excitation of neighbouring slices [236]. Acquisition time was 4 min. Image reconstruction of RUFIS data was performed offline in MATLAB using the same method as in section 6.4.6<sup>1</sup>.

#### Results

Figures 6.21 and 6.22 shows the reconstructed images for the healthy volunteer, from the fast and slow MUPA protocols. The first images (TI<sub>x</sub>) show the expected change in T<sub>1</sub> contrast from inversion to steady state. In both cases, the T<sub>2</sub> weighted images are almost

<sup>1</sup>N.B. The file size of the raw data from the slow protocol was over 17 Gb, making reconstruction in MATLAB cumbersome.

iso-intense with little WM to GM contrast. The intensity in the  $T_2$  prepared image is a mix of  $T_1$  and  $T_2$  contrast from adding  $T_2$  weighting to the initially  $T_1$  weighted image, as well as  $T_1$  saturation from the RUFIS readout.

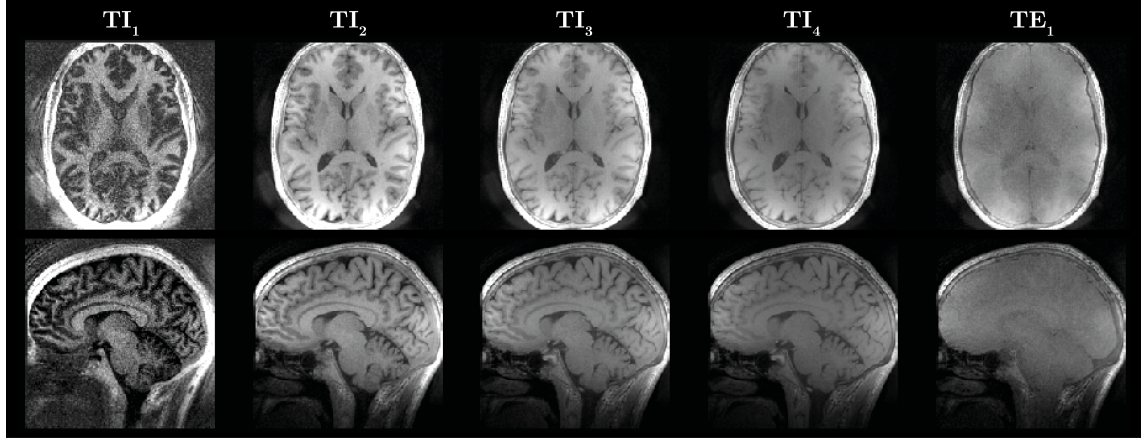


**Figure 6.21:** Reconstructed images from the slow MUPA protocol showing the 4  $T_1$  weighted images following the inversion pulse (TI 1-4) and the  $T_2$  weighted volume.

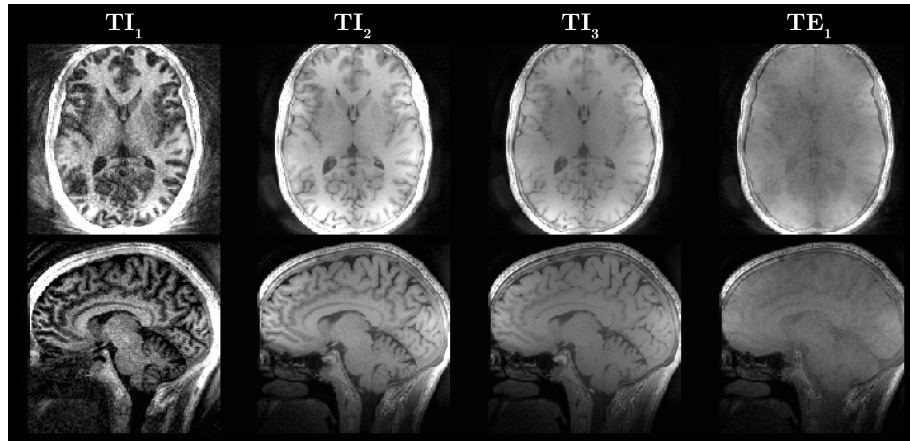


**Figure 6.22:** Reconstructed images from the fast MUPA protocol showing the 3  $T_1$  weighted images following the inversion pulse (TI 1-3) and the  $T_2$  weighted volume.

Quantitative  $T_1$  and  $T_2$  estimates of the phantom data shown in figure 6.23 showed excellent correlation between the two protocols (figure 6.23A).  $T_1$  values deviated from the calibrated values for long  $T_1$ , figure 6.23B, similarly to the previous phantom experiments (figure 6.19). The main difference between the protocols used here and that used in figure 6.19 is the excitation flip angle. Here,  $\alpha = 3.5^\circ$  was used compared to  $\alpha = 2^\circ$ . Higher flip angles increase the effect of  $B_1$  variation and, indeed, the vials which shows the largest  $T_1$  variation are around the edge of the phantom setup, and would thus be more affected by

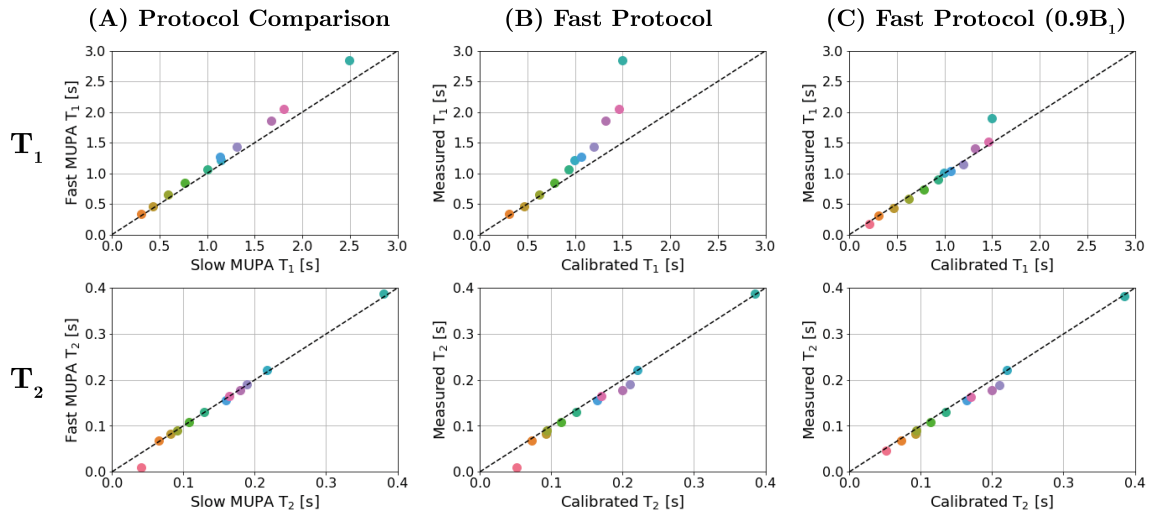


**Figure 6.23:** Results from phantom experiment. Each vial is colour coded for comparison between  $T_1$  and  $T_2$  results. Top row showing  $T_1$  and bottom row  $T_2$ . (a) Comparison between the two protocols showing close to perfect agreement. (b) Fast protocol compared to calibrated phantom values. (c) Fast protocol with reduced  $B_1$  showing better correlation to the calibrated values. Black dashed line indicate line of unity in all plots.

$B_1$  variation. Running the fitting process with a simulated lower flip angle, here  $0.9 \cdot 3.5^\circ = 3.15^\circ$ , resulted in better agreement in  $T_1$  to the calibrated values, figure 6.23C. The  $T_2$  estimates showed a good correlation to the calibrated values, and appear to be unaffected by the flip angle.

The quantitative  $T_1$ ,  $T_2$  and PD maps obtained from the in vivo data are shown in figure 6.24, together with the  $T_2$  and PD map from the spin echo acquisition. The  $T_1$  map showed good WM/GM contrast but the quantitative values were lower than expected, with  $T_1$  around 650 in WM and 750 in GM, see table 6.3. The fast and slow protocol produced slightly different values, but within the error of margin for each ROI. For both protocols, the  $T_1$  estimate in CSF was very noisy, and the estimated  $T_1$  was very low for CSF at around 1.2s. The MUPA  $T_2$  maps produced overall lower  $T_2$  values compared to the spin echo reference data. With MUPA,  $T_2$  in WM was measured as 40ms, while the spin echo acquisition gave a value of approximately 80ms, table 6.3. The MUPA PD maps showed similar WM to GM contrast as the spin echo PD map. However PD estimates in CSF with MUPA were abnormally low, with PD values lower than WM and GM.

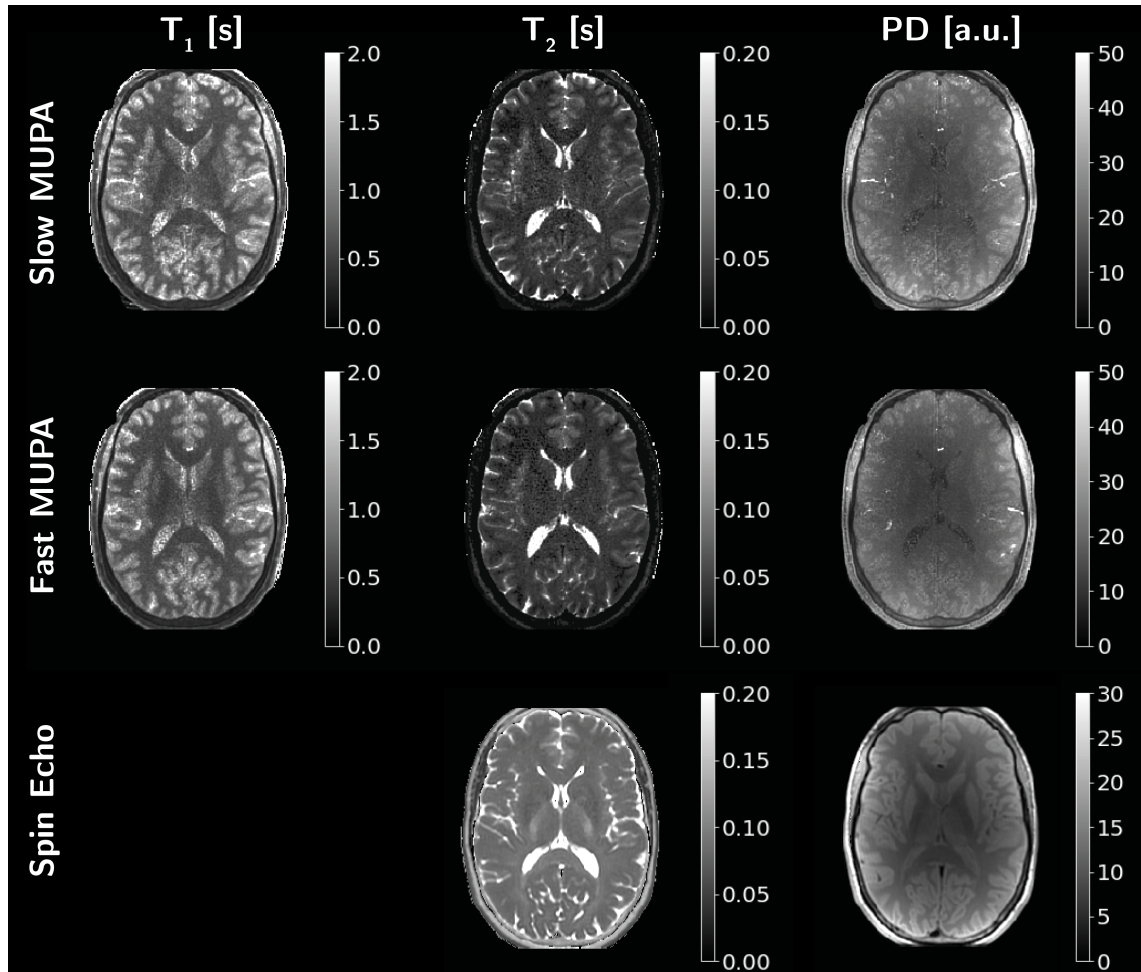


**Figure 6.24:** Quantitative  $T_1$ ,  $T_2$  and PD maps from the two MUPA experiments and  $T_2$  map from the spin echo acquisition. There is a clear underestimation in  $T_2$  with MUPA, and the proton density is also badly estimated with apparent lower PD in CSF than WM and GM.

**Table 6.3:** ROI  $T_1$  and  $T_2$  values given as average values within ROI  $\pm \sigma$ . (WM - Frontal WM, GM - Caudate Nucleus, CSF - Lateral Ventricle)

ROIs	$T_1$ [ms]		$T_2$ [ms]		
	Slow	Fast	Slow	Fast	Spin Echo
WM	$622 \pm 64$	$658 \pm 59$	$39 \pm 7$	$40 \pm 6$	$80 \pm 3$
GM	$767 \pm 111$	$761 \pm 134$	$49 \pm 8$	$47 \pm 10$	$82 \pm 4$
CSF	$1246 \pm 295$	$1271 \pm 429$	$393 \pm 281$	$436 \pm 876$	$1814 \pm 52$

## Discussion

In this section, an optimised MUPA protocol was evaluated in a quantitative phantom and in vivo. Similarly to the previous phantom experiment, good correlation to the calibrated values was observed in the phantom. Despite this, the in vivo results showed discrepancies relative to the reference  $T_2$  map obtained with spin echo acquisition, however. Estimated  $T_1$  values in vivo were also lower than typical values expected in the brain. The estimated PD map showed lower PD values in CSF compared to WM and GM, potentially indicating an issue with the underlying model. Looking at the in vivo images in figure 6.21 and 6.22, the signal in CSF is very low throughout the experiment which would make it difficult to obtain a good fit to the signal model.

### 6.4.8 Discussion about Combined $T_1$ and $T_2$ Mapping

Using magnetisation preparation modules, namely adiabatic inversion and  $T_2$  preparation, RUFIS can be used for quantitative  $T_1$  and  $T_2$  mapping. Through investigation of the sequence design using Bloch simulations and phantom experiments, a new flexible pulse sequence was designed with the capability of quantifying  $T_1$  and  $T_2$  in phantoms accurately. Translation of the method to in vivo experiments, however, proved to be more challenging, producing  $T_1$ ,  $T_2$ , and PD values outside the expected ranges, with underestimated  $T_1$  and  $T_2$ , and with lower PD in CSF than WM and GM. While these values appear to be abnormal relative to conventional measurements, they are similar to those published in the MR fingerprinting (MRF) literature. Recent work by Hilbert et al., studying the effects of MT in MRF, for example, measured  $T_2=35$  ms in frontal WM, when MT effects were not accounted for [237]. Including MT effects in the model increased the value to  $T_2=47$  ms, which is still significantly lower than their CPMG measurement of  $T_2=74$  ms. Hilbert et al. also measured lower PD in CSF than WM and GM, but did not give any further explanation to why this might occur. 3D MRF experiments by Ma et al. also reported low  $T_2$  in WM (35 ms) [238]. Although MUPA is not a MRF method *per se*, there are similarities in that it is a non-steady state sequence with little deadtime.

The parameter estimation in CSF was shown to be very poor with the proposed protocol, with underestimated  $T_1$ ,  $T_2$  and abnormally low PD in CSF. This is likely a result of overall low SNR and small dynamic range of the signal in CSF. The in vivo images in figure 6.21 and 6.22 clearly shows that the signal in CSF is consistently very low, which would make any parameter estimation very difficult. One approach, supported by unpublished

results from our collaborators at GE Healthcare, is to acquire a purely PD weighted image separately and use this as additional information in the fitting process. In particular, they found that the PD estimation was more accurate when this additional acquisition was included, and this also led to some improvement to the other quantitative maps. However, they still observed lower than normal  $T_2$  values, as also observed here, suggesting that there are still gaps in the model.

In the initial phantom experiments where MUPA schemes with multiple  $T_2$  preparations were investigated, the improvement in  $T_2$  fitting was only observed in the long  $T_2$ , and therefore a single  $T_2$  preparation was used in the optimised in vivo experiment. Adding in additional  $T_2$  preparations could potentially improve the  $T_2$  estimation in vivo as it adds additional  $T_2$  information. The process for calculating the optimal TE presented previously only applies to a single TE, and should therefore be extended to multi-TE acquisitions as well as taking the  $T_1$  effects into account. Another aspect of the acquisition scheme is that while sampling at the Ernst angle gives the highest acquired signal, it will result in a lower steady-state longitudinal magnetisation, thus reducing the dynamic range of the  $T_1$  recovery. Further work will focus on implementation of a Monte Carlo simulation framework where different acquisition schemes can be evaluated with different levels of added noise to find the optimal sampling scheme.

As discussed in chapter 2 in section *Theories, Models, and Representations*, a quantitative measurement of  $T_1$  and  $T_2$  is based on a theory, a model and a signal representation. Here, the same theory, model and signal representation is used in phantoms and in vivo, and given that results in the latter have proved to be erroneous, it must be asked which part of the measurement process is inaccurate or inappropriate. The theory used here is that the spin dynamics are governed only by  $T_1$  and  $T_2$  relaxation, and that the signal is proportional to the proton density. One effect that this theory ignores is magnetisation transfer, which recent studies have shown to be non-negligible in steady state acquisitions [70]. This simplified theory remains appropriate in the phantoms, since their macromolecular content is very small, and thus MT effects are negligible, but it leads to incorrect values in vivo. Including MT effects in the theory used here requires expanding the model, and modifying the signal representation. Section 6.5 will outline a signal representation framework for MUPA which incorporates MT effects.



## 6.5 Simulating MT Effects in Multi-Contrast RUFIS

### 6.5.1 Introduction

Quantitative measurement of a given MR tissue parameter is inherently very difficult to perform as the measurement will, to some degree, always be affected by other features of the tissue as well. For instance, in a spin echo experiment, the signal is mainly  $T_2$  weighted, but with a finite TR, there will also be  $T_1$  weighting, although this is typically ignored. In chapter 2, the concept of *Theories, Models, and Representations* in quantitative MRI was discussed, and in this chapter these concepts will be revisited to further investigate the MUPA sequence.

The in vivo MUPA experiments presented in the previous section showed  $T_2$  values that were below the expected range in WM and GM, and strongly deviating from  $T_2$  values obtained with the spin echo acquisition. This was in contrast to the phantom experiments, where an almost perfect agreement was found between the  $T_1$  and  $T_2$  values obtained with MUPA and the calibrated values. The phantom used in these experiments, the EUROSPIN phantom [168], consists of a number of vials with doped agarose gels. There is unfortunately limited documentation on the actual content of the vials, such as agarose concentration and how exactly they are doped, but work from the authors who initially created the phantom suggests that the agar content is in the range of 2-4% (i.e. low) [239]. Low agar concentration means low macromolecular content, typically quantified as the bound pool fraction  $F$  in the magnetisation transfer (MT) literature. Studies on MT have shown that agar content of 2-4% results in  $F$  between 0.5-1% [240, 241], which is much smaller than typical values for brain tissue which are  $F=14\%$  for WM and  $F=6\%$  for GM [242]. This means that the MT effect in vivo is much larger than in the phantom, and therefore MT is a possible candidate for the discrepancy in the quantitative values in vivo.

Briefly, MT is an effect occurring in tissues with both free protons (i.e. water), with a narrow absorption lineshape, and protons bound to macro molecules, with a wide absorption lineshape [182]; referred to as the two pool model. If a narrow bandwidth RF pulse is applied off resonance with respect to the free water signal, it will not excite water protons, but instead saturate the bound protons. Since the two pools are tightly coupled, they can exchange magnetisation in both directions, i.e. saturated magnetisation will exchange from the bound pool into the free pool, and unsaturated magnetisation will exchange from the

free pool into the bound pool. This will lead to a partial saturation of the free pool, and accelerated recovery of the bound pool magnetisation. The partial saturation effect can then be measured by exciting the free water pool, and comparing the resulting signal to an acquisition collected without applying the off resonance pulse. The difference is commonly expressed as the magnetisation transfer ratio (MTR), and has been used extensively to study brain pathology [243, 244, 245].

Even if off-resonance pulses are not explicitly included in an acquisition, MT effects can still manifest in many different ways. In 2D multi-slice experiments, for instance, excitation of one slice effectively acts as an off-resonance pulse on adjacent slices, potentially introducing MT effects [236]. MT effects can also be produced by an on-resonance (excitation) pulse, since the lineshape of the bound and free pool overlap. Recent work by Teixeira et al. showed that quantitative  $T_1$  and  $T_2$  maps acquired with DESPOT1/2 [59] are strongly influenced by MT effects from the excitation pulse [69]. The effect can be mitigated by using multi-band pulses to maintain a constant pulse power while changing the excitation flip angle, thus maintaining the same level of saturation of the bound pool [69]. Work from the same group has also introduced simulation frameworks for modelling the effects of MT on quantitative measurements via the Bloch-McConnell equations, using either the extended phase graph formalism [236] or, more recently, a steady state approach [70].

In the current work, the framework developed by Malik et al. will be used to model the MT effects in  $T_1$  and  $T_2$  prepared RUFIS [70].

### 6.5.2 Purpose

To quantify the effects of magnetisation transfer (MT) on quantitative  $T_1$  and  $T_2$  estimates obtained with MUPA.

### 6.5.3 Method

#### A Matrix Solution to the Bloch-McConnell Equations

The simulation framework presented by Malik et al. was adapted to include the mBIR4  $T_2$  preparation pulse and the Silver-Hoult inversion pulse used in the MUPA experiments [70]. A brief description of the simulation framework and its implementation will be presented here; for details, please refer to the publication by Malik et al. and the source code available online<sup>2</sup> [70].

---

<sup>2</sup>[https://github.com/mriphysics/ihMT\\_steadystate](https://github.com/mriphysics/ihMT_steadystate)

As previously mentioned, brain tissue can be modelled as being composed of two pools: a free water pool ( $f$ ) and a bound, or semi-solid, pool ( $b$ ). To model the magnetisation evolution, including exchange, the Bloch-McConnell (BM) equations, which are a combination of two different theories, can be used. The most fundamental description of the magnetisation are the Bloch equation which can be used to model the magnetisation evolution of a single component under the influence of  $T_1$  and  $T_2$  relaxation [13]. The Bloch equations were modified by McConnell to also include exchange between two pools [246], here between the free and bound pool.

In the model used in the framework presented by Malik et al., the bound pool is further divided into two components: one with dipolar ordering, which gives rise to the inhomogeneous magnetisation transfer (ihMT) effect [247]; and one without dipolar ordering. However, to produce the ihMT effect, off-resonance excitation is required, and as all excitation is on-resonance for MUPA, the dipolar ordered pool is ignored in the following simulations. Thus the magnetisation vector  $\mathbf{M}$  has four components, three for the free pool ( $M_x^f, M_y^f, M_z^f$ ) and one for the bound pool  $M_z^b$ .

The BM model is composed of a set of differential equations which describes the effect of an RF pulse on the system, modelling: nutation of the free pool, saturation of the bound pool, relaxation, and exchange between the pools. Periods during which no RF is applied are described in a similar way but without nutation or saturation. Malik et al. showed that the evolution of the magnetisation vector can be described as a homogeneous differential equation in matrix form as

$$\dot{\tilde{\mathbf{M}}} = \tilde{\mathbf{A}}\tilde{\mathbf{M}} \quad \text{where} \quad \tilde{\mathbf{M}} = \begin{bmatrix} \mathbf{M} \\ 1 \end{bmatrix} \quad \tilde{\mathbf{A}} = \begin{bmatrix} \mathbf{A} & \mathbf{C} \\ 0 & 0 \end{bmatrix} \quad (6.17)$$

The matrix  $\mathbf{A}$  describes the effects of an applied  $B_1$  field, relaxation effects, and exchange, according to the BM theory, while the matrix  $\mathbf{C}$  describes the regrowth of the longitudinal component from  $T_1$  recovery. If matrix  $\mathbf{A}$  is constant over a short time period  $\Delta t$ , i.e. for constant  $B_1$ , the magnetisation evolution can be described as

$$\tilde{\mathbf{M}}(t + \Delta t) = \exp(\tilde{\mathbf{A}}(t)\Delta t)\tilde{\mathbf{M}}(T). \quad (6.18)$$

The net effect of an RF pulse or delay of duration  $\tau = N\Delta t$  can be described as

$$\tilde{\mathbf{M}}(t + \tau) = \tilde{\mathbf{X}}\tilde{\mathbf{M}}(t) \quad (6.19)$$

where

$$\tilde{\mathbf{X}} = \prod_{n=1}^N \exp(\tilde{\mathbf{A}}(n\Delta t)\Delta t) \quad (6.20)$$

which can include time varying  $B_1$  fields as is necessary for modelling adiabatic RF pulses for instance.

In an MR acquisition, it is common to have recurrent sequence elements, such as identical RF pulses and delays of constant length. With this framework, simulation of an MR acquisition can be reduced to calculation of a small number of  $\tilde{\mathbf{X}}$  matrices which are repeatedly used. For the MUPA experiment, the following matrices are needed

- $\tilde{\mathbf{X}}_{T_1}$ : Effect of the inversion pulse
- $\tilde{\mathbf{X}}_{T_2}$ : Effect of the  $T_2$  preparation pulse
- $\tilde{\mathbf{X}}_{\alpha}$ : Effect of the excitation RF pulse
- $\tilde{\mathbf{X}}_{TR}$ : Effect of the TR, i.e. time between RF pulses
- $\tilde{\mathbf{X}}_{ramp}$ : Effect of the ramps between segments
- $\Phi = \text{diag}[0, 0, 1, 1]$ : Spoiling of the transverse magnetisation

Using these matrices, the dynamics of the whole MUPA sequence can be modelled through repeated multiplication of the different  $\tilde{\mathbf{X}}$  matrices and the spoiling matrix with the magnetisation vector  $M$ .

## Simulations

Simulations of the MUPA sequence were performed in MATLAB using the framework described above. RF pulses were discretised with  $2\mu\text{s}$  resolution. A tissue model based on parameters from the internal capsule was used, with  $T_1/T_2$  of the free pool of 650/80 ms and a bound pool fraction of 14.7% [247]. A MUPA sequence was simulated for parameters equivalent to the "fast protocol" in the in vivo experiment in the previous section. The result of the simulation is a time series of the magnetisation at each time-point during the acquisition. From this, the average transverse magnetisation within each RUFIS segment

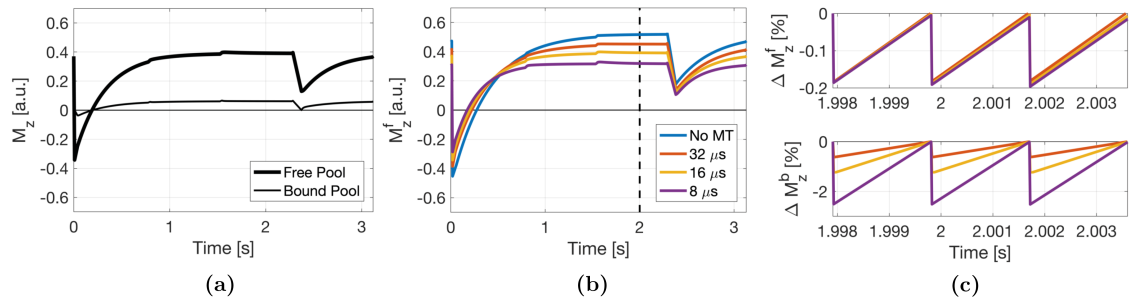
was calculated as a representation of the voxel value expected in an MRI experiment. The simulation ran the MUPA sequence five times, in order to reach steady, with only the results of the last loop stored. The fitting routine used for the in vivo experiment, described in section 6.4.6, was then used to obtain  $T_1$ ,  $T_2$  and PD estimates from the simulation.

In the MUPA acquisition, there are two types of RF pulses: adiabatic preparation pulses ( $T_1$  and  $T_2$ ) and ultra-short hard excitation pulses. While there is expected to be some MT effect from the preparation pulses, the most relevant effect here is from the excitation pulses. To quantify this effect, the simulation was performed with excitation RF pulse widths from 4 to 60  $\mu$ s. The nominal pulse width for this flip angle would typically be 16 $\mu$ s, this will therefore be the reference. For comparison purposes, the simulation was also performed without MT effects included, which was achieved by setting the exchange constant between the free and solid pool to 0.

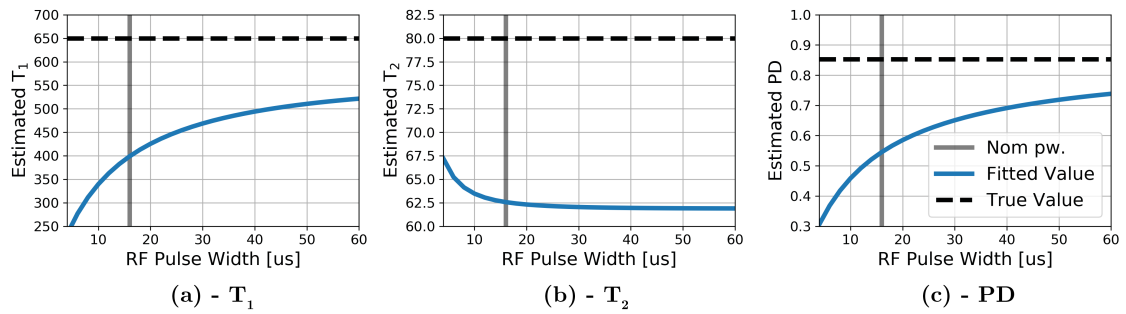
#### 6.5.4 Results

Figure 6.25 shows the magnetisation evolution of the MUPA sequence, from which several key results can be observed. Firstly, figure 6.25a shows that the longitudinal magnetisation of the free and bound pools evolve in a similar way during the acquisition, first being inverted, recovering, and then being attenuated by the  $T_2$  preparation. In figure 6.25b, the longitudinal magnetisation of the free pool is shown in the absence of MT, and under the MT effect of three different RF pulse widths. When MT effects are included, the signal from the free pool is decreased, with greater decrease for shorter pulse width, which can be explained by the results in 6.25c, showing greater saturation of the bound pool with shorter pulse width. The more the bound pool is saturated, the more the free pool will be saturated through exchange with it. Shorter pulse width will thus lead to an overall decrease in the free pool signal, as seen in 6.25b.

If MT is not included in the simulation, the MUPA fitting should produce  $T_1$  and  $T_2$  estimation that are identical to the true values used in the simulation. Indeed, the estimated values correspond well to the true values:  $T_1=0.65$ s,  $T_2=0.08$ s, PD=0.86 (i.e. 1-F). When MT is included, all parameters are underestimated, as shown in figure 6.26. As the pulse width is increased, i.e. as MT effects are reduced,  $T_1$  and PD increase, with PD appearing to asymptotically approach its true value while  $T_1$  appears to converge towards a value which remains a large underestimation.  $T_2$  is consistently underestimated at all



**Figure 6.25:** Results from MT simulation of the MUPA acquisition using the BM theory. (a) Time evolution of the longitudinal magnetisation of the free and bound pool with 16µs RF pulse width. (b) Evolution of the free pool with different pulse widths, and without MT, showing signal reduction as the pulse width is decreased. (c) Percentage signal change of the free pool ( $M_{zf}$ , top) and bound pool ( $M_{zb}$ , bottom) over 3 TRs, at  $t = 2$  s, as indicated by the dashed line in (b), normalised to the first data point. With shorter pulse widths, the bound pool saturation is greater, which in turn causes a reduction in the signal of the free pool, as indicated by the lower signal amplitude of the purple line.



**Figure 6.26:** Effects of MT on the MUPA parameter estimates showing the estimated  $T_1$  (a),  $T_2$ , (b) and PD (c). All quantitative parameters are consistently underestimated. (Nom pw.: nominal pulse width)

pulse widths, only showing a small increase (i.e. trend towards the correct value) at short pulse widths.

### 6.5.5 Conclusion and Discussion

Magnetisation transfer is expected to have a substantial effect on the quantitative parameter estimates in the MUPA experiment, as demonstrated here through simulations. Simulations suggest that  $T_1$  and  $T_2$  will be consistently underestimated, which is consistent with the results observed in vivo. These effect cannot be corrected for using simple correction factors or functions, since the MT effect depends on the tissue composition and would therefore have to be included into the fitting process. The signal representation used here to model MT could be used for the curve fitting, however it is very compu-

tationally demanding as the  $\tilde{X}$  matrices have to be calculated for each combination of parameters. The search space of parameters also increases when the bound pool fraction  $F$  is included in addition to  $T_1$ ,  $T_2$ , and PD. The BM model also requires parameters for the exchange time between the different pools. This can be included in the fitting, as is done in mcDESPOT [248], but will further increase the multi-dimensional search space and is thus likely to reduce the quality of the fit. Alternatively, a fixed value for the exchange rate between the two pools can be assumed, typically chosen as the expected value for WM [237]. While this makes the fitting easier, it is an obvious simplification of the system and limits the applicability of the technique to only healthy brain tissue.

## 6.6 Chapter Discussion and Conclusion

### 6.6.1 Silent $T_2$ Mapping

The work presented in this chapter developed from the aim of performing silent  $T_2$  mapping with RUFIS. Simulations and phantom experiments using a multi-TE RUFIS acquisition demonstrated that  $T_2$  weighting can be obtained but that  $T_1$  will influence quantitative measurements with RUFIS, and therefore a multi-contrast approach with combined  $T_1$  and  $T_2$  mapping, MUPA, was developed. The MUPA sequence estimated  $T_1$  and  $T_2$  with high accuracy in a quantitative phantom, but the results diverged from the expected values in vivo. The variations observed here indicate that additional degrees of freedom need to be taken into account, most likely MT.

However, variability between methods for quantitative parameter mapping is not uncommon and one of the major issues in qMRI [249]. The issue is well known in the  $T_1$  mapping literature, where numerous commonly used methods produce different values [177].  $T_2$  mapping on the other hand is most typically performed with spin echo sequences, which reduces the variability. However, with steady state techniques such as DESPOT2 [59], PLANET [250], and MRF [60, 237] there is variability in their quantitative estimates. One explanation for variability between techniques could be that the models and signal representations used are too simplistic. Important features of the acquisition, such as spoiling errors and MT effects are commonly ignored as it is too difficult to model properly. In some situations, it is enough to achieve high precision in the measurement over a long period of time, such as in a longitudinal clinical trial. The accuracy, or bias,

in the measurement only becomes relevant when the measurement is compared to other techniques or other sites, which, eventually will be required if qMRI is to be used clinically.

While the MUPA sequence is the first realisation of quantitative  $T_2$  mapping with RUFIS, Schulte et al. used a combination of spin echo and BURST-ZTE readouts for silent  $T_2$  mapping (11.6dB(A) increase above ambient noise levels) [251]. They reported  $T_2$  in WM of 65-75ms which corresponds well to literature values. The acquisition time for a dual echo acquisition, with  $TE=89.7$  and 179ms, at  $1.7 \times 1.7 \times 1.7 \text{ mm}^3$  isotropic resolution was 11.5 min. Another approach to  $T_2$  mapping with reduced acoustic noise is to use sinusoidal waveforms with a spin echo acquisition. Hennel demonstrated fast spin echo imaging with up to 40dB(A) reduction in acoustic noise compared to standard a pulse sequence with linear ramps [95].

### 6.6.2 MT Effects and Multi-Component $T_2$ Relaxation

Magnetisation transfer effects were shown to affect the magnetisation evolution of the free water pool in the MUPA experiments. Simulations showed that both  $T_1$  and  $T_2$  will be underestimated if MT effects are not included in the fitting, consistent with what was observed in the in vivo experiment. The phantom experiments on the other hand did not show the same discrepancy, which is likely to be explained by the low macromolecular content in agarose gels used, highlighting the importance of in vivo evaluation of quantitative methods. While phantoms are useful for initial validation of the pulse sequence, unless the composition of the phantom is the same as brain tissue, it will not be a fully representative measurement. In addition, factors such as physiological noise, including motion and fluctuations in  $B_0$  from breathing, and coil loading would also need to be accounted for to achieve a realistic tissue phantom.

Further work on MUPA will include MT in the theory and signal representation to achieve accurate and precise measurements of  $T_1$  and  $T_2$ . To account for the MT effects, there also needs to be enough information in the measurement to accurately estimate, here, the bound pool fraction  $F$ . It is not known if the current schemes would support such measurement, but additional MT information could be encoded by changing the width of the excitation RF pulses while maintaining the same flip angle. Or, the scheme could potentially be combined with interleaved off-resonance saturation, as in a standard MT experiment.



One aspect of  $T_2$  relaxometry that has yet not be discussed in this chapter is the multi-component  $T_2$  relaxation that occurs, in particular, in white matter [19]. Water trapped between the myelin bi-layers has a  $T_2 \approx 20\text{ms}$ , compared to the intra-extra cellular water with  $T_2 \approx 80\text{ms}$  [19]. In a spin echo acquisition with a TE that is longer than the myelin water  $T_2$ , the influence of the short  $T_2$  component is low. With  $T_2$  prepared RUFIS on the other hand, the RUFIS segment before the  $T_2$  preparation has an effective TE=0, and will thus contain signal from the myelin water. The  $T_2$  weighted volume, with TE $\approx 80\text{ms}$  will have no contribution of the myelin water, thus resulting in an apparently fast decay of the signal. This could lead to an underestimation of  $T_2$ , however, simulations will be required to verify this hypothesis. Related to this is the exchange between the myelin water and intra-extra cellular water, similar to the exchange between the free and solid pool in the Bloch-McConnell theory. The simulation framework used to model MT effects could be reformulated to model both the bi-exponential  $T_2$  decay and the exchange between the two water pools.

## 6.7 Publications and Contribution

### 6.7.1 Publications

This work has in part been published in

1. Wiesinger F, **Ljungberg E**, Engström M, Kaushik S, Wood T, Williams S, et al. *PSST... Parameter mapping Swift and Silent*. In: Proc Intl Soc Mag Reson Med 28. 2020. (Accepted)
2. **Ljungberg E**, Wood T, Solana AB, Burns B, Williams SCR, Wiesinger F, & Barker GJ, (2019). *Silent Multi-Contrast Neuroimaging*. In ESMRMB 2019, 36th Annual Scientific Meeting, Rotterdam, NL (p. S07.03). Rotterdam.
3. **Ljungberg E**, Burns B, Wood T, Kolind S, Wiesinger F, & Barker GJ, (2019). *Rapid, multi-TE, T2-prepared RUFIS for Silent T2-weighted imaging*. In Proc. Intl. Soc. Mag. Reson. Med 27 (p. 4571). Montreal.
4. Wiesinger F, Janich MA, **Ljungberg E**, Barker GJ, Solana AB. *Silent, 3D MR Parameter Mapping using Magnetization Prepared Zero TE*. In: Proc Intl Soc Mag Reson Med 26. Paris; 2018. p. 0061.

### 6.7.2 Contribution

The original idea to combine  $T_1$  and  $T_2$  mapping came from Dr. Wiesinger and was presented at ISMRM 2018 [205]. I was co-author on this work and contributed to the abstract. After the abstract I developed a PSD independently as well as the fitting method. Dr. Brian Burns provided the pulse sequence code for the  $T_2$  preparation and MATLAB code for designing the mBIR-4  $T_2$  preparation pulse. Dr. Tobias Wood provided very helpful guidance on the Bloch-McConnell equations and implementation of the simulation framework.

## Chapter 7

# Motion Correction with Self-Navigated RUFIS

### Contents

---

7.1	Introduction	196
7.2	The Spiral Phyllotaxis Trajectory	199
7.3	Translation and Rotation Correction in k-space	213
7.4	A Numerical Brain Phantom	215
7.5	Using 3D Phyllotaxis for Rotation Correction	216
7.6	Using 3D Phyllotaxis for Translation Correction	229
7.7	Rigid Body Motion Correction	232
7.8	Chapter Discussion and Conclusion	241
7.9	Publications and Contribution	245

---

### Summary

IN this chapter, a new k-space trajectory, the 3D spiral phyllotaxis trajectory, is introduced into RUFIS, to enable a self-navigated acquisition. A motion correction framework built on volume co-registration in k-space is developed and verified through simulations in a numerical brain phantom and in a MR experiment using a phantom.

## 7.1 Introduction

### 7.1.1 Motion in MRI

Image acquisition in Magnetic Resonance Imaging (MRI) requires the object being imaged to be static over the time scale of the acquisition to avoid image artefacts. Rapid imaging techniques such as echo-planar imaging (EPI), used for functional MRI (fMRI), where images are acquired in a few few seconds, can resolve some patient motion and correct for motion between images in post processing [170]. High resolution structural image however typically requires several minutes to acquire a single image, and thus subject motion during this time will produce artefacts [252].

Motion artefacts manifest in different ways depending on the k-space sampling strategy. Figure 7.1 shows a simple comparison of image artefacts produced by head motion in an acquisition using the Rotating Ultra-Fast Imaging Sequence (RUFIS), compared to Cartesian spoiled gradient echo (SPGR). In a Cartesian acquisition, motion manifests mainly as ghosting artefacts in the phase encode direction, due to inconsistencies between phase encoding steps. This is seen in figure 7.1d where the phase encode direction is left-right. In radial imaging, the topic of this thesis, motion instead manifests as blurring and streaking artefacts, as seen in figure 7.1b. With each spoke sampling the centre of k-space, the low spatial frequencies are repeatedly sampled, resulting in averaging of the motion during the acquisition, i.e. blurring. Radial imaging techniques are therefore considered to be more motion robust, however details are still lost in the final image and thus ability to visualise lesions, for example, is still reduced. Motion correction (MOCO) is therefore still necessary for radial imaging to obtain uncorrupted, high resolution, images.

To reduce motion artefacts in MRI, numerous MOCO techniques have been developed [253], which can be divided into two general classes: prospective and retrospective. In prospective MOCO, the data acquisition is constantly updated with a motion estimate of the subject, in order to acquire and store data that are internally consistent despite the motion, thereby minimising artifacts. In retrospective MOCO, motion corrupted data are acquired and correction is performed in post processing. Both techniques requires a method for estimating the motion of the subject, which will be discussed in the next section.

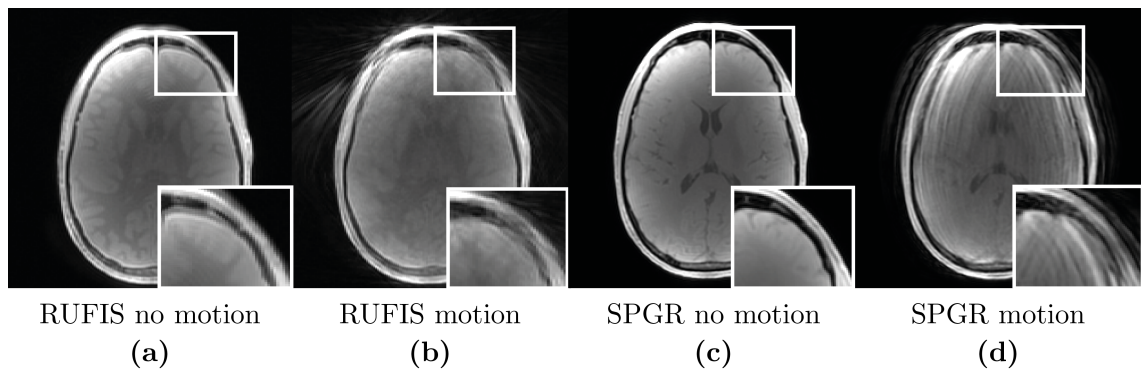


**Figure 7.1:** Comparison of motion artefacts using RUFIS, (a) and (b), and Cartesian spoiled gradient echo, (c) and (d). With RUFIS, streaking and blurring artefacts are observed, while with SPGR, motion appear as ghosting artefacts in the phase encode direction (left-right here). Participant was instructed to move freely throughout the acquisition.

A complete review of MOCO techniques is outside the scope of this thesis. Instead, an overview of the main types of methods available will be given and a more detailed discussion will be devoted to methods that are relevant for MOCO in RUFIS.

### 7.1.2 Estimating Subject Motion in MRI

In order to correct for motion in an MRI experiment, the motion has to be measured. Again, two categories of methods can be identified: external sensors, and methods using data acquired by the MRI scanner. Both of these approaches will be described in this section.

There is a range of external tracking devices that can be used for measuring subject motion during MRI data acquisition. Subject motion can be measured using a camera mounted outside the scanner [254], inside the bore [255], or inside the coil [256], typically coupled with markers attached to the subject. Marker-less optical motion tracking system have also recently been developed, utilising advanced surface registration methods [257]. Motion can also be estimated using active markers, effectively nuclear magnetic resonance (NMR) probes, attached to the subject using a headband for instance [258]. The position of the markers is measured using a rapid imaging sequence interleaved with data collection for the main acquisition; see navigators echoes in the next section. A recent improvement of active markers include the use wireless inductively coupled markers [259].

Methods that use MRI data for measuring motion are referred to as navigator based methods. Navigator is a generic term for a quick acquisition, performed either 1D, 2D or 3D, to estimate the position of the subject, with processing occurring either in k-space [260,

261, 262, 263] or image space [264, 265]. The advantage of using navigators is that motion estimates are obtained directly from MRI data, and thus no additional hardware is required. Two types of navigators will be distinguished: navigator echoes, and self-navigation.

A navigator echo is an additional, short, acquisition inserted into the main imaging sequence in order to estimate the subject position. In lung imaging, for instance, where motion is mainly in the anterior-posterior (AP) direction, a 1D projection in the sagittal plane is sufficient to estimate the position of the chest wall [105]. A popular technique using 2D navigators for prospective MOCO is PROMO (PROspective MOtion correction) [264], in which three orthogonal 2D spiral navigator echoes are acquired in order to estimate head motion. The technique was designed to be used in IR-SPGR or FSE acquisitions where there is an inherent deadtime for  $T_1$  recovery, which leaves a window to acquire the navigators without time penalty. For 3D navigators, spirals are again a commonly used sampling scheme, as they offers rapid sampling of k-space [262, 266].

Self-navigated acquisitions reconstruct multiple low-resolution images from the data acquired in the main acquisition (at  $n$  time points), taking advantage of pulse sequences which include repeated sampling of the centre of k-space. The PROPELLER method (Periodically Rotated Overlapping Parallel Lines with Enhanced Reconstruction) acquires strips of k-space consisting of a number of parallel lines sampling the whole of k-space in one in-plane direction but with very restricted k-space coverage in the perpendicular direction. These strips (or "blades") are centred on the centre of k-space and rotated throughout the acquisition, like a propeller, to obtain full k-space coverage [263]. Motion parameters can be estimated from each strip of k-space and corrected for during reconstruction of the final, complete, data-set in order to obtain a motion free image.

Radial acquisitions lend themselves particularly well to self-navigation since the centre of k-space is inherently repeatedly sampled [267, 268]. With full radial acquisitions (i.e.  $-k_r$  to  $+k_r$ ), 1D projections can be calculated and used for MOCO [267]. RUFIS, however, acquires centre-out spokes (i.e. 0 to  $\pm k_r$  rather than a full acquisition) and thus a 1D projection cannot be readily reconstructed for MOCO.

### 7.1.3 Self-Navigation with RUFIS

In this chapter, a new retrospective MOCO technique, using a self-navigated 3D radial acquisitions with RUFIS is presented, hereafter referred to as *MERLOT* (Motion Elimination in Radial acquisition Leveraging Overlapping Trajectories). To achieve this, a new

k-space trajectory, the 3D spiral phyllotaxis trajectory, is introduced which enables self-navigated acquisition with RUFIS. The implementation details of the new trajectory will be discussed, as well as the effects on the image quality. In vivo experiments will be used to demonstrate how the acquisition can be used to obtain motion estimates from a high resolution, single volume, acquisition.

The MOCO method proposed here is similar to that underlying PROPELLER [263] in that it is a self-navigated acquisition, and thus the similarity in the naming. The data acquisition however is more similar to spherical navigators [262], but instead of only acquiring a single shell, a filled 3D k-space sphere is collected. Rigid body MOCO is, also similar to PROPELLER, divided into rotation and translation estimation, both of which are performed in k-space, as explained in section 7.3. Rotation correction is applied directly to the k-space trajectory (avoiding re-sampling the data themselves) and correction for translational motion is applied as a phase correction to the k-space data. The corrected data can then be combined and the full, motion-corrected, image can be reconstructed. The performance of MERLOT is demonstrated through simulations and phantom experiments in section 7.7. Finally, limitations and potential future improvements are discussed.

## 7.2 The Spiral Phyllotaxis Trajectory

In this section, a new k-space trajectory, the spiral phyllotaxis is introduced. The term *phyllotaxis* (Ancient greek: *phýllon*=leaf and *táxis*=arrangement) comes from the field of botany, in which it refers to the geometric arrangement of leaves on plants. Two forms of phyllotaxis exist: decussate, where the leaves grow in pairs on opposite side of a stem, as commonly seen on flowers and trees; and spiral, where leaves and seeds are arranged in a spiral pattern, found in plants such as sunflowers [269].

The spiral phyllotaxis observed in the head of the sunflower, or pine cones follows a consistent pattern, example in figure 7.2 [269]. Vogel observed that the organisation of branches (leafs or seeds) in spiral phyllotaxis follows two rules [270]. First, the angle between subsequent branches is the same, i.e. a fixed angular increment. Secondly, each new branch is placed at a constant fraction within the largest available gap. Given these two conditions he showed that an angular increment of the golden angle  $\alpha_g = 137.5^\circ$  satisfies both of these criterion. See appendix E for further details about the golden angle and its relation to the golden ratio.

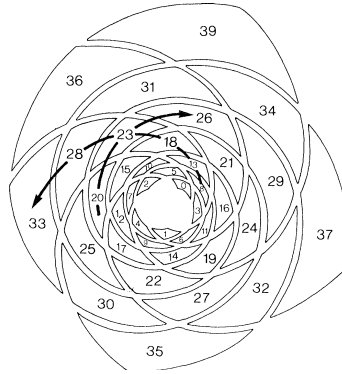


**Figure 7.2:** Spiral phyllotaxis arrangement of leaves. From *Mitchison G.J. Phyllotaxis and the Fibonacci Series. Science, 1977;196(4287):270–5. [269].* Reprinted with permission from AAAS.

The connection between arrangement of flower petals and k-space sampling in MRI might not be obvious, but the two features of the phyllotaxis trajectory described by Vogel makes it particularly useful for MRI applications [271]. Instead of leaves, consider the distribution of spokes in a radial MR acquisition. The first feature, constant angular increment, results in a simple pulse sequence implementation. Secondly, the fact that new spokes will occupy the largest unfilled gap results in a more or less even distribution of spokes, no matter the total number of spokes [271, 272]. Furthermore, any subset of spokes during the acquisition also will form a uniform distribution of spokes, and thus images can be reconstructed at different time points [272]. Radial acquisitions with the golden angle are therefore commonly used for dynamic acquisitions such as heart [273] or contrast enhanced imaging [274]. It should be noted here that there is a difference in golden angle sampling between radial out (as in RUFIS), and full diameter spokes (as commonly used in non-ZTE radial MRI). In full diameter sampling  $\alpha_g = 111.2^\circ$ , while in centre-out sampling  $\alpha_g = 137.5^\circ$ , for more details the reader is referred to appendix E.

Distribution of radial spokes by the golden angle is straight forward in 2D (constant angular increment of  $\alpha_g$ ), but there is no direct analogy in 3D. Piccini et al. introduced a 3D spiral phyllotaxis over one hemisphere in spherical coordinates as [113]

$$r = \text{constant} \quad (7.1)$$

$$\phi_n = \frac{2\pi}{360} \cdot n \cdot \alpha_g, \quad \alpha_g = 137.51^\circ \quad (7.2)$$

$$\theta_n = \frac{\pi}{2} \sqrt{\frac{n}{N}}. \quad (7.3)$$



where  $\phi_n$  and  $\theta_n$  is the azimuthal and polar angle for each spoke. The azimuthal angle  $\phi_n$  is incremented by the golden angle for each sample, while the polar angle  $\theta_n$  changes with the square root of the ratio between the spoke number to the total number of spokes  $N$ . The trajectory calculation can be generalised to cover a whole sphere as

$$r = \text{constant} \quad (7.4a)$$

$$\phi_n = \frac{2\pi}{360} \cdot n \cdot \alpha_g, \quad \alpha_g = 137.51^\circ \quad (7.4b)$$

$$\theta_n = \begin{cases} \frac{\pi}{2} \sqrt{\frac{n}{N/2}}, & \text{if } n < N/2 \\ \pi - \frac{\pi}{2} \sqrt{\frac{N-n}{N/2}}, & \text{if } n > N/2 \end{cases} \quad (7.4c)$$

An alternative formulation of the 3D phyllotaxis trajectory was given by Swinbank and Purser who proposed a  $\cos^{-1}$  modulation of the polar angle [275], which results in a linear  $z$  gradient trajectory<sup>1</sup>. With the square-root modulation used by Piccini et al., slightly more time is spent around the equator in  $k$ -space.

Since only the *spiral* phyllotaxis trajectory is relevant for MRI  $k$ -space sampling, the term *spiral* will be removed for brevity in the remainder of the chapter. The following sections will discuss the practical details of the implementation of such a phyllotaxis trajectory with RUFIS, along with evaluation of the resulting image quality.

### 7.2.1 A New RUFIS $k$ -space Trajectory

To implement the phyllotaxis trajectory in a 3D RUFIS acquisition, the trajectory is first converted from polar coordinates to Cartesian coordinates. This is achieved through the following transformation, where  $G$  is the maximum gradient amplitude

$$x_n = G \cdot \sin \theta_n \cdot \cos \phi_n \quad (7.5)$$

$$y_n = G \cdot \sin \theta_n \cdot \sin \phi_n \quad (7.6)$$

$$z_n = G \cdot \cos \theta_n. \quad (7.7)$$

Given the large increment of the azimuthal angle between spokes ( $\alpha_g = 137.5^\circ$ ), subsequent spokes will be spaced far apart, thus not producing a silent  $k$ -space trajectory. This is shown in figure 7.3 where the phyllotaxis and standard trajectories are compared, showing the

<sup>1</sup>Swinbank et al. used a latitude/longitude coordinate system where  $\theta = 0$  is at the equator, instead of along the  $z$ -axis as used here.

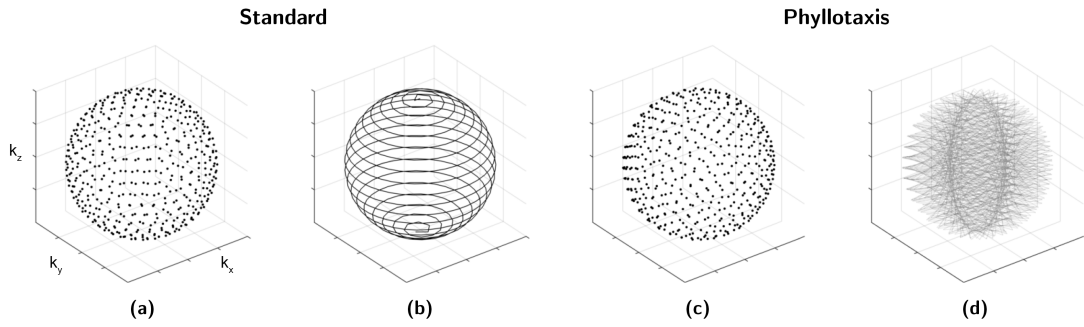


**Figure 7.3:** Comparison of the standard trajectory (a,b) and phyllotaxis (c,d) for a trajectory with 1000 spokes. In (a) and (c) the spoke distribution is visualised as points. In (b) and (d), subsequent spokes are connected by lines, showing a non-smooth path with the phyllotaxis trajectory. (The transparency of the lines were reduced in (d) to better visualise the overlapping lines)

distribution of spokes as points (a,c) and subsequent spokes connected by lines (b,d). When subsequent spokes are connect in the phyllotaxis trajectory, large steps are required, resulting in a seemingly erratic trajectory.

To achieve smooth transitions between spokes, thus enabling silent acquisition, the phyllotaxis trajectory needs to be sub-sampled by a factor  $k \in F_n$  where  $F_n$  is a number in the Fibonacci sequence [113]<sup>2</sup>. The connection between the golden angle and the Fibonacci numbers is not directly apparent, but in short, the angle  $\Delta\phi_0$  between the first and  $k^{th}$  spoke will be the smallest for spoke  $k = F_n$ , and  $\Delta\phi_0$  will scale by  $1/g^n$  [271, 272], see appendix E for further details. The subsampled trajectory is referred to as an *interleave*, corresponding to a full traverse through k-space from pole to pole. Therefore, sub-sampling with a factor of  $k$  results in  $k$  interleaves, denoted as  $n_{int}$ . Figure 7.4 show examples of a phyllotaxis trajectory sub-sampled with  $k = (8, 13, 14)$ . The distance between spokes is smaller with  $k = 13$  than  $k = 8$ , and the path of the interleave is shorter. With  $k = 14$ , i.e. not a Fibonacci number, large steps appear in the trajectory which would result in a non-silent acquisition.

To make the phyllotaxis k-space trajectory practically useful with RUFIS, the individual interleaves are acquired in sequence, resulting in a trajectory traversing k-space along the z-axis  $n_{int}$  times. Due to the limitation of using a segmented structure with equal segment lengths in the implementation of RUFIS used here, each interleave is divided into a whole number of segments which are acquired in order, shown in figure 7.5a. After all segments in one interleave has been acquired, a full pass through k-space has been achieved

<sup>2</sup>The Fibonacci sequence is described by  $F_n = F_{n-2} + F_{n-1}, \forall n > 1$ , where  $F_0 = 0, F_1 = 1$ .

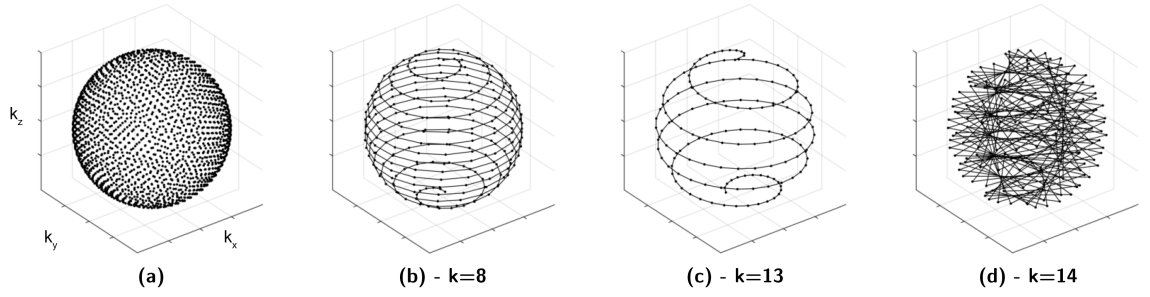


**Figure 7.4:** Phyllotaxis trajectory with 2000 spokes. (a) Spoke distribution as points. Trajectory sub-sampled by factor (b)  $k = 8$ , (c)  $k = 13$ , and (d)  $k = 14$ .

and a low-resolution navigator image can be reconstructed. The next interleave is then acquired, which follows a similar trajectory, but rotated by  $\alpha_g$ . This is similar to a 2D radial golden angle acquisition where each spoke fills the largest gap, but since this acquisition is in 3D, the 2D spoke is now a 3D trajectory through k-space.

The requirement of having a whole number of segments per interleave, and  $F_n$  number of interleaves puts practical limitations on the acquisition. If the total number of spokes in the trajectory is  $N_{total}$ , the spokes per segment  $n_{sps}$ , and number of segments per interleave is  $n_{seg}$  then it should hold that

$$N_{total} = n_{sps} \cdot n_{int} \cdot n_{seg} \quad \text{where} \quad n_{int} \in F_n, \quad n_{sps}, n_{seg} \in \mathbf{N} \quad (7.8)$$

To satisfy these requirements the total number of spokes cannot be freely chosen, but instead has to be a multiple of the relevant Fibonacci numbers. These restrictions which do not exist in 2D golden angle acquisitions comes from the added dimension of 3D sampling. Further investigation will look into how the trajectory design can be made more flexible, but in this thesis the phyllotaxis trajectory will be designed given the requirements in (7.8).

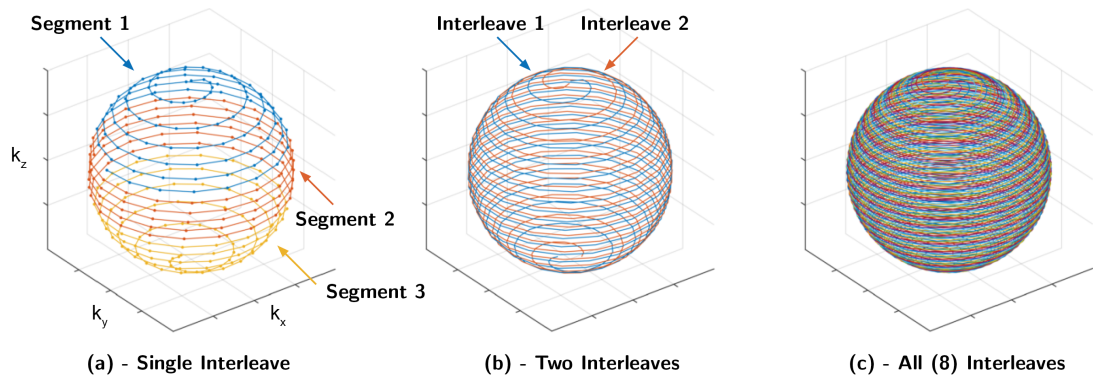


**Figure 7.5:** Description of interleaves and segments in the phyllotaxis trajectory. **(a)** Each interleave consists of a few segments, here example shown with three segments, which are acquired in order. **(b)** As new interleaves are acquired, they fill up current gaps in k-space. **(c)** After all interleaves have been acquired, uniform sampling density has been achieved.

### 7.2.2 Impact on the Acoustic Noise

With the phyllotaxis trajectory, k-space is traversed from pole to pole multiple times to enable reconstruction of separate interleaves. This results in larger updates in the gradient amplitude between spokes, which in turn will impact the acoustic noise. In this section, the acoustic noise produce by RUFIS with different 3D phyllotaxis trajectories is studied and compared to the standard k-space trajectory.

#### Method

Acoustic noise measurements were performed on a 3T GE MR750, using an MR safe microphone (Casella, CEL-495), mounted on a cylindrical phantom placed in the centre of a 32-channel head coil (Nova Medical). The microphone was calibrated prior to the measurements using the provided calibration unit. Measurements were taken for a period of 20s. The microphone was connected to a sound meter (Casella, CEL-63X) which performed the processing of the sound recordings. The time period average A-weighted equivalent continuous sound level (LAeq) as well as the A-weighted sound levels at 11 different octave bands from 16Hz to 16kHz were recorded. To get an estimate of variations in sound pressure over time, the LAfmax and LAfmin (max and min A-weighted sound pressure levels at a fast sampling rate (0.125s)) were also recorded.

The RUFIS acquisition was set up with field of view (FOV)= $192 \times 192 \times 192 \text{ mm}^3$ , resolution= $1 \times 1 \times 1 \text{ mm}^3$ , and flip angle= $1^\circ$ . The acquisition was performed at three different bandwidths 7.8/15.6/3.12 kHz resulting in TRs=6.5/3.4/1.8ms. The standard k-

**Table 7.1:** Trajectories used for the acoustic noise measurement comparing the standard trajectory  $T_s$  and the three phyllotaxis trajectories  $T_{p,x}$ , where  $x$  indicate the number of interleaves. The total number of spokes were matched as closely as possible.

Trajectory	$n_{int}$	$n_{seg}$	$n_{sps}$	$N_{total}$
$T_s$	-	-	512	36864
$T_{p,21}$	21	4	440	36960
$T_{p,13}$	13	6	472	36816
$T_{p,8}$	8	10	460	36800

space trajectory with 36864 number of spokes was compared to three different phyllotaxis trajectories with 21, 13, and 8 interleaves ( $n_{int}$ ), corresponding to different temporal resolutions, listed in table 7.1. The number of segments ( $n_{seg}$ ) per interleave was minimised such that the number of spokes per segment ( $n_{sps}$ ) was less than the maximum of 512. The total number of spokes for each of the phyllotaxis trajectories were matched as closely as possible to the standard trajectory.

## Results

The phyllotaxis trajectory produced a slight increase in the acoustic noise, compared to the standard trajectory for all configurations and bandwidths, figure 7.6. Similar to the acoustic noise measurements presented in chapter chapter 3, the noise levels increased with higher bandwidth. An increase in acoustic noise was observed when the number of interleaves was reduced, as expected since more interleaves will result in a smoother trajectory as shown in figure 7.4. At  $\pm 31.5\text{kHz}$  bandwidth, the difference between the standard trajectory and phyllotaxis with  $N_{int} = 8$ , i.e. the lowest number of interleaves evaluated, was 14.7dB(A), suggesting that a higher number of interleaves should be used to minimise the acoustic noise.

Studying the frequency profile of the acoustic noise produced by the phyllotaxis trajectory, figure 7.7, shows a clear increase in the frequency bands between 1-8kHz, compared to the standard trajectory. With decreasing number of interleaves, the profile stays roughly the same but the overall amplitude across all bands  $> 500\text{Hz}$  increase.

At the point in the trajectory where the spokes cross the equator, the gradient steps in the  $x$  and  $y$  direction are the largest, and thus higher acoustic noise will be produced. Figure 7.8a shows the difference in noise levels during the 20s measurement period. With the standard trajectory, the difference was about 4dB(A) between LAFmax and LAFmin,

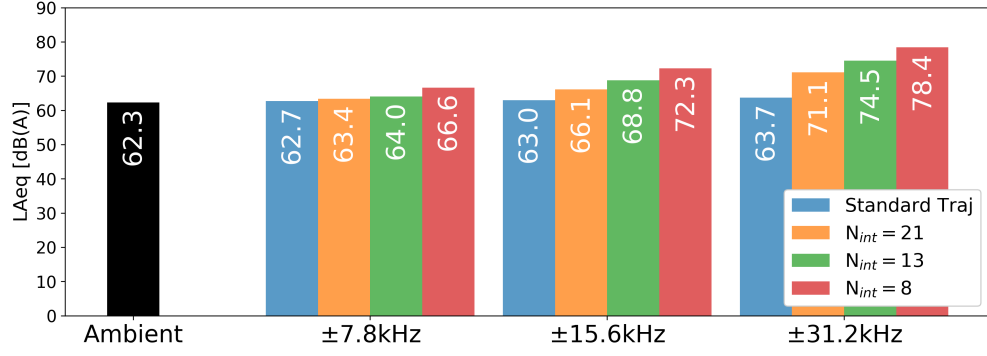


**Figure 7.6:** Comparison of acoustic noise levels with phyllotaxis trajectories with different number of interleaves ( $n_{int}$ ) at different readout bandwidths, compared to the standard trajectory and ambient background noise levels. Numbers in bars show the LAeq sound pressure level in dB(A).

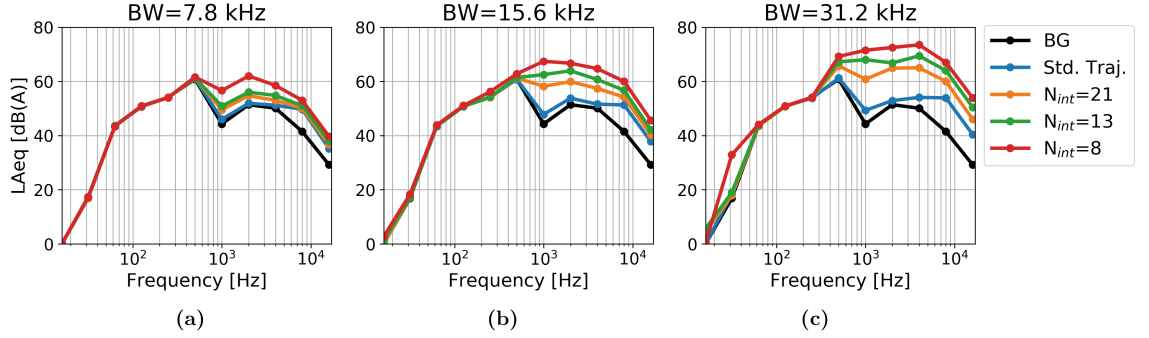


**Figure 7.7:** Comparison of frequency profile of produced by the phyllotaxis trajectory with different number of interleaves ( $n_{int}$ ) at readout bandwidths of (a)  $\pm 7.8\text{kHz}$ , (b)  $\pm 15.6\text{kHz}$ , and (c)  $\pm 31.2\text{kHz}$ , compared to the standard trajectory and background noise levels.

compared to the phyllotaxis trajectory, where 12.4dB(A) difference was observed with  $N_{int} = 8$  at  $\pm 31.2\text{kHz}$ . In general, bigger differences in sound levels were observed with lower number of interleaves, as also shown in figure 7.6. This can be explained by studying the magnitude of the gradient of the gradient waveform from a single interleave  $|\nabla G_{int}|$  played out by the scanner, shown in figure 7.8b. Large  $|\nabla G_{int}|$  means large steps in the gradient waveform, which would predict higher acoustic noise. As expected,  $|\nabla G_{int}|$  reaches a maximum in the middle of the interleave, i.e. when the spokes cross the equator in k-space. With fewer interleaves, the gradient steps in the angular direction are bigger which produces larger  $|\nabla G_{int}|$ , and as a result higher acoustic noise as observed. These results also shows that the gradient waveform steps along the  $z$  axis, i.e. the polar angle, which will increase with larger number of interleaves, appear to be negligible in comparison to the gradient steps in  $x$  and  $y$ , at least for the configurations evaluated here.

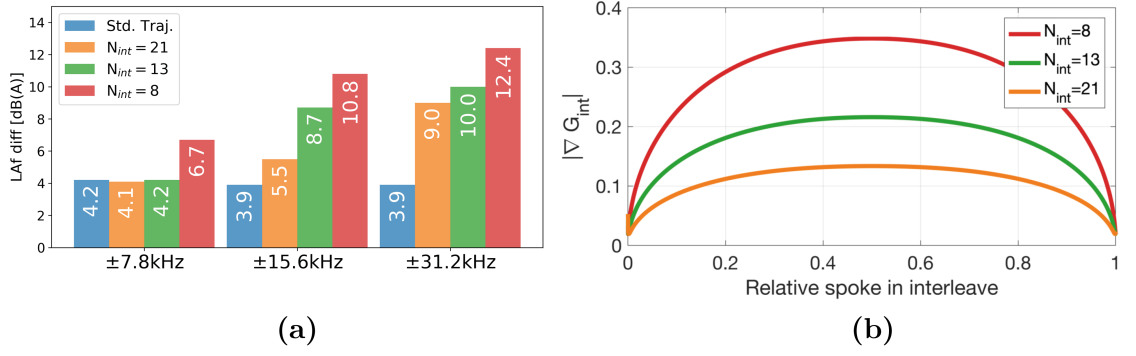


**Figure 7.8:** (a) Difference between LAFmax and LAFmin during the measurement period for the three phyllotaxis trajectories with different number of interleaves ( $N_{int}$ ) compared to the standard trajectory. (b) Magnitude of gradient of the MR gradient waveform for one interleave from the three phyllotaxis trajectories.

## Discussion

Introducing the phyllotaxis trajectory in the RUFIS sequence was shown to affect the acoustic noise levels and frequency profile. Higher number of interleaves produced lower acoustic noise, since sub-sampling with a higher Fibonacci number results in smaller increments of the azimuthal angle between spokes, as shown in section 7.2.1. With a fixed total number of spokes, a higher number of interleaves results in more passes through k-space in the same time, and thus bigger gradient steps in  $z$ . However, the gradient steps in  $z$  appear to be negligible compared to the steps in  $x$  and  $y$  from these measurements.

With  $n_{int} = 21$ , the increase in LAeq compared to the standard trajectory was the highest at 31.2kHz, 7.4dB(A) above ambient. However, the acquisition was still very quiet, measuring only 71.1dB(A). The loudest acoustic noise was measured using the phyllotaxis trajectory with  $n_{int} = 8$  at 31.2kHz, 78.4dB(A).

The requirement for using a large number of interleaves for low acoustic noise puts a practical limitation on the phyllotaxis trajectory. For low resolution acquisitions, which require fewer spokes, the phyllotaxis formulation will require large steps in the polar angle in order to maintain small steps in the azimuthal angle, likely resulting in high acoustic noise. In these situations, the standard trajectory formulation for a single interleave would be better [112].

In conclusion, using the phyllotaxis trajectory increases the acoustic noise levels with RUFIS slightly, but with a high number of interleaves, the increase can be minimised. For all combinations presented here, the noise was below the threshold of 85dB(A).

### 7.2.3 Point Spread Function and Effective Resolution

The point spread function (PSF) can be used to evaluate how the k-space sampling pattern affects image resolution. Introduction of a new k-space sampling trajectory, the spiral phyllotaxis, therefore warrants a study of the PSF. A simulation was performed, comparing the phyllotaxis and standard k-space trajectories. An acquisition with  $N_1 = 13312$  and  $N_2 = 2 \cdot N_1$  spokes, and 128 points per spoke with two-fold oversampling was simulated. A simulated k-space dataset consisting of ones was reconstructed using the Kaiser-Bessel method, from which 2D and 1D point spread functions were obtained.

Figure 7.9 shows a comparison of the PSF obtained from the phyllotaxis and the standard RUFIS trajectory. In the X/Y plane, both the phyllotaxis and standard trajectory produce a relatively similar, radially symmetric, PSF, albeit with the phyllotaxis PSF displaying less abrupt changes at the edge of the field of view. In the X/Z plane however, the trajectories differ substantially.

The image resolution was defined as the full width half max (FWHM) of the PSF. This is equivalent to the distance required between two point sources such that their intensity profiles overlap where they are reduced to half the maximum intensity. The FWHM of the PSF was narrower with phyllotaxis trajectory along  $X$  and  $Y$  but wider in  $Z$  compared to the standard trajectory, as shown in table 7.2.

**Table 7.2:** Full Width Half Max (FWHM) of the point spread function obtained with the phyllotaxis and standard trajectory along each axis.

Axis	Phyllotaxis		Standard	
	N=13312	N=26624	N=13312	N=26624
<b>X</b>	1.41	1.41	1.48	1.48
<b>Y</b>	1.41	1.41	1.48	1.48
<b>Z</b>	1.67	1.67	1.48	1.48

Each interleave in the phyllotaxis acquisition can be reconstructed as a low resolution image, as it covers the whole k-space sphere, albeit in a heavily undersampled manner. A phyllotaxis interleave with  $n$  spokes has a very different sampling pattern compared to an acquisition with  $n$  spokes using the standard trajectory. Each interleave is essentially an undersampled k-space trajectory, and the Nyquist sampling criterion will, by definition, be violated to some extent.



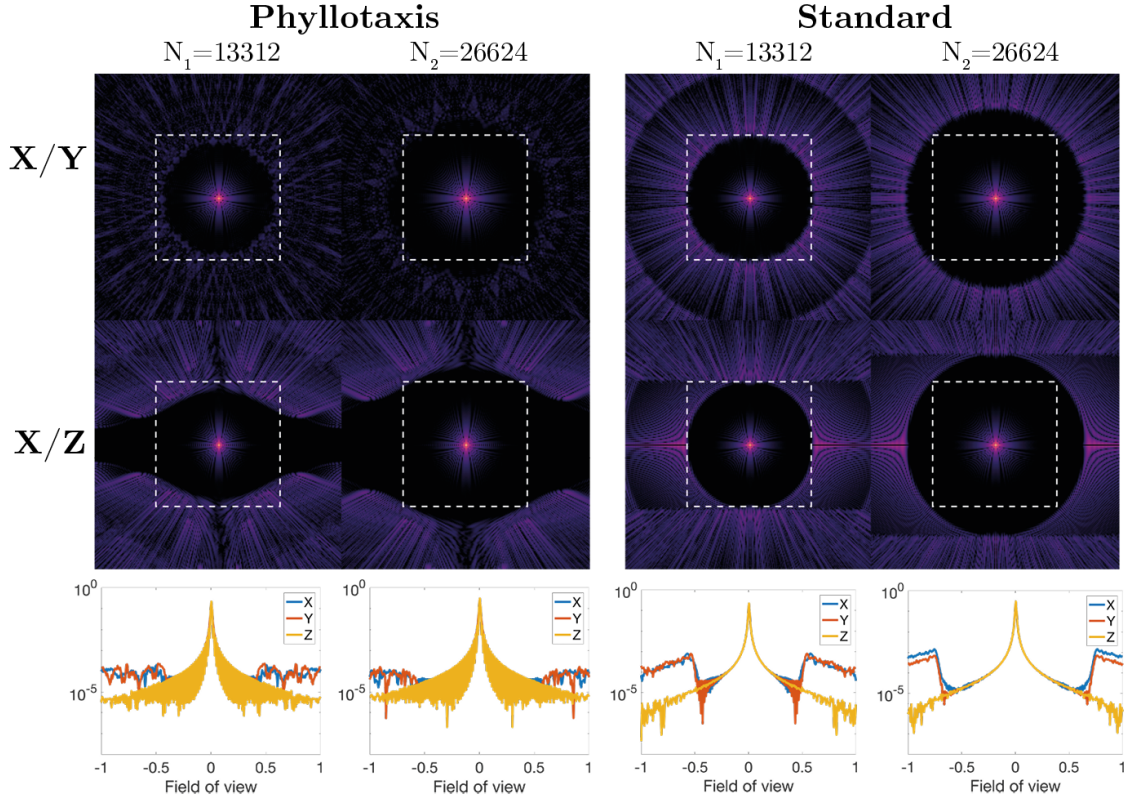


**Figure 7.9:** Point spread function in 1D and 2D using the phyllotaxis and standard trajectories. The dashed white lines shows the nominal field of view, as the RUFIS acquisition typically is twice oversampled.

The distance between neighbouring spokes provides an estimate of the degree to which the Nyquist criterion is violated. To study this further, a simple simulation was performed by generating a phyllotaxis trajectory with  $N_{spk} = \pi \cdot MAT^2$  number of spokes, i.e. fully sampled according to Nyquist, split up over  $N_{int} = 5$  (undersampled) interleaves. A standard trajectory was then generated with  $N_{spk}/N_{int}$  number of spokes, which yields an evenly undersampled trajectory. Figure 7.10a and b shows the phyllotaxis trajectory compared to the standard trajectory. The phyllotaxis trajectory produces a sampling pattern with sparse lines that are densely sampled, whereas the standard trajectory produces an even undersampling across the whole domain.

Given two spokes  $r_1$  and  $r_2$ , the angle  $\theta$  between the two spokes can be calculated using the dot product

$$r_1 \cdot r_2 = |r_1| \cdot |r_2| \cos \theta \rightarrow \theta = \arccos(r_1 \cdot r_2) \quad (7.9)$$

The distance between the two spokes at the edge of k-space  $\Delta k$  can be estimated using the small angle approximation as  $\Delta k \approx N_{pts} \cdot \theta$ . If  $\Delta \hat{k} = \Delta k / MAT / 2 > 1$  then the

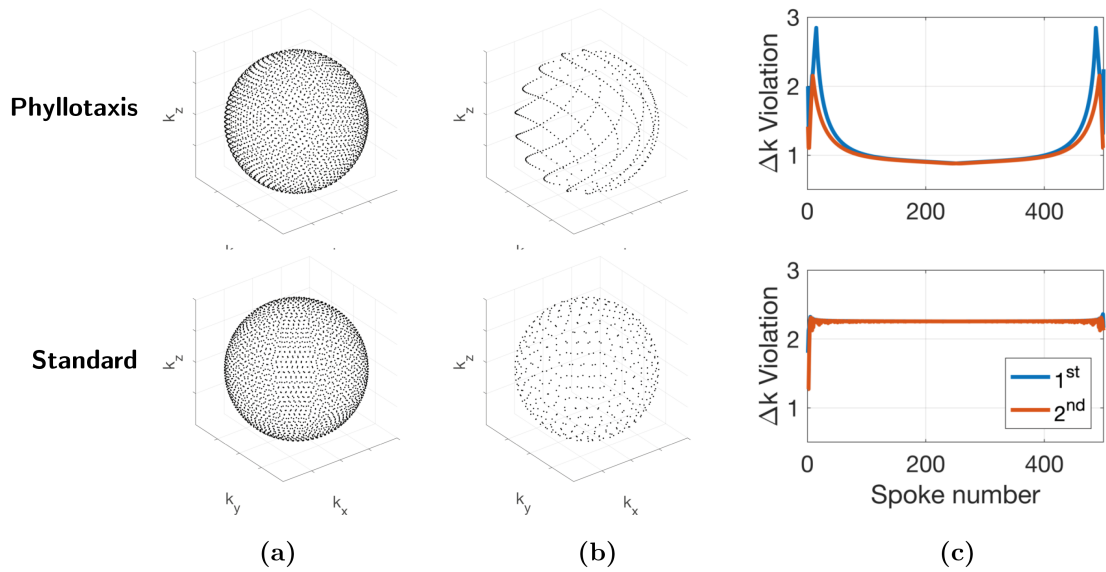


**Figure 7.10:** Comparison of the sampling density in k-space with the phyllotaxis and standard trajectory. **(a)** Fully sampled trajectory with 2500 spokes, phyllotaxis trajectory with 5 interleaves. **(b)** Undersampled trajectories with 500 spokes. Phyllotaxis is undersampled by taking one interleave, standard trajectory by taking every 5<sup>th</sup> spoke. **(c)** Comparison of how much the Nyquist criterion is violated with the two trajectories for the two closest spoke to every spoke.

Nyquist criterion is violated, and the magnitude of  $\Delta \hat{k}$  will indicate by how much. For the phyllotaxis and standard trajectory,  $\Delta \hat{k}$  was calculated for each spoke to its two nearest neighbouring spokes, the result of which is shown in figure 7.10c. For each spoke in the phyllotaxis trajectory, there is a pair of spokes which are almost at the same distance away. The distance to these spokes changes during the trajectory, and in the middle, when data are being collected around the equator in k-space, the spokes satisfy Nyquist, even though the trajectory is undersampled by a factor of 5. For the standard trajectory, the distance to the two closest spokes are overlapping lines with  $\Delta \hat{k} = 2.256 \approx \sqrt{5}$ , as expected with 5 fold undersampling. These results can be related back to the 2D visualisations of the PSF in figure 7.9, where the PSF in the X/Z is noticeably different between the standard and phyllotaxis trajectory. With the phyllotaxis trajectory, the apparent FOV extends left-right (i.e. in X) much further than the standard trajectory, due to the higher sampling density around the k-space equator, as k-space sampling density corresponds to field of view in the image domain. Practically, this suggests that the choice of scan-plane is more relevant for an undersampled acquisition with the phyllotaxis trajectory compared to the standard trajectory.

### 7.2.4 Time Resolved Acquisition

The phyllotaxis trajectory with multiple interleaves enables multi-volume, time resolved, acquisition with RUFIS, with each volume being sampled over a unique set of k-space points. While each interleave, i.e. each sparsely sampled sphere in k-space, can be reconstructed as a separate volume, all interleaves can also be jointly reconstructed to obtain a single high resolution image. To demonstrate this, a RUFIS acquisition was performed using a phyllotaxis trajectory with 21 interleaves, 6 segments per interleave, and 512 spokes per segment, resulting in a total of 64512 spokes. Data were acquired with  $1 \times 1 \times 1 \text{ mm}^3$  isotropic resolution,  $192 \times 192 \times 192 \text{ mm}^3$  field of view,  $\pm 15.6 \text{ kHz}$  bandwidth, flip angle of  $4^\circ$ .  $T_1$  preparation using an inversion pulse and inversion time of 400ms was used to increase contrast between white and gray matter. Total acquisition time was 4:47min, resulting in 14s per interleave. The data were reconstructed offline in MATLAB, using Kaiser-Bessel gridding.

Reconstructing each interleave as a separate image produce severe streaking artefacts, figure 7.11a, as expected from section 7.2.3. The images from the individual interleaves appear superficially identical, but the streaking pattern is unique to each image. Reconstructing the k-space data from all interleaves together produced a high resolution image without streaking artefacts, figure 7.11b. These results demonstrate that the phyllotaxis trajectory can, in principle, be used to collect data for a self-navigated RUFIS acquisition, since if motion occurs during the scan, it can be detected in the individual interleaves. Motion can then be corrected for before the data are combined to form the final image, which is the core of the method presented in the remainder of this chapter.

It is also possible to visualise how the image quality gradually improves as additional interleaves are acquired, as shown in figure 7.12. While the reconstructed resolution is the same in all 21 images, the image quality increase and streaking artefacts are reduced as more spokes are included in the acquisition. Given appropriate computing hardware, this type of dynamic image quality enhancement could be achieved online on the scanner, and combined with various image analysis techniques to determine when the image quality is sufficient for radiological reporting or for image analysis [276].

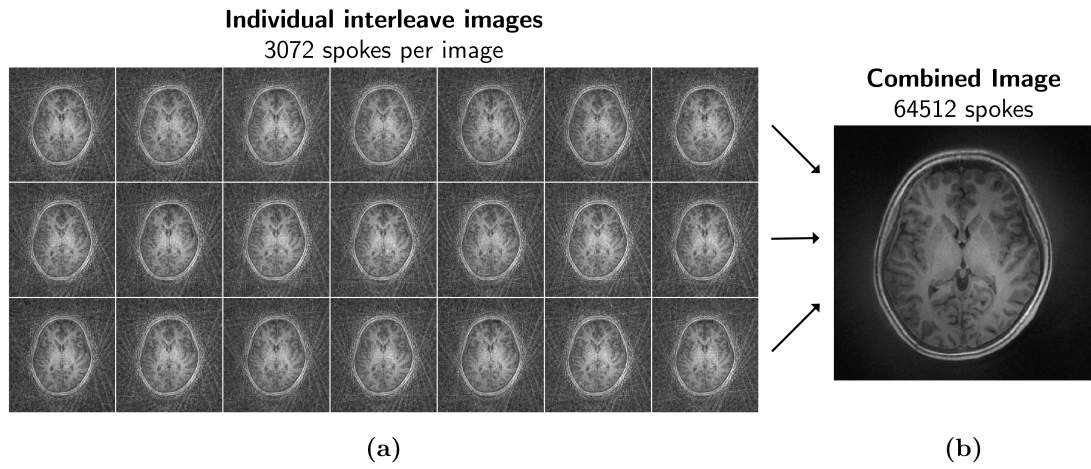


**Figure 7.11:** Example of time resolved ZTE acquisition where each interleave is reconstructed individually (a) and then combined into a single high resolution image (b).

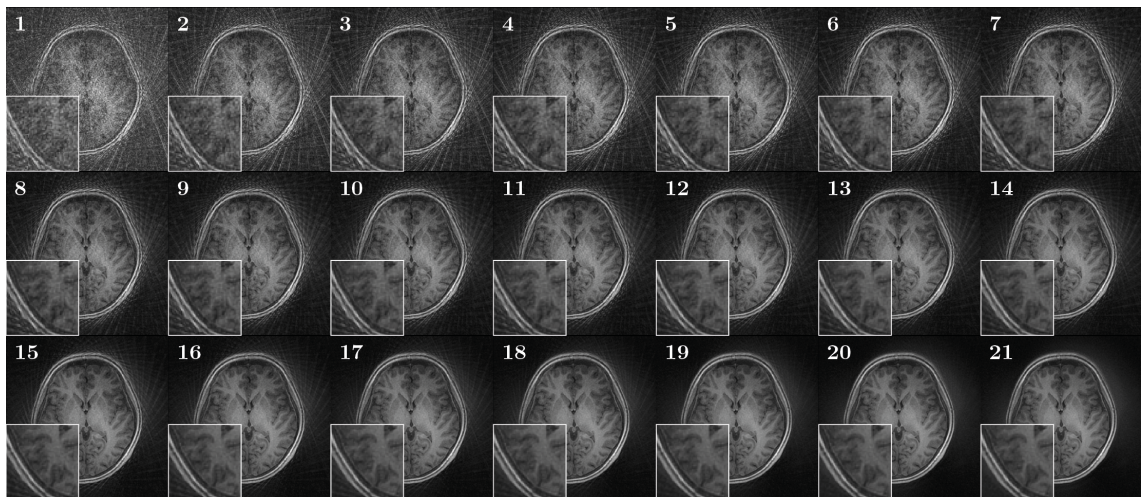


**Figure 7.12:** Example of dynamic increase of image quality as additional data from a phyllotaxis sampling scheme are included. The numbers in each image indicate the number of interleaves used to reconstruct the image.

## 7.3 Translation and Rotation Correction in k-space

### 7.3.1 Introduction

Rigid body motion in 3D can be described by a translation  $\bar{t}$  and rotation  $\bar{\theta}$  using six parameters  $(t_x, t_y, t_z, \theta_x, \theta_y, \theta_z)$ . The goal of MOCO is to estimate these six parameters from the data. Image based MOCO techniques typically employ registration algorithms which estimate translation and rotation simultaneously [196, 171]. With k-space methods, rotation and translation can be separated and corrected separately, as in PROPELLER, for example [263]. This section outlines how motion affects k-space data, setting the stage for development of the MOCO techniques used later.

To simplify the derivations in this chapter, a set of mathematical operators, listed in table 7.3, will be used. To describe a MOCO experiment, the term *motion state* will be used for an image acquired in a given position of the subject. In reality, motion is continuous and a motion state will represent an average position during the acquisition time, while in simulations, discrete motion states will be assumed for simplicity.

### 7.3.2 The Phase Correlation Algorithm for Estimating Translation

Translational motion during an MR acquisition can be observed as changes in the k-space data, described by the Fourier shift theorem, which in 1D states that

$$f(x - x_1) \leftrightarrow F(\xi)e^{-i\xi x_1}, \quad (7.10)$$

which means that translation in image space appear as a linear phase gradient in k-space. Similar to image domain based registration methods, an iterative algorithm could be used to find the phase shift in k-space which best describes the motion, but it is also possible to estimate this phase shift without iterative methods, using the phase correlation method (PCM). The PCM is built on the Fourier shift theorem (7.10) and the cross-correlation similarity metric, and has been used in the field of image processing [277, 278] and MRI previously [279, 280, 281].

Consider a 1D example with two functions  $f(x)$  and  $g(x)$ , where  $g(x) = f(x - x_1)$  i.e. a shifted version of  $f$ , and the goal is to estimate this shift. According to the Fourier shift theorem in (7.10), the Fourier transform of  $g$  can therefore be expressed as

$$\mathcal{F}(g(x)) = G(\xi) = F(\xi) \cdot e^{-i\xi x_1}. \quad (7.11)$$

**Table 7.3:** Mathematical notations used in this chapter.

$X_k^r$	Radial k-space data from motion state $k$
$X_k^c$	Cartesian k-space data from motion state $k$
$Y_k$	Image for motion state $k$
$Y$	Image reconstructed from combining all interleaves
$t_k$	K-space trajectory for motion state $k$
$\mathcal{G}(t)$	Gridding operator for trajectory $t$
$\mathcal{F}/\mathcal{F}^{-1}$	Forward/Inverse fast Fourier transform
$\mathcal{D}(t, t_0)$	Delauny interpolation from trajectory $t$ to $t_0$
$\bar{\delta} = (\delta_x, \delta_y, \delta_z)$	Estimated translation of the object
$\bar{\theta} = (\theta_z, \theta_y, \theta_x)$	Estimated rotation of the object
$\mathcal{R}(\bar{\theta})$	Rotation matrix
$\mathcal{H}(\bar{\delta})$	Phase shift operator for translation

The phase term can then be isolated as

$$Q = \frac{F^*(\xi) \cdot G(\xi)}{|F(\xi)| \cdot |G(\xi)|} = \frac{F^*(\xi) \cdot F(\xi) \cdot e^{-i\xi x_1}}{|F(\xi)|^2} = e^{-i\xi x_1}. \quad (7.12)$$

In the absence of noise or any other factor that will influence the phase, the shift  $x_1$  can be estimated by the Fourier transform of  $Q$ . The same method applies to 3D applications, as is the case in the methods described in the current work.

The main advantage of using PCM over iterative methods is that translation is estimated directly without multiple iterations being needed, which speeds up calculations. However it should be noted that in a real MR acquisition there are other factors that can influence the phase, and any phase variations between two volumes that are being compared using PCM will influence the translation estimation. While this could be a concern, there is very little time for phase accumulation using RUFIS due to the ZTE readout.

### 7.3.3 Rotation Correction in 3D Radial k-space

Rotation of an image manifests as an equivalent rotation of the magnitude data in k-space [282, 263]. If the rotation is limited to 2D, it can be converted into a translation along the polar angle of the magnitude k-space data, and the PCM can be used (in the same way as for translation) to find the rotation angle. Rotations in 3D, however, cannot be expressed as translations in spherical coordinates, so the PCM cannot be directly applied. Several



approaches have been suggested to enable the use of PCM for rotations in 3D [283, 280], motivated by the non-iterative nature of the algorithm.

Alternatively, the 3D rotation problem can be solved using an iterative technique, as in conventional image registration approaches. Because of the equivalence of the rotation in the two domains, such iterative algorithms can operate either in image space or on magnitude k-space data. Previous studies have shown that rotation correction can be performed in k-space. Pipe performed rotation correction in 2D with magnitude k-space data, acquired with PROPELLER, and Welch et al. followed the same idea but with 3D data acquired using spherical navigators [263, 262].

### 7.3.4 Combining Rotation and Translation Correction in k-space

The two previous sections have described methods for estimating rotation and translation from k-space data. By combining these two methods, the PCM and iterative rotation correction, rigid body image registration can be achieved [263]. The order in which rotation and translation estimation are performed, however, are crucial for the technique to work.

First, rotation is estimated from magnitude k-space data. Since translational motion is encoded in the phase of the k-space data, operating with magnitude data removes the effect of translation, and thus rotations will always appear around the centre of k-space. The estimated rotation is then used to correct the k-space trajectory, which is used to grid the radial data for translation estimation using the PCM. The result of the PCM is a phase correction matrix which can be used together with the corrected trajectory to obtain a motion-free image.

## 7.4 A Numerical Brain Phantom

To develop and evaluate the MERLOT MOCO framework, the numerical BrainWeb T<sub>1</sub> phantom [284, 285, 45], shown in figure 7.13, was used. RUFIS k-space sampling with a given trajectory was simulated using the forward NUFFT function in BART [28], to generate synthetic 3D radial k-space data. For simplicity, the effect of missing samples in the centre of k-space, as described in chapter 3, was ignored. To simulate motion, the phantom was rotated and translated before NUFFT sampling. Rotation was performed in MATLAB using `imrotate3` with cubic interpolation. Translation was achieved by shifting the phantom an integer number of voxels.

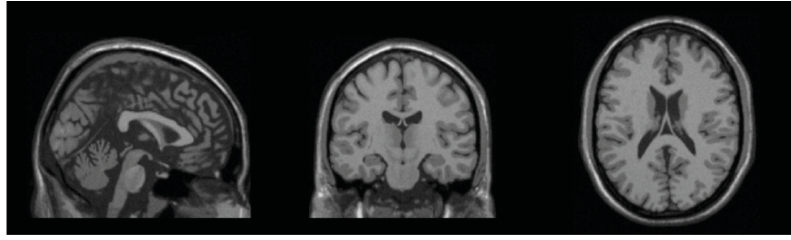


**Figure 7.13:** The Brainweb T<sub>1</sub>-weighted phantom used for the simulated MERLOT MOCO experiments.

## 7.5 Using 3D Phyllotaxis for Rotation Correction

### 7.5.1 Introduction

This section outlines the implementation of rotation correction using an interleaved RUFIS acquisition with a 3D phyllotaxis trajectory. The centre-out radial sampling strategy in RUFIS results in spherical coverage in k-space, which is excellent for estimating rotation. Previous studies have used single shot spherical, single shell, navigators for motion correction [262, 266, 286]. Self-navigated motion correction with RUFIS is similar to these methods, but instead of collecting a spherical navigator, a full 3D acquisition is used with multiple shells thus providing more data for rotation estimation, but with longer acquisition time.

### 7.5.2 Quantifying Rotation

A key step in all registration algorithms is the interpolation step, where the moving data are interpolated onto the grid of the fixed data in order to evaluate the cost function. In RUFIS, k-space data are sampled along radial spokes on concentric spherical shells, and k-space samples are therefore suitably described by spherical coordinates  $(r, \theta, \phi)$ . Since the spokes are straight, the polar ( $\theta$ ) and azimuthal ( $\phi$ ) angle is the same along the whole spoke. Interpolation of data acquired with a given trajectory onto a common grid can therefore be reduced to calculating an interpolation in a 2D space  $(\theta, \phi)$  and then apply the same interpolation at each point along the spoke.

Previous studies using spherical navigators for motion correction have utilised the Delaunay triangulation as a linear interpolation method between a given trajectory  $t_x$  and a common grid  $t_0$  in spherical coordinates [262, 266]. The Delaunay triangulation is a commonly used method for interpolation of non-uniformly scattered data, and was chosen instead of gridding as it provides a very efficient method for tri-linear interpolation [287].



Briefly, the method creates a triangular grid where each data point is a vertex of a triangle, and no other data point falls within the circumcircle of another triangle. To calculate the interpolation of a new point  $p$ , the triangle within which the point falls is found, and then the barycentric coordinates of the point inside the triangle are calculated. The interpolated value is calculated as a linear combination of the values at the vertices, weighted by the distance to each vertex, which is given by the barycentric coordinates. Further details about the Delaunay interpolation can be found in appendix A.

An example of the triangulation over  $\theta$  and  $\phi$  from a single shell is shown in figure 7.14a. Around the poles ( $\theta = 0$  and  $\theta = \pi$ ) there are fewer sampling points and therefore the convex hull of the triangulation (red line) does not cover the whole domain of  $\phi = [0, 2\pi], \theta = [0, \pi]$ . This is problematic, as it does not allow data to be interpolate onto points outside the convex hull. To address this, points are added in the missing corners  $[(0, 0), (0, 2\pi), (\pi, 2\pi), (\pi, 0)]$ , and assigned to the k-space value of the respective pole point. Doing so, the triangulation is expanded to the full domain and any point on the sphere can be interpolated, as shown in figure 7.14b.

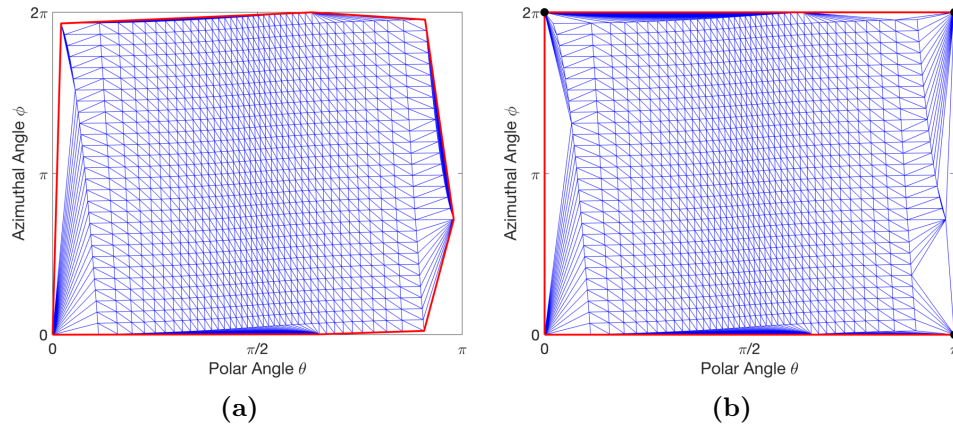


**Figure 7.14:** Example of a Delaunay triangulation for a single shell of a RUFIS trajectory. **(a)** By default, the triangulation will not cover the full domain, as indicated by the convex hull shown in red. **(b)** Adding in the missing points, black markers, which are assigned the same value as the point acquired at the pole, the triangulation covers the full spherical domain.

As discussed previously, rotation in image space results in an equivalent rotation in k-space. Figure 7.15 shows two images, one image rotated by  $20^\circ$  relative to the other, together with the corresponding k-space data, visualised on a single shell. It can clearly be seen that the two k-space spheres are rotated relative to each other, in a manner that directly corresponds to the rotation in image space.

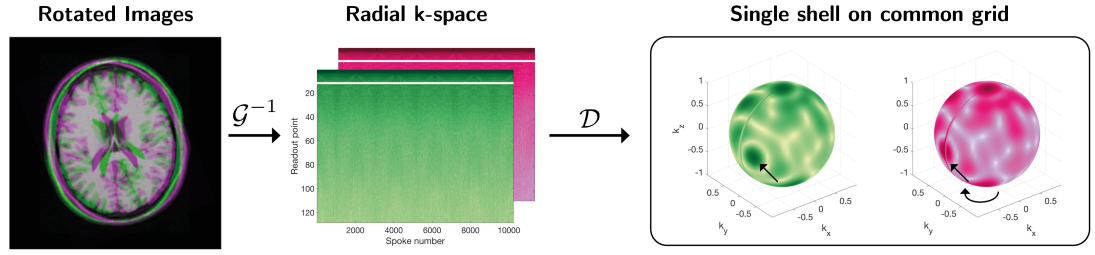


**Figure 7.15:** Rotation of an image results in an equivalent rotation in k-space, here demonstrated by projecting the radial k-space data onto a sphere. The radius used for the spherical projection is indicated with a white line in the radial k-space data, an arbitrary choice but it shows the effect clearly.

To find the rotation between two radial k-space datasets,  $X_1^r$  and  $X_2^r$ , the following cost function is minimised

$$E = 1 - NC(|\mathcal{D}_1 X_1^r|, |\mathcal{D}_2(\bar{\theta}) X_2^r|) \quad (7.13)$$

where  $\mathcal{D}_1 = \mathcal{D}(t_1, t_0)$  and  $\mathcal{D}_2 = \mathcal{D}(\mathcal{R}(\bar{\theta})t_2, t_0)$ ,  $\mathcal{R}(\bar{\theta})$  rotates the trajectory points by  $\bar{\theta}$ , and  $NC$  is the normalised correlation calculated as [170]

$$NC(X, Y) = \frac{\sum X \cdot Y}{\sqrt{\sum X^2} \cdot \sqrt{\sum Y^2}}. \quad (7.14)$$

The normalised correlation is well suited as a cost function, as its value always ranges between -1 and 1. The cost function  $E$  will thus cover the domain 0..2, where 0 indicates perfect correlation between the two datasets. Other common choice of cost functions are entropy [288] and the  $L_2$  norm [289]. In this work, the normalised correlation was used as it has been used in previous studies for rotation correction of magnitude k-space data [282, 263].

### 7.5.3 Implementation

The rotation correction framework was implemented in MATLAB (The Mathworks Inc., Natick, MA). All code was implemented using the base MATLAB library, which includes the Delaunay triangulation algorithm. Equation (7.13) was solved using a constrained non-linear solver, (`fmincon`), with the *active-set* optimiser algorithm, constrained to an angular search range of  $-45^\circ$ - $45^\circ$  along each axis. The default common grid for interpolation consisted of 360 azimuthal and 180 polar grid points.

### 7.5.4 Radially Symmetric Spokes

RUFIS data are collected as centre-out radial projections, and the trajectory is typically designed such that there are no mirrored spokes, i.e. no spoke is paired with parallel spoke projecting in the opposite direction from the centre of k-space. However, the magnitude k-space data  $|S(k_x, k_y, k_z)|$ , which is used for rotation correction, is symmetric in k-space and thus the number of spokes can be doubled by mirroring each spoke. This can be shown through a simple 1D proof. The power spectrum of a complex valued function  $f(x) \in \mathbb{C}$  is given by its autocorrelation as [290]

$$R_{ff}(u) = \int_{-\infty}^{\infty} f^*(x)f(u+x)dx = |F(u)|^2 \quad (7.15)$$

where  $F(u)$  is the Fourier transform of  $f(x)$ . The autocorrelation function is an even function, i.e.  $R_{ff}(u) = R_{ff}(-u)$ , and thus, the magnitude of k-space data, which is the square root of the power spectrum, is also an even function<sup>3</sup>. Therefore, for the purpose of rotation correction, spokes can be directly mirrored to double the number of spokes and thus increase the angular resolution of the data. The k-space coordinates of the mirrored spokes are given by

$$\theta_{mirror} = \pi - \theta \quad (7.16)$$

$$\phi_{mirror} = \pi + \phi. \quad (7.17)$$

### 7.5.5 Quantifying the Accuracy of Rotation Correction

To evaluate the rotation correction technique, a measure of the accuracy of the technique is required. Rotations in 3D around the  $(x, y, z)$  coordinate axes can be described by three matrices, part of the  $SO(3)$  group

$$\mathbf{R}_x(\theta) = \begin{bmatrix} 1 & 0 & 0 \\ 0 & \cos \theta & -\sin \theta \\ 0 & \sin \theta & \cos \theta \end{bmatrix} \quad \mathbf{R}_y(\theta) = \begin{bmatrix} \cos \theta & 0 & \sin \theta \\ 0 & 1 & 0 \\ -\sin \theta & 0 & \cos \theta \end{bmatrix} \quad \mathbf{R}_z(\theta) = \begin{bmatrix} \cos \theta & -\sin \theta & 0 \\ \sin \theta & \cos \theta & 0 \\ 0 & 0 & 1 \end{bmatrix}. \quad (7.18)$$

---

<sup>3</sup>This can be proved by making the substitution  $p = u + x$ .

A combined rotation around all three axes can be described by multiplication of the three matrices as

$$\mathbf{R}(\theta_x, \theta_y, \theta_z) = \mathbf{R}_x(\theta_x) \cdot \mathbf{R}_y(\theta_y) \cdot \mathbf{R}_z(\theta_z). \quad (7.19)$$

While there are multiple combinations of individual rotations which result in the same final result, any rotation matrix can be decomposed into a single rotation  $\theta$  around a unit vector  $u$ , providing unique values which we can use when evaluating accuracy. Given a rotation matrix  $\mathbf{R}(\theta_x, \theta_y, \theta_z)$ , the vector  $u$  around which the rotation is performed is an eigenvector of  $\mathbf{R}$ , as it has to satisfy

$$\mathbf{R}u = u \quad (7.20)$$

with corresponding eigenvalue  $\lambda = 1$ . The angle of rotation  $\theta$  around  $u$  can be found by applying  $R$  to a vector  $v$  orthogonal to  $u$ , and calculating the angle between  $\mathbf{R}v$  and  $v$  using the dot product.

For the simulations performed in this chapter, motion is simulated by rotating the phantom around a given axis by a certain angle. The result from the rotation correction on the other hand is the three rotation angles  $\theta_x, \theta_y, \theta_z$ , which gives a rotation matrix  $\mathbf{R}_{est}$ . To estimate the accuracy, the effective axis of rotation  $u$  and rotation angle  $\theta$  were calculated from  $\mathbf{R}_{est}$  and compared to the true values. The angle between the estimated and true rotation axis was calculated using the dot product.

### 7.5.6 Cost Function Characterisation

To design an effective optimisation algorithm for rotation correction, it is helpful to develop an understanding of how the cost function behaves under different conditions and its sensitivity to variation in the optimisation variables, here the rotation angles.

#### Methods

To find the rotation angle between two sets of k-space data, the optimisation algorithm finds the value that minimises the cost function  $E$ . In image space, all voxels are typically given equal weighting in the cost function evaluation. However, using k-space this is not necessarily the optimal solution. In the reconstruction of radial k-space data, a density compensation filter has to be applied to achieve even energy in k-space. It would therefore seem appropriate to apply the same correction to k-space data for rotation correction.

In practice, rotation correction will be applied to undersampled data which means that the density of samples in the edge of k-space is lower than the Nyquist criterion. If MOCO was being performed in image space, it would be reasonable to apply a low-pass filter with a cut-off around the radius for which the Nyquist criterion is satisfied. A similar cut-off could therefore also be applied to the k-space. Note that with RUFIS, undersampling by a factor of  $\pi$  is typically acceptable, and therefore the Nyquist radius is defined here as

$$R_{NQ} = \sqrt{n_{spokes}} \quad (7.21)$$

where  $n_{spokes}$  is the number of spokes in the trajectory. Decreasing the radius of k-space data used in the registration also has the additional advantage of reducing computation time.

To study the effect on the cost function of applying density compensation and applying a radial cut-off, a simulation was performed using radial k-space data generated from the BrainWeb T<sub>1</sub> phantom. A phyllotaxis trajectory was generated with 21 interleaves and 2048 spokes per interleave. Two volumes were generated using 8 different interleaves each, resulting in 16384 spokes per volume, corresponding to  $\pi$  undersampling, which is considered "fully sampled" for RUFIS. The cost function was evaluated for rotations between  $-10^\circ$  and  $10^\circ$  along the z-axis. The simulation was repeated with and without density compensation.

To study the effect of undersampling, a volumes with four times undersampling  $K = 4$ , i.e. 4096 spokes per volume, were generated. For these volumes, the Nyquist radius is  $R_{NQ} = \sqrt{4096} = 64$ , i.e. only half that data would be used. The simulation was performed with and without limiting the radius to  $R_{NQ}$ , as well as with and without density compensation as in the fully sampled simulation.

## Results

The results from the simulations are presented in figure 7.16 and table 7.4. Without any filtering, the cost function has a very shallow profile, 7.16a, with almost no difference between the fully sampled and undersampled acquisition. With density compensation filter, 7.16b, the cost function has a more narrow minimum around  $\theta_z = 0^\circ$ , and larger dynamic range. When the undersampled acquisition is limited to k-space radius of  $r = R_{NQ}$  the cost function profile changes, and the minima is closer to the full sampled case. The FWHM

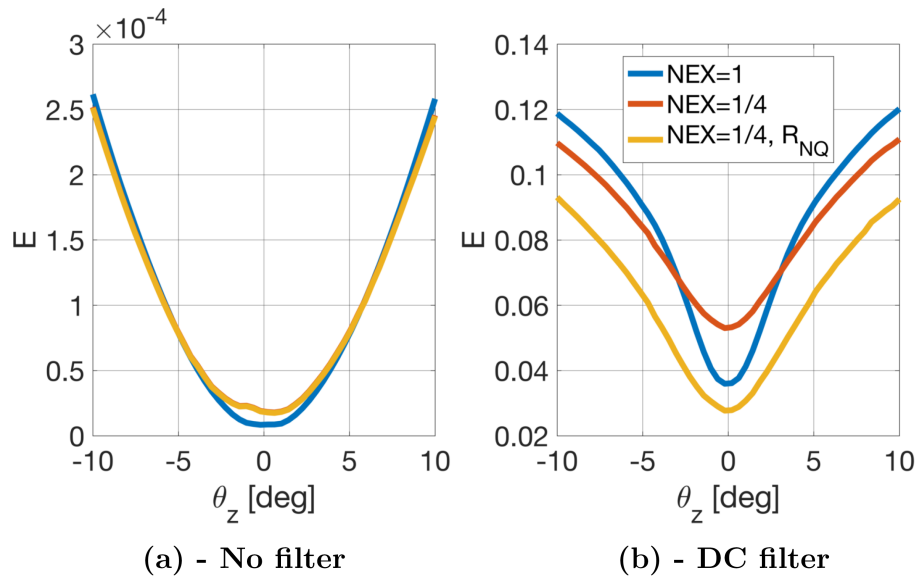


**Figure 7.16:** Results from the simulation showing the cost function evaluated as a function of rotation angle around the z-axis without filter in (a) and with density compensation filter in (b).

**Table 7.4:** Quantitative results from the cost function experiment with DC filter, as shown in figure 7.16b. The dynamic range is defined as the max-min value of the cost function. (FWHM: Full width half max, i.e. how narrow the valley of the cost function is)

Acquisition	FWHM [°]	Dynamic Range
NEX=1	7.33	0.084
NEX=1/4	9.30	0.058
NEX=1/4 with $r_{max} = R_{NQ}$	9.30	0.065

of the cost function, shown in table 7.4, is slightly narrower when limiting the radius. The dynamic range, calculated as the difference between the minimum and maximum of the cost function, over the range of rotation angles investigated here, is greater when limiting the radius.

## Discussion and Conclusion

Application of a density compensation filter to the radial k-space data is essential for an accurate rotation correction, as clearly shown in figure 7.16. When the data is under-sampled, the registration algorithm can be limited to only using k-space shells up to the Nyquist radius with equivalent, if not better, performance of the registration, indicated by narrower FWHM and larger dynamic range of the cost function. Reducing the number of

data points in the registration process, by limiting the radius, will also reduce computation time.

In experiments to follow, unless stated otherwise, density compensation will always be applied and the k-space radius used in the registration will be limited to the Nyquist radius  $R_{NQ} = \sqrt{n_{spokes}}$ .

### 7.5.7 Orthogonal Axis Rotation Validation

After characterising the cost function in the previous section, the rotation correction algorithm is demonstrated in a phantom experiment using the BrainWeb phantom with rotations around each of the three coordinates axes.

#### Methods

The BrainWeb phantom was sampled using the same strategy as in section 7.5.6. The reference volume was generated using the first 8 interleaves, and the rotated volumes were all generated using the 8 following interleaves. Three images were generated, rotated  $5^\circ$  around the  $x$ ,  $y$ , and  $z$  axis respectively. The same trajectory was used for the rotated volumes to ensure that the results could be easily compared. The registration was performed with the full k-space, which in this case is equivalent to the Nyquist radius. Maas et al. proposed initialising the registration algorithm at  $45^\circ$  to maintain sensitivity to small rotations [282]. Here, the registration algorithm was initialised at  $\theta_x = \theta_y = \theta_z = 10^\circ$  to speed up convergence and avoid local minima.

#### Results

Figure 7.17 shows the results from the registration, including the evolution of the optimisation algorithm. In all three cases, the correct rotation was estimated with less than  $0.2^\circ$  error around the main axes of rotation. The optimiser converged after 30 iterations or less in all three cases.

#### Discussion and Conclusion

This experiment shows that the registration algorithm will converge to the correct rotation with high accuracy ( $<0.2^\circ$  error) and within a reasonable number of iterations, less than 30. These results are similar to those presented by Welch et al., using spherical navigators [262]. Their algorithm converged within 20-50 iterations and they found that the estimated rotation was always within  $0.2^\circ$  of the actual rotation. Here, fully sampled

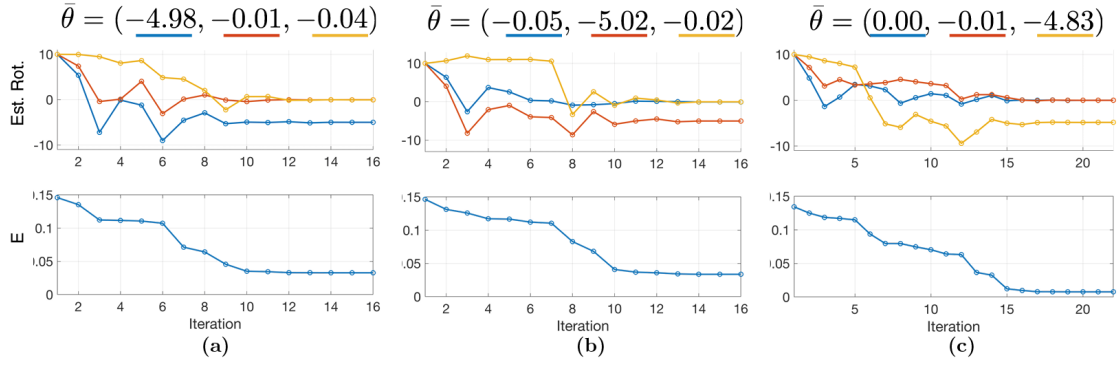


**Figure 7.17:** Evolution of the minimisation algorithm in the registration algorithm for rotation around the  $x$  (a),  $y$  (b) and  $z$  (z) axes.

volumes were used, which in section 7.5.6 was shown to produce a very narrow minimum in the cost function. A real acquisition will use undersampled data, acquired with different interleaves and with rotations around all three axes simultaneously, which will be investigated in the next experiment.

### 7.5.8 Interleaved Acquisition Simulation

After demonstrating that the algorithm can estimate rotation in a fully sampled acquisition, the phyllotaxis trajectory is used to simulate a real acquisition where each undersampled interleave is rotation corrected and a combined reconstruction is performed.

#### Methods

A phyllotaxis trajectory was generated with 21 interleaves, 3072 spokes per interleave, and 256 points readout points per spoke. Each volume was sampled with a separate interleave, to simulate a real acquisition. The simulation was performed with and without doubling the number of spokes through mirroring as described in section 7.5.4. The first volume was used as reference volume and therefore not rotated. The following 20 volumes were rotated by a random angle around a random axis. The rotation angle was sampled from a uniform distribution between  $-15^\circ$  and  $15^\circ$ . The  $z$ -axis was chosen as the main axis of rotation, as this is typical motion in MRI, and the rotation axis  $u$  was given by

$$u = \frac{u'}{\|u'\|}, \quad u' = [0, 0, 1] + [\delta_x, \delta_y, \delta_z] \quad (7.22)$$

where  $\delta_x, \delta_y, \delta_z$  were sampled from a normal distribution centred around 0, and with  $\sigma = 0.25$ . The accuracy of the rotation correction was evaluated by calculating the principal



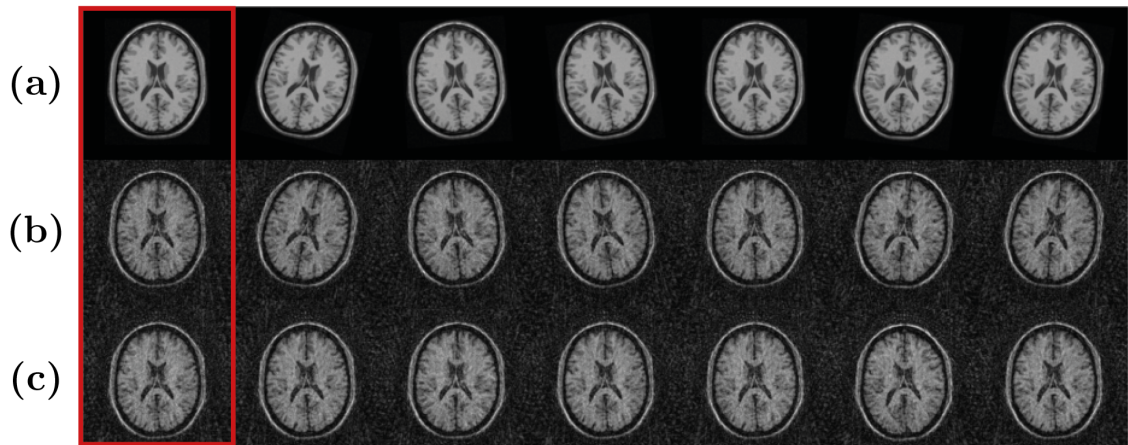


**Figure 7.18:** Example of the rotation correction algorithm applied to the BrainWeb T<sub>1</sub> phantom showing the first seven interleaves in the experiment. (a) Rotated phantom images. (b) Phantom sampled using the undersampled phyllotaxis trajectory. (c) Interleaves after rotation correction with the nominal number of spokes.

axis of rotation  $\hat{u}$  and the effective rotation angle  $\hat{\theta}$  and comparing it to the true rotation axis and angle.

When the effective rotation has been estimated by the registration algorithm, the rotation correction is achieved by rotating the trajectory points, which means that the distribution of samples is no longer even in k-space, which can lead to incoherent streaking artefacts in the reconstructed image. Furthermore, the density compensation used previously in this thesis, the  $r^2$  correction, also requires even sample distribution to be valid, which is no longer the case. To study this further, the reference image was sampled with the corrected (i.e. non-uniform) trajectory and then reconstructed. This should produce a motion free image since the same trajectory is used for both forward and inverse gridding, and therefore any artefacts are due to the trajectory.

### Results - Interleaves

Figure 7.18b shows the first seven images in the series of motion images after NUFFT sampling, with the reference highlighted with red border. After MOCO with the nominal number of spokes, shown in figure 7.18c, the images appear visually to align well with reference.

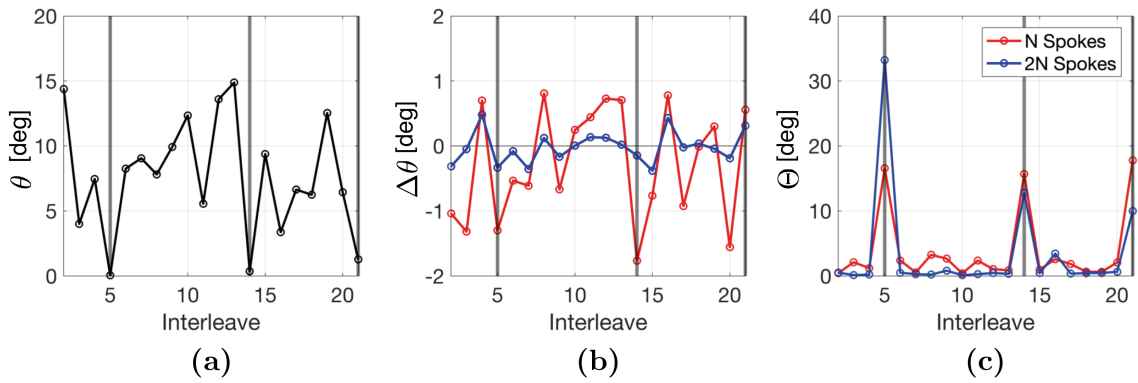


**Figure 7.19:** Accuracy of the rotation correction. (a) The true rotation angle  $\theta$ , (b) the error in the estimated effective rotation angle with nominal and double number of spokes  $\Delta\theta = \theta - \hat{\theta}$ . (c) The angle between estimated and true axis of rotation  $\Theta$ . Interleave 5, 14, and 21 shows large errors in the estimated rotation axis; for these interleaves the true rotation angle is close to zero, as indicated with gray vertical lines in (a).

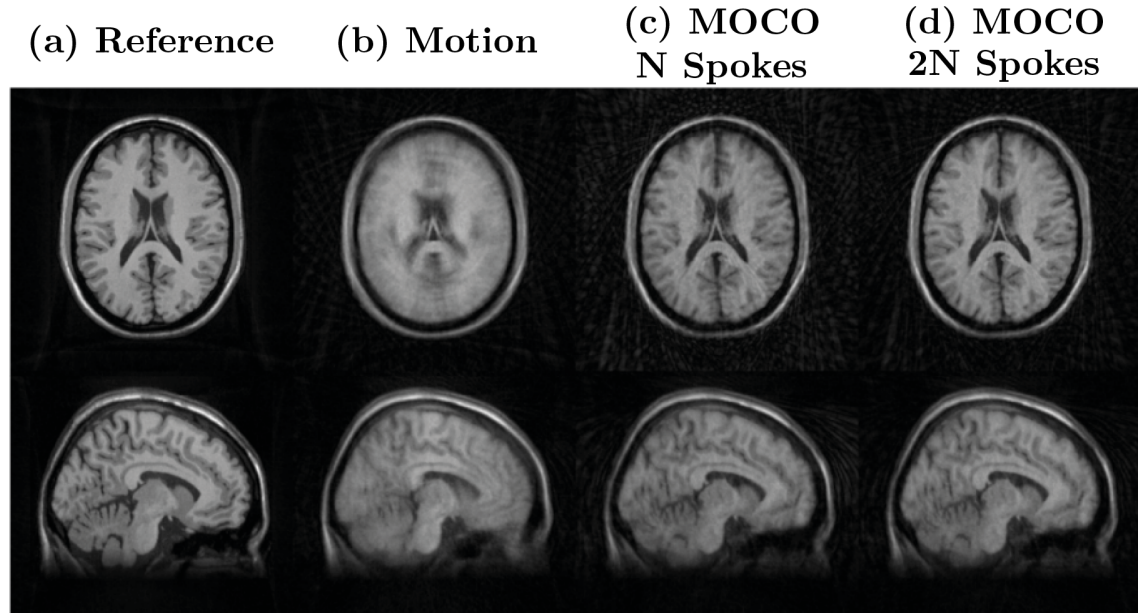
### Results - Rotation Accuracy

Figure 7.19 shows the errors in the estimated rotation angle  $\Delta\theta = \theta - \hat{\theta}$ , and the angle  $\Theta$  between the estimated ( $\hat{u}$ ) and true rotation axis ( $u$ ). Increasing the number of spokes through mirroring improved the accuracy of the rotation estimation, as shown in figure 7.19b. The average absolute error in estimating the rotation angle was  $\bar{\Delta\theta} = 0.75^\circ$  (range:  $-1.77^\circ$ - $0.81^\circ$ ) for nominal number of spokes and  $\bar{\Delta\theta} = 0.18^\circ$  (range:  $-0.38^\circ$ - $0.48^\circ$ ) for double the number of spokes. Estimation of the effective rotation axis was also improved with doubling the number of spokes. In figure 7.19c, showing the error in the estimated rotation axis, three interleaves shows very large deviations from the true axis. These have been highlighted with gray vertical lines in all three sub figures, which in figure 7.19a is seen to be the interleaves where the true rotation angle was the smallest, close to  $0^\circ$ . Therefore, the implication of estimating the axis of rotation incorrectly is negligible.

### Results - Combined Reconstruction

In order to correct for motion, the k-space trajectories (as opposed to the data themselves) are adjusted by rotating the trajectory points by the angles found by the registration algorithm. Using the corrected trajectories, a single, motion corrected, image can be reconstructed. Figure 7.20 shows the combined reconstruction after MOCO, compared to the motion free image and the corrupted image reconstructed without MOCO. It is clear from visual inspection that the MOCO algorithm greatly improves image quality,

particularly within the brain itself. It can also be seen that doubling the number of spokes improves the results still further, in particular by reduction of streaking artefacts outside the brain.



**Figure 7.20:** Result from MOCO experiment showing the reference image without motion **(a)**, the motion corrupted image **(b)**, and the motion corrected image with the nominal **(c)** and twice **(d)** the number of spokes.

### Results - Residual Artefacts

Despite the clear improvements given by the MOCO algorithm, it is nevertheless clear that the corrected image in figure 7.20d does not fully recover the high image quality of the original motion free image. There are two explanations to this. First, as observed in figure 7.19, the algorithm does not find the exact angle, and therefore there will be some residual motion in the motion corrected image. However, the residuals are very small and thus the more likely cause of the artefacts is uneven sampling density in k-space after correcting the trajectory. The latter is supported by figure 7.21 showing a comparison between the phantom sampled with the corrected and non-corrected trajectory, showing clear artefacts when the corrected trajectory is used.

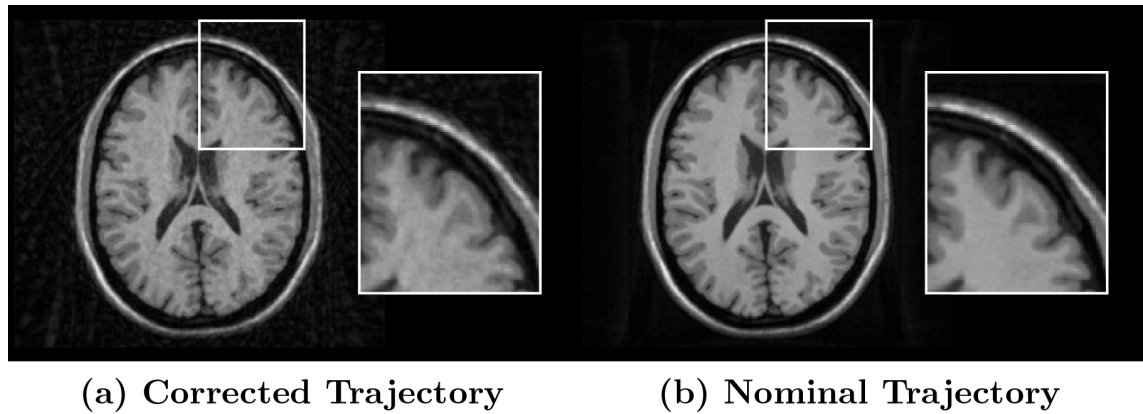


**Figure 7.21:** Comparison of reference volume sampled and reconstructed with the trajectory obtained from rotation correction (a) compared to the nominal trajectory (b), showing streaking artefacts with the corrected trajectory

### Discussion and Conclusion

This simulation showed that it is possible to use the proposed rotation correction method for an undersampled acquisition, similar to that which would be used in vivo. By mirroring the spokes, the angular resolution was doubled, which improved the MOCO, shown both by the accuracy of the algorithm (figure 7.19) and the final combined reconstruction, figure 7.20d. The accuracy of the rotation estimation here was  $<0.2^\circ$  using mirrored spokes, comparable to the fully sampled experiment in the previous section, and also to the results obtained by Welch et al. using spherical navigators [262].

The motion corrected image, after combined reconstruction, showed streaking artefacts inside and outside the brain. Sampling and reconstructing the reference volume with the trajectory corresponding to the results of the MOCO showed streaking artefacts (7.21) similar to those observed in the motion corrected image. Therefore, it was concluded that the residual artefacts are due to the trajectory, not residual motion. The nominal trajectory was designed to achieve uniform k-space sampling when all interleaves were reconstructed together. After MOCO, however, the trajectory points from each interleave are rotated according to the estimated motion, which results in an uneven overall sampling density.

Prospective MOCO techniques, such as PROMO [264], avoid the issue of uneven sampling in k-space by updating the acquisition based on the current motion estimate *before* the data are acquired, thus retaining even density in k-space. For retrospective approaches such as MERLOT, it is possible that iterative SENSE reconstruction methods could be used to reduce the trajectory related artefacts [134]. Previous studies have implemented such iterative methods for 2D radial data to reduce streaking artefacts with total variation

(TV) [291] and generalise total variation (TGV) [126] regularisation with great results. Translation to 3D radial can be difficult though, as the whole data set has to be processed simultaneously, with correspondingly high memory requirements [292], and was beyond the scope of this thesis.

## 7.6 Using 3D Phyllotaxis for Translation Correction

### 7.6.1 Introduction

This section introduces an implementation of the PCM for correction of translation motion in an interleaved RUFIS acquisition, inspired by the work of Pipe[263].

### 7.6.2 Quantifying Translation

#### Methods

After bulk rotation has been corrected, as demonstrated in the previous section, the relative translation between two sets of k-space data  $X_1^r$  and  $X_2^r$ , with associated k-space trajectories  $t_1$  and  $t_2$ , can be estimated using PCM in Cartesian k-space. Both sets of k-space data are first gridded onto a common Cartesian grid where PCM is applied as

$$\Delta\bar{r} = \underset{\bar{r}}{\operatorname{argmax}} \left( \mathcal{F}^{-1} \frac{X_1^c \circ X_2^c}{|X_1^c| \cdot |X_2^c|} \right) \quad (7.23)$$

After the translation  $\Delta\bar{r} = (\Delta x, \Delta y, \Delta z)$  has been estimated, a radial phase correction matrix  $\mathcal{H}(\Delta\bar{r})$  can be calculated, containing the elements

$$\mathcal{H}_{i,j}(\Delta\bar{r}) = \exp(i\pi \cdot \Delta\bar{r} \cdot \bar{\xi}_{i,j}) \quad (7.24)$$

where  $i$  is the spoke index,  $j$  the readout point index, and  $\bar{\xi}$  the spatial frequency encoded at point  $(i, j)$ , i.e. the normalised k-space trajectory coordinate. Similar to rotation correction, the phase correction matrix  $\mathcal{H}$  is a correction that can be applied to the raw data prior to gridding through elementwise multiplication.

To demonstrate the 3D-radial PCM algorithm, a RUFIS acquisition was simulated using the Brainweb T<sub>1</sub>-weighted phantom [45]. A phyllotaxis trajectory with 8 interleaves and 2048 spokes per interleave was used, resulting in 16384 spokes per volume. The same trajectory was used for the reference and moving volume to better visualise the PCM algorithm. Motion was simulated by translating the moving volume by 20 pixels in  $x$  and

10 in  $y$ . Gridding was performed using the Kaiser-Bessel method, after which the PCM algorithm was used to estimate the translation. The moving volume was then reconstructed again using the phase correction.

## Results

Figure 7.22 shows the important steps of the registration algorithm. The radial data are first interpolated onto a Cartesian grid, after which the PCM is applied in Cartesian space. The translation is identified as  $\Delta\bar{r}$  and the radial phase correction matrix  $\mathcal{H}$  is calculated using (7.24). This phase correction is then applied to the original, radial, k-space data to produce an image to aligns perfectly with the reference.

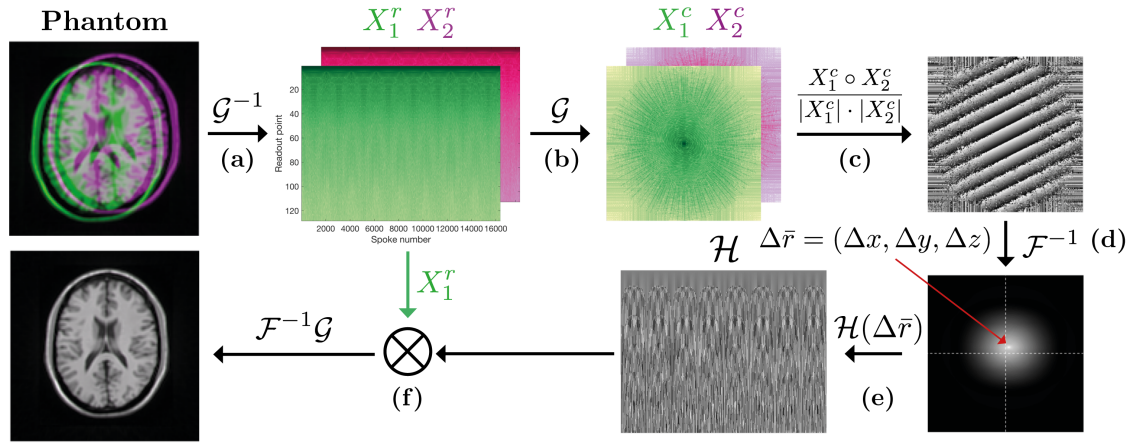


**Figure 7.22:** Overview of the steps in the translation correction. (a) Radial k-space is generated from the BrainWeb phantom, and (b) gridded to Cartesian k-space. (c) Element wise multiplication of the two sets of k-space reveals wrapped phase ramp produced by the relative translation. (d) After an inverse Fourier transform the "phase roll" is transformed into a translation in the inverse domain. (e) The estimated translation of the data in this domain is then used to calculate a radial phase correction matrix  $\mathcal{H}$  (using equation (7.24)) which is applied to the original k-space data  $X_1^r$  (f). Comparison of the corrected image to the reference now shows no shift.

## Discussion

The PCM is an efficient method for estimating relative translation between two images using k-space data, however, the disadvantage of using it with radial data is that gridding is required. In this small experiment, the utility of PCM for estimating translation in 3D radial data was demonstrated. Translation is corrected by calculating a phase correction matrix  $\mathcal{H}$  which is applied to the original, motion corrupted, data. This example used fully sampled data sets, using the same k-space trajectory, to clearly demonstrate how the



translation appears as a phase ramp in the PCM. With undersampled data, using different k-space trajectories, the phase difference will not be as clearly visible. The next section will investigate a more realistic example using PCM for translation correction with the 3D phyllotaxis trajectory.

### 7.6.3 Interleaved Acquisition Simulation

In this simulation, the utility of using PCM for translation motion correction is demonstrated using an undersampled acquisition, similar to section 7.5.8.

#### Methods

The same numerical phantom and simulated acquisition was used as in the experiment studying rotation optimisation in section 7.5.8. Motion was simulated by translating the phantom in 3D, prior to obtaining the radial k-space through NUFFT sampling. The translation for each interleave was sampled from a uniform distribution ranging from -15 to 15 voxels shift in each dimension.

To combine data from all interleaves and reconstruct as a single, motion corrected volume, the phase correction matrix was applied to the raw data from each interleave and the data was concatenate along the spoke dimension. Gridding and FFT was then used to reconstruct the motion corrected volume in a single step.

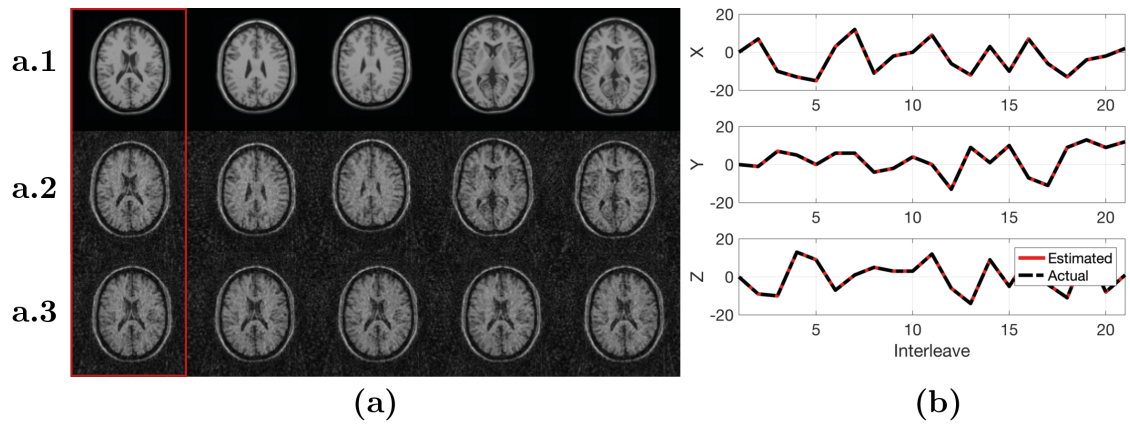
#### Results

Figure 7.23a shows axial slices of the phantom for the first five interleaves before (7.23a1) and after (7.23a2) radial sampling. Although not clearly visible here, the translation was applied in all three dimensions, as shown by the black line in figure 7.23b.

The PCM algorithm estimated the translation correctly for all 21 interleaves, shown by the aligned volumes in figure 7.23a3 and the red line in figure 7.23b which overlaps perfectly with the actual translation in black. Figure 7.24 shows the combined reconstruction of the phantom without and with motion, clearly showing the effect of the MOCO. The corrected image appears identical to the reference image.

#### Discussion

This experiment demonstrated that the PCM algorithm can be used for translation correction with an undersampled phyllotaxis trajectory, where each volume is sampled with a



**Figure 7.23:** (a) Axial slices of the BrainWeb  $T_1$  phantom with translation motion. Top row shows the phantom with motion, middle row sampled phantom with motion, and bottom row motion corrected sampled data. (b) Actual and estimated translation of each interleave along  $x$ ,  $y$  and  $z$ . Perfect overlap is observed for all interleaves along all axes.

unique set of spokes. The correct translation was estimated for all 21 interleaves and the combined reconstruction after MOCO produced an image identical to the reference image.

In vivo, motion will not appear as discrete translations for each interleaves, but instead as an average motion throughout an interleave. It would be possible to simulate this as well, however this will be better tested through actual in vivo experiment. From this simulation it can be concluded that the PCM can be used for translation correction. In the next section, it will be combined it with rotation correction to perform rigid body MOCO.

## 7.7 Rigid Body Motion Correction

### 7.7.1 Introduction

In this section, the methods outlined previously for rotation and translation are combined into a complete MOCO framework, which together with the self-navigated RUFIS acquisition, comprise the MERLOT method. The method is validated in the BrainWeb numerical phantom, and on phantom data acquired in the scanner.



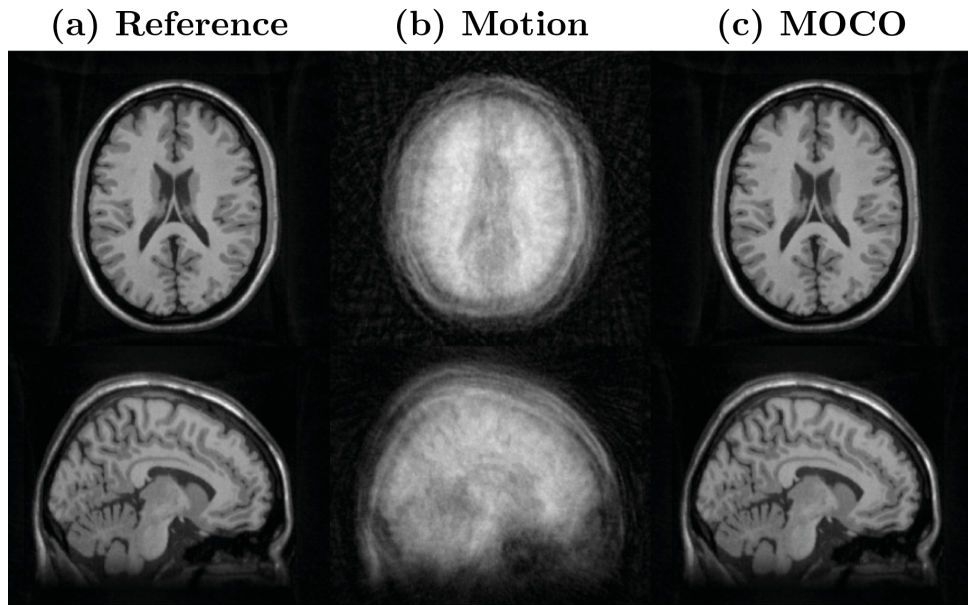


**Figure 7.24:** Results from the translation correction. (a) Reference image without motion. (b) Motion corrupted image, showing severe motion artefacts. After MOCO (c), the image quality is restored, appearing identical to the reference.

### 7.7.2 Simulated Rigid Body Motion

#### Methods

The BrainWeb phantom was sampled using a 3D phyllotaxis trajectory with 21 interleaves, 1024 spokes per interleave, and 128 readout points per spoke. For each interleave, random subject motion was simulated by first translating the phantom, with the same parameters as in section 7.6.3, and then apply rotation, with the same parameters as used in section 7.5.8. The first seven interleaves of the moving phantom is shown in figure 7.25a. Each interleave was then sampled with the respective trajectory, figure 7.25b.

MOCO was performed in two steps. First, rotation was estimated from the magnitude of the radial k-space data. The number of spokes was doubled for this step by mirroring each spoke. The rotation estimates were then used to update, i.e. rotate, the trajectories for each interleave. In the second step, translational motion was estimated using the PCM. Radial k-space data were gridded using the nearest neighbour method (for speed) using the corrected trajectories from the first step. From the estimated translation, a radial phase correction matrix was calculated for each interleave. Finally, the individual interleaves were reconstructed separately and combined using the phase correction and the corrected trajectories.

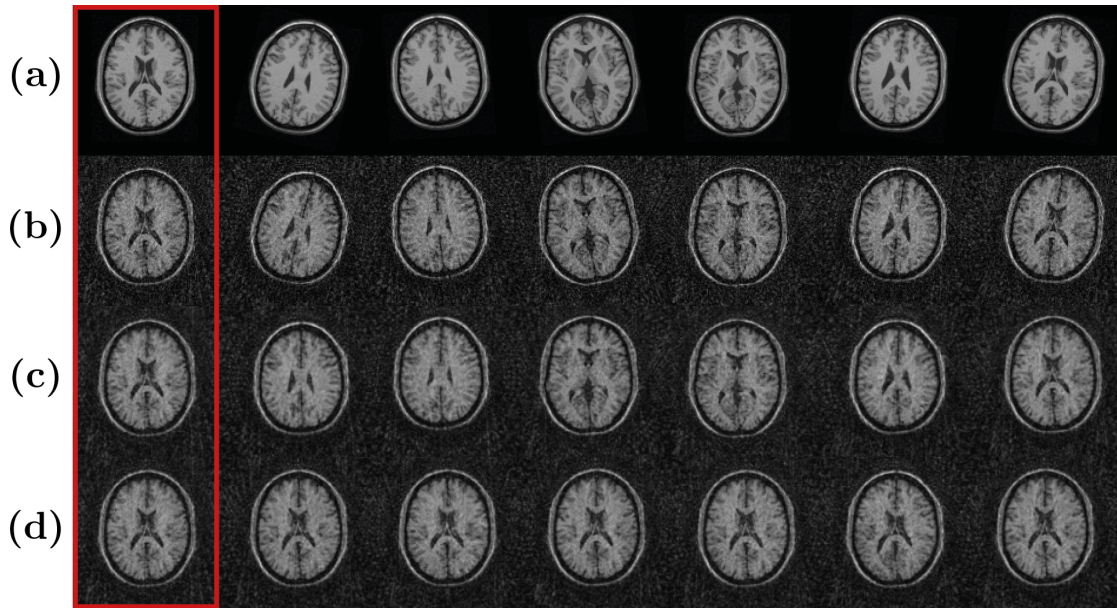


**Figure 7.25:** Overview of the first seven interleaves in the simulated MERLOT experiment. Reference image for MOCO is indicated with red border. **(a)** Fully sampled BrainWeb phantom with motion. **(b)** Phantom sampled with phyllotaxis trajectory. **(c)** Rotation corrected. **(d)** Translation and rotation corrected.

## Results

Results from MOCO of individual interleaves are presented in figure 7.25. In the first step, rotation was successfully corrected, resulting in the images shown in figure 7.25c. Followingly, translation motion was corrected, as shown in figure 7.25D, in which it visually can be seen that the interleaves align with the reference image (identified with red border).

The combined reconstruction at each step, figure 7.26, shows that the MOCO reduces the motion artefacts substantially, but, as with the rotation correction results in section 7.5.8, there are still residual artefacts produced by the uneven sampling distribution in k-space.

## Discussion and Conclusion

In this section, the full MERLOT framework was demonstrated in the BrainWeb  $T_1$  phantom. The results from this experiment show that rigid body motion, i.e. rotation and translation, can be separated into two MOCO steps as hypothesised, and that these can then be corrected for separately, through trajectory correction and phase correction. The final reconstructed image after MOCO still shows some residual motion artefacts, however. These appear similar to the residual artefacts observed in section 7.5.8, in which rotation

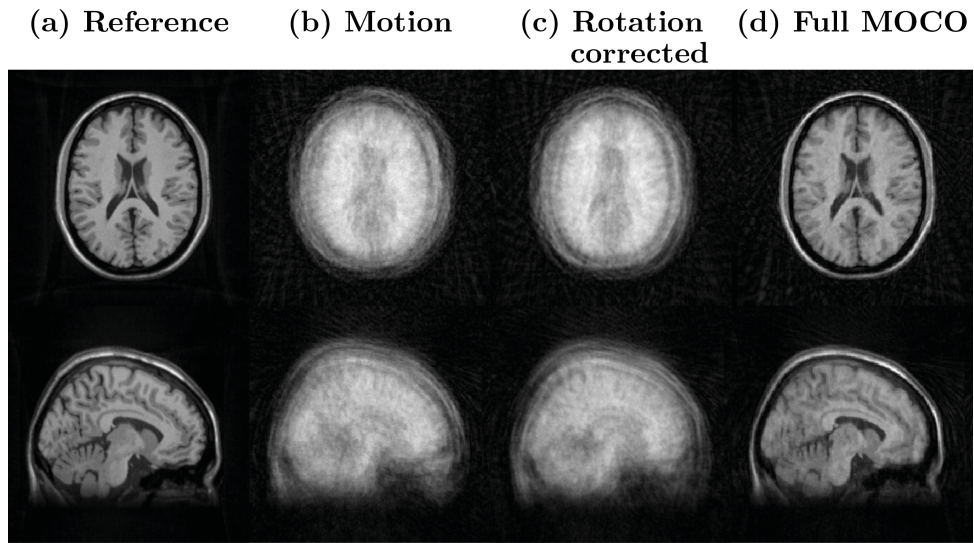


**Figure 7.26:** Results from simulated rigid body MOCO experiment showing the combined reconstruction of all interleaves. **(a)** Fully sampled reference image. **(b)** Motion corrupted image. **(c)** Rotation corrected. **(d)** Full MOCO with both rotation and translation corrected.

was corrected for in the absence of any translation, but such artifacts were not seen in the example where only translational motion was considered, section 7.6.3. This strongly suggests that it is the rotation correction step which results in the residual artefact seen, likely due to the uneven distribution of spokes in k-space following the trajectory correction. Additionally, the simple radial density correction used ( $r^2$ ) may not be totally appropriate, as the spokes are no longer evenly distributed. Ideally, iterative methods would therefore be used in the final reconstruction step, in order to determine and apply a more appropriate, data driven, density compensation. Iterative methods would also allow use to be made of data from multiple coils [134]. An investigation of such iterative approaches is beyond the scope of the current thesis, however.

### 7.7.3 MR Experiment

#### Introduction

The previous sections have provided thorough evidence that the MERLOT method works in a simulation environment. In this section, the theoretical results will be substantiated through MR experiment using a phantom.

One major difference between the simulated experiments and an actual MR experiment is the multiple receiver coils typically used in the latter, which modulate the k-space data

by a coil geometry specific sensitivity profile. For MOCO in image space, simple coil combination using sum of squares can be used to produce a single high SNR image from data from multiple coils [293]. The same is not possible for the k-space data themselves, however, since the data from each coil effectively is convolved with the Fourier transform of the sensitivity profile. A simple solution to this would be to perform MOCO on the k-space data from each coil separately, however initial in vivo experiments (not shown) showed that the SNR of the data from individual coils was too low for this to be effective. Therefore, for this phantom validation, a single channel transmit and receive (TX/RX) coil was used in order to remove the confound of multiple receiver channels, allowing the experiment to be focused on the MOCO technique itself.

## Methods

A phantom constructed from a cantaloupe and two pears<sup>4</sup> (see appendix B.2 for photo of the phantom) was scanned on a 3T GE MR750 with a single channel transmit-receive head coil. A steady state RUFIS acquisition was used with the following acquisition parameters: FOV=225 × 225 × 225 mm<sup>3</sup>, voxel size=2 × 2 × 2 mm<sup>3</sup>,  $\alpha = 6^\circ$ , TR=3.96ms. A phyllotaxis trajectory with 13 interleaves and 2048 spokes per interleave was used, resulting in a total of 26624 spoke. Total acquisition time was 2 min. A low bandwidth of  $\pm 7.8$ kHz was used to ensure centre of k-space was sufficiently sampled such that no separate filling of the centre k-space was required, again allowing the experiment to be focused on the MOCO technique itself, rather than other confounds.

To simulate motion, the acquisition was repeated six times, with the phantom being moved (both translated and rotated) between each acquisition. This resulted in six fully sampled volumes, each with a different phantom orientation. From this dataset, a single motion-corrupted volume was compiled by combining 2 interleaves from each acquisition, as described in figure 7.27. The first interleave from the first volume was excluded, in order to have an equal number of interleaves from each volume, resulting in 12 interleaves in total. (Since the acquisition was oversampled, removing one interleave in this way does not degrade the image quality significantly). MOCO was then applied to the motion corrupted volume, using the framework described previously. As previously, during the rotation correction, the number of spokes was doubled by mirroring.

<sup>4</sup>The standard phantoms at our disposal are all symmetrical and are therefore not suitable for evaluating MOCO.

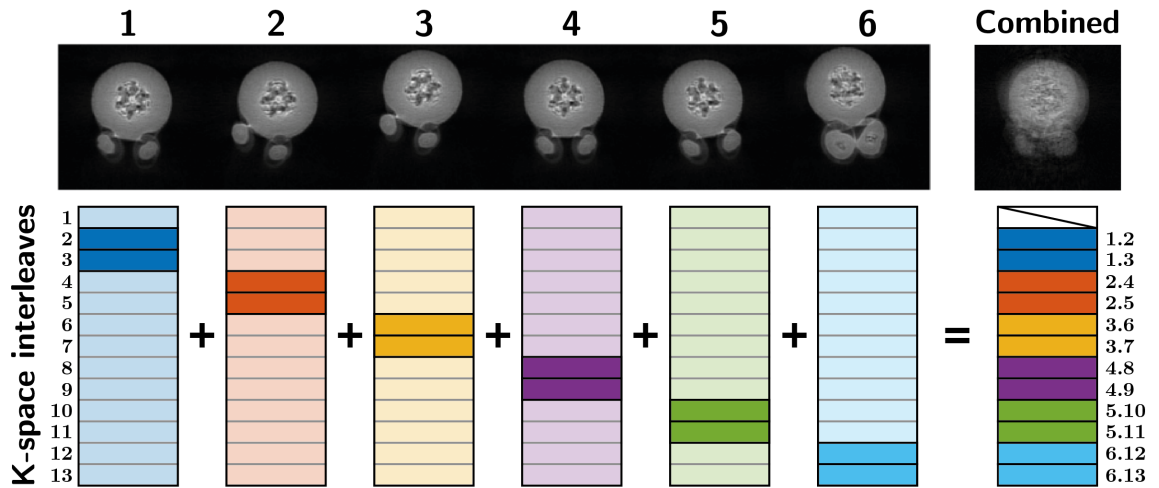


**Figure 7.27:** Schematic showing how interleaves from the six different volumes, each in a different position, are combined into a single motion corrupted k-space data set.

To assess the accuracy of the rotation and translation correction, the MOCO was repeated on images created using different permutations of interleaves. The reference volume was always the first two interleaves in the first acquisition. For each of the remaining volumes, all possible permutations of interleave pairs from interleaves 4-13 were used for the MOCO, giving a total of 36 permutations ( $\binom{9}{2}$ ). Since all pairs of interleaves in the same volume encode the same motion state, any permutation should yield the same rotation and translation estimation. Residual variability in the MOCO results can therefore be considered as an estimate of the accuracy of the method.

## Results

Figure 7.28a shows reconstructed images from the two interleaves used for MOCO from each volume. Although the individual images have poor SNR, it can clearly be seen that the phantom has been rotated and translated between the acquisitions. Combining and reconstructing interleaves from each acquisition produced a single motion corrupted volume, shown in figure 7.28b.

MOCO was successfully applied to the motion corrupted volume, resulting in substantially improved image quality figure 7.29b. The structure of the core in the cantaloupe is now clearly visible, and the edge is much sharper, similar to the reference in figure 7.29c. Figure 7.29d shows line profiles through the phantom clearly showing improved edge contrast after MOCO. There are still residual errors in the motion corrected image, however, resulting in slight variations in the image intensity, compared to the reference volume.



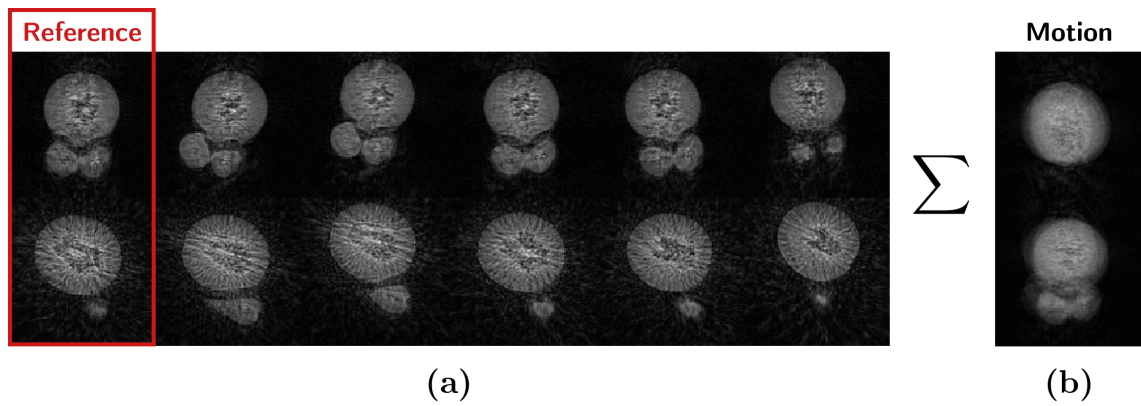


**Figure 7.28:** (a) Overview the six acquired volumes reconstructed with two interleaves each, and (b) the combined reconstruction. Slices from two orthogonal planes at the same position are shown for each volume, chosen as they highlight structure of the phantom. The rotation and translational motion applied between the volumes can be clearly seen.

Results from running the MOCO with different permutations of the interleaves are presented in figure 7.30. Overall, the technique appears stable, however for some interleave permutations, the registration fails, resulting in large errors, indicated with filled circles in figure 7.30a. It was consistently the same interleave combinations that resulted in poor registration ( $i_{pair} = (7, 13, 18, 22, 36)$ ). Inspection of the results from the optimiser shows that the final value of the cost function  $E$  is higher in all these cases compared to the otherwise almost constant value across the other interleaves (figure 7.30b), indicating that the optimiser has become stuck in a local minimum. Errors in rotation estimation also propagate into the translation correction step (figure 7.30c), with a clear correspondence between permutations showing problems in rotation and translation estimates. (Note that translation is estimated in integer number of voxels, resulting in discrete steps in the results).

To estimate the accuracy of the registration, the permutations where the registration failed (indicated with filled dots in figure 7.30) were excluded for two reasons. First, using a better minimisation techniques these local minima can most likely be avoided. Secondly, and most importantly, studying the cases where the optimisation was successful provides a better characterisation of the cost function. A shallow cost function can result in wide variations even if the global minimum is found. The mean and standard deviation for the rotation estimation, calculated over the remaining permutations, are presented in table 7.5. The standard deviation of the rotation estimates ranged between  $0.13^\circ$  and  $1.03^\circ$ . The variability in translation estimation was much lower, as seen in figure 7.30c. For the

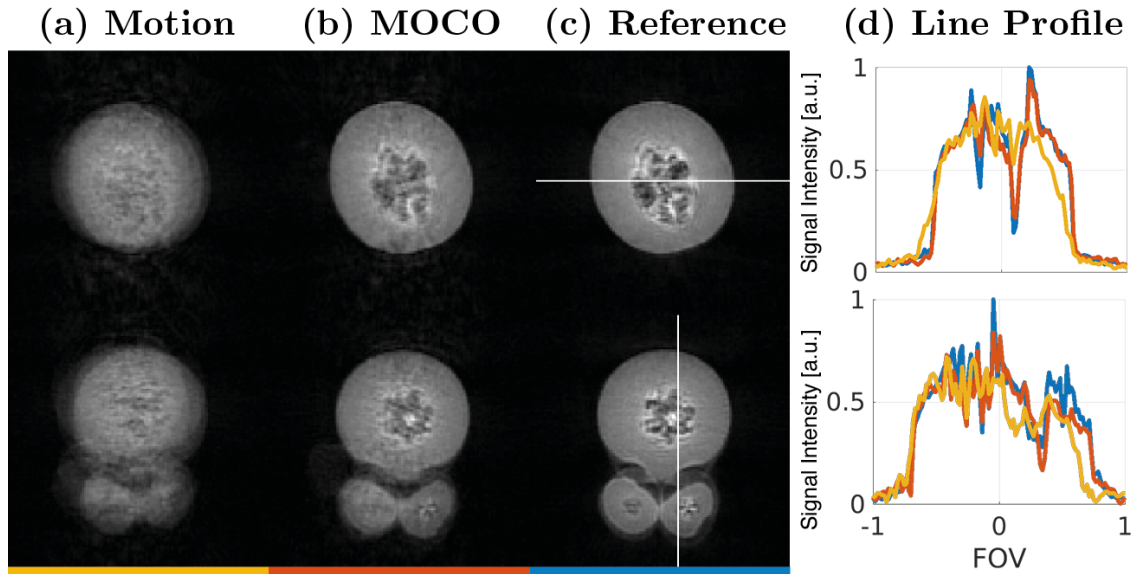


**Figure 7.29:** (a) Motion corrupted volume, (b) Volume after successful MOCO, (c) Fully sampled reference volume. (d) Line profiles through the phantom, as indicated with white lines in (c) comparing the image intensity in each voxel.

**Table 7.5:** Results from rotation estimation using permutations of different interleaves pairs. Values are reported as  $\text{mean} \pm \sigma$ . Permutations where the rotation estimated failed were ignored.

Axis	Vol. 2	Vol. 3	Vol. 4	Vol. 5	Vol. 6
X	$1.47^\circ \pm 1.03$	$1.77^\circ \pm 0.39$	$2.11^\circ \pm 0.32$	$4.47^\circ \pm 0.37$	$4.61^\circ \pm 0.37$
Y	$-17.48^\circ \pm 0.22$	$-12.63^\circ \pm 0.22$	$7.15^\circ \pm 0.19$	$14.57^\circ \pm 0.13$	$11.91^\circ \pm 0.15$
Z	$-1.16^\circ \pm 0.41$	$-2.71^\circ \pm 0.16$	$0.74^\circ \pm 0.53$	$1.28^\circ \pm 0.26$	$17.07^\circ \pm 0.18$

volumes where rotation estimation was successful, the estimated translation is identical in almost all cases, and varies by only 1 voxel in the remainder.

## Discussion and Conclusion

Through MR phantom experiments, the MERLOT framework was shown to work with real acquired data, in addition to simulated data, albeit only in a phantom. Large motion, with rotation up to  $17^\circ$  and translation up to 20mm, was successfully corrected, resulting in greatly improved image quality.

Similarly to the simulated results, the final motion corrected image is not of as high a quality as the static reference image, however. Again, this can be attributed to both residual motion and uneven sampling density in k-space following trajectory correction. In this experiment, the accuracy of the MOCO was estimated by running the algorithm for

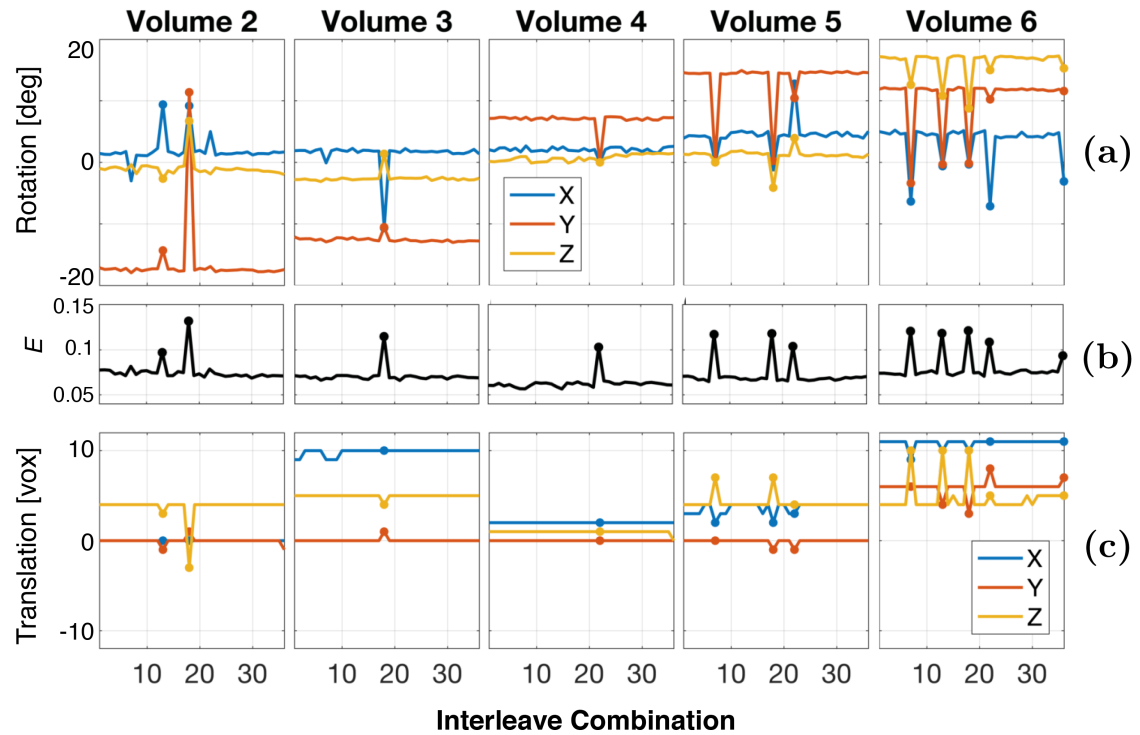


**Figure 7.30:** (a) Estimated rotation on each axis. (b) Value of cost function for the rotation correction. (c) Estimated translation along each axis. Interleave permutations where the rotation registration algorithm failed are indicated with filled circles.

all possible permutations of interleaves in each volume, resulting in a standard deviation of the estimated rotation angle  $<0.5^\circ$ , except for the x-axis in one volume which had a standard deviation of  $1.03^\circ$ . It is therefore likely that the residual artefacts seen are due to uneven sampling density in k-space following rotation of the trajectory.

Running the registration with different permutations of interleaves revealed that the registration algorithm did not always reach the global minimum, resulting in the wrong rotation estimate. Further work is required to improve the optimisation algorithm to ensure that the global minimum is always reached. One method, commonly used in image registration algorithms, is to run multiple iterations of the algorithm with different initial values, or at different scales [171]. Another approach, specifically designed for spherical navigators, is to calculate the spherical harmonic expansion of the k-space data [286], and use discrete formulation of the harmonic to estimate rotation, which removes ambiguities that could result in local minima.

In a real, in vivo, MR acquisition, patient motion is not stepwise, as simulated here, but rather continuous and/or erratic, resulting in *intra-segment* motion which cannot be



corrected for with the current framework. One way to overcome this is to this would be to achieve a high temporal resolution in the acquisition, i.e. acquire interleaves quickly. In the current experiment, the time resolution was  $4048 \cdot TR \approx 16\text{s}$ , but this can be improved. Most importantly, the TR can be reduced by using a higher readout bandwidth, here  $\pm 7.8\text{kHz}$  was used, and thus time reduction of x4 can be achieved at  $\pm 31.2\text{kHz}$  readout bandwidth. The minimum number of spokes required for accurate motion correction is not known, and will be the subject of further investigation.

## 7.8 Chapter Discussion and Conclusion

### 7.8.1 Motion Correction using Self-Navigation

In this chapter, a novel self-navigated motion correction method, MERLOT, was introduced which utilises a 3D spiral phyllotaxis trajectory together with motion correction in k-space. The technique can be seen as a 3D extension to PROPELLER, using rotating spherical volumes instead of rotating blades in k-space. Using self-navigated MR acquisitions for MOCO has the benefit that no external hardware, such as cameras or sensors, are needed, and that the structure of the pulse sequence does not need to be modified to make room for separate navigators. It is relatively easy to make RUFIS into a self-navigated sequence, since each spoke originates in the centre of k-space, and thus the only necessary modification is to alter the temporal ordering of the spokes.

The temporal resolution of MERLOT is limited by the number of spokes required for accurate motion correction as well as the signal to noise ratio (SNR). The limit of the temporal resolution was not studied in this chapter, however, previous studies using spherical navigators have found that between 2000-4000 points on a sphere was required for motion correction [262, 266]. With RUFIS, that means 2000-4000 spokes, which, depending on the acquisition settings, can result in temporal resolutions around 2 to 8s. In the acoustic noise measurements presented in section 7.2.2, the trajectory with 21 interleaves had 1760 spokes per interleave, resulting in a temporal resolution of 3.2s. This could be compared to PROPELLER, where about 30 lines of k-space are required for a motion estimate, which can be acquired in a single turbo spin echo acquisition for instance, resulting in sub-second temporal resolution [279]. Recent work have also demonstrated quiet PROPELLER imaging at 1.5 and 3T with less than 6dB(A) increase in the acoustic noise relative to the ambient noise [294, 295]. The acquisition time of the quiet PROPELLER sequences were

about 50% longer compared to the comparable noisy sequence, in both these studies. Also, PROPELLER only allows for in-plane MOCO, i.e. in 2D, while MERLOT is 3D.

Using radial k-space data for rotation correction makes it possible to utilise the inherent symmetry in the k-space magnitude data to mirror the radial spokes. Here, it was used double the angular resolution, however it could also be used to double the temporal resolution for the rotation correction, while still maintaining the same angular resolution. The full k-space, as required for translation correction, could then be obtained using partial k-space techniques with an initial centre k-space acquisition [296].

### 7.8.2 Improvements to Registration Framework

There are several potential future improvements to the MERLOT image registration framework presented here. The first issue, which was highlighted in the interleaved rotation correction simulation, were the image artefacts after rotating the k-space trajectories to account for rotation of each individual volume. The final combined image showed streaking artefacts, with a similar pattern to a volume sampled and reconstructed with the same trajectory, indicating that it was the trajectory, and not imperfect rotation correction, that caused the artefacts. It is the uneven distribution of points in k-space which give rise to these incoherent artefacts. Iterative SENSE reconstruction methods with total variation (TV) [291] or total generalised variation (TGV) [126] have shown great promise for artefact reduction in radial acquisitions, and could be combined with MERLOT in the final image reconstruction step.

The MR phantom experiment presented in this chapter was performed on a single channel transmit and receive coil to remove the confound of multiple coils. Receive coils with multiple channels have several advantages for motion correction in general, but incorporation into MERLOT has not yet been achieved. One advantage with multi-channel coils is the localised signal reception, which potentially can remove non-linear motion from the neck for instance. Array coils can also achieve higher SNR. Finally, the sensitivity profile of the different channels in an array coil can also be used to estimate motion. Kober et al. used FID navigators to detect motion in an MP-RAGE sequence where motion was determined from changes in the FID signal [297] (note that motion was only *detected* and not *corrected*). In RUFIS, FIDs are repeatedly acquired, and thus there might be an opportunity to estimate bulk motion by studying the relative change in the first points in the FID from each coil. The main difficulty with incorporating multi-channel data into MERLOT

is how to best utilise k-space data from multiple coils for rotation correction. Either, the registration is performed on all the data from all coils simultaneously, effectively  $N$ -fold number of data points, using a receive coil with  $N$  channels. Alternatively, the data could be combined into a single k-space data set with high SNR, however the mathematical model for achieving this has not been resolved yet. Further work will explore these opportunities and develop a method for incorporating multi-channel data into MERLOT.

### 7.8.3 A Modular Framework

One of the main strengths of the MERLOT method, is the modular structure of the technique, as outlined in figure 7.31. The k-space trajectory, which determines the temporal resolution, is sent to the scanner and motion corrupted data is acquired. At this point, the standard image reconstruction pipeline can be invoked, which would result in a motion corrupted image, pathway A in figure 7.31. With MERLOT, pathway B in figure 7.31, rigid body motion correction is performed by separating rigid body motion into rotation and translation. Rotation correction produces a corrected MOCO trajectory, and translation correction applies a phase correction to the k-space data. These data are in exactly the same shape and format as the data initially collected on the scanner, and thus the standard image reconstruction pipeline can be invoked. Alternatively, advanced compressed sensing or deep learning reconstruction methods can be used to improve image quality [127, 298]. Practically, this means that the MERLOT pulse sequence and motion correction can be implemented to feed directly into the standard image reconstruction pipeline on the scanner. It could even be combined with more sophisticated data driven auto-focusing methods for MOCO [289, 288], where MERLOT is used to remove the effects of bulk movement and additional software to "fine tune" the correction.

Using MERLOT only requires modification of the k-space trajectory, and it is thus compatible with any contrast weighting. Steady-state acquisitions will provide the highest frame rate for motion estimates, since there is no deadtime in the sequence. MERLOT could also be used in multi-contrast acquisitions such as MUPA by distributing the spokes in each interleave over the different contrast weighting, thus obtaining a fully sampled, albeit mixed contrast, interleave for each loop in the MUPA sequence. Further work is required to evaluate how changes in contrast weighting across k-space will affect the motion correction.

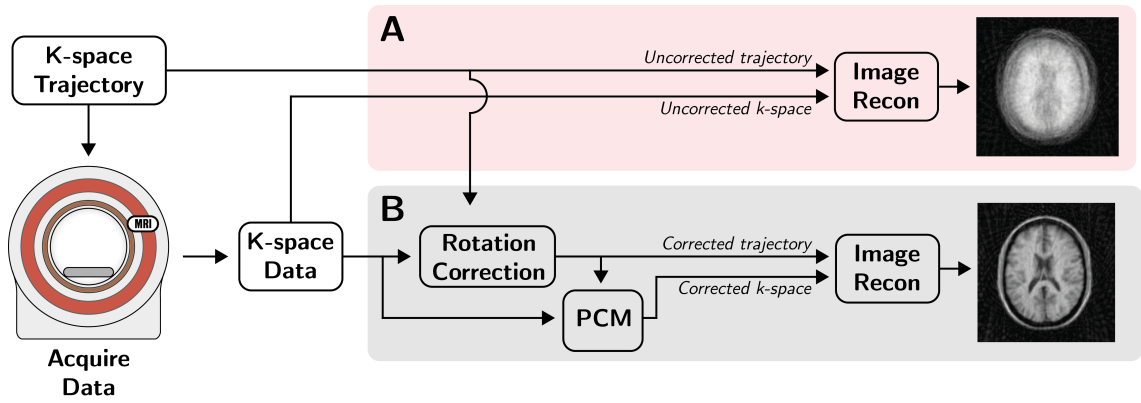


**Figure 7.31:** Schematic of the modular structure of MERLOT and how it can be integrated into the image acquisition pipeline before the standard image reconstruction step. Pathway **A** shows the standard reconstruction, resulting in a motion-corrupted image, while pathway **B** incorporates the motion correction step before the standard image reconstruction step.

#### 7.8.4 Conclusion

In this chapter, a novel method, for motion correction with RUFIS, was presented. The method named MERLOT (Motion Elimination Radial acquisition Leveraging Overlapping Trajectories) uses the 3D phyllotaxis trajectory with the RUFIS sequence to enable a self-navigated acquisition. Measurements of the acoustic noise showed a slight increase using the phyllotaxis trajectory, but it was still well below 85dB(A). It was found that higher number of interleaves, i.e. higher temporal frame rate, produce the lowest acoustic noise. A k-space based MOCO framework, in which rigid body motion is decomposed into rotation and translation, was presented and validated through simulations. The MERLOT technique, including acquisition and motion correction, was evaluated through simulations and in an MR experiment using a phantom, demonstrating that the technique can correct for rigid body motion.

## 7.9 Publications and Contribution

### 7.9.1 Publications

The content of this chapter has not been presented previously.

### 7.9.2 Contribution

Collaborators at GE Healthcare have previously investigated a different implementation of the phyllotaxis trajectory for motion correction. The implementation of the 3D phyllotaxis trajectory used here was developed by me. The idea to use an interleaved RUFIS acquisition for retrospective MOCO originated from discussions between me and my supervisors. I performed the implementation of the pulse sequence and developed technique for retrospective MOCO. Thanks to Prof. Barker and Nikou Damestani for helping me coming up with the *MERLOT* acronym.

## Chapter 8

# Conclusions and Further Work

Magnetic Resonance Imaging (MRI) is today one of the most important techniques for brain research [299, 300], as well as in clinical practice where it can provide soft-tissue contrast not achievable with CT. One limitation of MRI, however, is the very loud acoustic noise produced by the scanner, which reduces patient comfort. For some patient groups, with for instance hyperacusis [89], the noise can be intolerable, making it difficult to complete scans. The acoustic noise is produced by mechanical vibrations in the gradient coils due to Lorentz forces, and can thus be reduced by minimising the gradient switching. In this thesis, the near-silent Rotating Ultra-Fast Imaging Sequence (RUFIS) has been studied. Silent MRI using RUFIS could have a wide-reaching impact in clinical practice as well as in research studies through improved patient comfort, increased accessibility for patients with hypersensitivity to noise, as well as by providing a better working environment for staff. In meetings with service users, I have repeatedly received positive feedback regarding the development of silent MRI techniques, with many service users saying that the noise was one of the major discomforts during the MRI exam.

One of the reasons that silent MRI with RUFIS has not reached the clinical setting, nor research studies yet, however, is that the standard RUFIS sequence can only produce proton density (PD) or weak  $T_1$  contrast, which limits its applications. This thesis aimed to improve our understanding of the RUFIS sequence through the development of quantitative imaging protocols for  $T_1$  and  $T_2$  mapping. In accordance with the title of this thesis, I would like to summarise the contributions made to the field in this thesis through the three main keywords: *Quick*, *Quiet*, and *Quantitative*.

## 8.1 Quick

RUFIS is a zero echo time (ZTE) sequence, in which excitation is performed with the readout gradient already turned on after which the free induction decay (FID) is acquired. The lack of slice and phase encoding gradients, as well as spoiling gradients, results in a TR that is only limited by the data sampling, resulting in almost 100% sampling efficiency. The effective TE=0 and quick readout enhances sensitivity to tissues with short  $T_2^*$  [301], but it also leads to several constraints and unique features of the acquisition, which were studied in detail in chapter 3. For example, the RF pulse width, which determines the flip angle when operating in the regime of peak  $B_1$ , is limited by the readout bandwidth as it is necessary to ensure that the excitation bandwidth encompass the readout bandwidth, a constraint not present in non-ZTE sequences. If high flip angles are desired for a given measurement, long pulse widths will be required and thus a low readout bandwidth must be used to ensure a uniform the excitation profile across the field of view. For qualitative, i.e. not quantitative, contrast weighted imaging the resulting non-uniformity can be partially compensated for using the same filtering techniques as currently typically used to address receive non-uniformity from surface and array coils [302]. However, such techniques cannot be used to compensate for changes in contrast due to changes in the flip angle, as required for quantitative imaging. In that situation, iterative simulations can be used to determine the effect of the resulting excitation profile and to incorporate it into quantitative measurements as an additional  $B_1^+$  correction, as demonstrated in chapter 4. Another feature unique to ZTE is the deadtime gap between RF excitation and beginning of data collection which, depending on the readout bandwidth, requires special considerations for filling the centre of k-space to avoid image artefacts [128]. After studying and understanding these constraints, it was shown that the RUFIS sequence can in general be treated as an SPGR/FLASH sequence with very short TR.

Another aspect of *quick*, which was studied in the last chapter of the thesis, is the rapid time-resolved acquisition with RUFIS, enabled by a 3D spiral phyllotaxis k-space trajectory. By acquiring a large number of low-resolution volumes at high temporal resolution, each volume with a unique set of k-space points, a self-navigated data acquisition was demonstrated. A new motion correction technique named Motion Elimination in Radial acquisition Leveraging Overlapping Trajectories (MERLOT) was developed, which features rotation and translation estimation, and correction, directly on k-space data. The technique was demonstrated in a simulated brain phantom, showing that rotation and

translation can be estimated in two separate steps and corrected for jointly. MR experiments using a phantom showed that the technique also works on real MR data. With a frame rate on the order of seconds, the method should be able to correct for movements such as when patients re-position themselves during a scan, but not for ongoing random or pseudo-random movement. Further work on MERLOT will investigate optimal incorporation of data from multiple coils, along with optimisation of the final reconstruction step, using iterative methods with regularisation for improved image quality [126].

One possible future modification to the RUFIS sequence, which has not been investigated in this thesis, is modification of the spoke readout. Acquiring straight spokes in k-space results in a sampling density which scales as  $k_r^2$ . An optimal sampling scheme, on the other hand, should have even sampling density across all of k-space. While perfect uniformity is impossible for any trajectory for which each spoke originates in the centre of k-space, the uniformity can be improved using curved spokes. Jackson et al. presented a k-space sampling strategy known as twisting radial lines (TWIRL) where each readout consists of a radial and spiral part [303]. The larger the proportion of the spoke that is spiral, the more uniform the sampling density is. However, a larger twist on the spoke also requires more switching of the gradients and thus potentially higher acoustic noise. If spokes are arranged such that the initial direction of a given spoke is the same as the direction at the end of the previous spoke, however, minimal gradient switching is required between spokes, potentially allowing the low acoustic noise properties of RUFIS to be maintained. The implementation of TWIRL presented by Jackson is only applicable to 2D imaging, and translation to 3D, required for RUFIS, is not straight forward. One possible 3D extension was proposed by Boada et al. for application to sodium imaging [304]. Their trajectory follows a straight spoke at first but then transitions into a cone. Depending on the length of the readout, the 3D radial/cone trajectory might be possible with RUFIS but this will require further investigation.

## 8.2 Quiet

Noise from the MRI scanner is commonly not considered a major issue, and in most cases, it can be handled with the proper use of hearing protection to reduce the acoustic noise down to the recommended 85dB(A) [2]. For patients with hypersensitivity to noise, studies involving sleep, or investigation of auditory or vocal phenomena however, a silent imaging protocol could be an important improvement to the environment during the MR



examination. Silent imaging would also improve the working environment for staff and enable easier communication with the subject undergoing the MR examination. It could also find applications in interventional MRI where surgeons are in the scan room with the patient.

Current methods, other than RUFIS, for reducing the acoustic noise have focused on modifying existing pulse sequences, mainly by smoothing the gradient waveforms and reduce gradient slew rates [95, 5]. RUFIS, on the other hand, is a silent pulse sequence by design, as the gradients are not rapidly ramped up and down between readouts, but instead gradually changed between spokes. The acoustic noise produced by conventional MR sequences can reach above 100dB(A), levels at which hearing protection is required to avoid hearing loss from prolonged exposure. With RUFIS, the acoustic noise can be limited to well below the 85dB(A) threshold for requiring hearing protection. In chapter 3 it was shown that the sound pressure level in a RUFIS acquisition depends on acquisition parameters such as readout bandwidth and resolution. The 3D phyllotaxis trajectory, introduced in chapter 6, was shown to increase the acoustic noise slightly, with the highest recorded sound pressure level of 78.4dB(A). Nevertheless, by choosing a higher number of interleaves (which resulted in equally good image quality) it was possible to reduce the noise to 71.1dB(A), relative to the ambient noise level of 62.3dB(A). In conclusion, within the wide range of acquisition parameters used in this thesis, the acoustic noise from RUFIS was always below the 85dB(A) threshold at which hearing protection is required, and in almost all cases it was within a few dB(A) of the background noise levels in the scan room.

The quantitative techniques developed in this thesis either utilised the inherent contrast in the RUFIS acquisition (i.e.  $T_1$ ) or added additional contrast ( $T_1$  and  $T_2$ ) through magnetisation preparation modules. Neither of these approaches increased the acoustic noise. Other contrast mechanisms, such as diffusion, rely on gradients for producing the desired contrast and therefore require special consideration. Nevertheless, recent work has shown a successful implementation of diffusion weighted RUFIS imaging [110].

The MERLOT motion correction technique presented in chapter 7 uses a self-navigated RUFIS acquisition and does therefore not introduce additional acoustic noise, as long as an appropriate k-space trajectory is used. Silent implementations of the PROPELLER method, which is similar to MERLOT but with acquisition of 2D Cartesian "blades", have been demonstrated [294, 295]. In these studies, the acquisition time was increased by about 50% in order to reduce the acoustic noise. With MERLOT, however, there is no increase

in acquisition time, making it a competitive method for silent, 3D, retrospective motion correction.

### 8.3 Quantitative

The main focus of the work in this thesis was quantitative  $T_1$  and  $T_2$  mapping with RUFIS. In chapter 3, the RUFIS sequence was studied in order to develop a quantitative signal equation for RUFIS, showing that a steady-state RUFIS acquisition can be treated as a spoiled gradient echo (SPGR) sequence, a crucial step in further developing quantitative methods with RUFIS. The most basic quantitative measurement that can be performed with SPGR, and thus RUFIS, is a  $T_1$  measurement using the variable flip angle (VFA) method, and this was therefore the first quantitative method that was evaluated with RUFIS. The VFA method is highly sensitive to variations in  $B_1^+$ , thus requiring a separate  $B_1^+$  map. A method for silent  $B_1^+$  mapping using magnetisation prepared RUFIS was therefore developed and shown to produce  $B_1^+$  maps very similar to the standard Bloch-Siegert method. VFA  $T_1$  mapping with RUFIS was then compared against a standard Cartesian SPGR acquisition in chapter 4, and found to produce similar  $T_1$  values, with equivalent repeatability but better reproducibility.

Following the successful implementation of VFA  $T_1$  mapping at 3T with RUFIS, the method was extended to 1.5T and 7T. At 1.5T,  $B_1^+$  inhomogeneity is negligible and separate  $B_1^+$  mapping was therefore not required. In addition, with lower SAR constraints at low field strength, higher flip angles can be used, thus resulting in a more optimal sampling scheme for VFA  $T_1$  mapping. At 7T on the other hand,  $B_1^+$  inhomogeneities range between  $\approx 50$ -200% of the prescribed flip angle, and with the increased SAR at 7T, the flip angles that can be achieved are limited. Nevertheless, good results were obtained at 7T by carefully choosing the flip angles and applying  $B_1^+$  corrections. This study showed that RUFIS can measure the field dependence of  $T_1$ , as shown theoretically and demonstrated in previous studies [30, 14], which provides further evidence of the  $T_1$  specificity of the acquisition. In conclusion, similarly to SPGR, VFA  $T_1$  mapping with RUFIS is challenging at 7T but very easy at 1.5T. For clinical applications, further work should focus on the implementation of VFA  $T_1$  mapping at 1.5T for generating clinically useful  $T_1w$  images. An alternative method for  $T_1$  mapping, that is an attractive choice at 7T, is MP2RAGE, where the flip angle bias is corrected for in the acquisition directly [49, 202].

To introduce  $T_2$  contrast into RUFIS, a  $T_2$  preparation was implemented using the adiabatic mBIR4 (modified  $B_1$  insensitive rotation) pulse. Simulations were used to demonstrate the  $B_0$  and  $B_1$  robustness of the  $T_2$  preparation. Experiments in phantoms and in vivo showed that interleaved  $T_2$  preparation can be used to produce multiple volumes with increasing  $T_2$  contrast, but the signal is contaminated by  $T_1$  from the repeated excitation during the RUFIS readout. The sequence was therefore combined with an inversion pulse followed by multiple RUFIS readouts, to achieve combined  $T_1$  and  $T_2$  mapping. The combined sequence was shown to accurately quantify  $T_1$  and  $T_2$  in quantitative phantoms, but in vivo, the results were consistently underestimated. Simulations using the Bloch-McConnell equations showed that magnetisation transfer (MT) effects are expected to result in underestimation of  $T_1$  and  $T_2$ , potentially explaining the discrepancy between the phantom and in vivo experiments. Future work will aim at developing an acquisition protocol and data fitting method which enables simultaneous quantification of  $T_1$ ,  $T_2$ , proton density, and the bound pool fraction ( $F$ ), which controls the magnitude of the MT effect.

The overarching goal of further work following this PhD will be to combine the multi-parametric  $T_1$  and  $T_2$  mapping protocol with the MERLOT framework for motion insensitive, multi-parametric, silent neuroimaging. Such a protocol could be instrumental, and a very competitive alternative, for research into conditions associated with hypersensitivity to noise.

## 8.4 Summary of Main Contributions

The results presented in this thesis have contributed to the field of neuroimaging through the following developments:

1. A framework for quantitative imaging with RUFIS was developed through derivations of a signal equation. A method for simulating the effective excitation profile was also developed. Constraints on the acquisition due to the interactions between different acquisition parameters were presented.
2. A new method for silent  $B_1^+$  mapping, SIMBA, using a magnetisation prepared RUFIS acquisition was developed.
3. A comparison study of variable flip angle (VFA)  $T_1$  mapping using RUFIS and Cartesian SPGR was performed, showing that steady-state RUFIS can be used for  $T_1$

mapping using the VFA method. Together with  $B_1^+$  correction using SIMBA, this produced a silent  $T_1$  mapping protocol.

4. A study showing that RUFIS can be utilised across three field strengths, 1.5, 3, and 7T, was presented, outlining issues and opportunities at each field strength.
5. A method and a pulse sequence for combined  $T_1$  and  $T_2$  mapping using magnetisation preparation was developed. The technique was shown to work well in phantoms, but in vivo, the results diverge from standard techniques. Simulations showed that magnetisation transfer (MT) effects will lead to underestimation of  $T_1$  and  $T_2$  and need to be accounted for, or minimised, to obtain correct  $T_1$  and  $T_2$  estimates.
6. A method for retrospective motion correction of RUFIS data, using a self-navigated acquisition with a 3D spiral phyllotaxis trajectory was developed. The technique was demonstrated in a simulated brain phantom, as well as through MR experiments using a phantom.

## Appendix A

# Delaunay Interpolation on Spherical Shells

One important step in image registration algorithms is evaluation of the cost function to determine how well aligned the moving and fixed images are. Interpolating data can be a very computationally expensive procedure. With 3D radial k-space sampling, the data are acquired along straight spokes, resulting in concentric shells in k-space on which the data lie. Interpolating two 3D radial k-space data sets onto a common set of grid points is equivalent to interpolating onto the same spokes. Therefore, a 2D interpolation method can be used which is only calculated once for the polar and azimuthal angles of a single shell and then applied across all shells.

The Delaunay triangulation method for 2D interpolation turns out to be a very powerful tool for this purpose [262, 266]. Given a set of  $N$  points with coordinates  $(i_x, i_y)$ , the method calculates a triangular mesh where each triangle needs to satisfy one important criterion: every circumcircle must be empty, as illustrated in figure A.1a. The triangle composed of  $(\mathbf{r}_1, \mathbf{r}_2, \mathbf{r}_3)$  is enclosed by the circle  $C_1$ . This circle does not include  $\mathbf{r}_4$  or any other point, and the same applies to  $C_2$ . The result of the Delaunay triangulation  $DT$  is a list  $P$  with size  $(N, 2)$  of points with coordinates of the vertices and a connectivity list  $K$  with size  $(N_k, 3)$  where  $N_k$  is the number of triangles in the triangulation.

For image registration, where the moving data has to be interpolated onto the same grid points as the fixed data, the list of coordinate points of the fixed image  $P_F$  is used to find which triangle in  $DT$  that each point is contained within. In addition to the information about which triangle the point is located within, it also produces the barycentric

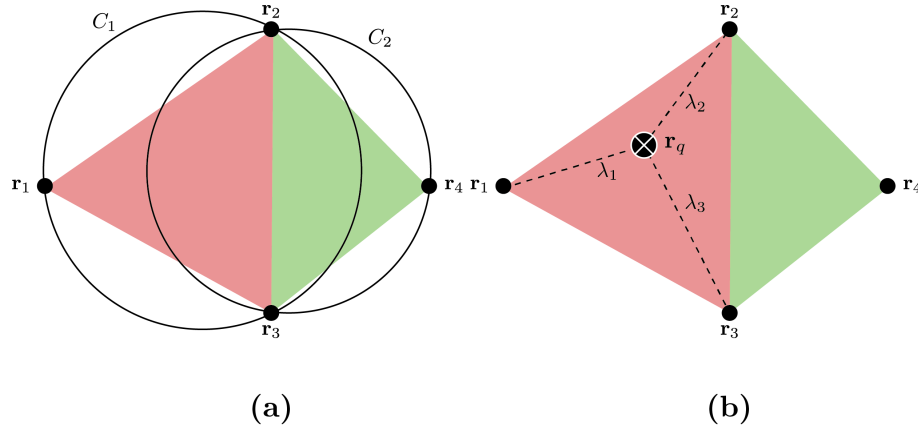


**Figure A.1:** (a): Triangle circumcircles in a valid Delaunay triangulation. The circles are not allowed to contain any other points. (b): Given a point within the triangle, it is possible to find barycentric coordinates  $(\lambda_1, \lambda_2, \lambda_3)$  representing the distance to each corner point

coordinates of the point within the triangles. This is shown in figure A.1b. The coordinates  $(\lambda_1, \lambda_2, \lambda_3)$  indicates how far from each corner of the triangle the point is located. Any point within the triangle can therefore be expressed as a linear combination of the coordinates of the corners as

$$\mathbf{r} = \lambda_1 \mathbf{r}_1 + \lambda_2 \mathbf{r}_2 + \lambda_3 \mathbf{r}_3. \quad (\text{A.1})$$

The barycentric coordinates will always obey

$$\lambda_1 + \lambda_2 + \lambda_3 = 1 \quad \text{and} \quad \lambda_1, \lambda_2, \lambda_3 > 0. \quad (\text{A.2})$$

If the function value is known at the corner points  $(\mathbf{r}_1, \mathbf{r}_2, \mathbf{r}_3)$  the function value at any point within the triangle  $\mathbf{r}_q$  can be calculated as a weighted sum of the function value at the vertices as:

$$f(\mathbf{r}) \approx \lambda_1 f(\mathbf{r}_1) + \lambda_2 f(\mathbf{r}_2) + \lambda_3 f(\mathbf{r}_3) \quad (\text{A.3})$$

## Appendix B

# Phantoms

### B.1 The Quantitative EUROSPIN Phantom

For the quantitative experiments presented in this thesis, the EUROSPIN test object 5 (T05)[168], consisting of a number of vials with doped agarose gels, was used. The vials are normally mounted in a plastic, water-filled, cylinder with space for 12 vials. Initial tests showed that this mount produced severe artefacts in 3D acquisitions. Therefore, a styrofoam mount of similar size, also with room for 12 vials, was manufactured, as shown in figure B.1. The phantom was placed in the head coil such that the vials were parallel with  $B_0$ , i.e. axial slices will cut through the vials. The relaxation time values for the vials used in this thesis are presented in table B.1 and figure B.2. Note that there is a temperature dependency for  $T_1$  and  $T_2$  of the EUROSPIN phantom. The manual provides calibrated values at 292, 296 and 300K. Our scan room is typically around 20°C and therefore the values here have been interpolated to give the relaxation times at 20°C.



**Figure B.1:** Photographs of the quantitative phantom consisting of vials from the EUROSPIN phantom in a Styrofoam mount.

Vial num.	$T_1$ [ms]	$T_2$ [ms]
1	206	51
2	308	72
5	464	92
7	623	93
9	778	113
11	931	134
12	1494	384
13	997	220
14	1066	163
15	1196	210
16	1316	199
18	1459	170

**Table B.1:**  $T_1$  and  $T_2$  values in the vials used from the EUROSPIN phantom at  $T=20^\circ\text{C}$ .

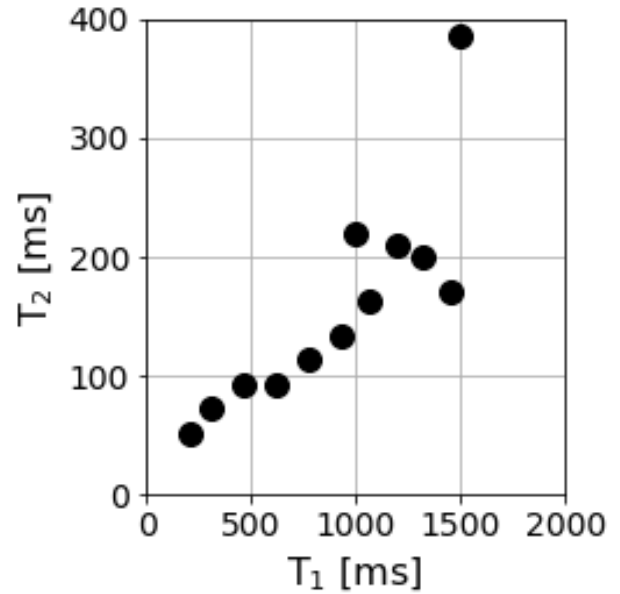


**Figure B.2:** Distribution of  $T_1$  and  $T_2$  values for the vials used from the EUROSPIN phantom at  $T=20^\circ\text{C}$



## B.2 Motion Correction Phantom

Figure B.3 shows photographs of the phantom used for investigation of motion correction in chapter 7. This phantom was constructed with three main goals: (1) to have some internal structure, here core of the cantaloupe; (2) to not be spherical symmetrical, thus the pears; and (3) to have relaxation times in the range of normal brain tissue, which is expected from the watery fruit flesh.



**Figure B.3:** Photographs of the home-made phantom used for the motion correction experiments in chapter 6, constructed of a cantaloupe and two British *Conference* pears kept together with Teflon tape.

## Appendix C

# Restricted Linear Flip Angle Sampling Scheme

This section outlines a method for calculating an evenly spaced flip angle scheme between a given minimum and maximum flip angle based on the method outlined by Helms et al.[148].

The SPGR equation, commonly expressed as

$$M(\alpha) = \sin \alpha \cdot \rho \frac{1 - E_1}{1 - E_1 \cos \alpha} \quad E_1 = e^{-TR/T_1} \quad (C.1)$$

can be rewritten using the following substitutions

$$\tau = 2 \cdot \tan \alpha / 2 \approx \alpha \quad \text{if } \alpha \text{ is small} \quad (C.2)$$

$$\phi = 2 \frac{1 - E_1}{1 + E_1} = 2 \cdot \tan(R_1 \cdot TR/2) \quad (C.3)$$

which transforms the SPGR equation into a lower order polynomial as

$$S(\tau) = \rho \cdot \frac{\tau}{1 + \tau^2/(2\phi)}. \quad (C.4)$$

This linearised version of the SPGR equation is typically plotted with  $X = S \cdot \tau, Y = S/\tau$ .

With this formulation, the Ernst angle is given by

$$\tau_E = \alpha_E = \sqrt{2\phi}. \quad (C.5)$$

An optimal flip angle scheme with  $n$  points, centred around the Ernst angle, can be calculated by

$$\tau_i = \alpha_i = \sqrt{\frac{n+1-i}{i}} \cdot \tau_E. \quad (\text{C.6})$$

The issue with this formulation for the RUFIS experiment is that the flip angles cannot be chosen freely but the maximum flip angle is limited by the readout bandwidth. Instead, a flip angle sampling scheme with  $N$  points between  $y(\tau_0) = S(\tau_0)/\tau_0$  and  $y(\tau_N) = S(\tau_N)/\tau_N$  is desired. The spacing between the samples on the y-axis  $\Delta y$  is then given by

$$\Delta y = (y_0 - y_N) \cdot \frac{1}{N-1} = \left( \frac{S(\tau_0)}{\tau_0} - \frac{S(\tau_N)}{\tau_N} \right) \cdot \frac{1}{N-1} \quad (\text{C.7})$$

Using (C.4),  $y_i$  can be expressed as

$$y_i = \frac{S(\tau_i)}{\tau_i} = \rho - \frac{S(\tau_i)\tau_i}{2\phi} \quad (\text{C.8})$$

Now,  $\tau_i$

$$S(\tau_i) = y_i \cdot \tau_i \rightarrow y_i = \rho - \frac{y_i \tau_i^2}{2\phi} \quad (\text{C.9})$$

Assuming normalized amplitude, i.e.  $A = 1$

$$y_i \tau_i^2 = 2\phi(1 - y_i) \quad (\text{C.10})$$

which using the linearised expression of the Ernst angle ( $\tau_E = \alpha_E = \sqrt{2\phi}$ ) can be simplified to

$$\tau_i = \tau_E \sqrt{\frac{1 - y_i}{y_i}}. \quad (\text{C.11})$$

The scheme for evenly spaced flip angles within a limited range can thus be expressed as

$$\tau_i = \tau_E \sqrt{\frac{1 - y(\tau_0) + i \cdot \Delta y}{y(\tau_0) - i \cdot \Delta y}} \quad (\text{C.12})$$

$$y(\tau) = S(\tau)/\tau, \quad \Delta y = \frac{y_0 - y_N}{N-1} \quad (\text{C.13})$$

## Appendix D

# Bloch-Simulations

The single pool Bloch-Simulator used in this thesis builds on compiled MATLAB code (MEX files) from Brian Hargraves at Stanford. The original source code is available from <http://mrsrl.stanford.edu/~brian/blochsim/>. In this thesis, a framework was developed, with Dr. Hargraves Bloch-Simulator code as its basis, specifically for simulating  $T_2$  preparation modules. Parts of the  $T_2$  preparation simulation code were provided by Dr. Brian Burns at GE and developed in collaboration with Peng Cao [216]. The time step was set to  $2\mu s$ , since this is the smallest time step available for specifying radio frequency (RF) waveforms on the scanner. Unless stated otherwise, the simulations were performed with  $T_1=10s$  to minimise effects of  $T_1$  relaxation and allowing the simulations to focus on  $T_2$ .

## Appendix E

# The Golden Angle and the 3D Spiral Phyllotaxis Trajectory

### E.1 Introduction

This appendix summarises some of the main concepts behind golden angle sampling in MRI, starting from the definition of the golden ratio, its connection to the Fibonacci sequence and practical implementations of golden angle sampling for 2D and 3D MRI applications. The material presented here does not contain novel results, but is merely a brief review of the current literature on the subject for the interested reader.

### E.2 The Golden Ratio and the Fibonacci Sequence

The golden ratio  $g$ <sup>1</sup> is defined as the ratio between two quantities, for example lengths, where the ratio of the larger quantity ( $a$ ) to the smaller quantity ( $b$ ) is the same as the ratio of their sum ( $a + b$ ) to the larger quantity ( $a$ ). This is expressed as

$$\frac{a+b}{a} = \frac{a}{b} \stackrel{\text{def}}{=} g \quad (\text{E.1})$$

The value of  $g$  is thus given by solving the quadratic equation

$$g^2 - g - 1 = 0 \quad \rightarrow \quad g = \frac{1 + \sqrt{5}}{2} \quad (\text{E.2})$$

---

<sup>1</sup>The golden ratio is typically written as  $\phi$ , here  $g$  is used to distinguish it from the azimuthal angle  $\phi$  used for the notation in spherical coordinate systems.

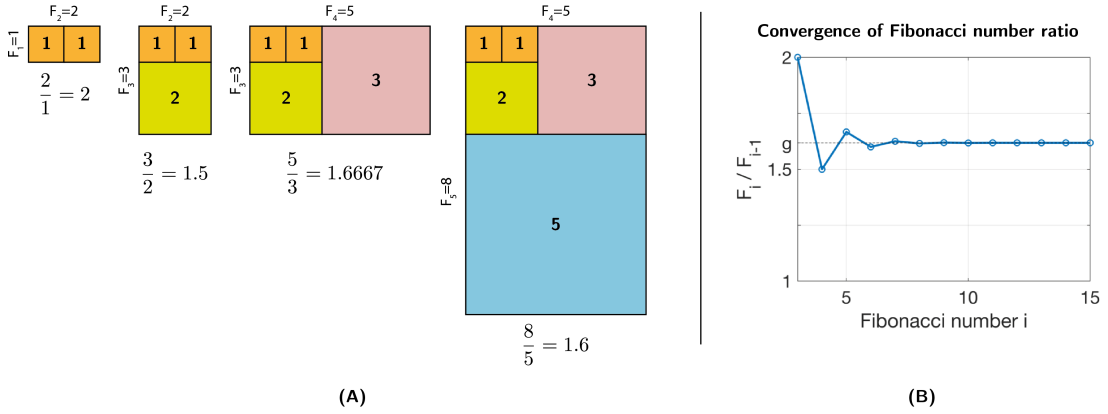


**Figure E.1:** (a) Graphical representation of the connection between the Fibonacci sequence and the golden ratio. Rectangles are built by squares with side length given by Fibonacci numbers. The ratio of the side lengths of the resulting rectangles approach the golden ratio. (b) Numerical example showing the convergence of the ratio of subsequent Fibonacci numbers towards the golden ratio.

The golden ratio has an interesting connection to the Fibonacci sequence  $F_n$ , which is defined as

$$F_n = F_{n-1} + F_{n-2}, \quad F_0 = 0, \quad F_1 = F_2 = 1 \quad \forall n > 0 \quad (\text{E.3})$$

It was observed by Johannes Kepler [305] that the ratio of subsequent Fibonacci numbers converges towards the golden ratio

$$\lim_{n \rightarrow \infty} \frac{F_{n+1}}{F_n} = g \quad (\text{E.4})$$

which also can be proved using Binet's formula [306].

To build an intuitive understanding of this limit, a graphical example is presented in figure E.1. The Fibonacci sequence is visualised as squares with side length equal to a Fibonacci number. Starting from the initial case of two squares with sides of 1, they combine to a rectangle with sides 1 and 2. The next Fibonacci number is given by the sum of two squares, i.e. 2. This is visualised by adding a square with side 2. As this continues, rectangles of increasing size, with side lengths that are Fibonacci numbers, are generated. The ratio of the sides in these rectangles will approach the golden ratio, as illustrated in figure E.1. Subsequent Fibonacci numbers can therefore be seen as integer solutions to equation (E.1), with a better solution for higher values.

### E.3 The Golden Angle - From Botany to Brain Imaging

Observations in botany have found that flowers and seeds growing in spiral patterns in plants tend to be distributed with a fixed angular increment of  $137.5^\circ$  [270]. This angle has become known as the *golden angle*, similar to the golden ratio. The golden angle, here notated as  $\alpha_g$ , can be explained similar to the golden ratio as the ratio of two angles in a circle divided into two segments, as shown in figure E.2.

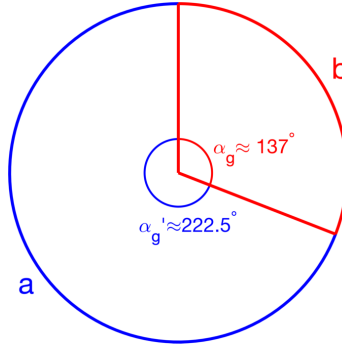


**Figure E.2:** Diagram of the golden angle in a circle

Let  $f$  be the fraction of the circumference occupied by  $b$

$$f = \frac{b}{a+b} = \frac{1}{1+g} \quad (\text{E.5})$$

where the second step used the definition of  $g = a/b$ . Since  $1+g = g^2$ ,  $f$  can be expressed as

$$f = \frac{1}{g^2} \quad (\text{E.6})$$

and the golden angle is thus given by

$$\alpha_g = \frac{360}{g^2} \approx 137.5^\circ. \quad (\text{E.7})$$

Alternatively,  $\alpha'_g = 360 - \alpha_g$  could also be used which, thanks to symmetry of the golden ratio is given by

$$\alpha'_g = 360 - \alpha_g = 360 \left(1 - \frac{1}{g^2}\right) = 360 \left(\frac{g^2 - 1}{g^2}\right) = 360 \left(\frac{g + 1 - 1}{g^2}\right) = \frac{360}{g}. \quad (\text{E.8})$$

This graphical description of the golden angle does not explain though why the golden angle is observed in distribution of leaves and flowers in plants. Instead, it is more informative to study the derivation of the golden angle as explained by Vogel [270]. By studying

the sunflower head, he concluded that the angular increment between subsequent seeds in the sunflower head is constant. Also, each new seed filled the biggest available gap, and was positioned at a constant fraction within that gap. Based on these observations, he proved that a  $137.5^\circ$  angular increment does satisfy these conditions, using the following approach. Assume that the angular increment can be expressed as  $\delta = z2\pi$ , where  $z$  is expressed as a ratio  $z = p/q$ , where  $p$  and  $q$  are co-primes, i.e. no common denominator. Start with the initial guess  $z_0 = 1/3$ , resulting in  $\delta = 120^\circ$ . The  $0^{th}$  leaf is placed at  $\delta_0 = 0$  and the following leaves at  $\delta_n = n \cdot z2\pi$ . This will result in the  $3^{rd}$  (i.e.  $q^{th}$ ) leaf overlapping with the  $0^{th}$ , see figure E.3a, which is not the desired result. Now, the guess is updated to  $z_1$  such that the third leaf instead occupy the gap between the  $0^{th}$  and the  $1^{st}$  leaf, cutting a fraction  $z_1$  into this gap, E.3b. The gap between leaf 0 and 1 was previously  $1/q_0$ . The location of leaf 3 is now  $\delta_3 = 2\pi(3 \cdot z_0 + z_1 \cdot 1/q_0)$ , or equivalently  $\delta_3 = 2\pi(3 \cdot z_1)$ . This can be expressed as a recursive equation as

$$z_{n+1} = \frac{p_n q_n}{q_n^2 - 1} = \frac{p_{n+1}}{q_{n+1}}. \quad (\text{E.9})$$

Vogel showed that the Fibonacci sequence satisfies this equation with

$$p_n = F_{2v} \quad q_n = F_{2v+2} \quad (\text{E.10})$$

and thus

$$z_n = \frac{F_{2v}}{F_{2v+2}}. \quad (\text{E.11})$$

Using the limit in (E.4), it can be seen that  $F_{n+1} = g \cdot F_n$  as  $n \rightarrow \infty$ , and therefore

$$z = \lim_{n \rightarrow \infty} \frac{F_{2v}}{F_{2v+2}} = \lim_{n \rightarrow \infty} \frac{F_{2v}}{g^2 \cdot F_{2v}} = \frac{1}{g^2} \quad (\text{E.12})$$

which yields

$$\delta = \frac{2\pi}{g^2} \approx 137.5^\circ. \quad (\text{E.13})$$

The derivation by Vogel demonstrates the key concept behind golden angle sampling in radial MRI; with a constant angular increment of  $137.5^\circ$ , any new spoke added to the acquisition will fill the largest available gap. And since the golden ratio is irrational, no two spokes will overlap. Any subset of a larger set of radial projections spaced with the golden angle will therefore be uniformly spaced over the whole angular domain. This enables



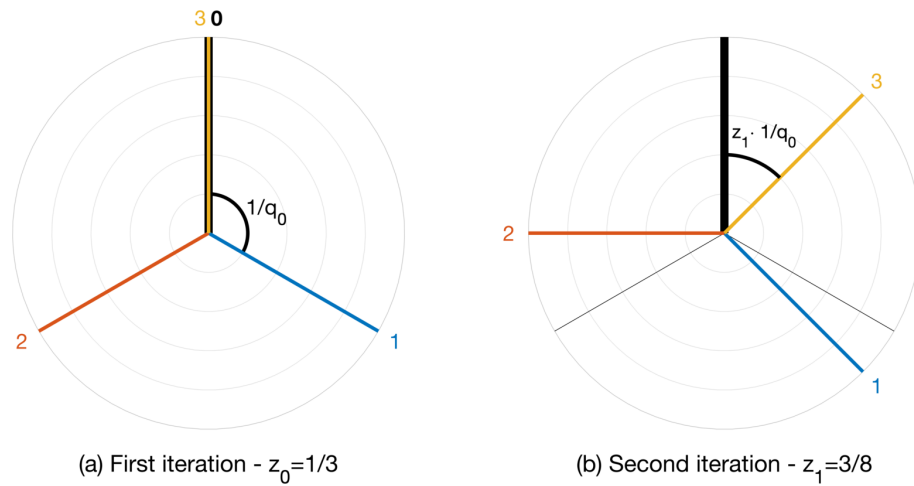


**Figure E.3:** The two first iterations in Vogel's approach to find the golden angle.

reconstruction of images along the temporal direction of the acquisition, commonly used in dynamic acquisitions [272].

The derivation of golden angle sampling presented above was built on radial-out distribution of leaves/spokes. In radial MRI, full radial projections, i.e. diameters, are most commonly used and then the golden angle will have to be defined over a half-circle, and thus  $\alpha_g = 111.2^\circ$  or  $\alpha_g = 68.8^\circ$  [271, 272]. It is therefore important to distinguish between centre-out (half), and full projection radial imaging as the angle between subsequent projections will be different

$$\begin{cases} \alpha_{g,half} = \frac{2\pi}{g^2} \approx 137.5^\circ \text{ or } \frac{2\pi}{g} \approx 222.5^\circ \\ \alpha_{g,full} = \frac{\pi}{g^2} \approx 68.8^\circ \text{ or } \frac{\pi}{g} \approx 111.2^\circ \end{cases} \quad (\text{E.14})$$

The work by Piccini et al., which introduced the 3D phyllotaxis trajectory used in this thesis, used  $\alpha_g = 137.5$  as this was designed for a spiral k-space trajectory on a sphere, equivalent to centre-out projections. Figure E.4 and E.5 demonstrates the effect of using the wrong angular increment for half and full projection radial imaging, resulting in unwanted grouping of spokes.

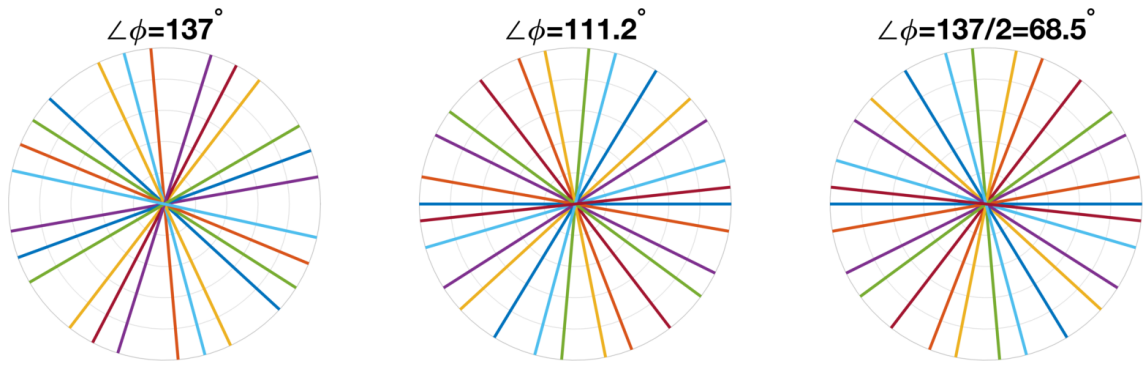


**Figure E.4:** Example of full diameter radial sampling with 13 spokes using different angular increments. Using  $\alpha_g = 137.5^\circ$ , spokes appear in groups due to the diameter overlap. With the golden angle reduced to half the circle  $\alpha_g = 111.2^\circ$  or  $\alpha_g = 68.5^\circ$ , uniform sampling is achieved.

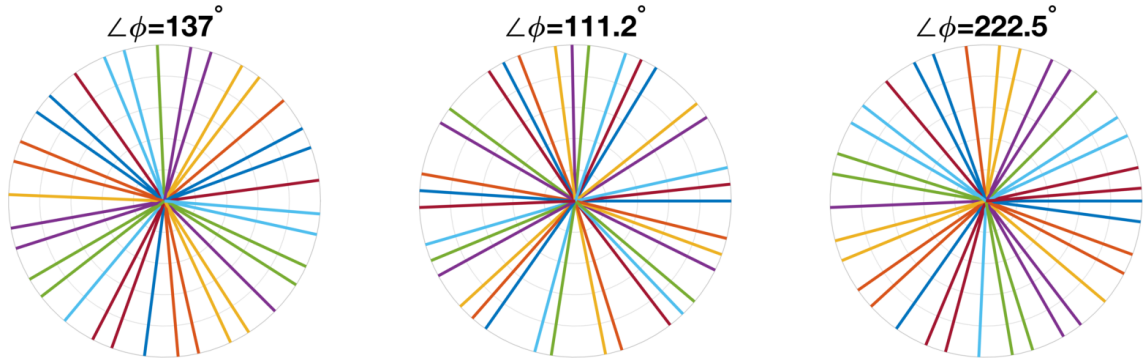


**Figure E.5:** Example of radial centre-out (half) sampling with 34 spokes using different angular increments. Using  $\alpha_g = 137.5^\circ$ , even sampling over the whole domain is achieved. With the golden angle reduced to half the circle  $\alpha_g = 111.2^\circ$ , the spokes appear in groups. Using  $\alpha_g = 360 - 137.5 = 222.5^\circ$  produces uniform sampling as well.

For most MRI applications of golden angle sampling, a full projection radial acquisition is used where the angle between subsequent spokes is the golden angle ( $111.2^\circ$ ). This results in large gradient steps between spokes. In 3D radial, silent imaging, a smooth gradient waveform is required and the golden angle trajectory cannot be used as it is. However, it is still desirable to use the golden angle distribution as it provides a uniform distribution of points over the sphere. To produce a smooth trajectory, spokes in the trajectory which are as close to each other as possible should be acquired in order. Köhler showed that after  $n$  spokes where  $n$  is the  $i^{th}$  Fibonacci number, the distribution of spokes will be even, with gaps between spokes equivalent to either  $2\pi/g^{i-1}$  or  $2\pi/g^{i-2}$  [271] (for a formal proof by induction, see appendix in Ref. [272]). Figure E.6a shows 13 (the  $7^{th}$  Fibonacci number) radial out spokes, spaced by  $\alpha_g = 137.5^\circ$ . Only two gaps between any two neighbouring

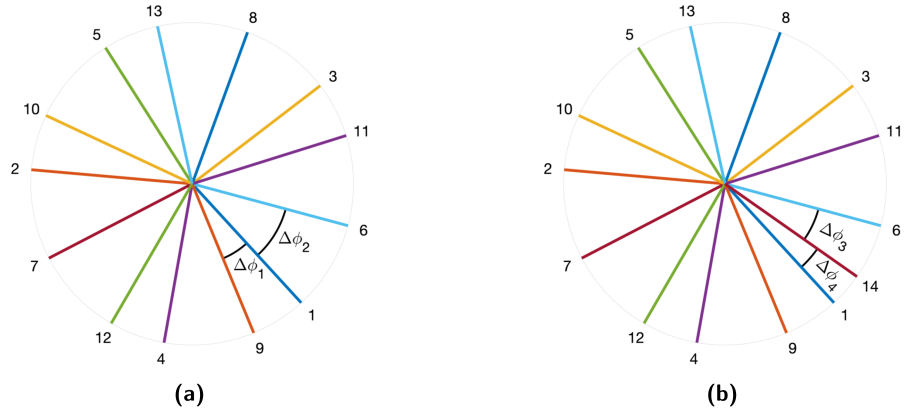


**Figure E.6:** Figure showing spacing between spokes using the golden angle distribution. **(a)** With 13 spokes (i.e. Fibonacci number 7) there are only two different gaps between spokes:  $|\Delta\phi_1| = 20.06^\circ$ ,  $|\Delta\phi_2| = 32.46^\circ$ . **(b)** Adding in a 14<sup>th</sup> spoke cuts the larger gap by the golden ratio creating two new smallest gaps of  $|\Delta\phi_3| = 20.06^\circ$ ,  $|\Delta\phi_4| = 12.40^\circ$ .

spokes with size  $\Delta\phi_1 = 20.06^\circ$  and  $\Delta\phi_2 = 32.46^\circ$  can be observed. These gaps correspond to, as predicted by Köhler,  $\Delta\phi_1 = 2\pi/g^6$  and  $\Delta\phi_2 = 2\pi/g^5$ . When a 14<sup>th</sup> spoke is added, as shown in figure E.6b, it will cut a gap given by the golden ratio into the largest available gap ( $\Delta\phi_2$ ), creating two new gaps with sizes

$$\Delta\phi_3 = \Delta\phi_2 \cdot \frac{1}{g} = \frac{2\pi}{g^6} \approx 20.06^\circ \quad (\text{E.15})$$

$$\Delta\phi_4 = \Delta\phi_2 \cdot \left(1 - \frac{1}{g}\right) = \frac{\Delta\phi_2}{g^2} = \frac{2\pi}{g^7} \approx 12.4^\circ. \quad (\text{E.16})$$

Sub-sampling a golden angle trajectory with a factor  $k = F_i$ , results in a trajectory consisting of spokes  $(1, 1+k, 1+2k, \dots, 1+nk)$ . Figure E.6 demonstrated that the spacing between spoke 1 and  $1+k$  will be  $\Delta\phi_k = 2\pi/g^i$ , for  $k = F_i$ . In conclusion, higher sub-sampling factors will lead to smaller angular gaps between spokes, and thus a smoother trajectory.

# Bibliography

- [1] John R. Foster, Deborah A. Hall, A. Quentin Summerfield, Alan R. Palmer, and Richard W. Bowtell. Sound-level measurements and calculations of safe noise dosage during EPI at 3 T. *Journal of Magnetic Resonance Imaging*, 12(1):157–163, 2000. doi:10.1002/1522-2586(200007)12:1<157::AID-JMRI17>3.0.CO;2-M. → pages 27, 54, 57
- [2] Medicines and Healthcare Products Regulatory Agency. Safety Guidelines for Magnetic Resonance Imaging Equipment in Clinical Use, 2015. → pages 27, 57, 248
- [3] Robert E. Brummet, J. Michael Talbot, and Peter Charuhas. Potential Hearing Loss Resulting from MR Imaging. *Magnetic Resonance Imaging*, 169:539–540, 1988. → pages 27
- [4] Chao Jin, Huan Li, Xianjun Li, Miaomiao Wang, Congcong Liu, Jianxin Guo, and Jian Yang. Temporary hearing threshold shift in healthy volunteers with hearing protection caused by acoustic noise exposure during 3-T multisequence MR neuroimaging. *Radiology*, 286(2):602–608, 2018. doi:10.1148/radiol.2017161622. → pages 27, 57
- [5] Mark Mcjury and Frank G Shellock. Auditory Noise Associated With MR Procedures: A Review. *Journal of Magnetic Resonance Imaging*, 45:37–45, 2000. doi:10.1002/1522-2586(200007)12:1<37::AID-JMRI5>3.0.CO;2-I. → pages 27, 28, 54, 249
- [6] M E Quirk, A J Letendre, R A Ciottone, and J F Lingley. Anxiety in patients undergoing MR imaging. *Radiology*, 170:463–466, 1989. doi:10.1148/radiology.170.2.2911670. → pages 27

- [7] David P Madio and Irving J Lowe. Ultra-Fast Imaging Using Low Flip Angles and FIDs. *Magnetic resonance in medicine*, 34(4):525–529, 1995. doi:10.1002/mrm.1910340407. → pages 28, 59, 62
- [8] Evan K. Fram, Robert J. Herfkens, G. Allan Johnson, Gary H. Glover, John P. Karis, Ann Shimakawa, Tom G. Perkins, and Norbert J. Pelc. Rapid calculation of T1 using variable flip angle gradient refocused imaging. *Magnetic Resonance Imaging*, 5(3): 201–208, 1987. doi:10.1016/0730-725X(87)90021-X. → pages 29, 47, 49, 93
- [9] E. K. Insko and L. Bolinger. Mapping of the Radiofrequency Field. *Journal of Magnetic Resonance*, 103(1):82–85, 1993. → pages 29, 97, 98
- [10] Lars G. Hanson. Is Quantum Mechanics Necessary for Understanding Magnetic Resonance? *Concepts in Magnetic Resonance*, 32(5):329–340, 2008. doi:10.1002/cmr.a.20123. → pages 32
- [11] Ruomin Hu, Dennis Kleimaier, Matthias Malzacher, Michaela A.U. Hoesl, Nadia K. Paschke, and Lothar R. Schad. X-nuclei imaging: Current state, technical challenges, and future directions. *Journal of Magnetic Resonance Imaging*, 51(2):355–376, 2020. doi:10.1002/jmri.26780. → pages 32
- [12] Robert W Brown, Yu-Chung Cheng, E. Mark Haacke, Michael R Thompson, and Ramesh Venkatesan. *Magnetic Resonance Imaging - Physical Principles and Sequence Design, Second Edition*. John Wiley & Sons, 2014. ISBN 978-0471720850. → pages 33, 34
- [13] F. Bloch. Nuclear induction. *Physical Review*, 70(7-8):460–474, 1946. doi:10.1103/PhysRev.70.460. → pages 34, 35, 187
- [14] William D. Rooney, Glyn Johnson, Xin Li, Eric R. Cohen, Seong Gi Kim, Kamil Ugurbil, and Charles S. Springer. Magnetic field and tissue dependencies of human brain longitudinal  $^1\text{H}_2\text{O}$  relaxation in vivo. *Magnetic Resonance in Medicine*, 57(2): 308–318, 2007. doi:10.1002/mrm.21122. → pages 35, 124, 125, 135, 142, 144, 250
- [15] Irene M. Vavasour, Cornelia Laule, David K B Li, Anthony L. Traboulsee, and Alex L. MacKay. Is the magnetization transfer ratio a marker for myelin in multiple sclerosis? *Journal of Magnetic Resonance Imaging*, 33(3):713–718, 2011. doi:10.1002/jmri.22441. → pages 35

- [16] Kenneth P. Whittall, Alex L. MacKay, Douglas a. Graeb, Robert a. Nugent, David K B Li, and Donald W. Paty. In vivo measurement of T2 distributions and water contents in normal human brain. *Magnetic Resonance in Medicine*, 37(1):34–43, 1997. doi:10.1002/mrm.1910370107. → pages 35, 46
- [17] Klaus-Armin Nave and Hauke B. Werner. Myelination of the Nervous System: Mechanisms and Functions. *Annual Review of Cell and Developmental Biology*, 30(1): 503–533, 2014. doi:10.1146/annurev-cellbio-100913-013101. → pages 36, 46
- [18] Cornelia Laule, Irene M Vavasour, Shannon H Kolind, David K B Li, Tony L Traboulsee, G R Wayne Moore, and Alex L Mackay. Magnetic Resonance Imaging of Myelin. *Neurotherapeutics*, 4(July):460–484, 2007. → pages 36
- [19] Alex Mackay, Kenneth Whittall, Julian Adler, David Li, Donald Paty, and Douglas Graeb. In vivo visualization of myelin water in brain by magnetic resonance. *Magnetic Resonance in Medicine*, 31(6):673–677, 1994. doi:10.1002/mrm.1910310614. → pages 36, 50, 52, 152, 172, 193
- [20] E L Hahn. Spin Echoes. *Phys. Rev.*, 80(4):580–594, nov 1950. doi:10.1103/PhysRev.80.580. → pages 36, 49, 152
- [21] G H Glover and J M Pauly. Projection Reconstruction Techniques for Reduction of Motion Effects in MRI. *Magnetic Resonance in Medicine*, 28(2):275–289, 1992. doi:10.1002/mrm.1910280209. → pages 40, 62
- [22] P. C. Lauterbur. Image Formation by Induced Local Interactions: Examples Employing Nuclear Magnetic Resonance. *Nature*, 242:190–191, 1973. doi:10.1038/242190a0. → pages 40
- [23] W A Edelstein, J M S Hutchinson, G Johnson, and T Redpath. Spin warp NMR imaging and applications to human whole-body imaging. *Physics in Medicine and Biology*, 25(4):751–756, 1980. doi:10.1088/0031-9155/25/4/017. → pages 40
- [24] S Ljunggren. A simple graphical representation of Fourier-based imaging methods. *Journal of Magnetic Resonance*, 54:338–343, 1983. doi:10.1016/0022-2364(83)90060-4. → pages 41

- [25] D O Kuethe, A Caprihan, I J Lowe, D P Madio, and H M Gach. Transforming NMR data despite missing points. *Journal of magnetic resonance*, 139(1):18–25, 1999. doi:10.1006/jmre.1999.1767. → pages 44, 68
- [26] Markus Weiger, Franciszek Hennel, and Klaas P. Pruessmann. Sweep MRI with algebraic reconstruction. *Magnetic Resonance in Medicine*, 64(6):1685–1695, 2010. doi:10.1002/mrm.22516. → pages 44
- [27] Jeffrey A. Fessler. On NUFFT-based gridding for non-Cartesian MRI. *Journal of Magnetic Resonance*, 188(2):191–195, 2007. doi:10.1016/j.jmr.2007.06.012. → pages 44, 69
- [28] Martin Uecker and Jonathan I. Tamir. BART Toolbox for Computational Magnetic Resonance Imaging, 2017. URL <https://doi.org/10.5281/zenodo.1066014>. → pages 44, 73, 100, 104, 215
- [29] Alex L. MacKay and Cornelia Laule. Magnetic Resonance of Myelin Water: An in vivo Marker for Myelin. *Brain Plasticity*, 2(1):71–91, 2016. doi:10.3233/BPL-160033. → pages 45
- [30] P. J. Wright, O. E. Mougin, J. J. Totman, A. M. Peters, M. J. Brookes, R. Coxon, P. E. Morris, M. Clemence, S. T. Francis, R. W. Bowtell, and P. A. Gowland. Water proton T1 measurements in brain tissue at 7, 3, and 1.5T using IR-EPI, IR-TSE, and MPRAGE: Results and optimization. *Magnetic Resonance Materials in Physics, Biology and Medicine*, 21(1-2):121–130, 2008. doi:10.1007/s10334-008-0104-8. → pages 45, 124, 142, 144, 250
- [31] T-Q Li and Sean C Deoni. Fast T1 Mapping of the Brain at 7T with RF Calibration Using Three Point DESPOT1 Method. In *Proceedings of International Society of Magnetic Resonance in Medicine*, page 2643, Seattle, WA, 2006. → pages 45
- [32] Sofia Chavez and Greg J. Stanisz. A novel method for simultaneous 3D B1 and T1 mapping: The method of slopes (MoS). *NMR in Biomedicine*, 25(9):1043–1055, 2012. doi:10.1002/nbm.2769. → pages 45
- [33] C Preibisch and R Deichmann. T1 Mapping Using Spoiled FLASH-EPI Hybrid Sequences and Varying Flip Angles. *Magnetic Resonance in Medicine*, 62:240–246, 2009. doi:10.1002/mrm.21969. → pages 45

- [34] Greg J. Stanisz, Ewa E. Odobina, Joseph Pun, Michael Escaravage, Simon J. Graham, Michael J. Bronskill, and R. Mark Henkelman. T1, T2 relaxation and magnetization transfer in tissue at 3T. *Magnetic Resonance in Medicine*, 54(3):507–512, 2005. doi:10.1002/mrm.20605. → pages 18, 45, 111, 124, 142, 173
- [35] Mark D. Does. Inferring brain tissue composition and microstructure via MR relaxometry. *NeuroImage*, 182:136–148, 2018. doi:10.1016/j.neuroimage.2017.12.087. → pages 46
- [36] Christian Labadie, Jing Huei Lee, William D. Rooney, Silvia Jarchow, Monique Aubert-Frécon, Charles S. Springer, and Harald E. Möller. Myelin water mapping by spatially regularized longitudinal relaxographic imaging at high magnetic fields. *Magnetic Resonance in Medicine*, 71(1):375–387, 2014. doi:10.1002/mrm.24670. → pages 46
- [37] Thorarin A. Bjarnason, I. M. Vavasour, C. L L Chia, and A. L. MacKay. Characterization of the NMR behavior of white matter in bovine brain. *Magnetic Resonance in Medicine*, 54(5):1072–1081, 2005. doi:10.1002/mrm.20680. → pages 46
- [38] Jiang Du, Vipul Sheth, Qun He, Michael Carl, Jun Chen, Jody Corey-bloom, and Graeme M Bydder. Measurement of T1 of the Ultrashort T2\* Components in White Matter of the Brain at 3T. *PLoS ONE*, 9(8), 2014. doi:10.1371/journal.pone.0103296. → pages 46
- [39] Shu-Juan Fan, Yajun Ma, Yanchun Zhu, Adam Searleman, Nikolaus M. Szeverenyi, Graeme M. Bydder, and Jiang Du. Yet more evidence that myelin protons can be directly imaged with UTE sequences on a clinical 3T scanner: Bicomponent T2\* analysis of native and deuterated ovine brain specimens. *Magnetic Resonance in Medicine*, 00, 2017. doi:10.1002/mrm.27052. → pages 46
- [40] Tanguy Boucneau, Peng Cao, Shuyu Tang, Misung Han, Duan Xu, Roland G. Henry, and Peder E. Z. Larson. In vivo characterization of brain ultrashort-T2 components. *Magnetic Resonance in Medicine*, 80(2):726–735, 2018. doi:10.1002/mrm.27037. → pages 46, 51
- [41] Alan C. Seifert, Cheng Li, Michael J. Wilhelm, Suzanne L. Wehrli, and Felix W. Wehrli. Towards quantification of myelin by solid-state MRI of the lipid matrix



- protons. *NeuroImage*, 163:358–367, 2017. doi:10.1016/j.neuroimage.2017.09.054. → pages 46, 112
- [42] Markus Weiger, Romain Froidevaux, David Otto Brunner, Manuela Rosler, and Klaas Paul Pruessmann. Advances in Direct Myelin Imaging. In *Proc. Intl. Soc. Mag. Reson. Med 27*, page 1118, Montreal, 2019. → pages 46
- [43] A. L. Hopkins, H. N. Yeung, and C. B. Bratton. Multiple field strength in vivo T1 and T2 for cerebrospinal fluid protons. *Magnetic Resonance in Medicine*, 3(2):303–311, 1986. doi:10.1002/mrm.1910030214. → pages 47
- [44] W.G Jr. Bradley. CSF Flow in the Brain in the Context of Normal Pressure. *AJNR. American journal of neuroradiology*, 36:831–838, 2015. doi:10.3174/ajnr.A4124. → pages 47
- [45] Remi K.S. Kwan, Alan C. Evans, and Bruce Pike. MRI simulation-based evaluation of image-processing and classification methods. *IEEE Transactions on Medical Imaging*, 18(11):1085–1097, 1999. doi:10.1109/42.816072. → pages 7, 48, 215, 229
- [46] Frederick H. Epstein, John P. Mugler, and James R. Brookeman. Spoiling of transverse magnetization in gradient-echo (GRE) imaging during the approach to steady state. *Magnetic Resonance in Medicine*, 35(2):237–245, 1996. doi:10.1002/mrm.1910350216. → pages 47
- [47] Peter B. Kingsley. Methods of measuring spin-lattice (T1) relaxation times: An annotated bibliography. *Concepts in Magnetic Resonance*, 11(4):243–276, 1999. doi:10.1002/(SICI)1099-0534(1999)11:4<243::AID-CMR5>3.0.CO;2-C. → pages 49
- [48] John P. Mugler and James R. Brookeman. Three-dimensional magnetization-prepared rapid gradient-echo imaging (3D MP RAGE). *Magnetic Resonance in Medicine*, 15(1):152–157, 1990. doi:10.1002/mrm.1910150117. → pages 49, 65
- [49] José P. Marques, Tobias Kober, Gunnar Krueger, Wietske van der Zwaag, Pierre François Van de Moortele, and Rolf Gruetter. MP2RAGE, a self bias-field corrected sequence for improved segmentation and T1-mapping at high field. *NeuroImage*, 49(2):1271–1281, 2010. doi:10.1016/j.neuroimage.2009.10.002. → pages 49, 65, 90, 135, 148, 250

- [50] Steven Kecskemeti, Alexey Samsonov, Samuel A. Hurley, Douglas C. Dean, Aaron Field, and Andrew L. Alexander. MPnRAGE: A technique to simultaneously acquire hundreds of differently contrasted MPRAGE images with applications to quantitative T1 mapping. *Magnetic Resonance in Medicine*, 75(3):1040–1053, 2016. doi:10.1002/mrm.25674. → pages 49
- [51] Kenner A. Christensen, David M. Grant, Edward M. Schulman, and Cheves Walling. Optimal determination of relaxation times of fourier transform nuclear magnetic resonance. Determination of spin-lattice relaxation times in chemically polarized species. *The Journal of Physical Chemistry*, 78(19):1971–1977, 1974. doi:10.1021/j100612a022. → pages 49, 78, 93
- [52] Raj K. Gupta. A new look at the method of variable nutation angle for the measurement of spin-lattice relaxation times using fourier transform NMR. *Journal of Magnetic Resonance*, 25(1):231–235, 1977. doi:10.1016/0022-2364(77)90138-X. → pages 49, 93
- [53] John Homer and Martin S. Beevers. Driven-equilibrium single-pulse observation of T1 relaxation. A reevaluation of a rapid "new" method for determining NMR spin-lattice relaxation times. *Journal of Magnetic Resonance (1969)*, 63(2):287–297, 1985. doi:10.1016/0022-2364(85)90318-X. → pages 49, 93
- [54] Sean C L Deoni. High-Resolution T1 Mapping of the Brain at 3T with Driven Equilibrium Single Pulse Observation of T1 with High-Speed Incorporation of RF Field Inhomogeneities (DESPOT1-HIFI). *Journal of Magnetic Resonance Imaging*, 26:1106–1111, 2007. doi:10.1002/jmri.21130. → pages 49, 93
- [55] S. Meiboom and D. Gill. Modified Spin-Echo Method for Measuring Nuclear Relaxation Times. *The Review of Scientific Instruments*, 29(8):688–691, 1958. doi:10.1063/1.1716296. → pages 50
- [56] Thanh D. Nguyen, Cynthia Wisnieff, Mitchell A. Cooper, Dushyant Kumar, Ashish Raj, Pascal Spincemaille, Yi Wang, Tim Vartanian, and Susan A. Gauthier. T2 prep three-dimensional spiral imaging with efficient whole brain coverage for myelin water quantification at 1.5 tesla. *Magnetic Resonance in Medicine*, 67(3):614–621, 2012. doi:10.1002/mrm.24128. → pages 50, 153

- [57] Robin A. DeGraaf and Klaas Nicolay. Adiabatic rf pulses: Applications to in vivo NMR. *Concepts in Magnetic Resonance*, 9(4):247–268, 1997. doi:10.1002/(SICI)1099-0534(1997)9:4<247::AID-CMR4>3.0.CO;2-Z. → pages 50
- [58] H. Y. Carr. Steady-State Free Precession in Nuclear Magnetic Resonance. *Physical Review*, 112(5):1693–1701, 1958. doi:10.1103/PhysRev.112.1693. → pages 50
- [59] Sean C L Deoni, Brian K. Rutt, and Terry M. Peters. Rapid combined T1 and T2 mapping using gradient recalled acquisition in the steady state. *Magnetic Resonance in Medicine*, 49(3):515–526, 2003. doi:10.1002/mrm.10407. → pages 50, 93, 136, 147, 186, 191
- [60] Dan Ma, Vikas Gulani, Nicole Seiberlich, Kecheng Liu, Jeffrey L. Sunshine, Jeffrey L. Duerk, and Mark A. Griswold. Magnetic resonance fingerprinting. *Nature*, 495:187–192, 2013. doi:10.1038/nature11971. → pages 51, 191
- [61] J. B.M. Warntjes, O. Dahlqvist Leinhard, J. West, and P. Lundberg. Rapid magnetic resonance quantification on the brain: Optimization for clinical usage. *Magnetic Resonance in Medicine*, 60(2):320–329, 2008. doi:10.1002/mrm.21635. → pages 51
- [62] Sofia Kvernby, Marcel J. van Bertus Warntjes, Henrik Haraldsson, Carl Johan Carlhäll, Jan Engvall, and Tino Ebbers. Simultaneous three-dimensional myocardial T1 and T2 mapping in one breath hold with 3D-QALAS. *Journal of cardiovascular magnetic resonance*, 16:102, 2014. doi:10.1186/s12968-014-0102-0. → pages 51, 166
- [63] Akifumi Hagiwara, Marcel Warntjes, Masaaki Hori, Christina Andica, Misaki Nakazawa, Kanako K Kumamaru, Osamu Abe, and Shigeki Aoki. SyMRI of the Brain. *Investigative Radiology*, 52(10):647–657, 2017. doi:10.1097/RLI.0000000000000365. → pages 51
- [64] Stephen J. Riederer, Steven A. Suddarth, Stuart A. Bobman, James N. Lee, Henry Z. Wang, and James R. Macfall. Automated MR Image Synthesis: Feasibility Studies. *Radiology*, 153:203–206, 1984. doi:10.1148/radiology.153.1.6089265. → pages 51, 148
- [65] Francesca Di Giuliano, Silvia Minosse, Eliseo Picchi, Girolama Alessandra Marfia, Valerio Da Ros, Massimo Muto, Mario Muto, Chiara Adriana, Andrea Laghi, Francesco Garaci, and Roberto Floris. Comparison between synthetic and conventional magnetic resonance imaging in patients with multiple sclerosis and controls.

- Magnetic Resonance Materials in Physics, Biology and Medicine*, pages 1–9, 2019. doi:10.1007/s10334-019-00804-9. → pages 51
- [66] René-Maxime Gracien, Alexandra van Wijnen, Michelle Maiworm, Franca Petrov, Nina Merkel, Esther Paule, Helmuth Steinmetz, Susanne Knake, Felix Rosenow, Marlies Wagner, and Ralf Deichmann. Improved synthetic T1-weighted images for cerebral tissue segmentation in neurological diseases. *Magnetic Resonance Imaging*, 2019. doi:10.1016/j.mri.2019.05.013. → pages 51
- [67] Akifumi Hagiwara, Masaaki Hori, Julien Cohen-Adad, Misaki Nakazawa, Yuichi Suzuki, Akihiro Kasahara, Moeko Horita, Takuya Haruyama, Christina Andica, Tomoko Maekawa, Koji Kamagata, Kanako Kunishima Kumamaru, Osamu Abe, and Shigeki Aoki. Linearity, Bias, Intrascanner Repeatability, and Interscanner Reproducibility of Quantitative Multidynamic Multiecho Sequence for Rapid Simultaneous Relaxometry at 3 T: A Validation Study with a Standardized Phantom and Healthy Controls. *Investigative Radiology*, 54(1):39–47, 2019. doi:10.1097/RLI.0000000000000510. → pages 51
- [68] Dmitry S. Novikov, Valerij G. Kiselev, and Sune N. Jespersen. On modeling. *Magnetic Resonance in Medicine*, 79:3172–3193, 2018. doi:10.1002/mrm.27101. → pages 51, 93
- [69] Rui Pedro A.G. Teixeira, Shaihan J. Malik, and Joseph V. Hajnal. Fast quantitative MRI using controlled saturation magnetization transfer. *Magnetic Resonance in Medicine*, 81(2):907–920, 2019. doi:10.1002/mrm.27442. → pages 52, 111, 113, 145, 146, 186
- [70] Shaihan J. Malik, Rui P. A. G. Teixeira, Daniel J. West, Tobias C. Wood, and Joseph V. Hajnal. Steady-state imaging with inhomogeneous magnetization transfer contrast using multiband radiofrequency pulses. *Magnetic Resonance in Medicine*, 83(3):935–949, 2020. doi:10.1002/mrm.27984. → pages 52, 116, 184, 186, 187
- [71] Barry N. Taylor and Chris E. Kuyatt. Guidelines for Evaluating and Expressing the Uncertainty of NIST Measurement Results. Technical report, National Institute of Standards and Technology (NIST), 1994. → pages 53, 105

- [72] P Mansfield, P M Glover, and J Beaumont. Sound generation in gradient coil structures for MRI. *Magnetic Resonance in Medicine*, 39(4):539–50, 1998. doi:10.1002/mrm.1910390406. → pages 54, 55, 58, 123
- [73] Richard Salvi and Adam Sheppard. Is noise in the MR imager a significant risk factor for hearing loss? *Radiology*, 286(2):609–610, 2018. doi:10.1148/radiol.2017172221. → pages 54
- [74] S. A. Counter, A. Olofsson, H. F. Grahn, and E. Borg. MRI acoustic noise: Sound pressure and frequency analysis. *Journal of Magnetic Resonance Imaging*, 7(3):606–611, 1997. doi:10.1002/jmri.1880070327. → pages 54
- [75] Michael E. Ravicz, Jennifer R. Melcher, and Nelson Y.-S. Kiang. Acoustic noise during functional magnetic resonance imaging. *The Journal of the Acoustical Society of America*, 108(4):1683–1696, 2002. doi:10.1121/1.1310190. → pages 54
- [76] M. J. McJury. Acoustic noise levels generated during high field MR imaging. *Clinical Radiology*, 50(5):331–334, 1995. doi:10.1016/S0009-9260(05)83427-0. → pages 54
- [77] David L Price, Janet P De Wilde, Annie M Papadaki, Jane S Curran, and Richard I Kitney. Investigation of Acoustic Noise on 15 MRI Scanners from 0.2 T to 3 T. *Journal of Magnetic Resonance Imaging*, 13:288–293, 2001. doi:10.1002/1522-2586(200102)13:2<288::AID-JMRI1041>3.0.CO;2-P. → pages 55, 58, 86, 124
- [78] William a. Edelstein, Robert a. Hedeem, Richard P. Mallozzi, Sayed Amr El-Hamamsy, Robert a. Ackermann, and Timothy J. Havens. Making MRI quieter. *Magnetic Resonance Imaging*, 20:155–163, 2002. doi:10.1016/S0730-725X(02)00475-7. → pages 55, 58, 123, 124
- [79] Electrotechnical International Commision. Electroacoustics - Sound level meters - Part 1: Specifications (IEC 61672-1:2013). Technical report, EIC, 2013. URL <https://webstore.iec.ch/publication/5708>. → pages 55
- [80] U.S. Department of Healthy Services and Human. Occupational Noise Exposure. Technical report, NIOSH, 1998. → pages 56, 57

- [81] Richard Neitzel and Noah Seixas. The effectiveness of hearing protection among construction workers. *Journal of Occupational and Environmental Hygiene*, 2(4): 227–238, 2005. doi:10.1080/15459620590932154. → pages 57
- [82] Internaional Electrotechnical Commission. Medical Electrical Equipment. Part 2-33: particular requirements for basic safety and essential performance of magnetic resonance equipment for medical diagnosis. (IEC 60601-2-33). Technical report, EIC, Geneva, 2002. URL <https://webstore.iec.ch/publication/2647>. → pages 57
- [83] P. Radomskij, M. A. Schmidt, C. W. Heron, and D. Prasher. Effect of MRI noise on cochlear function. *Lancet*, 359(9316):1485–1486, 2002. doi:10.1016/S0140-6736(02)08423-4. → pages 57
- [84] P Glover, J Hykin, P Gowland, J Wright, I Johnson, and P Mansfield. An assessment of the intrauterine sound intensity level during obstetric echo-planar magnetic resonance imaging. *The British Journal of Radiology*, 68(814):1090–1094, oct 1995. doi:10.1259/0007-1285-68-814-1090. → pages 57
- [85] Michael J. Reeves, Marian Brandreth, Elspeth H. Whitby, Anthony R. Hart, Martyn N. J. Paley, Paul D. Griffiths, and John C. Stevens. Neonatal Cochlear Function: Measurement after Exposure to Acoustic Noise during in Utero MR Imaging. *Radiology*, 257(3):802–809, 2010. doi:10.1148/radiol.10092366. → pages 57
- [86] M. Kathleen Philbin, Katherine H. Taber, and L. Anne Hayman. Preliminary report: Changes in vital signs of term newborns during MR. *American Journal of Neuroradiology*, 17(6):1033–1036, 1996. → pages 58
- [87] Su Zhen Dong, Ming Zhu, and Dorothy Bulas. Techniques for minimizing sedation in pediatric MRI. *Journal of Magnetic Resonance Imaging*, pages 1047–1054, 2019. doi:10.1002/jmri.26703. → pages 58
- [88] Matthew J. Barkovich, Duan Xu, Rahul S. Desikan, Cassandra Williams, and A. James Barkovich. Pediatric neuro MRI: tricks to minimize sedation. *Pediatric Radiology*, 48(1):50–55, 2018. doi:10.1007/s00247-017-3785-1. → pages 58
- [89] David M Baguley. Hyperacusis. *Journal of the Royal Society of Medecine*, 96:16–19, 2003. doi:10.1177/014107680309601203. → pages 58, 246

- [90] Omer Zarchi, Chen Avni, Josef Attias, Amos Frisch, Miri Carmel, Elena Michaelovsky, Tamar Green, Abraham Weizman, and Doron Gothelf. Hyperactive auditory processing in Williams syndrome: Evidence from auditory evoked potentials. *Psychophysiology*, 52(6):782–789, 2015. doi:10.1111/psyp.12407. → pages 58
- [91] Udi Katzenell and Samuel Segal. Hyperacusis: Review and clinical guidelines. *Otology and Neurotology*, 22(3):321–326, 2001. doi:10.1097/00129492-200105000-00009. → pages 58
- [92] Stéphanie Khalfa, Nicole Bruneau, Bernadette Rogé, Nicolas Georgieff, Evelyne Veuillet, Jean-Louis Adrien, Catherine Barthélémy, and Lionel Collet. Increased perception of loudness in autism. *Hearing Research*, 198(1-2):87–92, 2004. doi:10.1016/j.heares.2004.07.006. → pages 58
- [93] Aries P. Suhnan, Philip M. Finch, and Peter D. Drummond. Hyperacusis in chronic pain: neural interactions between the auditory and nociceptive systems. *International Journal of Audiology*, 56(11):801–809, 2017. doi:10.1080/14992027.2017.1346303. → pages 58
- [94] Maarten J. Versluis, Wouter M. Teeuwisse, Hermien E. Kan, Mark A. Van Buchem, Andrew G. Webb, and Matthias J. Van Osch. Subject tolerance of 7 T MRI examinations. *Journal of Magnetic Resonance Imaging*, 38(3):722–725, 2013. doi:10.1002/jmri.23904. → pages 58
- [95] Franciszek Hennel. Fast spin echo and fast gradient echo MRI with low acoustic noise. *Journal of magnetic resonance imaging : JMRI*, 13(6):960–6, 2001. doi:10.1002/jmri.1138. → pages 58, 59, 86, 192, 249
- [96] Sean C.L. Deoni, Douglas C. Dean, Jonathan O’Muircheartaigh, Holly Dirks, and Beth A. Jerskey. Investigating white matter development in infancy and early childhood using myelin water fraction and relaxation time mapping. *NeuroImage*, 63(3):1038–1053, 2012. doi:10.1016/j.neuroimage.2012.07.037. → pages 58
- [97] F Hennel, F Girard, and T Loenneker. "Silent" MRI with soft gradient pulses. *Magnetic Resonance in Medicine*, 42:6–10, 1999. doi:10.1002/(SICI)1522-2594(199907)42:1<6::AID-MRM2>3.0.CO;2-D. → pages 59

- [98] Sedat Alibek, Mika Vogel, Wei Sun, David Winkler, Christopher A. Baker, Michael Burke, and Hubertus Gloger. Acoustic noise reduction in MRI using Silent Scan: An initial experience. *Diagnostic and Interventional Radiology*, 20(4):360–363, 2014. doi:10.5152/dir.2014.13458. → pages 59, 62, 111
- [99] Mauro Costagli, Mark R. Symms, Lorenzo Angeli, Douglas A.C. Kelley, Laura Biagi, Andrea Farnetani, Catarina Rua, Graziella Donatelli, Gianluigi Tiberi, Michela Tosetti, and Mirco Cosottini. Assessment of Silent T1-weighted head imaging at 7 T. *European Radiology*, 26(6):1879–1888, 2016. doi:10.1007/s00330-015-3954-2. → pages 59, 62
- [100] Susanne Ohlmann-Knafo, Melanie Morlo, David Laszlo Tarnoki, Adam Domonkos Tarnoki, Barbara Grabowski, Melanie Kaspar, and Dirk Pickuth. Comparison of image quality characteristics on Silent MR versus conventional MR imaging of brain lesions at 3 Tesla. *British Journal of Radiology*, 89(August):1–10, 2016. doi:10.1259/bjr.20150801. → pages 59
- [101] M Weiger and K P Pruessmann. MRI with Zero Echo Time. *eMagRes*, 1:311–322, 2012. doi:10.1002/9780470034590.emrstm1292. → pages 61
- [102] Dwight G. Nishimura, John I. Jackson, and John M. Pauly. On the nature and reduction of the displacement artifact in flow images. *Magnetic Resonance in Medicine*, 22(2):481–492, 1991. doi:10.1002/mrm.1910220255. → pages 62
- [103] Florian Wiesinger, Laura I. Sacolick, Anne Menini, Sandeep S. Kaushik, Sangtae Ahn, Patrick Veit-Haibach, Gaspar Delso, and Dattesh D. Shanbhag. Zero TE MR bone imaging in the head. *Magnetic Resonance in Medicine*, 75(1):107–114, 2016. doi:10.1002/mrm.25545. → pages 62, 63
- [104] Peder E.Z. Larson, Misung Han, Roland Krug, Angela Jakary, Sarah J. Nelson, Daniel B. Vigneron, Roland G. Henry, Graeme McKinnon, and Douglas A.C. Kelley. Ultrashort echo time and zero echo time MRI at 7T. *Magnetic Resonance Materials in Physics, Biology and Medicine*, 29(3):359–370, 2016. doi:10.1007/s10334-015-0509-0. → pages 62, 66, 67
- [105] Fabio Gibiino, Laura Sacolick, Anne Menini, Luigi Landini, and Florian Wiesinger. Free-breathing, zero-TE MR lung imaging. *Magnetic Resonance Materials in*



- Physics, Biology and Medicine*, 28:207–215, 2015. doi:10.1007/s10334-014-0459-y. → pages 62, 63, 198
- [106] Pablo Irarrazabal and Dwight G. Nishimura. Fast Three Dimensional Magnetic Resonance Imaging. *Magnetic Resonance in Medicine*, 33(5):656–662, 1995. doi:10.1002/mrm.1910330510. → pages 62
- [107] David P Madio, Michael Gach, and Irving J. Lowe. Ultra-fast Velocity Imaging in Stenotically Produced Turbulent Jets Using RUFIS. *Magnetic Resonance in Medicine*, 39(574-580), 1998. doi:10.1002/mrm.1910390410. → pages 62
- [108] Jung Jiin Hsu and Irving J. Lowe. Spin-lattice relaxation and a fast T1-map acquisition method in MRI with transient-state magnetization. *Journal of Magnetic Resonance*, 169(2):270–278, 2004. doi:10.1016/j.jmr.2004.05.001. → pages 62, 77
- [109] Ana Beatriz Solana, Anne Menini, Laura I Sacolick, Nicolas Hehn, and Florian Wiesinger. Quiet and Distortion-Free, Whole Brain BOLD fMRI Using T2 -Prepared RUFIS. *Magnetic Resonance in Medicine*, 75:1402–1412, 2016. doi:10.1002/mrm.25658. → pages 62, 63, 149, 152
- [110] Jianmin Yuan, Yuxin Hu, Anne Menini, Christopher M. Sandino, Jesse Sandberg, Vipul Sheth, Catherine J. Moran, Marcus Alley, Michael Lustig, Brian Hargreaves, and Shreyas Vasanawala. Near-silent distortionless DWI using magnetization-prepared RUFIS. *Magnetic Resonance in Medicine*, 00(June):1–12, 2019. doi:10.1002/mrm.28106. → pages 62, 90, 152, 249
- [111] Mathias Engström, Graeme McKinnon, Cristina Cozzini, and Florian Wiesinger. In-phase zero TE musculoskeletal imaging. *Magnetic Resonance in Medicine*, 83(1):195–202, 2020. doi:10.1002/mrm.27928. → pages 63, 90, 112, 120
- [112] Sam T.S. Wong and Mark S. Roos. A strategy for sampling on a sphere applied to 3D selective RF pulse design. *Magnetic Resonance in Medicine*, 32(6):778–784, 1994. doi:10.1002/mrm.1910320614. → pages 63, 207
- [113] Davide Piccini, Arne Littmann, Sonia Nielles-Vallespin, and Michael O. Zenge. Spiral phyllotaxis: The natural way to construct a 3D radial trajectory in MRI. *Magnetic Resonance in Medicine*, 66(4):1049–1056, 2011. doi:10.1002/mrm.22898. → pages 63, 200, 201, 202, 265

- [114] Y. Zur, M. L. Wood, and L. J. Neuringer. Spoiling of Transverse Magnetization in Steady-State Sequences. *Magnetic Resonance in Medicine*, 21(2):251–263, 1991. doi:10.1002/mrm.1910210210. → pages 64, 113
- [115] Florian Wiesinger, Anne Menini, and Ana Beatriz Solana. Looping Star. *Magnetic Resonance in Medicine*, 81(1):57–68, 2019. doi:10.1002/mrm.27440. → pages 64, 149, 152
- [116] C Preibisch and R Deichmann. Influence of RF Spoiling on the Stability and Accuracy of T1 Mapping Based on Spoiled FLASH With Varying Flip Angles. *Magnetic Resonance in Medicine*, 61:125–135, 2009. doi:10.1002/mrm.21776. → pages 64, 114
- [117] Ralf Deichmann, Simon Baudrexel, and N Ulrike. T1 Mapping With the Variable Flip Angle Technique: A Simple Correction for Insufficient Spoiling of Transverse Magnetization. *Magnetic Resonance in Medicine*, 79:3082–3092, 2018. doi:10.1002/mrm.26979. → pages 64, 114
- [118] Volkert Roeloffs, Dirk Voit, and Jens Frahm. Spoiling without additional gradients: Radial FLASH MRI with randomized radiofrequency phases. *Magnetic Resonance in Medicine*, 75(5):2094–2099, 2016. doi:10.1002/mrm.25809. → pages 64, 114
- [119] A. Haase, J. Frahm, D. Matthaei, W. Hanicke, and K. D. Merboldt. FLASH imaging. Rapid NMR imaging using low flip-angle pulses. *Journal of Magnetic Resonance*, 67(2):258–266, 1986. doi:10.1016/0022-2364(86)90433-6. → pages 65
- [120] A. Haase. Snapshot FLASH MRI. Applications to T1, T2, and Chemical-Shift imaging. *Magnetic Resonance in Medicine*, 13(1):77–89, 1990. doi:10.1002/mrm.1910130109. → pages 65
- [121] Matt A Bernstein, Kevin F King, and Xiaohong J Zhou. *Handbook of MRI Pulse Sequences*. Elsevier Science, 2004. ISBN 9780080533124. doi:10.1016/b978-0-12-092861-3.x5000-6. → pages 66, 123, 126
- [122] H. J. Landau. Necessary density conditions for sampling and interpolation of certain entire functions. *Acta Mathematica*, 117(1):37–52, 1967. doi:10.1007/BF02395039. → pages 66

- [123] Moshe Mishali and Yonina C. Eldar. Blind multiband signal reconstruction: Compressed sensing for analog signals. *IEEE Transactions on Signal Processing*, 57(3): 993–1009, 2009. doi:10.1109/TSP.2009.2012791. → pages 66
- [124] Klaas P. Pruessmann, Markus Weiger, Markus B. Scheidegger, and Peter Boesiger. SENSE: Sensitivity encoding for fast MRI. *Magnetic Resonance in Medicine*, 42(5):952–962, 1999. doi:10.1002/(SICI)1522-2594(199911)42:5<952::AID-MRM16>3.0.CO;2-S. → pages 66, 70
- [125] Florian Knoll, Christian Clason, Clemens Diwok, and Rudolf Stollberger. Adapted random sampling patterns for accelerated MRI. *Magnetic Resonance Materials in Physics, Biology and Medicine*, 24(1):43–50, 2011. doi:10.1007/s10334-010-0234-7. → pages 66
- [126] Florian Knoll, Kristian Bredies, Thomas Pock, and Rudolf Stollberger. Second order total generalized variation (TGV) for MRI. *Magnetic Resonance in Medicine*, 65(2): 480–491, 2011. doi:10.1002/mrm.22595. → pages 66, 229, 242, 248
- [127] Michael Lustig, David Donoho, and John M. Pauly. Sparse MRI: The application of compressed sensing for rapid MR imaging. *Magnetic Resonance in Medicine*, 58(6): 1182–1195, 2007. doi:10.1002/mrm.21391. → pages 67, 243
- [128] Romain Froidevaux, Markus Weiger, David Otto Brunner, Benjamin Emanuel Dietrich, Bertram Jakob Wilm, and Klaas Paul Pruessmann. Filling the dead time gap in zero echo time MRI: principles compared. *Magnetic Resonance in Medicine*, 79(4):2036–2045, 2018. doi:10.1007/s10334-015-0487-2. → pages 67, 68, 247
- [129] Yaotang Wu, Guangping Dai, Jerome L. Ackerman, Mirko I. Hrovat, Melvin J. Glimcher, Brian D. Snyder, Ara Nazarian, and David A. Chesler. Water- and fat-suppressed proton projection MRI (WASPI) of rat femur bone. *Magnetic Resonance in Medicine*, 57(3):554–567, 2007. doi:10.1002/mrm.21174. → pages 68, 69
- [130] David M. Grodzki, Peter M. Jakob, and Bjoern Heismann. Ultrashort echo time imaging using pointwise encoding time reduction with radial acquisition (PETRA). *Magnetic Resonance in Medicine*, 67(2):510–518, 2012. doi:10.1002/mrm.23017. → pages 68, 82, 85, 122

- [131] John I. Jackson, Craig H. Meyer, Dwight G. Nishimura, and Albert Macovski. Selection of a Convolution Function for Fourier Inversion Using Gridding. *IEEE Transactions on Medical Imaging*, 10(3):473–478, 1991. doi:10.1109/42.97598. → pages 69, 70
- [132] Claudia Oesterle, Michael Markl, Ralph Strecker, Falk M. Kraemer, and Jürgen Hennig. Spiral reconstruction by regridding to a large rectilinear matrix: A practical solution for routine systems. *Journal of Magnetic Resonance Imaging*, 10(1):84–92, 1999. doi:10.1002/(SICI)1522-2586(199907)10:1<84::AID-JMRI12>3.0.CO;2-D. → pages 69, 70, 75
- [133] Charles A. McKenzie, Ernest N. Yeh, Michael A. Ohliger, Mark D. Price, and Daniel K. Sodickson. Self-calibrating parallel imaging with automatic coil sensitivity extraction. *Magnetic Resonance in Medicine*, 47(3):529–538, 2002. doi:10.1002/mrm.10087. → pages 71, 100
- [134] Klaas P. Pruessmann, Markus Weiger, Peter Börnert, and Peter Boesiger. Advances in Sensitivity Encoding With Arbitrary k-Space Trajectories. *Magnetic Resonance in Medicine*, 46(4):638–651, 2001. doi:10.1002/mrm.1241. → pages 85, 228, 235
- [135] Alexei A. Samsonov, Eugene G. Kholmovski, Dennis L. Parker, and Chris R. Johnson. POCSENSE: POCS-based reconstruction for sensitivity encoded magnetic resonance imaging. *Magnetic Resonance in Medicine*, 52(6):1397–1406, 2004. doi:10.1002/mrm.20285. → pages 85
- [136] Michael Lustig and John M. Pauly. SPIRiT: Iterative self-consistent parallel imaging reconstruction from arbitrary k-space. *Magnetic Resonance in Medicine*, 64(2):457–471, 2010. doi:10.1002/mrm.22428. → pages 85
- [137] Konrad Schieban, Markus Weiger, Franciszek Hennel, Andreas Boss, and Klaas P. Pruessmann. ZTE imaging with enhanced flip angle using modulated excitation. *Magnetic Resonance in Medicine*, 74(3):684–693, 2015. doi:10.1002/mrm.25464. → pages 85
- [138] Robert A. Hedeem and William A Edelstein. Characterization and prediction of gradient acoustic noise in MR imagers. *Magnetic Resonance in Medicine*, 37(1):7–10, 1997. doi:10.1002/mrm.1910370103. → pages 86

- [139] J A Elder and C K Chou. Auditory Response to Pulsed Radiofrequency Energy. *Bioelectromagnetics*, 6:S162–S173, 2003. doi:10.1002/bem.10163. → pages 89
- [140] Allan H. Frey. Human auditory system response to modulated electromagnetic energy. *Journal of applied physiology*, 17:689–692, 1962. doi:10.1152/jappl.1962.17.4.689. → pages 89
- [141] Allan H. Frey. Human Perception of Illumination with Pulsed Ultrahigh-Frequency Electromagnetic Energy. *Science*, 181, 1973. doi:10.1126/science.181.4097.356. → pages 89
- [142] Peter Roschmann. Human Auditory System Response to Pulsed Radiofrequency Energy in RF Coils for Magnetic Resonance at 2.4 to 170 MHz. *Magnetic*, 21:197–215, 1991. doi:10.1002/mrm.1910210205. → pages 89
- [143] M Bydder, J Du, A Takahashi, A Shimakawa, G Hamilton, S Sinha, and G. M. Bydder. Chemical Shift Artifact in Center-Out Radial Sampling: A Potential Pitfall in Clinical Diagnosis. In *Proc. Intl. Soc. Mag. Reson. Med 15*, page 1811, Berlin, 2007. → pages 90
- [144] Gunther Helms, Henning Dathe, and Peter Dechent. Quantitative FLASH MRI at 3T using a rational approximation of the Ernst equation. *Magnetic Resonance in Medicine*, 59(3):667–672, 2008. doi:10.1002/mrm.21542. → pages 93
- [145] Simon Baudrexel, Sarah C. Reitz, Stephanie Hof, René Maxime Gracien, Vinzenz Fleischer, Hilga Zimmermann, Amgad Droby, Johannes C. Klein, and Ralf Deichmann. Quantitative T1 and proton density mapping with direct calculation of radiofrequency coil transmit and receive profiles from two-point variable flip angle data. *NMR in Biomedicine*, 29(3):349–360, 2016. doi:10.1002/nbm.3460. → pages 93
- [146] Henry Z. Wang, Stephen J. Riederer, and James N. Lee. Optimizing the precision in T1 relaxation estimation using limited flip angles. *Magnetic Resonance in Medicine*, 5(5):399–416, 1987. doi:10.1002/mrm.1910050502. → pages 93
- [147] G. H. Glover, C. E. Hayes, N. J. Pelc, W. A. Edelstein, O. M. Mueller, H. R. Hart, C. J. Hardy, M. O'Donnell, and W. D. Barber. Comparison of linear and circular polarization for magnetic resonance imaging. *Journal of Magnetic Resonance (1969)*, 64(2):255–270, 1985. doi:10.1016/0022-2364(85)90349-X. → pages 93, 96

- [148] Gunther Helms, Henning Dathe, Nikolaus Weiskopf, and Peter Dechent. Identification of signal bias in the variable flip angle method by linear display of the algebraic ernst equation. *Magnetic Resonance in Medicine*, 66(3):669–677, 2011. doi:10.1002/mrm.22849. → pages 10, 94, 133, 134, 258
- [149] Tobias Charles Wood. Improved formulas for the two optimum VFA flip-angles. *Magnetic Resonance in Medicine*, 74(1):1–3, 2015. doi:10.1002/mrm.25592. → pages 94, 133, 146, 174
- [150] R. R. Ernst and W. A. Anderson. Application of fourier transform spectroscopy to magnetic resonance. *Review of Scientific Instruments*, 37(1):93–102, 1966. doi:10.1063/1.1719961. → pages 94
- [151] D. I. Hoult and R. E. Richards. The Signal-to-Noise Ratio of the Nuclear Magnetic Resonance Experiment. *Journal of Magnetic Resonance*, 24(1):71–85, 1976. doi:10.1016/0022-2364(76)90233-X. → pages 96
- [152] D. I. Hoult. The principle of reciprocity in signal strength calculations - A mathematical guide. *Concepts in Magnetic Resonance*, 12(4):173–187, 2000. doi:10.1002/1099-0534(2000)12:4<173::AID-CMR1>3.0.CO;2-Q. → pages 96
- [153] Steffen Volz, Ulrike Nöth, Alina Jurcoane, Ulf Ziemann, Elke Hattingen, and Ralf Deichmann. Quantitative proton density mapping: Correcting the receiver sensitivity bias via pseudo proton densities. *NeuroImage*, 63(1):540–552, 2012. doi:10.1016/j.neuroimage.2012.06.076. → pages 96
- [154] Vasily L Yarnykh. Actual Flip-Angle Imaging in the Pulsed Steady State: A Method for Rapid Three-Dimensional Mapping of the Transmitted Radiofrequency Field. *Magnetic Resonance in Medicine*, 57:192–200, 2007. doi:10.1002/mrm.21120. → pages 96, 97, 137
- [155] Mathieu Boudreau, Christine L. Tardif, Nikola Stikov, John G. Sled, Wayne Lee, and G. Bruce Pike. B1 mapping for bias-correction in quantitative T1 imaging of the brain at 3T using standard pulse sequences. *Journal of Magnetic Resonance Imaging*, 46(6):1673–1682, 2017. doi:10.1002/jmri.25692. → pages 97

- [156] Rolf Pohmann and Klaus Scheffler. A theoretical and experimental comparison of different techniques for B1 mapping at very high fields. *NMR in Biomedicine*, 26(3): 265–275, 2013. doi:10.1002/nbm.2844. → pages 97
- [157] Laura I. Sacolick, Florian Wiesinger, Ileana Hancu, and Mika W. Vogel. B1 mapping by Bloch-Siegert shift. *Magnetic Resonance in Medicine*, 63(5):1315–1322, 2010. doi:10.1002/mrm.22357. → pages 97, 101, 136, 147
- [158] Kay Nehrke and Peter Börnert. DREAM-a novel approach for robust, ultrafast, multislice B1 mapping. *Magnetic Resonance in Medicine*, 68(5):1517–1526, 2012. doi:10.1002/mrm.24158. → pages 97
- [159] F Jiru and U Klose. Fast 3D radiofrequency field mapping using echo-planar imaging. *Magnetic resonance in medicine*, 56(6):1375–1379, 2006. doi:10.1002/mrm.21083. → pages 97
- [160] Nicholas G. Dowell and Paul S. Tofts. Fast, accurate, and precise mapping of the RF field in vivo using the 180° signal null. *Magnetic Resonance in Medicine*, 58(3): 622–630, 2007. doi:10.1002/mrm.21368. → pages 97
- [161] Hai-Ling Margaret Cheng and Graham A. Wright. Rapid High-Resolution T1 Mapping by Variable Flip Angles: Accurate and Precise Measurements in the Presence of Radiofrequency Field Inhomogeneity. *Magnetic Resonance in Medicine*, 55:566–574, 2006. doi:10.1002/mrm.20791. → pages 97
- [162] Charles H. Cunningham, John M. Pauly, and Krishna S. Nayak. Saturated double-angle method for rapid B1+ mapping. *Magnetic Resonance in Medicine*, 55(6): 1326–1333, 2006. doi:10.1002/mrm.20896. → pages 97
- [163] Glen R. Morrell. A phase-sensitive method of flip angle mapping. *Magnetic Resonance in Medicine*, 60(4):889–894, 2008. doi:10.1002/mrm.21729. → pages 97
- [164] Sohae Chung, Daniel Kim, Elodie Breton, and Leon Axel. Rapid B1+ Mapping Using a Preconditioning RF Pulse with TurboFLASH Readout. *Magnetic Resonance in Medicine*, 64(2):439–446, 2010. doi:10.1002/mrm.22423. → pages 97
- [165] Gareth A. Morris and Ray Freeman. Selective excitation in Fourier transform nuclear magnetic resonance. *Journal of Magnetic Resonance*, 29:433–462, 1978. doi:10.1016/j.jmr.2011.08.031. → pages 99

- [166] Emil Ljungberg, Tobias Wood, Ana Beatriz Solana, Shannon Kolind, Steven C R Williams, Florian Wiesinger, and Gareth J Barker. Silent T1 mapping using the variable flip angle method with B1 correction. *Magnetic Resonance in Medicine*, 84(2):813–824, 2020. doi:10.1002/mrm.28178. → pages 9, 10, 99, 100, 107, 108, 109
- [167] Emil Ljungberg, Florian Wiesinger, Ana Beatriz Solana, and Gareth J Barker. Silent Magnetization Prepared B1-map Acquisition - SIMBA. In *Proc. Intl. Soc. Mag. Reson. Med 27*, page 0448, Montreal, 2019. → pages 9, 101, 102
- [168] R. A. Lerski and J. D. de Certaines. II. Performance assessment and quality control in MRI by Eurospin test objects and protocols. *Magnetic Resonance Imaging*, 11(6):817–833, 1993. doi:10.1016/0730-725X(93)90199-N. → pages 103, 161, 185, 255
- [169] Martin Uecker, Peng Lai, Mark J Murphy, Patrick Virtue, Michael Elad, John M Pauly, Shreyas S Vasanawala, and Michael Lustig. ESPIRiT - An eigenvalue approach to autocalibrating parallel MRI: Where SENSE meets GRAPPA. *Magnetic Resonance in Medicine*, 71(3):990–1001, 2014. doi:10.1002/mrm.24751. → pages 104
- [170] Mark Jenkinson, Peter Bannister, Michael Brady, and Stephen Smith. Improved optimization for the robust and accurate linear registration and motion correction of brain images. *NeuroImage*, 17(2):825–841, 2002. doi:10.1016/S1053-8119(02)91132-8. → pages 104, 196, 218
- [171] Brian B. Avants, Nicholas J. Tustison, Gang Song, Philip A. Cook, Arno Klein, and James C. Gee. A reproducible evaluation of ANTs similarity metric performance in brain image registration. *NeuroImage*, 54(3):2033–2044, feb 2011. doi:10.1016/j.neuroimage.2010.09.025. → pages 104, 137, 213, 240
- [172] Bruce Fischl, David H Salat, Evelina Busa, Marilyn Albert, Megan Dieterich, Christian Haselgrove, Andre Van Der Kouwe, Ron Killiany, David Kennedy, Shuna Klavenness, Albert Montillo, Nikos Makris, Bruce Rosen, and Anders M Dale. Whole Brain Segmentation: Automated Labeling of Neuroanatomical Structures in the Human Brain. *Neuron*, 33(3):341–355, 2002. doi:10.1016/S0896-6273(02)00569-X. → pages 104, 137
- [173] Krzysztof Gorgolewski, Christopher D. Burns, Cindee Madison, Dav Clark, Yaroslav O. Halchenko, Michael L. Waskom, and Satrajit S. Ghosh. Nipype: A



- Flexible, Lightweight and Extensible Neuroimaging Data Processing Framework in Python. *Frontiers in Neuroinformatics*, 5(August), 2011. doi:10.3389/fninf.2011.00013. → pages 104
- [174] Tobias Charles Wood. QUIT: QUantitative Imaging Tools. *Journal of Open Source Software*, 3(26):656, 2017. doi:<https://doi.org/10.21105/joss.00656>. URL <https://github.com/spinacist/QUIT>. → pages 105, 137
- [175] J.M. Bland and D.G. Altman. Statistical Methods for Assessing Agreement Between Two Methods of Clinical Measurement. *Lancet*, 327:307–310, 1986. doi:10.1016/S0140-6736(86)90837-8. → pages 105, 106, 111
- [176] Daniel C. Sullivan, Nancy A. Obuchowski, Larry G. Kessler, David L. Raunig, Constantine Gatsonis, Erich P. Huang, Marina Kondratovich, Lisa M. McShane, Anthony P. Reeves, Daniel P. Barboriak, Alexander R. Guimaraes, and Richard L. Wahl. Metrology Standards for Quantitative Imaging Biomarkers. *Radiology*, 277(3):813–825, 2015. doi:10.1148/radiol.2015142202. → pages 105
- [177] Nikola Stikov, Mathieu Boudreau, Ives R Levesque, Christine L Tardif, Joelle K Barral, and G Bruce Pike. On the Accuracy of T1 Mapping: Searching for Common Ground. *Magnetic Resonance in Medicine*, 73:514–522, 2015. doi:10.1002/mrm.25135. → pages 111, 191
- [178] Sean C L Deoni, Steven C R Williams, Peter Jezzard, John Suckling, Declan G M Murphy, and Derek K Jones. Standardized structural magnetic resonance imaging in multicentre studies using quantitative T1 and T2 imaging at 1.5T. *NeuroImage*, 40:662–671, 2008. doi:10.1016/j.neuroimage.2007.11.052. → pages 111
- [179] Nikolaus Weiskopf, John Suckling, Guy Williams, Marta M. Correia, Becky Inkster, Roger Tait, Cinly Ooi, Edward T. Bullmore, and Antoine Lutti. Quantitative multi-parameter mapping of R1, PD\*, MT, and R2\* at 3T: a multi-center validation. *Frontiers in Neuroscience*, 7(95):1–11, 2013. doi:10.3389/fnins.2013.00095. → pages 111
- [180] Stephen M. Smith. Fast robust automated brain extraction. *Human Brain Mapping*, 17(3):143–155, 2002. doi:10.1002/hbm.10062. → pages 112

- [181] Markus Weiger, Romain Nicolas Froidevaux, David Otto Brunner, Manuela Barbara Rosler, and Klaas Paul Pruessmann. Advances in Direct Myelin Imaging. In *Proceedings of the 27th Annual meeting ISMRM*, page 1118, Montreal, QC, Canada, 2019. → pages 112
- [182] R. M. Henkelman, G. J. Stanisz, and S. J. Graham. Magnetization transfer in MRI: A review. *NMR in Biomedicine*, 14(2):57–64, 2001. doi:10.1002/nbm.683. → pages 112, 113, 185
- [183] Daniel A. Finelli and Damon R. Reed. Flip angle dependence of experimentally determined T1(sat) and apparent magnetization transfer rate constants. *Journal of Magnetic Resonance Imaging*, 8(3):548–553, 1998. doi:10.1002/jmri.1880080306. → pages 112
- [184] Stefan Ropele, Rudolf Stollberger, Hans Peter Hartung, and Franz Fazekas. Estimation of magnetization transfer rates from PACE experiments with pulsed RF saturation. *Journal of Magnetic Resonance Imaging*, 12(5):749–756, 2000. doi:10.1002/1522-2586(200011)12:5<749::AID-JMRI13>3.0.CO;2-2. → pages 112, 113
- [185] Lin Wei and Kwon Song Hee. Improved signal spoiling in fast radial gradient-echo imaging: Applied to accurate T1 mapping and flip angle correction. *Magnetic Resonance in Medicine*, 62(5):1185–1194, 2009. doi:10.1002/mrm.22089. → pages 114
- [186] Bo Zhao, Wenmiao Lu, T. Kevin Hitchens, Fan Lam, Chien Ho, and Zhi Pei Liang. Accelerated MR parameter mapping with low-rank and sparsity constraints. *Magnetic Resonance in Medicine*, 74(2):489–498, 2015. doi:10.1002/mrm.25421. → pages 116
- [187] Tao Zhang, John M. Pauly, and Ives R. Levesque. Accelerating parameter mapping with a locally low rank constraint. *Magnetic Resonance in Medicine*, 73(2):655–661, 2015. doi:10.1002/mrm.25161. → pages 116
- [188] U.S. Food and Drug Administration. FDA clears first 7T magnetic resonance imaging device, 2017. URL <https://www.fda.gov/news-events/press-announcements/fda-clears-first-7t-magnetic-resonance-imaging-device>. → pages 119

- [189] Martin Graves, Paul Malcolm, Alex Lipton, Erica Scurr, and Horne. Magnetic Resonance Imaging (MRI) Equipment, Operations and Planning in the NHS. Report from the Clinical Imaging Board, 2017. → pages 119
- [190] Paul T. Callaghan. *Principles of nuclear magnetic resonance microscopy*. Oxford University Press on Demand, 1993. ISBN 0198539975. → pages 124
- [191] Paul A Bottomley, Thomas H Foster, Raymond E Argersinger, and Leah M Pfeifer. A review of normal tissue hydrogen NMR relaxation times and relaxation mechanisms from 1–100 MHz: Dependence on tissue type, NMR frequency, temperature, species, excision, and age. *Medical Physics*, 11(4):425–448, 1984. doi:10.1118/1.595535. → pages 124, 125, 141, 144
- [192] Helmut W. Fischer, Peter A. Rinck, Yves van Haverbeke, and Robert N. Muller. Nuclear relaxation of human brain gray and white matter: Analysis of field dependence and implications for MRI. *Magnetic Resonance in Medicine*, 16(2):317–334, 1990. doi:10.1002/mrm.1910160212. → pages 125, 144
- [193] W. A. Edelstein, G. H. Glover, C. J. Hardy, and R. W. Redington. The intrinsic signal-to-noise ratio in NMR imaging. *Magnetic Resonance in Medicine*, 3(4):604–618, 1986. doi:10.1002/mrm.1910030413. → pages 126
- [194] Steffen Volz, Ulrike Nöth, and Ralf Deichmann. Correction of systematic errors in quantitative proton density mapping. *Magnetic Resonance in Medicine*, 68(1):74–85, 2012. doi:10.1002/mrm.23206. → pages 128
- [195] Anup Singh, Kejia Cai, Mohammad Haris, Hari Hariharan, and Ravinder Reddy. On B1 inhomogeneity correction of in vivo human brain glutamate chemical exchange saturation transfer contrast at 7T. *Magnetic Resonance in Medicine*, 69(3):818–824, 2013. doi:10.1002/mrm.24290. → pages 131
- [196] Mark Jenkinson, Christian F. Beckmann, Timothy E.J. Behrens, Mark W. Woolrich, and Stephen M. Smith. Fsl. *NeuroImage*, 62(2):782–790, 2012. doi:10.1016/j.neuroimage.2011.09.015. → pages 137, 213
- [197] Hampus Olsson, Mads Andersen, Jimmy Lätt, Ronnie Wirestam, and Gunther Helms. Reducing bias in dual flip angle T1-mapping in human brain at 7T. *Magnetic*

- Resonance in Medicine*, 00:1–12, 2020. doi:10.1002/mrm.28206. → pages 142, 145, 146, 147
- [198] Yicun Wang, Peter van Gelderen, Jacco A. de Zwart, and Jeff H. Duyn. B0-field dependence of MRI T1 relaxation in human brain. *NeuroImage*, 213(February), 2020. doi:10.1016/j.neuroimage.2020.116700. → pages 145
- [199] Umamaheswar Duvvuri, David A. Roberts, J. S. Leigh, and Lizann Bolinger. Magnetization transfer imaging of the brain: A quantitative comparison of results obtained at 1.5 and 4.0 T. *Journal of Magnetic Resonance Imaging*, 10(4):527–532, 1999. doi:10.1002/(SICI)1522-2586(199910)10:4<527::AID-JMRI5>3.0.CO;2-0. → pages 145
- [200] Matthias J. P. van Osch and Andrew G. Webb. Safety of Ultra-High Field MRI: What are the Specific Risks? *Current Radiology Reports*, 2(8):61, 2014. doi:10.1007/s40134-014-0061-0. → pages 147, 149
- [201] Kieran R. O’Brien, Tobias Kober, Patric Hagmann, Philippe Maeder, José Marques, Francois Lazeyras, Gunnar Krueger, and Alexis Roche. Robust T1-weighted structural brain imaging and morphometry at 7T using MP2RAGE. *PLoS ONE*, 9(6): 1–7, 2014. doi:10.1371/journal.pone.0099676. → pages 148
- [202] Emil Ljungberg, Florian Wiesinger, and Tobias C Wood. Silent Structural Imaging and T1-mapping with a Rapid-Radial Twice-Prepared (R2P2) Sequence. In *Proc. Intl. Soc. Mag. Reson. Med 27*, page 4636, Montreal, 2019. → pages 148, 149, 152, 250
- [203] Mark Symms, Florian Wiesinger, Mauro Costagli, Doug Kelley, Mirco Cosottini, and Michela Tosetti. Silent Corrected Using Second Image (SCUSI) - Application of the MP2RAGE formalism to T1-weighted Zero Time Echo Imaging. In *Proc. Intl. Soc. Mag. Reson. Med 26*, page 2048, Paris, 2018. → pages 148
- [204] Emil Ljungberg, Brian Burns, Tobias Wood, Shannon Kolind, Florian Wiesinger, and Gareth J Barker. Rapid, multi-TE, T2-prepared RUFIS for Silent T2-weighted imaging. In *Proc. Intl. Soc. Mag. Reson. Med 27*, page 4571, Montreal, 2019. → pages 149, 152

- [205] Florian Wiesinger, Martin A Janich, Emil Ljungberg, Gareth J Barker, and Ana Beatriz Solana. Silent, 3D MR Parameter Mapping using Magnetization Prepared Zero TE. In *Proc. Intl. Soc. Mag. Reson. Med 26*, page 0061, Paris, 2018. → pages 152, 166, 194
- [206] Tobias C Wood, Emil Ljungberg, Ana-beatriz Solana Sanchez, and Florian Wiesinger. Silent Myelin Imaging with a dipolar-coupled / inhomogeneous MT-Prepared ZTE Radial Sequence. In *Proc. Intl. Soc. Mag. Reson. Med 27*, page 4896, Montreal, 2019. → pages 152
- [207] Xin Liu, Pedro Gomez, Tim Sprenger, Ana-Beatriz Solana Sanchez, Florian Wiesinger, Marion Menzel, Jonathan Sperl, and Bjoern Menze. Fast, Volumetric and Silent Multi-contrast Zero Echo Time Imaging. In *Proc. Intl. Soc. Mag. Reson. Med 25*, page 4035, 2017. → pages 152
- [208] Michael Garwood and Yong Ke. Symmetric pulses to induce arbitrary flip angles with compensation for RF inhomogeneity and resonance offsets. *Journal of Magnetic Resonance (1969)*, 94(3):511–525, 1991. doi:10.1016/0022-2364(91)90137-I. → pages 152, 154
- [209] Michael Garwood and Lance DelaBarre. The return of the frequency sweep: Designing adiabatic pulses for contemporary NMR. *Journal of Magnetic Resonance*, 153(2):155–177, 2001. doi:10.1006/jmre.2001.2340. → pages 152, 154
- [210] David G. Norris. Adiabatic radiofrequency pulse forms in biomedical nuclear magnetic resonance. *Concepts in Magnetic Resonance Part B: Magnetic Resonance Engineering*, 14(2):89–101, 2002. doi:10.1002/cmr.10007. → pages 152
- [211] Thanh D. Nguyen, Kofi Deh, Elizabeth Monohan, Sneha Pandya, Pascal Spince-maille, Ashish Raj, Yi Wang, and Susan A. Gauthier. Feasibility and Reproducibility of Whole Brain Myelin Water Mapping in 4 Minutes Using Fast Acquisition with Spiral Trajectory and Adiabatic T2prep (FAST-T2) at 3T. *Magnetic Resonance in Medicine*, 72(2):456–465, 2016. doi:10.1002/mrm.25877. → pages 152, 153, 154, 159
- [212] John P. Mugler III, Thomas A. Spraggins, and James R. Brookeman. T2-weighted Three-dimensional MP-RAGE MR Imaging. *Journal of Magnetic Resonance Imaging*, 1:731–737, 1991. doi:10.1002/jmri.1880010621. → pages 153

- [213] R. Deichmann, H. Adolf, U. Noth, S. Morrissey, C. Schwarzbauer, and A. Haase. Fast T2-mapping with SNAPSHOT FLASH Imaging. *Magnetic Resonance Imaging*, 13(4):633–639, 1995. → pages 153
- [214] Joonmi Oh, Eric T. Han, Daniel Pelletier, and Sarah J. Nelson. Measurement of in vivo multi-component T2 relaxation times for brain tissue using multi-slice T2 prep at 1.5 and 3 T. *Magnetic Resonance Imaging*, 24(1):33–43, 2006. doi:10.1016/j.mri.2005.10.016. → pages 153
- [215] Bram F. Coolen, Frank F.J. Simonis, Tessa Geelen, Rik P.M. Moonen, Fatih Arslan, Leonie E.M. Paulis, Klaas Nicolay, and Gustav J. Strijkers. Quantitative T2 mapping of the mouse heart by segmented MLEV phase-cycled T2 preparation. *Magnetic Resonance in Medicine*, 72(2):409–417, 2014. doi:10.1002/mrm.24952. → pages 153
- [216] Peng Cao, Xucheng Zhu, Shuyu Tang, Andrew Leynes, Angela Jakary, and Peder E.Z. Larson. Shuffled magnetization-prepared multicontrast rapid gradient-echo imaging. *Magnetic Resonance in Medicine*, 79(1):62–70, 2018. doi:10.1002/mrm.26986. → pages 154, 166, 260
- [217] Reza Nezafat, Ronald Ouwerkerk, Andrew J. Derbyshire, Matthias Stuber, and Elliot R. McVeigh. Spectrally selective B1-insensitive T2 magnetization preparation sequence. *Magnetic Resonance in Medicine*, 61(6):1326–1335, 2009. doi:10.1002/mrm.21742. → pages 154
- [218] Elizabeth R. Jenista, Wolfgang G. Rehwald, Enn Ling Chen, Han W. Kim, Igor Klem, Michele A. Parker, and Raymond J. Kim. Motion and flow insensitive adiabatic T2-preparation module for cardiac MR imaging at 3 tesla. *Magnetic Resonance in Medicine*, 70(5):1360–1368, 2013. doi:10.1002/mrm.24564. → pages 154
- [219] Robin A. de Graaf, Douglas L. Rothman, and Kevin L. Behar. Adiabatic RARE imaging. *NMR in Biomedicine*, 16(1):29–35, 2003. doi:10.1002/nbm.811. → pages 154
- [220] Irene M.L. Van Kalleveen, Wouter Koning, Vincent O. Boer, Peter R. Luijten, Jaco J.M. Zwanenburg, and Dennis W.J. Klomp. Adiabatic turbo spin echo in human applications at 7T. *Magnetic Resonance in Medicine*, 68(2):580–587, 2012. doi:10.1002/mrm.23264. → pages 154

- [221] G. Wang, A. M. El-Sharkawy, W. A. Edelstein, M. Schär, and P. A. Bottomley. Measuring T2 and T1, and imaging T2 without spin echoes. *Journal of Magnetic Resonance*, 214:273–280, 2012. doi:10.1016/j.jmr.2011.11.016. → pages 154
- [222] Dominik Weidlich, Sarah Schlaeger, Hendrik Kooijman, Peter Börnert, Jan S. Kirschke, Ernst J. Rummeny, Axel Haase, and Dimitrios C. Karampinos. T2 mapping with magnetization-prepared 3D TSE based on a modified BIR-4 T2preparation. *NMR in Biomedicine*, 30(11):1–14, 2017. doi:10.1002/nbm.3773. → pages 154
- [223] Anton J. Johnson, Michael Garwood, and Kamil Ugurbil. Slice Selection with Gradient-Modulated Adiabatic Excitation Despite the Presence of Large B1 Inhomogeneities. *Journal of Magnetic Resonance*, 81:653–660, 1989. doi:10.1016/0022-2364(89)90109-1. → pages 154
- [224] R. Scott Staewen, Anton J Johnson, Brian D. Ross, Todd Parrish, Hellmut Merkle, and Michael Garwood. 3-D FLASH Imaging Using a Single Surface Coil and a New Adiabatic Pulse, BIR-4. *Investigative radiology*, 25:559–567, 1989. doi:10.1097/00004424-199005000-00015. → pages 154
- [225] Nicolas Boulant. T1 and T2 effects during radio-frequency pulses in spoiled gradient echo sequences. *Journal of Magnetic Resonance*, 197(2):213–218, 2009. doi:10.1016/j.jmr.2008.12.023. → pages 155
- [226] Tim Sinnecker, Paul Mittelstaedt, Jan Dörr, Caspar F. Pfueller, Lutz Harms, Thoralf Niendorf, Friedemann Paul, and Jens Wuerfel. Multiple sclerosis lesions and irreversible brain tissue damage: a comparative ultrahigh-field strength magnetic resonance imaging study. *Archives of neurology*, 69(6):739–745, 2012. doi:10.1001/archneurol.2011.2450. → pages 165
- [227] Wallace J Brownlee, Todd A Hardy, Franz Fazekas, and David H Miller. Diagnosis of multiple sclerosis: progress and challenges. *The Lancet*, 6736(16):1–11, 2016. doi:10.1016/S0140-6736(16)30959-X. → pages 165
- [228] D. C. Look and D. R. Locker. Time saving in measurement of NMR and EPR relaxation times. *Review of Scientific Instruments*, 41(2):250–251, 1970. doi:10.1063/1.1684482. → pages 166

- [229] M. S. Silver, R. I. Joseph, and D. I. Hoult. Highly selective  $\pi/2$  and  $\pi$  pulse generation. *Journal of Magnetic Resonance (1969)*, 59(2):347–351, 1984. doi:10.1016/0022-2364(84)90181-1. → pages 167
- [230] Siu Kwan Lam, Antoine Pitrou, and Stanley Seibert. Numba: A llvm-based python jit compiler. In *Proceedings of the Second Workshop on the LLVM Compiler Infrastructure in HPC*, page 7. ACM, 2015. doi:10.1145/2833157.2833162. → pages 170
- [231] Matt Newville, Renee Otten, Andrew Nelson, Antonino Ingargiola, Till Stensitzki, Dan Allan, Austin Fox, Faustin Carter, Michał, Dima Pustakhod, Yoav Ram, Glenn, Christoph Deil, Stuermer, Alexandre Beelen, Oliver Frost, Nicholas Zobrist, Gustavo Pasquevich, Allan L R Hansen, Alexander Stark, Tim Spillane, Shane Caldwell, Anthony Polloreno, Andrewhannum, Jose Borreguero, Jonathan Fraine, Deep-42-thought, Benjamin F Maier, Ben Gamari, and Anthony Almarza. lmfit/lmfit-py 0.9.14, aug 2019. URL <https://doi.org/10.5281/zenodo.3381550>. → pages 170
- [232] Kenneth P. Whittall. Recovering Compartment Sizes from NMR Relaxation Data. *Journal of Magnetic Resonance*, 94:486–492, 1991. doi:10.1016/0022-2364(91)90134-F. → pages 172
- [233] Lazar Fleysher, Roman Fleysher, Songtao Liu, Wafaa Zaaraoui, and Oded Gonen. Optimizing the precision-per-unit-time of quantitative MR metrics: Examples for T1, T2, and DTI. *Magnetic Resonance in Medicine*, 57(2):380–387, 2007. doi:10.1002/mrm.21144. → pages 172, 174
- [234] Roman Fleysher, Lazar Fleysher, and Oded Gonen. The optimal MR acquisition strategy for exponential decay constants estimation. *Magnetic Resonance Imaging*, 26(3):433–435, 2008. doi:10.1016/j.mri.2007.08.014. → pages 172
- [235] R. I. Shrager, G. H. Weiss, and R. G.S. Spencer. Optimal time spacings for T2 measurements: Monoexponential and biexponential systems. *NMR in Biomedicine*, 11(6):297–305, 1998. doi:10.1002/(SICI)1099-1492(199810)11:6<297::AID-NBM531>3.0.CO;2-A. → pages 172, 173, 174
- [236] Shaihan J. Malik, Rui Pedro A.G. Teixeira, and Joseph V. Hajnal. Extended phase graph formalism for systems with magnetization transfer and exchange. *Magnetic*



- Resonance in Medicine*, 80(2):767–779, 2018. doi:10.1002/mrm.27040. → pages 179, 186
- [237] Tom Hilbert, Ding Xia, Kai Tobias Block, Zidan Yu, Riccardo Lattanzi, Daniel K. Sodickson, Tobias Kober, and Martijn A. Cloos. Magnetization Transfer in Magnetic Resonance Fingerprinting. *Magnetic Resonance in Medicine*, 00(October):1–14, 2019. doi:10.1002/mrm.28096. → pages 183, 191
- [238] Dan Ma, Yun Jiang, Yong Chen, Debra McGivney, Bhairav Mehta, Vikas Gulani, and Mark Griswold. Fast 3D magnetic resonance fingerprinting for a whole-brain coverage. *Magnetic Resonance in Medicine*, 79(4):2190–2197, 2018. doi:10.1002/mrm.26886. → pages 183
- [239] P. Walker, R.A. Lerski, R. Mathur-De Vre, J. Binet, and F Yane. VI. Preparation of Agarose Gels as Reference Substances for NMR Relaxation Time Measurement. *Magnetic Resonance Imaging*, 6:215–222, 1988. doi:10.1016/0730-725X(88)90452-3. → pages 185
- [240] R. Mark Henkelman, Xuemei Huang, Qing-San Xiang, G. J. Stanisz, Scott D. Swanson, and Michael J. Bronskill. Quantitative interpretation of magnetization transfer. *Magnetic Resonance in Medicine*, 29(6):759–766, 1993. doi:10.1002/mrm.1910290607. → pages 185
- [241] John G. Sled and G. Bruce Pike. Quantitative Interpretation of Magnetization Transfer in Spoiled Gradient Echo MRI Sequences. *Journal of Magnetic Resonance*, 145(1):24–36, 2000. doi:10.1006/jmre.2000.2059. → pages 185
- [242] Monika Gloor, K. Scheffler, and O. Bieri. Quantitative magnetization transfer imaging using balanced SSFP. *Magnetic Resonance in Medicine*, 60(3):691–700, 2008. doi:10.1002/mrm.21705. → pages 185
- [243] Ives R. Levesque, Paul S. Giacomini, Sridar Narayanan, Luciana T. Ribeiro, John G. Sled, Doug L. Arnold, and G. Bruce Pike. Quantitative magnetization transfer and myelin water imaging of the evolution of acute multiple sclerosis lesions. *Magnetic Resonance in Medicine*, 63(3):633–640, 2010. doi:10.1002/mrm.22244. → pages 186
- [244] Alfonso Lema, Courtney Bishop, Omar Malik, Miriam Mattoscio, Rehiana Ali, Richard Nicholas, Paolo A. Muraro, Paul M. Matthews, Adam D. Waldman, and

- Rexford D. Newbould. A Compararison of Magnetization Transfer Methods to Assess Brain and Cervical Cord Microstructure in Multiple Sclerosis. *Journal of Neuroimaging*, 27(2):221–226, 2017. doi:10.1111/jon.12377. → pages 186
- [245] John G. Sled. Modelling and interpretation of magnetization transfer imaging in the brain. *NeuroImage*, 182(15):128–135, 2018. doi:10.1016/j.neuroimage.2017.11.065. → pages 186
- [246] Harden M. McConnell. Reaction rates by nuclear magnetic resonance. *The Journal of Chemical Physics*, 28(3):430–431, 1958. doi:10.1063/1.1744152. → pages 187
- [247] Samira Mchinda, Gopal Varma, Valentin H. Prevost, Arnaud Le Troter, Stanislas Rapacchi, Maxime Guye, Jean Pelletier, Jean Philippe Ranjeva, David C. Alsop, Guillaume Duhamel, and Olivier M. Girard. Whole brain inhomogeneous magnetization transfer (ihMT) imaging: Sensitivity enhancement within a steady-state gradient echo sequence. *Magnetic Resonance in Medicine*, 79(5):2607–2619, 2018. doi:10.1002/mrm.26907. → pages 187, 188
- [248] Sean C L Deoni, Lucy Matthews, and Shannon H. Kolind. One component? Two components? Three? the effect of including a nonexchanging "free" water component in multicomponent driven equilibrium single pulse observation of T1 and T2. *Magnetic Resonance in Medicine*, 70(1):147–154, 2013. doi:10.1002/mrm.24429. → pages 191
- [249] Kathryn E Keenan, Joshua R Biller, Jana G Del, Michael A Boss, Mark D Does, Jeffrey L Evelhoch, Mark A Griswold, Jeffrey L Gunter, R Scott Hinks, Stuart W Hoffman, Geena Kim, Riccardo Lattanzi, Xiaojuan Li, Luca Marinelli, Gregory J Metzger, Pratik Mukherjee, Robert J Nordstrom, Adele P Peskin, Elena Perez, Stephen E Russek, Berkman Sahiner, Natalie Serkova, Amita Shukla-dave, Michael Steckner, Karl F Stupic, Lisa J Wilmes, Holden H Wu, Huiming Zhang, Edward F. Jackson, and Daniel C. Sullivan. Recommendations Towards Standards for Quantitative MRI (qMRI) and Outstanding Needs. *Journal of Magnetic Resonance Imaging*, 49(7):e25–e39, 2019. doi:10.1002/jmri.26598. → pages 191
- [250] Yulia Shcherbakova, Cornelis A T Van Den Berg, Chrit T W Moonen, and Lambertus W Bartels. PLANET: An Ellipse Fitting Approach for Simultaneous T1 and

- T2 Mapping Using Phase-Cycled Balanced Steady-State Free Precession. *Magnetic Resonance in Medicine*, 79(2):711–722, 2018. doi:10.1002/mrm.26717. → pages 191
- [251] Rolf F. Schulte, Guido Buonincontri, Mauro Costagli, Anne Menini, Florian Wiesinger, and Ana Beatriz Solana. Silent T2\* and T2 encoding using ZTE combined with BURST. *Magnetic Resonance in Medicine*, 81(4):2277–2287, 2018. doi:10.1002/mrm.27552. → pages 192
- [252] Daniel Stucht, K. Appu Danishad, Peter Schulze, Frank Godenschweger, Maxim Zaitsev, and Oliver Speck. Highest resolution in vivo human brain MRI using prospective motion correction. *PLoS ONE*, 10(7):1–17, 2015. doi:10.1371/journal.pone.0133921. → pages 196
- [253] F. Godenschweger, U. Kägebein, D. Stucht, U. Yarach, A. Sciarra, R. Yakupov, F. Lüsebrink, P. Schulze, and O. Speck. Motion correction in MRI of the brain. *Physics in Medicine and Biology*, 61(5):R32–R56, 2016. doi:10.1088/0031-9155/61/5/R32. → pages 196
- [254] M. Zaitsev, C. Dold, G. Sakas, J. Hennig, and O. Speck. Magnetic resonance imaging of freely moving objects: prospective real-time motion correction using an external optical motion tracking system. *NeuroImage*, 31(3):1038–1050, 2006. doi:10.1016/j.neuroimage.2006.01.039. → pages 197
- [255] Lei Qin, Peter Van Gelderen, John Andrew Derbyshire, Fenghua Jin, Jongho Lee, Jacco A. De Zwart, Yang Tao, and Jeff H. Duyn. Prospective head-movement correction for high-resolution MRI using an in-bore optical tracking system. *Magnetic Resonance in Medicine*, 62(4):924–934, 2009. doi:10.1002/mrm.22076. → pages 197
- [256] Phillip Digiaco, Julian Maclaren, Murat Aksoy, Elizabeth Tong, Mackenzie Carlson, Bryan Lanzman, Syed Hashmi, Ronald Watkins, Jarrett Rosenberg, Brian Burns, Timothy W Skloss, Dan Rettmann, Brian Rutt, Roland Bammer, and Michael Zeineh. A within-coil optical prospective motion-correction system for brain imaging at 7T. *Magnetic Resonance in Medicine*, 00(July 2019):1–11, 2020. doi:10.1002/mrm.28211. → pages 197
- [257] Robert Frost, Paul Wighton, F. Işık Karahanoğlu, Richard L. Robertson, P. Ellen Grant, Bruce Fischl, M. Dylan Tisdall, and André van der Kouwe. Markerless high-

- frequency prospective motion correction for neuroanatomical MRI. *Magnetic Resonance in Medicine*, 82(1):126–144, 2019. doi:10.1002/mrm.27705. → pages 197
- [258] Melvyn B. Ooi, Sascha Krueger, William J. Thomas, Srirama V. Swaminathan, and Truman R. Brown. Prospective real-time correction for arbitrary head motion using active markers. *Magnetic Resonance in Medicine*, 62(4):943–954, 2009. doi:10.1002/mrm.22082. → pages 197
- [259] Saikat Sengupta, Sasidhar Tadanki, John C. Gore, and E. Brian Welch. Prospective real-time head motion correction using inductively coupled wireless NMR probes. *Magnetic Resonance in Medicine*, 72(4):971–985, 2014. doi:10.1002/mrm.25001. → pages 197
- [260] André J.W. Van Der Kouwe, Thomas Benner, and Anders M. Dale. Real-time rigid body motion correction and shimming using cloverleaf navigators. *Magnetic Resonance in Medicine*, 56(5):1019–1032, 2006. doi:10.1002/mrm.21038. → pages 197
- [261] Zhuo Wu Fu, Y. Wang, R. C. Grimm, P. J. Rossman, J. P. Felmlee, S. J. Riederer, and R. L. Ehman. Orbital navigator echoes for motion measurements in magnetic resonance imaging. *Magnetic Resonance in Medicine*, 34:746–753, 1995. doi:10.1002/mrm.1910340514. → pages 198
- [262] Edward Brian Welch, Armando Manduca, Roger C Grimm, Heidi A Ward, and Clifford R Jack. Spherical Navigator Echoes for Full 3D Rigid Body Motion Measurement in MRI. *Magnetic Resonance in Medicine*, 47:32–41, 2002. doi:10.1002/mrm.10012. → pages 198, 199, 215, 216, 223, 228, 241, 253
- [263] James G Pipe. Motion Correction With PROPELLER MRI: Application to Head Motion and Free-Breathing Cardiac Imaging. *Magnetic Resonance in Medicine*, 42: 963–969, 1999. doi:10.1002/(SICI)1522-2594(199911)42:5<963::AID-MRM17>3.0.CO; 2-L. → pages 198, 199, 213, 214, 215, 218, 229
- [264] Nathan White, Cooper Roddey, Ajit Shankaranarayanan, Eric Han, Dan Rettmann, Juan Santos, Josh Kuperman, and Anders Dale. PROMO: Real-Time Prospective Motion Correction in MRI Using Image-Based Tracking. *Magnetic Resonance in Medicine*, 63:91–105, 2010. doi:10.1002/mrm.22176. → pages 198, 228

- [265] M Dylan Tisdall, Aaron T Hess, Martin Reuter, Ernesta M Meintjes, Bruce Fischl, and André J W van der Kouwe. Volumetric Navigators for Prospective Motion Correction and Selective Reacquisition in Neuroanatomical MRI. *Magnetic Resonance in Medicine*, 68:389–399, 2012. doi:10.1002/mrm.23228. → pages 198
- [266] Daniel W. Petrie, Andreu F. Costa, Atsushi Takahashi, Yi Fen Yen, and Maria Drangova. Optimizing spherical navigator echoes for three-dimensional rigid-body motion detection. *Magnetic Resonance in Medicine*, 53(5):1080–1087, 2005. doi:10.1002/mrm.20445. → pages 198, 216, 241, 253
- [267] Edward Brian Welch, Phillip J. Rossman, Joel P. Felmlee, and Armando Manduca. Self-navigated motion correction using moments of spatial projections in radial MRI. *Magnetic Resonance in Medicine*, 52(2):337–345, 2004. doi:10.1002/mrm.20151. → pages 198
- [268] Sungheon Kim, Lawrence Dougherty, Mark A. Rosen, Hee Kwon Song, and Harish Poptani. Automatic correction of in-plane bulk motion artifacts in self-navigated radial MRI. *Magnetic Resonance Imaging*, 26(3):367–378, 2008. doi:10.1016/j.mri.2007.08.001. → pages 198
- [269] G.J. Mitchison. Phyllotaxis and the Fibonacci Series. *Science*, 196(4287):270–275, 1977. → pages 13, 199, 200
- [270] Helmus Vogel. A Better Way to Construct the Sunflower Head. *Mathematical Biosciences*, 44:179–189, 1979. doi:10.1016/0025-5564(79)90080-4. → pages 199, 263, 264
- [271] Thomas Köhler. A projection access scheme for iterative reconstruction based on the golden section. *IEEE Nuclear Science Symposium Conference Record*, 6(C):3961–3965, 2004. doi:10.1109/nssmic.2004.1466745. → pages 200, 202, 265, 266, 267
- [272] Stefanie Winkelmann, Tobias Schaeffter, Thomas Koehler, Holger Eggers, and Olaf Doessel. An optimal radial profile order based on the golden ratio for time-resolved MRI. *IEEE Transactions on Medical Imaging*, 26(1):68–76, 2007. doi:10.1109/TMI.2006.885337. → pages 200, 202, 265, 266

- [273] Simone Coppo, Davide Piccini, Gabriele Bonanno, Jérôme Chaptinel, Gabriella Vincenti, Hélène Feliciano, Ruud B. Van Heeswijk, Juerg Schwitter, and Matthias Stuber. Free-running 4D whole-heart self-navigated golden angle MRI: Initial results. *Magnetic Resonance in Medicine*, 74(5):1306–1316, 2015. doi:10.1002/mrm.25523. → pages 200
- [274] Li Feng, Robert Grimm, Kai Tobias Block, Hersh Chandarana, Sungheon Kim, Jian Xu, Leon Axel, Daniel K. Sodickson, and Ricardo Otazo. Golden-angle radial sparse parallel MRI: Combination of compressed sensing, parallel imaging, and golden-angle radial sampling for fast and flexible dynamic volumetric MRI. *Magnetic Resonance in Medicine*, 72(3):707–717, 2015. doi:10.1002/mrm.24980. → pages 200
- [275] Richard Swinbank and R. James Purser. Fibonacci grids: A novel approach to global modelling. *Quarterly Journal of the Royal Meteorological Society*, 132(619):1769–1793, 2006. doi:10.1256/qj.05.227. → pages 201
- [276] J. H. Cole, S. J. Ritchie, M. E. Bastin, M. C. Valdés Hernández, S. Muñoz Maniega, N. Royle, J. Corley, A. Pattie, S. E. Harris, Q. Zhang, N. R. Wray, P. Redmond, R. E. Marioni, J. M. Starr, S. R. Cox, J. M. Wardlaw, D. J. Sharp, and I. J. Deary. Brain age predicts mortality. *Molecular Psychiatry*, 23(5):1385–1392, 2018. doi:10.1038/mp.2017.62. → pages 211
- [277] C D Kuglin and D C Hines. The phase correlation image alignment method. In *IEEE International Conference on Cybernetics and Society*, pages 163–165, New York, 1975. → pages 213
- [278] Jignesh Sarvaiya, Suprava Patnaik, and Kajal Kothari. Image Registration Using Log Polar Transform and Phase Correlation to Recover Higher Scale. *Journal of Pattern Recognition Research*, 7:90–105, 2012. doi:10.13176/11.355. → pages 213
- [279] James G. Pipe, Wende N. Gibbs, Zhiqiang Li, John P. Karis, Michael Schar, and Nicholas R. Zwart. Revised motion estimation algorithm for PROPELLER MRI. *Magnetic Resonance in Medicine*, 72(2):430–437, 2014. doi:10.1002/mrm.24929. → pages 213, 241

- [280] Jakub Bican and Jan Flusser. 3D Rigid registration by cylindrical phase correlation method. *Pattern Recognition Letters*, 30(10):914–921, 2009. doi:10.1016/j.patrec.2009.03.015. → pages 213, 215
- [281] W. Scott Hoge and Carl Fredrik Westin. Identification of translational displacements between N-dimensional data sets using the high-order SVD and phase correlation. *IEEE Transactions on Image Processing*, 14(7):884–889, 2005. doi:10.1109/TIP.2005.849327. → pages 213
- [282] Luis C. Maas, Blaise De B. Frederick, and Perry F. Renshaw. Decoupled automated rotational and translational registration for functional MRI time series data: The DART registration algorithm. *Magnetic Resonance in Medicine*, 37(1):131–139, 1997. doi:10.1002/mrm.1910370119. → pages 214, 218, 223
- [283] Yosi Keller, Yoel Shkolnisky, and Amir Averbuch. Volume registration using the 3-D pseudopolar Fourier transform. *IEEE Transactions on Signal Processing*, 54(11):4323–4331, 2006. doi:10.1109/TSP.2006.881217. → pages 215
- [284] Remi K S. Kwan, Alan C Evans, and G Bruce Pike. An extensible MRI simulator for post-processing evaluation. In Karl Heinz Höhne and Ron Kikinis, editors, *Höhne K.H., Kikinis R. (eds) Visualization in Biomedical Computing. VBC 1996. Lecture Notes in Computer Science, vol 1131*, pages 135–140, Berlin, Heidelberg, 1996. Springer Berlin Heidelberg. ISBN 978-3-540-70739-4. → pages 215
- [285] D L Collins, A P Zijdenbos, V Kollokian, J G Sled, N J Kabani, C J Holmes, and A C Evans. Design and construction of a realistic digital brain phantom. *IEEE Transactions on Medical Imaging*, 17(3):463–468, 1998. doi:10.1109/42.712135. → pages 215
- [286] Andreu F. Costa, Yi Fen Yen, and Maria Drangova. Registering spherical navigators with spherical harmonic expansions to measure three-dimensional rotations in magnetic resonance imaging. *Magnetic Resonance Imaging*, 28(2):185–194, 2010. doi:10.1016/j.mri.2009.07.010. → pages 216, 240
- [287] Mark De Berg, Otfried Cheong, and Marc Van Kreveld. Delaunay Triangulations, Height Interpolation. In Mark Overmars, editor, *Computational Geometry: Algo-*

- rithms and Applications*, chapter 9, pages 191–218. Springer-Verlag, 2008. ISBN 9783540779735. doi:10.1007/978-3-662-04245-8. → pages 216
- [288] David Atkinson, Derek L.G. Hill, Peter N.R. Stoye, Paul E. Summers, and Stephen F. Keevil. Automatic correction of motion artifacts in magnetic resonance images using an entropy focus criterion. *IEEE Transactions on Medical Imaging*, 16(6):903–910, 1997. doi:10.1109/42.650886. → pages 218, 243
- [289] Lucilio Cordero-Grande, Giulio Ferrazzi, Rui Pedro A. G. Teixeira, Jonathan O’Muircheartaigh, Anthony N. Price, and Joseph V. Hajnal. Motion corrected MRI with DISORDER: Distributed and Incoherent Sample Orders for Reconstruction Deblurring using Encoding Redundancy. *Magnetic Resonance in Medicine*, 0(October 2019):1–14, 2019. doi:10.1002/mrm.28157. → pages 218, 243
- [290] Ronald N. Bracewell. *The Fourier Transform and Its Properties If*. McGraw-Hill Book - Singapore, 2000. ISBN 0-07-303938-1. → pages 219
- [291] Kai Tobias Block, Martin Uecker, and Jens Frahm. Undersampled radial MRI with multiple coils. Iterative image reconstruction using a total variation constraint. *Magnetic Resonance in Medicine*, 57(6):1086–1098, 2007. doi:10.1002/mrm.21236. → pages 229, 242
- [292] Frank Ong, Zhu Xucheng, Peder E.Z. Larson, Joseph Y Cheng, Shreyas S Vasanaawala, and Michael Lustig. Extreme MRI: Super-High-Res Dynamic Volumetric MRI from Continuous Non-Gated Acquisition. In *Proceedings of the 27th Annual Meeting of ISMRM.*, page 1176, Montreal, QC, Canada, 2019. → pages 229
- [293] Erik G. Larsson, Deniz Erdogmus, Rui Yan, Jose C. Principe, and Jeffrey R. Fitzsimmons. SNR-optimality of sum-of-squares reconstruction for phased-array magnetic resonance imaging. *Journal of Magnetic Resonance*, 163(1):121–123, 2003. doi:10.1016/S1090-7807(03)00132-0. → pages 236
- [294] I. Corcuera-Solano, A. Doshi, P. S. Pawha, D. Gui, A. Gaddipati, and Lawrence N. Tanenbaum. Quiet PROPELLER MRI techniques match the quality of conventional PROPELLER brain imaging techniques. *American Journal of Neuroradiology*, 36(6):1124–1127, 2015. doi:10.3174/ajnr.A4235. → pages 241, 249



- [295] Hyun Gi Kim, Jin Wook Choi, Soo Han Yoon, and Sieun Lee. Image quality assessment of silent T2 Propeller sequence for brain imaging in infants. *British Journal of Radiology*, 91(1083):1–6, 2018. doi:10.1259/bjr.20170680. → pages 241, 249
- [296] Douglas C. Noll, Dwight G. Nishimura, and Albert Macovski. Homodyne Detection in Magnetic Resonance Imaging. *IEEE Transactions on Medical Imaging*, 10(2): 154–163, 1991. doi:10.1109/42.79473. → pages 242
- [297] Tobias Kober, José P. Marques, Rolf Gruetter, and Gunnar Krueger. Head motion detection using FID navigators. *Magnetic Resonance in Medicine*, 66(1):135–143, 2011. doi:10.1002/mrm.22797. → pages 242
- [298] Kerstin Hammernik, Teresa Klatzer, Erich Kobler, Michael P. Recht, Daniel K. Sodickson, Thomas Pock, and Florian Knoll. Learning a variational network for reconstruction of accelerated MRI data. *Magnetic Resonance in Medicine*, 79(6): 3055–3071, 2018. doi:10.1002/mrm.26977. → pages 243
- [299] Hye Jeong Kim, Dae Young Yoon, Eun Soo Kim, Kwanseop Lee, Jong Seok Bae, and Ju-Hun Lee. The 100 most-cited articles in neuroimaging: A bibliometric analysis. *Neuroimage*, 139:149–156, 2016. doi:10.1016/j.neuroimage.2016.06.029. → pages 246
- [300] Waleed Brinjikji, Alexa Klunder, and David F. Kallmes. The 100 most-cited articles in the imaging literature. *Radiology*, 269(1):272–276, 2013. doi:10.1148/radiol.13122242. → pages 246
- [301] Markus Weiger, Klaas P. Pruessmann, Anna Katinka Bracher, Sascha Köhler, Volker Lehmann, Uwe Wolfram, Franciszek Hennel, and Volker Rasche. High-resolution ZTE imaging of human teeth. *NMR in Biomedicine*, 25(10):1144–1151, 2012. doi:10.1002/nbm.2783. → pages 247
- [302] Nicholas J. Tustison, Brian B. Avants, Philip A. Cook, Yuanjie Zheng, Alexander Egan, Paul A. Yushkevich, and James C. Gee. N4ITK: Improved N3 bias correction. *IEEE Transactions on Medical Imaging*, 29(6):1310–1320, 2010. doi:10.1109/TMI.2010.2046908. → pages 247
- [303] John I. Jackson, Dwight G. Nishimura, and Albert Macovski. Twisting Radial Lines with Application to Robust Magnetic Resonance Imaging of Irregular Flow. *Magnetic*

- Resonance in Medicine*, 25:128–139, 1992. doi:10.1002/mrm.1910250113. → pages 248
- [304] Fernando E. Boada, Joseph S. Gillen, Gary X. Shen, Sam Y. Chang, and Keith R. Thulborn. Fast three dimensional sodium imaging. *Magnetic Resonance in Medicine*, 37(5):706–715, 1997. doi:10.1002/mrm.1910370512. → pages 248
- [305] Johannes Kepler. *The Six-Cornered Snowflake*. Oxford University Press, 1966. ISBN 978-0-19-858120-8. URL <https://larouchepac.com/snowflake>. → pages 262
- [306] Eric W. Weisstein. Binet’s Fibonacci Number Formula, 2020. URL <https://mathworld.wolfram.com/BinetsFibonacciNumberFormula.html>. → pages 262